# Intelligent controller for a hybrid energy storage system

# MJ van Jaarsveld

iD orcid.org/ 0000-0001-7654-4440

Dissertation accepted in fulfilment of the requirements for the degree Master of Engineering in Electrical and Electronic Engineering at the

North-West University

Supervisor: Prof R Gouws

# Executive Summary

The performance and range of electric vehicles are largely determined by the characteristics of the electrical energy storage (EES) device used. The EES should be sufficiently sized to be able to provide the necessary power and energy requirements of the vehicle. Batteries are typically energy dense, although batteries that are both energy and power dense exist, they are much more expensive. The life and usable capacity of batteries are negatively impacted by power impulses. Battery packs in electric vehicles (EV) are typically oversized to be able to provide enough power during these impulses experienced when the vehicle accelerates.

Hybrid energy storage systems (HESS) have been proposed in the literature to solve these problems. HESS beneficially combines two or more EES devices with complementary characteristics. An additional EES device with a high-power density, such as an ultracapacitor, can be used as a buffer to provide power during power surges to reduce the power impulses experienced by the battery. Isolating the battery from the power impulses would allow the EV to utilize more energy dense batteries, increasing the range of the EV as well as increasing the lifetime of the utilized batteries.

The research presented in this paper documents the implementation of an active HESS that combined a battery pack and an ultracapacitor bank. The implemented HESS was used to reduce the peak-power that the battery needs to provide to the load. An active topology utilising two DC/DC converters and a switch was used to implement the hybrid energy storage system. Fuzzy logic was used as a close-loop control structure to control the DC/DC converters in the topology, whilst a rule-based control strategy was used to control the operating states of the HESS.

Experimental implementation of the system showed that the system was able to actively control the flow of power throughout the HESS in order to limit the power drawn from the battery to a user-defined limit. The performance of the fuzzy logic controllers was also experimentally found to be sufficient when used in conjunction with the rule-based control strategy. The system allows one to utilize batteries that are optimized for energy density seeing that the system was able to actively limit the power drawn from the battery, whilst providing the required power to the load by utilising the ultracapacitor bank.

The controller and HESS were simulated in MATLAB®/Simulink® and practically implemented through the Simulink® Real-Time environment with a STM32 Nucleo microcontroller. The active topology reduced the peak-power drawn from the battery by 46.05% for a pulse train load profile whilst the system reduced the peak-power drawn from the battery by 90.1% for a real-world drive cycle. The developed active HESS is not only suitable for EVs, but can be used to hybridize different energy sources, such as fuel cells, photovoltaic cells and any other EES devices that have complementary characteristics.

# Acknowledgements

The completion of this thesis would not have been possible without the contributions of those mentioned below.

# Table of Contents

# List of figures

# List of tables

# List of Acronyms

| | |
|---|---|
| **ADC** | Analog-to-Digital Converter |
| **AFC** | Alkaline Fuel Cells |
| **AGM** | Absorbent Glass Mat |
| **ANFIS** | Adaptive Neuro-Fuzzy Interference System |
| **ANN** | Artificial Neural Network |
| **BP** | Back-Propagation |
| **CCM** | Continuous Conduction Mode |
| **CPU** | Central Processing Unit |
| **DC** | Direct Current |
| **DMFC** | Direct-Methanol Fuel Cell |
| **DoD** | Depth-of-Discharge |
| **EDLC** | Electrochemical Double-Layer Capacitor |
| **EEPROM** | Electrically Erasable Programmable Read-Only Memory |
| **EES** | Electrical Energy Storage |
| **EFuNN** | Evolving Neural Fuzzy Network |
| **EMF** | Electromotive Force |
| **EPR** | Equivalent Parallel Resistance |
| **ESR** | Equivalent Series Resistance |
| **ESS** | Energy Storage System |
| **EUDC** | Extra-Urban Driving Cycle |
| **EV** | Electric Vehicle |
| **FALCON** | Fuzzy Adaptive Learning Control Network |
| **FNN** | Fuzzy Neural Network |
| **GARIC** | Generalized Approximate Reasoning based Intelligence Control |
| **GPIO** | General Purpose Input/Output |
| **GPU** | Graphics Processing Unit |
| **HDMI** | High Definition Media Interface |
| **HEC** | Hybrid Electrochemical Capacitor |
| **HESS** | Hybrid Energy Storage System |
| **HEV** | Hybrid Electric Vehicle |
| **I2C** | Inter-integrated Circuit |
| **IC** | Integrated Circuit |
| **ICEV** | Internal Combustion Engine Vehicle |
| **LCO** | Lithium Cobalt Oxide |
| **LFP** | Lithium Iron Phosphate |
| **LMO** | Lithium Manganese Oxide |
| **MOSFET** | Metal-oxide-semiconductor field-effect transistor |
| **NCA** | Lithium Nickel Cobalt Aluminium Oxide |
| **NEDC** | New European Driving Cycle |

| | |
|---|---|
| **NYCC** | New-York City Cycle |
| **PAFC** | Phosphoric Acid Fuel Cell |
| **PCB** | Printed Circuit Board |
| **PD** | Proportional Derivative |
| **PEM-FC** | Proton Exchange Membrane Fuel Cell |
| **PEV** | Plug-in Electric Vehicle |
| **PI** | Proportional Integral |
| **PID** | Proportional Integral Derivative |
| **PLC** | Programmable Logic Controller |
| **PWM** | Pulse Width Modulated |
| **RAM** | Random Access Memory |
| **RBF** | Radial Basis Function |
| **RFC** | Regenerative Fuel Cell |
| **RISC** | Reduced Instruction Set Computer |
| **SEI** | Solid Electrolyte Interphase |
| **SoC** | State-of-Charge |
| **SoH** | State-of-Health |
| **SPI** | Solid Permeable Interphase |
| **SPI** | Serial Peripheral Interface (SPI) |
| **SRAM** | Static Random Access Memory |
| **UC** | Ultracapacitor |
| **UNECE** | United Nations Economic Commission for Europe |
| **UPS** | Uninterrupted Power Supply |
| **USB** | Universal Serial Bus |
| **VRLA** | Valve-Regulated Lead-Acid |
| **WLTC** | Worldwide harmonized Light vehicle Test Cycles |

# List of Units & Symbols

## List of Units

| | |
|---|---|
| *Wh.kg$^{-1}$* | Watt-hour per kilogram |
| *W.kg$^{-1}$* | Watt per kilogram |
| *F* | Farad |
| *Hz* | Hertz |
| *kB* | Kilobyte |
| *Ω* | Ohm |
| *V* | Volt |
| *W* | Watt |
| *A* | Ampere |
| *Ah* | Ampere-hours |
| *kHz* | Kilohertz |
| *MHz* | Megahertz |
| *mAh* | Milliamps-hour |
| *s* | Second |
| *GHz* | Gigahertz |

## List of Symbols

| | |
|---|---|
| $\mu$ | Micro |
| $\rho_a$ | Air Density |
| $c_D$ | Drag Coefficient |
| $A_f$ | Vehicle Frontal Area |
| $m_t$ | Vehicle Mass |
| $\theta_v$ | Total vehicle inertia |
| $v$ | Velocity |
| $G_r$ | Gear Ratio |

# Chapter 1 – Introduction

*This section gives an introduction to the project. The project background, project objectives, the problem statement and the key research questions are discussed. The methodology used to investigate the problem is also described. The layout of the document and what can be expected in each chapter are also discussed.*

## 1.1 Background

Fossil fuels are considered as the main cause of global warming. Growing consumer expectations and legislation to reduce fossil fuel's impact on the environment has resulted in the automotive industry focusing on electric and hybrid electric vehicles (EVs, HEVs). By the end of 2018, the cumulative sales of plug-in EVs (PEVs) have surpassed 5 million units, with 49.1% of new car sales in Norway consisting out of PEVs [1]. The limiting factor in developing EVs that have adequate performance compared to that of internal combustion vehicles (ICEV) is the energy storage system (ESS) [2], [3]. Batteries are the most commonly used ESS in EVs due to their high energy density and reliability compared to other ESSs. However, batteries have a low cycle life, are expensive and their energy density pales in comparison to that of gasoline/diesel as used in ICEVs. Batteries also have a low power density and exhibit poor performance at low temperature.

One-third of the total production cost of an EV is dedicated to the ESS, but this is dependent on the type of ESS used [4]. The ESS should be sufficiently sized to be able to provide the necessary power and energy requirements of the vehicle. EVs require a high power, high energy-dense ESS, but batteries in general possess either of these characteristics, not both [5], [6]. Considering the cost, size and weight of the battery pack, a small energy dense pack would be ideal, but they are usually unable to provide the necessary power to the vehicle during acceleration. This requires the use of additional batteries, increasing the weight and cost of the battery pack; or more power-dense batteries need to be used, reducing the total amount of energy stored.

The life and usable capacity of batteries are negatively impacted by power impulses [7]- [13]. Battery packs in electric vehicles (EVs) are typically oversized to be able to provide enough power during these impulses experienced when the vehicle accelerates. Reports suggest that the common power to energy ratio of batteries in electric vehicles is, P/E ~ 8:1, which suggests that battery packs employed are optimized for power rather than energy [14]. This is done to accommodate the high power draw from the motor during acceleration.

An additional ESS with a high power density, such as an ultracapacitor (UC), can be used as a buffer to provide power during power surges to reduce the power impulses experienced by the battery. Isolating the battery from the power impulses would allow the EV to utilize more energy-dense batteries, increasing the range of the EV as well as increasing the lifetime of the utilized batteries. A hybrid energy storage system (HESS) allows one to utilize the complementary characteristics of both the battery and ultracapacitor in one system.

# 1.1.1 Electrical energy storage

An EES (electrical energy storage) device is a device that is used to store electrical energy. Batteries of various types such as Lead-Acid, Li-ion, Ni-Cd and Ni-MH are examples of EES devices. Capacitors and ultracapacitors are also commonly used EES units. EES devices have different desirable characteristics which determine the performance and applicable applications for each EES device. These characteristics are as follow:

- **Cycle efficiency**: The cycle efficiency of an EES device is defined as the ratio of the amount of energy outputted by the device to the amount of energy inputted to the device during charging.

- **Cycle life:** The cycle life is the maximum number of charging/discharging cycles that the device can perform before the energy storage capacity of the device drops below a certain percentage of the original capacity of the device.

- **Energy density:** The amount of energy that a device can store per unit volume or weight is defined as the energy density of the device. Comparing the energy of the device per unit volume is called the volumetric energy density, whilst the gravimetric energy density compares the energy to the mass of the device.

- **Power density:** Power density is the maximum power that can be delivered per unit of volume of the device.

- **Self-discharge rate:** The rate at which an EES device loses its stored energy whilst no load is connected to the device.

Ultracapacitors and batteries are typically the two energy sources used in HESSs [15]. Ultracapacitors are power dense with a low energy density, whilst batteries are typically energy-dense but have a low power density. A HESS combines the characteristics of these two or more different energy storage mediums to employ the advantages of the available energy storage systems

A HESS combining batteries and ultracapacitors has a high energy density as well as power density, whilst increasing the cycle life of the batteries [8], [16]. The power demand of an electric vehicle is variable and is dependent on the road profile, vehicle weight and the acceleration of the vehicle. Peak power demand occurs during acceleration, which typically only last for a short time. The ratio of peak power to average power can be over 10:1 [17]. A Ragone plot, which plots the specific energy versus the specific power of a source, is shown in figure 1.1. For batteries, there is a trade-off between the specific power of the battery and the specific energy of the battery, as can be seen in figure 1.1 [18].

Batteries optimized for a high specific energy can be used with an ultracapacitor in a HESS system to create a system capable of delivering a high peak-to-average power output for a short duration and that has a relatively high specific energy. In a HESS, the power-dense energy source, in this case the ultracapacitor, is able to deliver energy during peak power situations. With the ultracapacitor providing power during peaks, the power required from the battery is closer to the
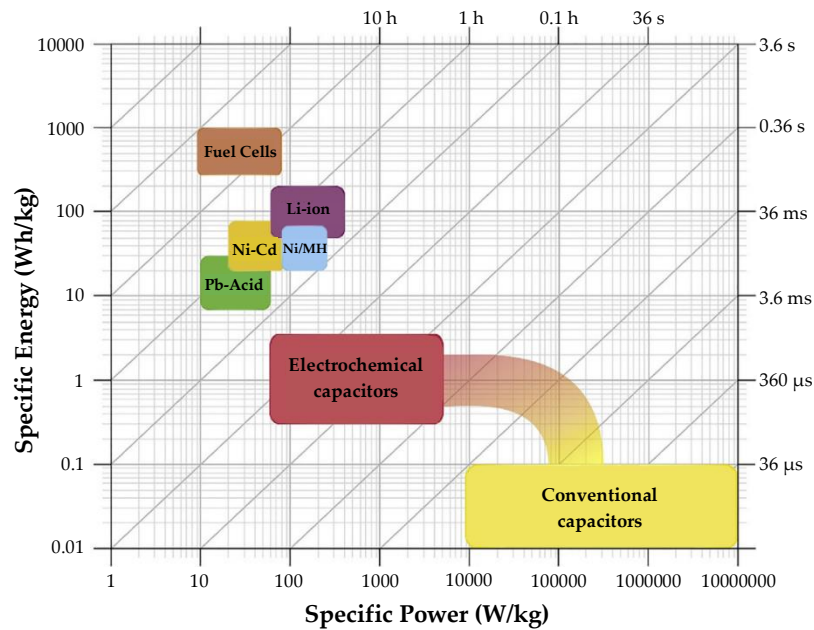
Figure 1.1: Ragone Plot (adapted from [18])

average power required by the load. Reducing the power spikes and power requirements on the battery increases the usable discharge capacity of the battery.

Peukert's law relates the discharge capacity of a battery to the discharge current [19]. This is especially applicable to lead-acid and deep cycle batteries. Peukert's capacity is given by the following equation:

$$C_p = I^k T \tag{1.1}$$

where $I$ is the discharge current, $k$ is a constant called the Peukert coefficient and $T$ is the discharge time in hours [20]. From equation 1 it is clear that when the battery is discharged at a faster rate the battery's effective capacity is lowered. This is due to the internal resistance of the battery.

## 1.1.2 Hybrid energy storage systems

Various HESS topologies exist, with both active and parallel connection schemes. The simplest of these topologies is the parallel connection scheme, in which the capacitor and battery are connected in parallel. The passive parallel connection scheme allows the system to deliver higher peak power and due to the smaller internal losses, increases the usable capacity of the battery compared to a battery-only system. The passive parallel topology is shown in figure 1.2.
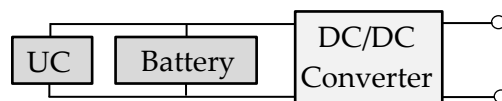


Figure 1.2: Passive HESS (adapted from [21])

This passive parallel structure has the advantage that no converters are used. The ultracapacitor acts as a low pass filter in this topology. This topology can however not utilize the energy stored within the ultracapacitor. To fully utilize the energy available in the ultracapacitor, an active topology is required. The topology showed in figure 1.3 allows the energy of the ultracapacitor to be fully utilized, at the cost

of requiring a bidirectional DC/DC converter. This also requires the DC/DC converter to have a higher power rating, to ensure that it can handle the power supplied by the ultracapacitor. This UC/battery configuration is one of the most studied and implemented HESS [21].
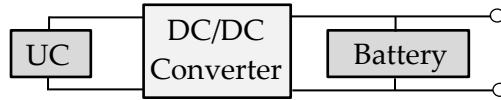
Figure 1.3: SC/Battery HESS (adapted from [21])

An alternative topology also commonly used to reduce the power impulses experienced by the battery is shown in figure 1.4. This configuration allows the batteries voltage to differ from that of the ultracapacitor. Seeing that the ultracapacitor is connected directly to the DC-link, it acts as a low pass filter [22]. The DC-link's voltage can vary within a range so that the ultracapacitor's stored energy can be utilized more effectively.

Figure 1.4: Battery/SC HESS (adapted from [22])

To improve on the aforementioned topology, an additional DC/DC converter can be placed between the ultracapacitor and the load, as shown in figure 1.5. This allows for a wider voltage operating range of the ultracapacitor, allowing more of the stored energy within the ultracapacitor to be used. This topology is more complex, seeing that two DC/DC converters are required.
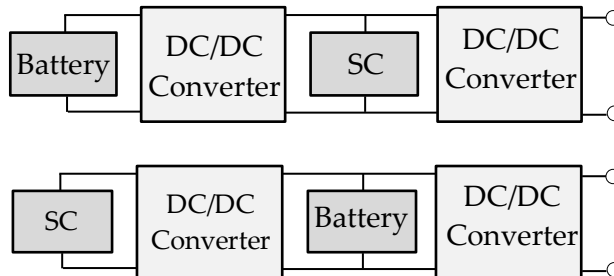
Figure 1.5: Cascaded Configuration (adapted from [22])

Instead of cascading the EES devices as was done in figure 1.5, multiple converters can be used in parallel. This topology is shown in figure 1.6. Both converters in this topology output the same DC-link voltage, but allows both the battery and the ultracapacitor to operate at their respective nominal voltages. The voltage of the ultracapacitor can vary through a wide range to ensure that most of the available energy stored in the capacitor can be used. This topology also has the drawback that two DC/DC converters are required.
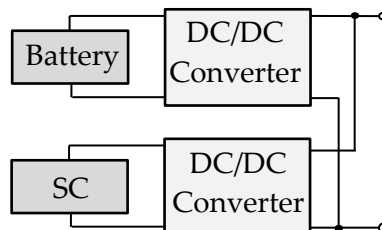
Figure 1.6: Multiple Converter HESS (adapted from [22])

Topologies utilizing multiple converters increase the overall system cost, complexity and system size. Topologies using only one multiple input converter have been proposed in order to reduce the cost and size of the HESS [23]. This topology is shown in figure 1.7.
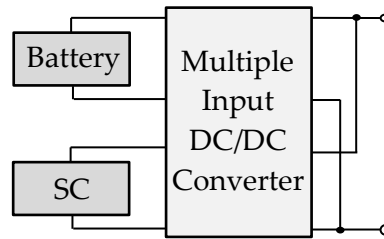


Figure 1.7: Multiple Input HESS (adapted from [23])

## 1.2 Problem Statement

Eskom, the South African state-owned utility company, is constantly searching for methods to reduce the load on the national grid. The GUM-truck (Green Underground Mining vehicle) project, which aims at developing an underground mining vehicle that is electrically driven, would reduce the impact that mining support vehicles have on the underground ventilation systems and on miners' health. Eskom states that the mining ventilation systems consume about 15% of the total energy consumption of the mines [24], [25]. Replacing the diesel-driven mining support vehicles with an electrically powered mining vehicle could reduce the energy consumption of the mines, as well as improve the quality of air inside the mine, reducing greenhouse gas production and reducing the payable carbon tax [26].

The energy storage medium used within electric vehicles is one of the biggest factors determining the performance and cost of the vehicle [7], [27], [28]. The most commonly used energy storage devices in electric and hybrid vehicles are batteries. The battery pack should be sufficiently sized so that it meets the power requirements of the vehicle. High power-dense batteries are available but are typically more expensive than lower dense batteries. An easy way to solve this problem is to increase the size of the battery pack. This increases the weight of the battery pack, as well as the overall cost of the system.

The life of a battery is negatively affected by spikes of high-power draw [7]. An additional EES device that can be used as a buffer that is capable of providing power during power surges could be used to increase the battery lifetime. Hybrid energy storage structures are one of the proposed systems that could be used to achieve better performance in an electric vehicle. An active HESS topology making use of an intelligent controller to control the flow of energy between different EES devices must be investigated to determine if an active HESS has any significant and practical benefits.

# 1.3 Study Objectives

## 1.3.1 Primary Objective

The primary objective of this research project is to investigate existing hybrid energy storage systems and the potential benefits that these systems may provide to battery-operated vehicles and devices. Active HESS topologies and the control methods used in controlling the topologies will be investigated. The end-goal of the study is to determine if an intelligent controller could be developed for an active HESS that reduces the peak power impulses experienced by the battery in a battery/ultracapacitor hybrid system and results in a system that has a higher power density than a standalone battery system.

## 1.3.2 Secondary Objective

The primary objective was accomplished by completing the following secondary objectives.

1. Design of the HESS and accompanying intelligent controller
   - Research existing HESS topologies.
   - Investigate the EES devices that can be used within the HESS topology.
   - Research control methods previously used to implement active HESS topologies.
   - Simulate the chosen active HESS topology with a simulated load that an electric vehicle might endure during a drive cycle.

2. Implement the HESS and conduct performance tests
   - Construct the active HESS and implement the intelligent controller.
   - Test the efficiency of the HESS as well as the effect that the HESS has on the EES devices used in the HESS.
   - Perform tests that simulate the load that an EES device would endure during a normal drive cycle of an electric vehicle on the HESS.

3. Determine the applicability of the HESS for an electrical vehicle
   - Determine the applicability of the HESS and benefits or drawbacks of implementing such a system in an electric vehicle.
   - Investigate if the HESS should be used within electric vehicles or if stand-alone EES devices are sufficient on their own.

## 1.3.3 Exclusions and limitations

The exclusion and limitations of the study are as follow:
   - Comparing the performance of the HESS to that of multiple different types of EES devices.

- Implementing the HESS in an electric vehicle.

- Implementing multiple controller types on the HESS.

# 1.4 Research Methodology

The thesis will be divided into the following parts: 1) Identifying the research problem, 2) Technology survey and literature study, 3) Conceptual and detail design, 4) Simulation, 5) System implementation, 6) System evaluation, 7) Analysis, Conclusion and Recommendations, 8) Verification and Validation.

## 1.4.1 Problem Identification

The first step in this research study was to identify the problem. The project scope and the objectives of the project are also identified in this phase. The goal of the study and the reason for conducting the study is identified in this section.

## 1.4.2 Literature Study and Technology Survey

A comprehensive literature study has to be done to ensure that all the necessary information regarding existing solutions are collected. The technology survey needed to be done to ensure that the current methods and technology used were taken into account during the design phase. The following topics are of importance for this study:

- **Hybrid Energy Storage Systems** – The different types of HESS were investigated. This included investigating passive, active and novel topologies.

- **Case Studies** – Prior studies and research surrounding HESS was done in this section. The results of the topologies that were used in these studies were documented.

- **Control Topologies** – Different control topologies were investigated and documented. The control topologies used by other studies with active HESS topologies were investigated.

- **Controller Types** – The different controller types were investigated. The control types used by similar studies were documented.

- **Electrical Energy Storage Devices** – The different electrical energy storage devices were investigated, researched and documented. The advantages and disadvantages of the various EES devices were documented.

## 1.4.3 Conceptual and Detail Design

The information obtained from the literature study and the technology survey was used to develop the conceptual design. The detail design was created from the conceptual design. This phase also included engineering trade-off studies and flow diagrams. The logic structures as well as the rules and criteria used for the intelligent controller were also developed in this section.

## 1.4.4 Simulation

The intelligent controller that was developed as well as the subsystems were simulated. The complete system was also simulated to verify that the integrated system functions as expected. The simulations also served as a base to compare the physical performance of the system to the simulated performance of the system. Mathematical simulation software such as MATLAB® and Simulink® were used for this purpose.

## 1.4.5 System Implementation

The different sub-systems that were designed and simulated was practically developed and implemented to determine if the designed system and controller work as designed. Integrated tests were also performed that the system as a whole performed as expected.

## 1.4.6 Analysis, Conclusion and Recommendations

The results and performance of the implemented system was compared to that of the simulated system. The real-world applications and the success of the project were discussed. Recommendations are also made in this chapter.

## 1.4.7 Validation and Verification

The validation and verification process was essential to the study to ensure that the study met the goals and requirements set out. Verification and validation are complementary processes. Validation is the process of checking if the implemented system is the right system, whilst verification is validation by empirical means. Verification compares and refers each chapter to one another whilst validation refers each chapter to the problem statement, ensuring that the right system is being created to solve the problem, as depicted in figure 1.8.
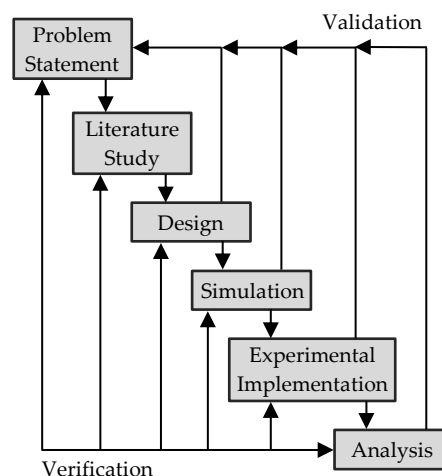


Figure 1.8: Validation and verification process

## 1.4.8 Key Research Questions

- Could a controller be developed that is able to control the flow of power in a HESS so that the power impulses experienced by the battery is minimized?
- Are there any benefits to using an active HESS compared to a passive HESS or a standalone battery?

# 1.5 Dissertation Overview

The dissertation has six chapters, what can be expected from each chapter is shortly discussed below.

Chapter 1, which is this chapter, provides the background to the project and the problem to be researched is discussed. The research methodology is discussed in this chapter and the chapter also gives an overview of this thesis. Chapter 2 contains the literature study that was done pertaining to the various components of the project. Case studies of similar research projects were conducted and documented in this chapter, which could be used for verification and validation purposes.

Chapter 3 is the design chapter, in which the concept design of the overall project and the detail design of the sub-sections of the project is documented. This includes the design of the DC/DC converters, the overhead controller and the other supplementary sub-sections. Chapter 4 contains the simulations that were done according to the calculated parameters in chapter 3. The sub-sections and the system as a whole were simulated, to verify that the system performs as designed.

Chapter 5 serves to document the experimental setup of the project and the results that were experimentally obtained. The chapter focusses on the performance of the system as a whole, but also briefly documents the performance of the sub-sections. Chapter 6 concludes the dissertation and gives recommendations for future work. The research questions are discussed in this section. Verification and validation of the project as a whole is also discussed in this chapter.

# 1.6 Publications and Peer Reviews

The preliminary findings of the research project were presented at the 2019 IEEE International Multidisciplinary Information Technology and Engineering Conference (IEEE IMITEC). An article was also submitted to the World Electric Vehicle Journal (WEVJ) with feedback still pending. Further information regarding the publications are given below, whilst the full articles are given in Appendix A.

- M. van Jaarsveld and R. Gouws, "Intelligent controller for a hybrid energy storage system", Article accepted at the IEEE International Multidisciplinary Technology and Engineering Conference (IMITEC) and presented on 21 November 2019, IEEE Explore ISBN: 978-1-7281-0040-1, IEEE Conference Number: #45504.

    **Abstract**— *The performance and range of electric vehicles are largely determined by the characteristics of the energy storage system (EES) used. The EES should be sufficiently sized to be able to provide the*

*necessary power and energy requirements of the vehicle. Batteries are typically energy dense, although batteries that are both energy and power dense exist, they are much more expensive. The life and usable capacity of batteries are negatively impacted by power impulses. Battery packs in electric vehicles (EV) are typically oversized to be able to provide enough power during these impulses experienced when the vehicle accelerates. An additional EES with a high power density, such as an ultracapacitor, can be used as a buffer to provide power during power surges to reduce the power impulses experienced by the battery. Isolating the battery from the power impulses would allow the EV to utilize more energy dense batteries, increasing the range of the EV as well as increasing the lifetime of the utilized batteries. A hybrid energy storage system (HESS) allows one to utilize the complimentary characteristics of both the battery and ultracapacitor in one system. The method proposed uses a fuzzy logic controller, multiple dc/dc converters, batteries and ultracapacitors in a HESS to minimize the power impulses experienced by the battery, thereby increasing the usable capacity of the battery, whilst being able to deliver high amounts of power for short duration.*

- M. van Jaarsveld and R. Gouws, "Active hybrid energy storage system utilising a fuzzy logic rule-based control strategy", Submitted to the World Electric Vehicle Journal on 3 November 2019, ISSN: 2032-6653 published by MDPI.

**Abstract**— *The research presented in this paper documents the implementation of an active hybrid energy storage system that combined a battery pack and an ultracapacitor bank. The implemented hybrid energy storage system was used to reduce the peak-power that the battery needs to provide to the load. An active topology utilising two DC/DC converters and a switch was used to implement the hybrid energy storage system. Fuzzy logic was used as a close-loop control structure to control the DC/DC converters in the topology, whilst a rule-based control strategy was used to control the operating states of the HESS. Experimental implementation of the system showed that the system was able to actively control the flow of power throughout the HESS in order to limit the power drawn from the battery to a user-defined limit. The performance of the fuzzy logic controllers was also experimentally found to be sufficient when used in conjunction with the rule-based control strategy. The system allows one to utilize batteries that are optimized for energy density seeing that the system was able to actively limit the power drawn from the battery, whilst providing the required power to the load by utilising the ultracapacitor bank.*

## 1.7 Conclusion

The introductory chapter provided background information about electrical energy storage devices and hybrid energy storage structures. The objectives of the research as well as the problem statement were also given in this chapter. The key research questions were presented as well as the abstracts of the peer-reviewed research papers that were generated from the findings of this thesis.

The next chapter presents the literature study that was conducted. The literature study was done to gain an understanding of existing research pertaining to hybrid energy storage structures, electrical energy storage systems and other topics relevant to the research. The literature study is used in later chapters for verification.

# Chapter 2 - Literature Study

*This section documents the literature study that was done in order to obtain a more thorough understanding of the key topics applicable to the study. Hybrid energy storage structures as well as the different types of electrical energy storage systems were investigated. Controllers and some different control techniques were also investigated. Figure 2.1 gives an overview of the different topics that were investigated. Figure 2.2 shows a summation of the citations that were used for each topic as well as the case studies that link the different topics applicable to the study.*
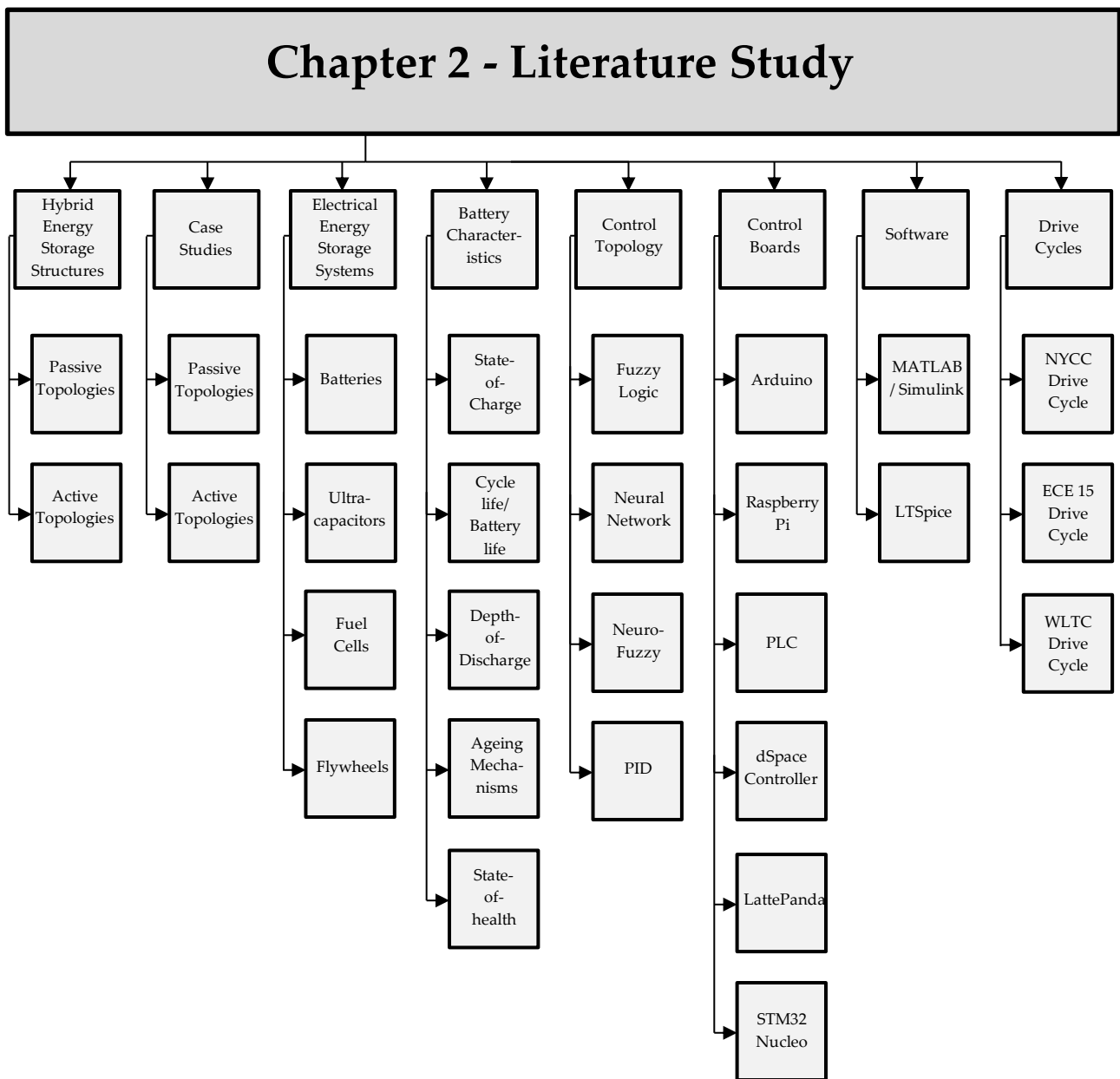


Figure 2.1: Literature study overview

**2.1 Hybrid Energy Storage Systems**

Passive Topologies — [31], [32]

Active Topologies — [7], [31], [33], [34]

**2.4 Battery Characteristics**

State-of-Charge (SOC) — [61], [68], [69]

Cycle life/ Battery life — [70-72]

Depth-of-Discharge — [73], [74]

Ageing Mechanisms — [70], [71], [75], [76]

State-of-Health (SOH) — [70], [77], [78]

**2.3 Electrical Energy Storage Systems**

Batteries — [17], [29], [44-55], [41-46], [38]

Ultracapacitor — [29], [38], [59 – 64], [42-45]

Fuel Cells — [17], [47], [48]

Fly wheels — [29], [48], [65-67]

**2.2 Case Studies**

Passive Topologies — [16], [38-40]

Active Topologies — [2], [7], [41-46]

[41-44]

[38-40]

[46]

**2.5 Control Topology**

Fuzzy Logic Control — [84-93]

Neural Network Control — [94-98]

PID Control — [99-102], [116]

Neuro-Fuzzy Control — [91], [95], [103-109]

**2.8 Drive Cycles**

NYCC Drive Cycles — [133], [135]

WLTC Class 2 Drive Cycle — [133], [136]

ECE 15 Drive Cycles — [133]

**2.6 Control Boards**

Arduino — [110 - 112]

Raspberry Pi — [113-116]

PLC — [117], [118]

dSpace Controller — [119 – 122]

LattePanda — [123], [124]

STMicro Nucleo Board — [125-128]

[128]

[115]

[127]

[121]

**2.7 Software**

MATLAB/ Simulink — [129], [130]

LTSpice — [122], [131], [132]

[122]

[128]

Figure 2.2: Citations and case studies

12

# 2.1 Hybrid Energy Storage Structures

Electrical energy storage devices are of vital importance in hybrid electric vehicles (HEVs), plug-in hybrid vehicles (PHEVs) and electric vehicles (EVs) [29], [30]. Hybrid energy storage structures aim to integrate different EES devices to combine the desirable characteristics of each device into one structure. The degree of improvement that the HESS provides depends intrinsically on how the sources are integrated and controlled. Various HESS have been developed and implemented. HESS structures are divided into passive and active topologies.

## 2.1.1 Passive topology

The simplest HESS topology is the passive parallel structure, in which the EES devices are simply connected in parallel, as shown in figure 2.3. If an ultracapacitor and battery are used as the EES devices in the passive HESS system, the ultracapacitor acts as a low-pass filter [31]. This topology is easy to implement seeing that no power electronics are required to interface the battery and ultracapacitor.
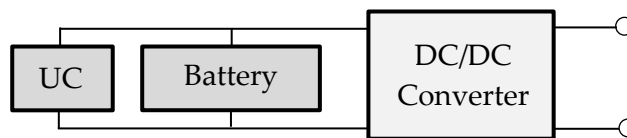


Figure 2.3: Passive Topology (adapted from [31])

The passive topology is unable to manage the power flow between the battery and the ultracapacitor. The state-of-charge (SoC) and the voltage of the passive parallel system is largely dictated by the characteristic curve of the battery and results in a non-linear curve [32]. Seeing that the battery and ultracapacitor operate at the same voltage, the power-sharing ratio of each ESS is determined by its internal resistance [8]. The passive topology has a low cost and implementation difficulty compared to actively controlled topologies. It is also easy to implement such a HESS in existing battery-only systems. The passive structure does, however, fail to effectively utilize the energy stored in the UC. If the voltage of the UC can be discharged to 50% of the initial voltage, 75% of the energy stored within the UC would be utilized. The passive topology typically only discharges the ultracapacitor to about 70% of its initial voltage depending on the type of battery being used in conjunction with the UC, utilizing only 50% of the energy stored within the UC [32]. In order to be able to manage the stored energy within the UC and control the flow of power from the energy sources, active topologies were developed.

## 2.1.2 Active topology

Various active topologies and control strategies have been developed and implemented [7], [31], [33]- [37]. Most active topologies make use of one or multiple power electronic circuits to interface the EES devices to one another and the DC-link. Certain topologies directly interface the battery tot the DC-link, whilst some power electronics circuit is placed between the UC and the battery. In

order to effectively utilize the power density of the UC, the power converter placed between the UC and battery should match the power density of the UC. This results in a converter that is large and contributes to a large portion of the cost of the HESS [7]. This topology in which the battery is directly connected to the DC-link, the battery is exposed to frequent charge and discharge cycles as well as high power pulses, depending on the load connected to the HESS.

## 2.1.2.1 UC/Battery Topology

The UC/battery topology as shown in figure 2.4 is the most commonly used HESS topology [7]. An unidirectional or bidirectional converter can be used to interface the UC with the battery. The converter allows the energy of the UC to be utilized more effectively but needs to be sufficiently sized. The nominal voltage of the UC doesn't have to match that of the battery as is the case in the passive parallel topology. Seeing that the UC is connected to the DC-link by means of a converter, the UC is unable to quickly provide power during short power pulses.
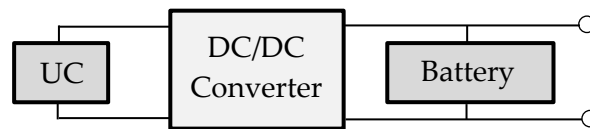


Figure 2.4: SC/Battery Topology (adapted from [7])

## 2.1.2.2 Battery/UC Topology

The battery/UC topology connects the UC directly to the DC-link. The battery is connected to the DC-link via a converter and the UC acts as a low-pass filter in this configuration [7]. This configuration allows the battery to operate at a different voltage than that of the UC and DC-link. Depending on the control strategy employed, the voltage of the DC-link can be varied in such a way as to utilize the energy stored within in the UC. The UC/battery has the advantage that the voltage of the DC-link is more stable than this topology [33]. The energy stored within the battery can also be used more effectively, seeing that there is no converter between the battery and the DC-link. The fact that the UC is directly connected to the DC-link allows the UC to absorb and provide power during the power pulses. The battery/UC topology is shown in figure 2.5.



Figure 2.5: Battery/SC Topology (adapted from [33])

## 2.1.2.3 Cascaded Topology

The cascaded topology is similar to the two previously discussed topologies, except that a DC/DC converter connects the battery/UC or UC/battery topology to the DC-link. These topologies are shown in figure 2.6 and figure 2.7. This topology allows the voltage of the UC and battery to be controlled and varied independent of the DC-link voltage [7]. This allows this topology to effectively use the energy stored within the UC. The DC-link voltage also can be kept at a certain voltage and

is not dependent on the voltage of the battery as in the UC/battery topology. Although this topology allows the effective use of the EES devices, additional costs and weight results from this topology, seeing that an additional converter is required. The converter connected to the DC-link should be sufficiently sized to be able to supply the required power from the load.
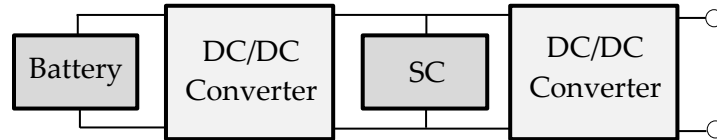


Figure 2.6: Battery/SC Cascaded Topology (adapted from [7])
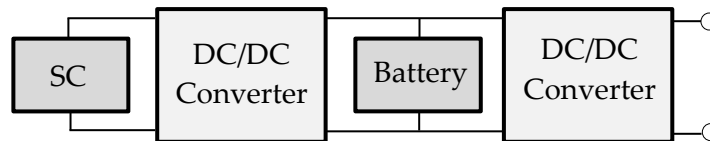


Figure 2.7: SC/Battery Cascaded Topology (adapted from [7])

## 2.1.2.4 Multiple Converter Topology

The cascaded topology above makes use of two converters to implement the topology. The multiple converter topology also makes use of two converters when only two EES devices are used. The multiple converter topology connects the two EES devices through the converter to the DC-link in parallel, as is shown in figure 2.8. The voltages of the UC and the battery can be varied independently to utilize the energy stored within these devices sufficiently. No balancing is required seeing that the device's voltages can be controlled independently. The current flow of the UC and battery can be easily controlled in this topology. The topology is also tolerant of failures seeing that even if the battery or UC or one of the converters fails, the DC-link can still be supplied with power [8].
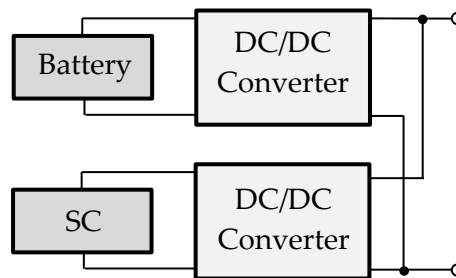


Figure 2.8: Multiple Converter Topology (adapted from [8])

## 2.1.2.5 Multiple Input Converter Topology

The multiple converter topology makes use of multiple converters, contributing to the cost of the topology. This topology makes use of a multiple-input converter, which is more cost-effective than using multiple converters. This converter topology is also able to individually control the current flowing from the EES devices. Figure 2.9a shows the multiple-input converter topology. The DC-link voltage can also be controlled, but this topology requires a more complicated control strategy when compared to that of the multiple converter topology [33].

### 2.1.2.6 Novel Converter Topology

An alternative converter topology as shown in figure 2.9b that tries to reduce the number of DC/DC converters required. This topology utilizes diodes and switches to reduce the losses and complexity associated with the DC/DC converters. The topology directly connects the UC or the battery to the load. This allows one to transfer power to load through the applicable source, depending on the amount of power required by the load. Power can also easily be absorbed by the UC or the battery simply by activating the appropriate switches.
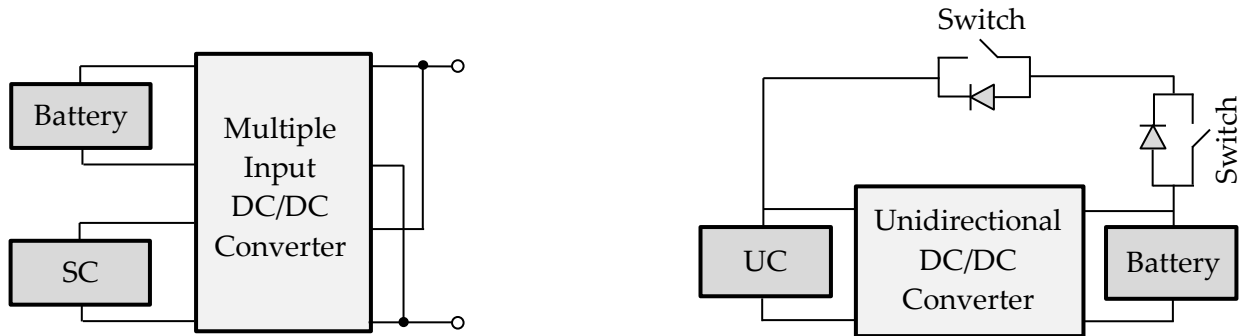


Figure 2.9: **a**) Multiple Input Converter Topology (adapted from [33]); **b**) Novel Topology (adapted from [33])

# 2.2 Hybrid Energy Storage Systems – Case Study

This chapter aims to investigate the benefits of using a HESS and document the results of previous studies and projects surrounding HESS. This section documents these results according to passive and active topologies.

## 2.2.1 Passive topology

The passive topology, employing an UC bank and battery in parallel, has been analysed, simulated and tested to determine the effectiveness of the topology.

L.H. Seim *et al.* (2011) investigated and analysed the passive topology in-depth [38]. The equivalent circuit of the topology was used to derive a model for the topology in the frequency domain and the Thevenin equivalent of the topology. Simulations done using the models derived showed that for a square pulsed load with a duty ratio of 0.1 that the ultracapacitor supplies a large percentage of the load current, as shown in figure 2.10. The power sharing between the ultracapacitor and battery was found to be solely determined by the internal resistance of the battery and the ultracapacitor.
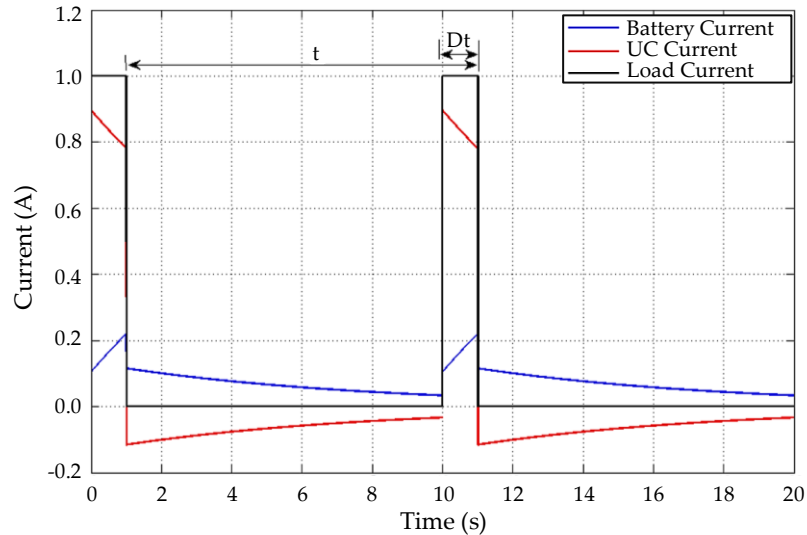
Figure 2.10: Pulsed load profile for passive topology (adapted from [38])

A lower ultracapacitor resistance results in more of the immediate power being delivered by the ultracapacitor. The work of L.H. Seim *et al.* also found that the power-sharing of the ultracapacitor is also dependent on the frequency and duty cycle of the pulsed load. The relationship between the amount of power/load shared between the ultracapacitor and the battery was found to be almost linearly decreasing as the duty cycle of the pulses increases.

A semi-active topology was also simulated by L.H. Seim *et al.* and was found to have some benefits over the passive topology. A UC/battery topology was used. These benefits include being able to more effectively use the energy stored in the ultracapacitor. Voltage matching of the ultracapacitors and the semi-active topology is not required. The size of the ultracapacitor can also be varied and optimized to reduce the cost and weight of the system.

A. Kuperman *et al.* (2010) also investigated the passive HESS for pulsed loads [39]. The passive HESS was simulated and was found that the passive topologies performance was higher than that of the battery only system. The capacitor supplies the majority of the dynamic current required by the load. The study also noted that by connecting the ultracapacitors in parallel results in a lower effective internal resistance of the ultracapacitor bank. This increases the ratio of the current shared by the ultracapacitor bank. The current shared between the ultracapacitor and the battery bank has a similar ratio to that shown in figure 2.10. Connecting more ultracapacitors in parallel to decrease the internal resistance of the ultracapacitor bank improved the performance of the HESS compared to the passive HESS with only one ultracapacitor in parallel.

R. A. Dougal *et al.* (2002) analytically analysed the passive topology and also found that the topology can supply power to a pulsed load with a higher peak power draw. The system has smaller internal losses and increases the effective battery life [16]. R. A. Dougal *et al.* used an ultracapacitor in parallel with a Li-ion battery. The study found that the addition of the ultracapacitor increased the peak power capacity of the system by 5 times and reduced the power loss by 74% when a pulsed load of 5A was used at a 1 Hz repetition rate and 10% duty cycle. This is in accordance with the two other

studies described above, showing that the passive topology has significant benefits when used for pulsed loads.

D. Haifeng *et al.* (2010) implemented a passive HESS with a lead-acid battery [40]. The passive HESS system was implemented in a city bus developed in China. D. Haifeng *et al.* also found that the HESS enhanced the peak power that the system was able to output. The system increases the life of the battery system, especially when the power demand was high. The system was also tested for a pulsed load at a certain frequency and duty cycle.

## 2.2.2 Active Topology

The various active topologies that make use of one or more DC-DC converters in the topology have been researched and implemented. Active topologies typically have advantages properties when compared to passive topologies.

C. Zhao *et al.* (2014) did a quantitative and comparative analysis on the passive HESS topology and the semi-active battery/UC HESS topology [41]. C. Zhao *et al.* made use of the ESR circuit model and a pulsed train load to analyse these two topologies. The study found that the difference in efficiency between the two systems depends on the internal resistance of the battery. The difference in efficiency was also dependent on the average load current and the variance of the load. It was also stated that the efficiency of the DC/DC converter has a big influence on the overall system efficiency. The study found that the passive topology is ideal for use with batteries with a large internal resistance, seeing that the power-sharing ratio in a passive topology is determined by the ratio of internal resistance of the ultracapacitor and the battery.

Z. Yingchao *et al.* (2013) simulated a semi-active HESS and used a pulsed load for the HESS scheme [42]. The ultracapacitor was directly connected to the DC-link. The topology was shown to decrease the high discharge currents experienced by the battery-only system. The charge and discharge cycles experienced by the battery was also reduced by the topology. The operation of the battery is optimised by allowing the battery to provide a relatively constant output current and reduces the internal losses experienced by the battery.

H. Min *et al.* (2017) did a comparative study between the battery/ultracapacitor and ultracapacitor/battery topologies [43]. The battery/ultracapacitor topology was also experimentally implemented and validated. H. Min *et al.* used a bidirectional DC/DC converter to interface between the battery and the ultracapacitor. The study found that the battery/ultracapacitor topology has a higher efficiency than that of the ultracapacitor/battery topology. The study found that the battery/ultracapacitor increased the range of the vehicle by 7%. The study did not take into account the reduction in power impulses and charge/discharge cycles experienced by the HESS.

Z. Song *et al.* (2015) compared four different semi-active HESS topologies [2]. The first topology used was the semi-active topology in which the battery is directly connected to the DC-link. The

second topology that was investigated was the semi-active topology in which the ultracapacitor was directly connected to the DC-link. The third and fourth topology used in the study is somewhat novel and is shown in figure 2.11 and figure 2.12.
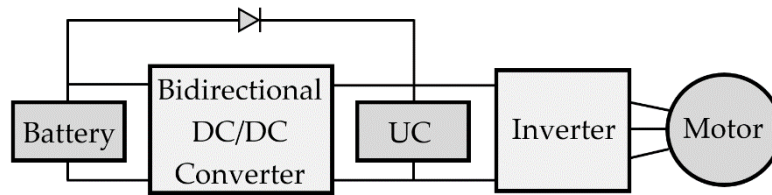


Figure 2.11: Bidirectional Novel Topology (adapted from [2])
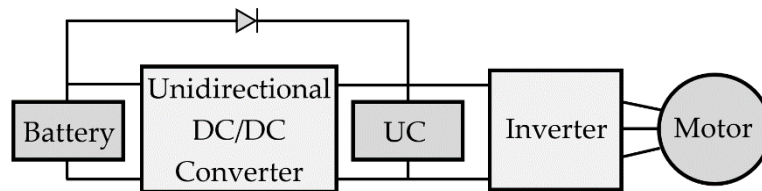


Figure 2.12: Unidirectional Novel Topology (adapted from [2])

The study used a dynamic degradation model for the LiFePO4 battery and made use of a component sizing strategy to determine the capacity of the ultracapacitor bank used in the topologies. The operational cost of the different HESS topologies was also calculated and taken into account. The power profile provided by both the ultracapacitor and the battery was recorded and compared for a load profile that could be representative of the power required by an electric vehicle. The ultracapacitor/battery and battery/ultracapacitor as well as the third topology demonstrated that they reduce the peak power impulses experienced by the battery. The fourth topology that was mentioned above did not perform as well as the conventional semi-active topologies. The operational costs of the topologies were also investigated as was found that the operational costs from low to high were as follow: ultracapacitor/battery topology, battery/ultracapacitor topology, topology three and then topology four. The study also concluded that the operational cost of the EES device was reduced by up to 50% by implementing a HESS.

J. Shen *et al*. (2016) investigated and implemented an ultracapacitor/battery topology [44]. J. Shen *et al.* made use of a 38V battery pack and a 16V ultracapacitor bank. Different drive cycles were used to represent a typical load profile that may be experienced by an electric vehicle. The New York, HWFET (Highway Fuel Economy Test) and ECE drive cycle (which is a normalized European drive cycle for an urban area) were used to test the performance of the semi-active topology during simulations. The implementation of the HESS showed experimentally that the peak currents experienced by the battery was reduced by up to 50%. The semi-active topology protects the battery from the aggressive transient demand of the load.

M. Michalczuk *et al.* (2012) simulated a semi-active HESS with the battery directly connected to the DC-link [45]. M. Michalczuk *et al.* made use of the ECE driving cycle to simulate the load experienced by the HESS. The simulations performed compared the performance of a battery-only system compared to that of the HESS at different temperatures. The HESS showed significant

improvement when compared to the standalone battery system at low temperatures. The range of the vehicle was more than doubled at 0°C whilst using LiFePO$_4$ batteries under the ECE driving cycle.

Z. Song *et al.* (2014) proposed a novel semi-active HESS topology [2]. The topology was simulated in Simulink®/MATLAB®. The China Bus Driving Cycle was used as the load profile in the simulation. LiFePO$_4$ batteries were used in the simulation model. The simulations done by Z. Song *et al.* showed that the proposed configuration reduced the peak currents experienced by the battery pack. The simulations showed that the ultracapacitor was also more effectively used in this topology, providing higher peaks of power when compared to that of the passive parallel system. The loss in the battery capacity over time was also reduced in the simulation.

R. Carter *et al.* (2012) simulated a HESS in an AC Cobra kit car. The car utilised an alternating-current induction motor that was water-cooled [46]. The AC Cobra kit car was developed by the University of Strathclyde. The vehicle makes use of lead-acid batteries that are connected in series. The HESS was simulated in Simulink®/MATLAB® using data obtained from driving tests of the vehicle. The study made use of two driving cycles, the George Square and ECE-15 cycle, to simulate the road profile driven by the vehicle. The study found that the addition of the ultracapacitor bank reduced the peak currents experienced by the battery. The smallest ultracapacitor bank that was simulated reduced the peak currents by up to 49%. The study also found that the life extension of lead-acid starter batteries was increased by 253%. The study also concluded that ultracapacitors are not an effective means of increasing the range of the vehicle, due to their low energy density, but are an effective method to increase battery lifetime and performance.

J. Cao *et al.* (2012) also proposed the topology suggested by Z. Song *et al* [7]. The HESS was simulated and implemented by J. Cao *et al.* and the designed topology was able to fully utilize the energy stored within the ultracapacitor, without requiring a DC/DC converter with a matching power DC/DC converter. The topology was capable of utilizing 75% energy stored in the ultracapacitor. The topology was also capable of creating a relatively constant load profile for the battery.

C. Xiang *et al.* (2014) proposed a novel topology which is somewhat similar to the aforementioned topologies but makes use of two switching devices and diodes to control the flow of energy between the EES devices and the load [33]. Depending on the load, the topology is operated in different modes. The combination in which the switches are connected or disconnected then determines how the power is provided to the load. The topology was simulated and implemented to verify the operation of the topology. The results showed that this topology was able to meet the power demands of the load whilst requiring a lower-capacity DC/DC converter than what is required in a conventional HESS topology.

## 2.3 Electrical Energy Storage Systems

This section aims to document the relevant systems that can be used for electrical energy storage. Various devices can be used to store electrical energy, but only these applicable to electric vehicles are documented in this section. Figure 2.13 shows the different systems that were researched and documented in this section.
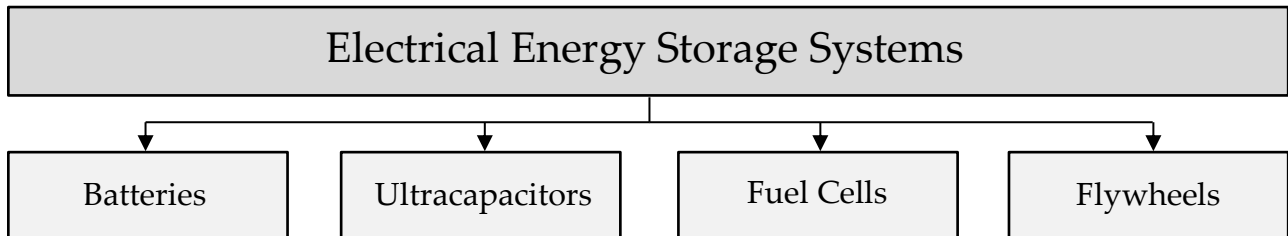


Figure 2.13: Electrical energy storage systems section overview

### 2.3.1 Batteries

Batteries are electrochemical devices that convert potential chemical energy into electrical energy during discharging and electrical energy into potential chemical energy during charging [17]. Batteries are made out of single or multiple cells that are stacked together. A battery cell exists out of the following components, namely a positive and negative electrode, an electrolyte and a separator. The electrodes are made out of a material that chemically reacts with the electrolyte via some form of ionic bonding [29]. The basic structure of a battery is shown in figure 2.14 [47].
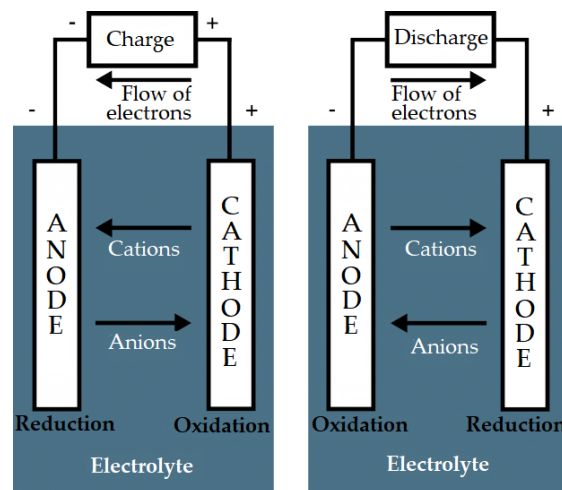


Figure 2.14: Battery structure (adapted from [47])

A battery's capacity is typically specified in terms of coulometric capacity (amp-hours). Generally, the coulometric capacity of the battery varies with discharging current. Various battery types and chemistries exist, but one of the oldest and most commonly used battery types is lead-acid.

## 2.3.1.1 Lead acid batteries

Lead-acid batteries' positive electrodes are made out of porous lead and the negative electrode out of porous lead oxide and have been used since the 1900s [29]. The electrolyte used in lead-acid batteries consists out of an aqueous solution of sulfuric acid. Three different types of lead-acid batteries exist, such as the valve regulated lead-acid battery (VRLA), absorbent glass mat battery (AGM) and deep cycle batteries. Some of these lead-acid batteries require the user to top up the battery with distilled water, whilst batteries such as VRLAs are sealed.

Lead-acid batteries are used in various applications due to their ruggedness, temperature tolerance, low cost and reliability [29], [48]. Lead-acid batteries are used in power quality applications, IC vehicles, UPS's and spinning reserve applications. These batteries, however, are not used in energy management applications, seeing that they have a low cycle life and low energy density [48]. Lead-acid batteries have a low specific power and energy due to the weight of the lead used in the battery.

The reversible redox reactions that take place deteriorates the battery electrodes, resulting in a cycle life of about 1200-1800 cycles or 5 - 15 years of operation [4], [49]. When these batteries are operated at partial state-of-charge and the battery is not periodically recharged sulphate crystals form that reduce the porosity of the electrodes and limits access to the active material, thereby reducing battery capacity [29]. High battery operating temperatures up to 45°C improves the battery capacity, but reduces the battery lifetime as well as efficiency [49]. The temperature characteristics of the battery at low temperatures are poor. The specific energy and specific power of the battery is greatly reduced at temperatures below 10°C, which limits the applicability of lead-acid batteries for EVs and HEVs.

Advancements have been made in lead-acid battery technology. Advanced sealed lead-acid batteries now have an energy density ranging from 30-50 Wh.kg$^{-1}$ [47], [50]. This has been done through the reduction of inactive materials such as the separators, current collectors and the casing. Further improvements were made by implementing bipolar designs as well as microtubular grid designs [47].

## 2.3.1.2 Nickel batteries

These batteries use an alkaline solution as the electrolyte and a nickel-based electrode. Four different nickel-based battery types, namely nickel-iron, nickel-metal hydride, nickel-cadmium and nickel-zinc [47]. All of these nickel-based batteries make use of some alkaline solution as the electrolyte, typically potassium hydroxide. The active material for the positive electrode of this battery is nickel-hydroxide and the active material for the negative electrode depends on the type of nickel-based electrode used.

Nickel-iron batteries make use of metallic iron for the negative electrode. These batteries suffer from self-discharge, corrosion and gassing problems [47]. These batteries are also somewhat complex seeing that they produce hydrogen and oxygen when the battery is discharged. These batteries also suffer from a reduced performance at low temperatures. The cost of the nickel used in these batteries

also results in a battery that is more expensive than lead-acid batteries. The nickel-iron and the nickel-zinc both have a low cycle life and require high maintenance intervals [4].

Nickel-cadmium (NiCd) batteries make use of a cadmium hydroxide negative electrode and the same positive electrode and electrolyte as the nickel-based batteries. These batteries have an energy density in the range of 50-80 Wh.kg$^{-1}$, require very little maintenance and are fairly robust [48]. These batteries are commonly used in portable devices, UPS systems and power tools. The nickel used in these batteries unfortunately result in a battery that has a high cost. An expensive manufacturing process is also required to produce these batteries. These batteries also suffer from the "memory effect" in which the battery's maximum energy capacity is reduced if the battery is only partially discharged before being recharged [4], [48]. The lifetime for these batteries range from 1500 cycles for the NiCd batteries using pocket plate vents and 3000 cycles for those using a sinter vent [49]. NiCd batteries are considerably more costly than lead-acid batteries, almost 10 times as expensive [51]. NiCd batteries are generally the only nickel-based alkaline batteries that are commercially used in industrial UPS applications [49].

Nickel-metal hydride (NiMH) batteries make use of hydrogen absorbed into a metal hydride to form the negative electrode, whilst the positive electrode and electrolyte are similar to that used in the other nickel-based batteries. This battery chemistry is advantageous over NiCd batteries, seeing that these batteries have a higher specific energy and do not use toxic or carcinogenic metals. The metal hydride in the negative electrode is oxidized and the nickel oxyhydroxide in the positive electrode is reduced to nickel hydroxide when the NiMH battery is discharged [47]. NiMH batteries have a specific power of 200 W.kg$^{-1}$ and a specific energy of about 65 Wh.kg$^{-1}$ and [47]. NiMH batteries are quite safe to operate, have a high volumetric energy and power and are tolerant of overcharging and discharging. NiMH batteries have an energy density of about twice that of a lead-acid battery and can be recycled [52]. The long cycle life of these NiMH batteries is reduced to 200-300 cycles when they are discharged at high loads. The memory effect also reduces the energy capacity of the battery in HEV or EV vehicle applications [53]. The state-of-charge of a NiMH battery is difficult to measure because the SoC versus voltage plot of the battery is non-linear. Throughout the 20%-80% SoC range the voltage of a NiMH battery is almost flat [29].

### 2.3.1.3 Lithium batteries

Lithium batteries are widely used in mobile devices, such as cell phones, laptops and other portable devices. Lithium has interesting electrochemical properties and is the lightest of all metals. This results in a battery type that has a very high specific energy and specific power [47]. Lithium-ion and other lithium-based batteries have one of the highest energy densities compared to other rechargeable battery chemistries. Two main types of lithium batteries exist, namely lithium-polymer and lithium-ion. The significant difference between these two types of batteries is the chemical electrolyte used between the anode and cathode. Li-ion batteries use a liquid electrolyte whilst the Li-Po batteries use a gel-like electrolyte or a porous chemical compound. Both battery types have a high energy efficiency, high energy density, a low self-discharge rate and require very low maintenance [49]. The energy density of Li-ion and Li-Po batteries range from 120 to 220 Wh.kg$^{-1}$

and a power density ranging from 150-315 Wh.kg$^{-1}$ [50], [54]. Both these battery types have an operating temperature range from -20$^\circ$C to 65$^\circ$C.

The most commonly used lithium-ion batteries make use of carbon anodes and some lithium-based material for the cathode. Some of the materials used for the cathode for these lithium batteries are LMO (Lithium Manganese Oxide), LFP (Lithium Iron Phosphate), LCO (Lithium Cobalt Oxide) and NCA (Lithium Nickel Cobalt Aluminium Oxide). Table 2.1 shows the type of electrodes used in some of the most common electric vehicles [55], [56].

Table 2.1: Electric vehicle battery composition (adapted from [55], [56])

| Vehicle | Positive electrode | Negative electrode | Vehicle release year |
|---------|-------------------|--------------------|--------------------|
| Tesla Roadster | Lithium Nickel Cobalt Aluminium Oxide | Carbon | 2008 |
| Nissan Leaf EV | Lithium Manganese Oxide | Carbon | 2010 |
| Chevrolet Volt | Lithium Manganese Oxide | Carbon | 2011 |
| Renault Fluence Z.E. | Lithium Manganese Oxide | Carbon | 2011 |
| Honda Fit EV | Lithium Nickel Cobalt Manganese Oxide | Lithium Titanate | 2012 |
| Tesla Model S | Nickel-type | Carbon | 2012 |
| Tesla Model 3 | Nickel Cobalt Aluminium | Carbon | 2017 |
| BMW i3 | Nickel Manganese Cobalt | Carbon | 2018 |

Lithium batteries have a higher production cost than that of Ni-Cd or Ni-MH battery packs. Regardless of the battery chemistry used, lithium-ion batteries have a good power discharge performance over a temperature band spread around room temperature [57]. The temperature band within which these batteries operate is difficult to widen, although using different chemistries and electrolyte solutions allows the midpoint of the temperature to be shifted. Asma Mohamad Aris *et al.* (2017) performed an experimental study in which the capacity of a lithium-ion cell was analysed at different operating temperatures at the same constant discharge current [58]. Figure 2.15 shows the experimental results of Asma Mohamad Aris *et al*. which shows how the capacity of the battery is reduced at lower temperatures.

Charging lithium-ion batteries at low temperatures is also detrimental to the performance of these batteries, reducing the cycle life of the battery. Charging the battery at temperatures below 0°C causes the metallic lithium to deposit on the carbon anode of the battery, resulting in the lower cycle life of the battery. The self-discharge rate for lithium-ion batteries is very-low, losing about 5% a month [49]. These batteries have a life cycle of about 1500 cycles but the cycle life is also temperature dependent [49].
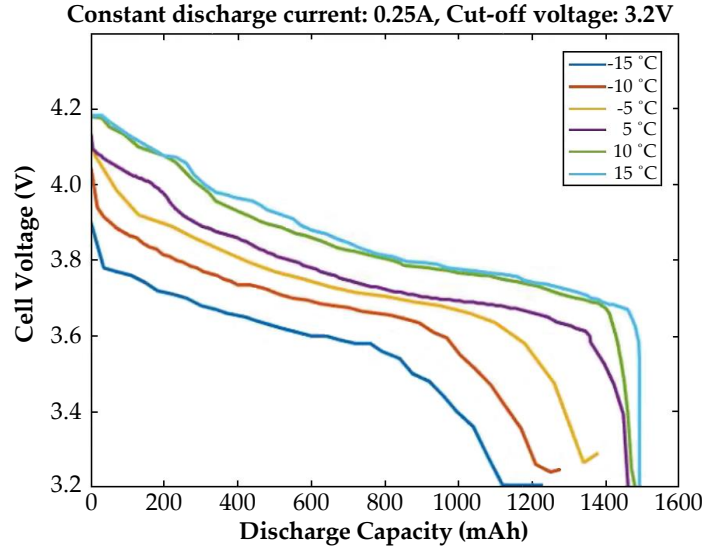
Figure 2.15: Battery capacity versus temperature variation (adapted from [58])

Lithium-ion batteries are also not very rugged, requiring a protection circuit to maintain safe operation and preventing the battery from being discharged too low. The protection circuit also limits the maxim voltage of each cell during charging. The charging and discharging currents also need to be limited to prevent damage to these batteries. Lithium-polymer batteries lifetime is somewhat lower than that of Li-ion batteries, with a typical life cycle of about 600 [49]. Lithium-polymer batteries are typically more temperature sensitive than lithium-ion batteries. These lithium-polymer batteries are lighter than lithium-ion batteries.

## 2.3.2 Ultracapacitors

A capacitor is an electrical component that stores energy in an electric field that was created by the accumulation of electric charge [38]. The electrical charge is stored on two parallel conducting plates which are divided by an insulating material called a dielectric. The energy stored within a capacitor is given by equation 2.1, where

$$W = \frac{1}{2}CV^2.$$ 
(2.1)

where $C$ is the capacitance of the capacitor, which is defined as the capacitor's ability to accumulate electric charge [38]. The capacitance of a capacitor is given as follow [38]:

$$C = \frac{\varepsilon A}{d}.$$ 
(2.2)

As we can note from equation 2.2, capacitance is determined by the dielectric constant of the dielectric between the plates, the distance between the plates and the effective area of the plates. Capacitors can generally be classified into three categories namely *electrochemical*, *electrolytic* and *electrostatic* [38]. The electrostatic capacitor is the conventional capacitor that consists out of two conducting plates and a dielectric material between the plates [38]. Electrolytic capacitors are polarized and make use of an electrolytic salt as the dielectric medium between the conducting plates, which results in a smaller effective distance between the conducting plates, increasing the

capacitance of the capacitor as described by equation 2.2. Electrochemical capacitors are similar to the electrolytic capacitors but make use of porous electrodes that has a high surface area to further increase the capacitance compared to electrolytic capacitors. Electrochemical capacitors can have up to 100 to 1000 times the capacitance of a conventional electrolytic capacitor [59]. Electrochemical capacitors are sometimes referred to as supercapacitors, ultracapacitors or double-layer capacitors.

Ultracapacitors can be divided into three general categories [60]:

i.  Pseudocapacitors – Charge is stored in pseudocapacitors by the adsorption of ions from the electrolyte into the electrode due to reduction-oxidation reactions [61]. Pseudocapacitors have a storage capacity and cycle life and between that of a battery and an ultracapacitor [61].

ii.  Electrochemical double-layer capacitors (EDLC) which makes use of two carbon-based electrodes. These carbon electrodes have the characteristic that they have a large surface area, high electric conductivity and high mechanical and chemical stability [60].

iii.  Hybrid capacitors – Hybrid capacitors or hybrid electrochemical capacitors (HECs) generally work by using a pseudocapacitive material as the cathode and has an asymmetric internal configuration. The pseudocapacitive electrodes accumulate charge through faradic redox reactions [62].

Ultracapacitors and capacitors, in general, have a maximum voltage limit, also called the breakdown voltage. When the breakdown voltage is reached, the dielectric medium between the conductive plates of the capacitor becomes conductive and the capacitor effectively becomes a short circuit. Placing capacitors in parallel increases the total capacitance of the capacitor bank, whilst keeping the potential drop over each capacitor the same. Connecting capacitors in series increase the maximum voltage rating of the bank, but reduces the effective capacitance of the bank as shown in equation 2.3.

$$\frac{1}{C_{eq}} = \frac{1}{C_1} + \frac{1}{C_2} + \cdots + \frac{1}{C_n}. \tag{2.3}$$

Mismatches between capacitors connected in series results in an uneven distribution of voltage over each capacitor, which may result in the voltage exceeding the individual maximum voltage of a capacitor. The state of charge (SoC) of a capacitor is the ratio of the remaining energy stored versus the ratio of the maximum stored energy of the capacitor [38]. The SoC is therefore:

$$SoC = \frac{W}{W_m} = \frac{V^2}{V_{max}^2}, \tag{2.4}$$

where $V$ is the voltage of the capacitor at the moment in which the SoC is calculated. The peak power per mass or gravimetric power density of an ultracapacitor at a frequency of 1 kHz is given by [38]:

$$P_{max} = \frac{(V_r)^2}{4 \cdot ESR \cdot mass}. \tag{2.5}$$

The circuit model for an ultracapacitor and capacitor in general is shown in figure 2.16 [63].
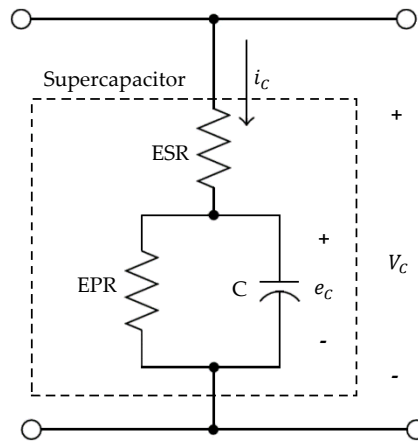


Figure 2.16: Ultracapacitor and capacitor circuit model (adapted from [63])

The circuit model for the ultracapacitor consists out of three components namely the equivalent parallel resistance EPR, the equivalent series resistance ESR and the capacitance $C$. The equivalent series resistance ESR is a loss term in the model that represents the internal heating loss within the capacitor. The ESR of the capacitor is the dominant term that determines the charging and discharging performance of the capacitor. It also plays a big role in the current sharing ratio of the passive HESS topologies, as was discussed in a previous chapter. The ESR is mathematically expressed as

$$ESR = \frac{\Delta V}{\Delta i},\qquad(2.6)$$

where $\Delta V$ is the change in voltage and $\Delta i$ is the change in current at the initiation of the load [63]. The EPR models the current leakage of the ultracapacitor and is expressed as

$$EPR = \frac{-(t_2 - t_1)}{\ln(V_2 - V_1)\,C}\qquad(2.7)$$

Ultracapacitors' capacitance has a frequency dependence, thus the capacitance of the ultracapacitor changes as the frequency changes. This is the result of the ions in the electrolyte that take a certain time to reach the electrode surface. At higher frequencies it is more difficult for the ions to follow the changing electric field and do not reach the pores of the electrodes. The second mechanism is the result of internal leakage pathways in the interface, which results in capacitance reduction and current leakage [38].

One of the advantages of using ultracapacitors in HESS is that the ultracapacitors' performance doesn't decrease as much as that of conventional batteries at low temperatures. The capacitance of the ultracapacitor does not vary much with temperature, but the ESR of the ultracapacitor varies due to the change of ionic resistance at different temperatures. Figure 2.17 shows the relationship between the capacitors ESR and capacitance versus temperature [64].
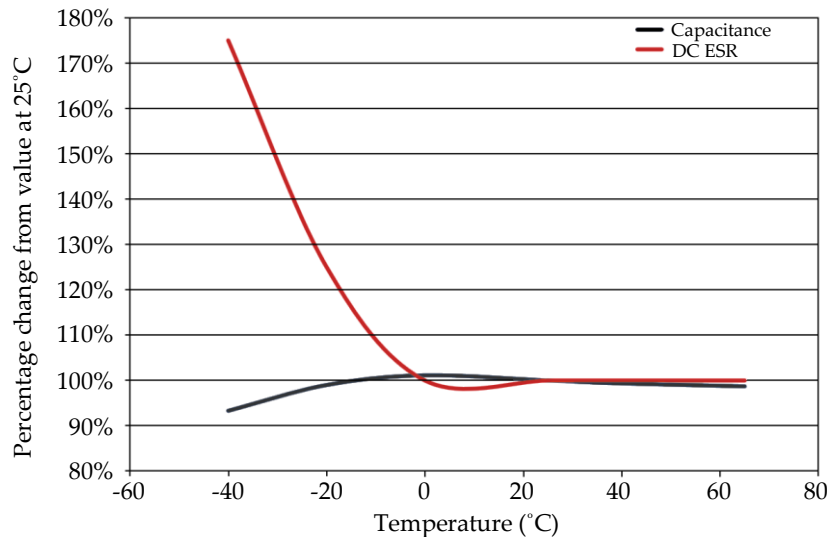
Figure 2.17: Capacitance and resistance versus temperature (adapted from [64])

Ultracapacitors also have a self-discharge rate in which the energy stored within the ultracapacitor is reduced due to some internal mechanism without any connections made between the electrodes. Just like batteries, ultracapacitors also suffer from self-discharge. Self-discharge in ultracapacitors occurs when the ultracapacitor is charged to its threshold value, wherein excess ionic concentration builds up close to the interface of the capacitor and once the ultracapacitor is disconnected from the charging source, a self-discharge redox reaction takes place due to impurities in the interface [38].

Figure 2.18 is used to illustrate the different characteristics between an ultracapacitor and the different battery types discussed in section 2.3.1. As noted from the figure, the biggest difference between the ultracapacitors and batteries is in their power density, energy density and cyclability.
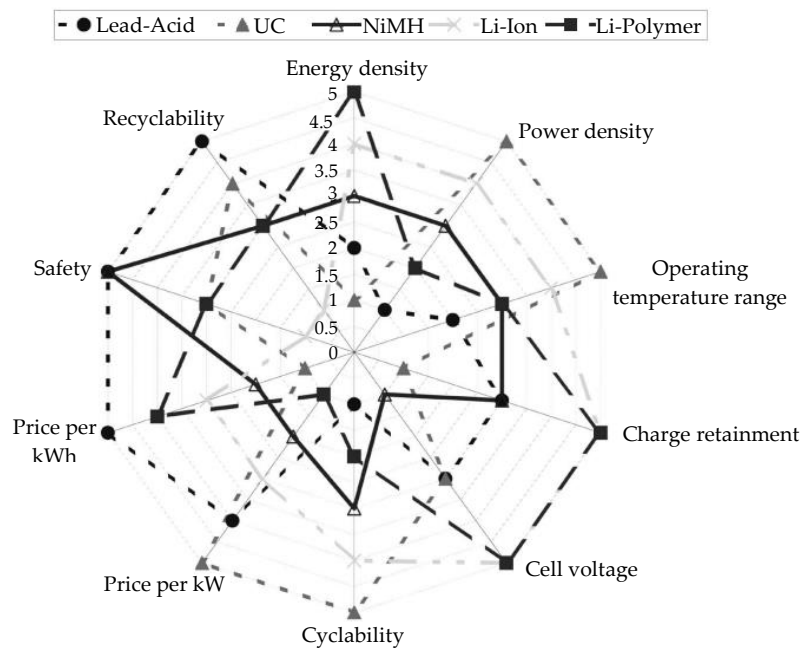


Figure 2.18: Electrical energy storage device comparison (adapted from [29])

## 2.3.3 Fuel Cells

A fuel cell converts electrochemical energy to electrical energy [48]. The fuel cell makes use of an external source of fuel, which reacts in the presence of an electrolyte. Fuel cells commonly use galvanic cells to convert chemical energy into electrical energy. The fuel is supplied to the positive electrode or anode, where electrons are released from the chemical fuel. The electrons flow from the anode through the external circuit to the cathode, due to the potential difference between the electrodes [17]. Fuels cells can virtually operate continuously and differ from batteries in the sense that they consume reactants while the reactants in a battery remain in a closed system. The electrodes within a fuel cell are relatively stable and do not change as quickly as in a battery.

Various fuels can be used in fuel cells. The most commonly used fuel is oxygen and hydrogen. Other fuels such as hydrocarbons and alcohols are used, while chlorine, air and chlorine dioxide can be used as an oxidant. The basic operation of a fuel cell is shown in figure 2.19 [47].
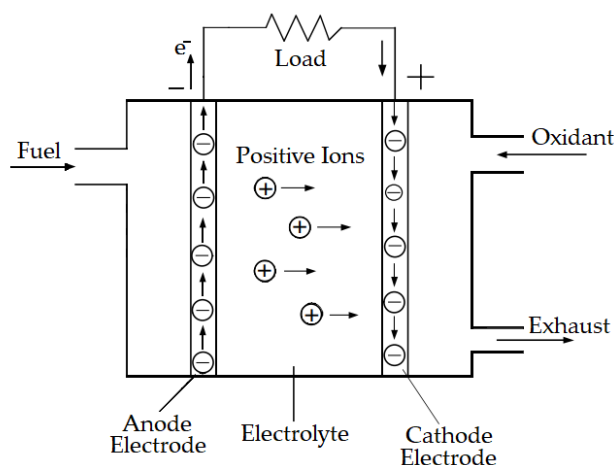


Figure 2.19: Fuel cell structure (adapted from [47])

*Hydrogen fuel cells* produce electricity by utilising oxygen and hydrogen. Reversible hydrogen fuel cells also exist, in which electricity is used to produce oxygen and hydrogen. Hydrogen can be produced by various means such as an electrolyser unit, thermo-chemical reactions or photochemical processes [48]. Different hydrogen fuel cell designs exist, such as Proton Exchange Membrane Fuel Cells (PEM-FCs), Regenerative Fuel Cells (RFCs), Phosphoric Acid Fuel Cells (PAFCs) and Alkaline Fuel Cells (AFCs).

Hydrogen fuel cells have different advantages, such as a high energy density in the range of 0.6 – 1.2kWh/kg. Fuel cells are also easy to implement over a wide range of power scales, from kW to MW applications. They also have a modular construction which allows one to easily add additional modules to the system. Fuel cells, unfortunately, are somewhat expensive when compared to battery systems and also have a slow response time to power changes.

*Direct-methanol fuel cells* are a subcategory of PEM-FCs in which the fuel is fed directly into the fuel cell. Methanol is used as the fuel and is easier to store than hydrogen, seeing that no low-temperature or high pressure storage vessels are required. The direct-methanol fuel cells (DMFC)

form carbon dioxide by the oxidation of methanol on the catalyst layer of the fuel cell. Water is consumed at the anode and produced at the cathode. These fuel cell cannot use pure methanol without utilising water which can be provided passively via osmosis or actively by pumping the water. The requirement for water reduces the energy density of the fuel cell, but methanol has a much higher energy density than hydrogen [48]. The efficiency of the DMFC is lower than that of hydrogen fuel cells.

*Molten carbonate fuel cells* work by using molten lithium sodium carbonate salts or lithium potassium [48]. When these salts are heated the salt generates carbonate ions as the salt melts; these ions then flow from the cathode to the anode. These fuel cells produce as a result of the reaction carbon dioxide, water and electrons. The electrons flow through an external circuit from the anode to the cathode. This type of fuel cell is unsuitable for automotive applications due to their high operating temperature as well as the long time it takes these cells to reach their operating temperature. These fuel cells have a high efficiency, which makes them attractive for industrial applications [48].

## 2.3.4 Flywheel

Flywheels store energy by means of the angular momentum in a rotating mass. The kinetic energy stored within the rotating flywheel can be converted into electrical energy by means of an electrical motor/generator. A motor is typically used to accelerate the flywheel, whilst a generator is used to transform the kinetic energy into electrical energy. The motor and generator used in the system could be the same electric motor. Figure 2.20 shows a typical flywheel system [65].
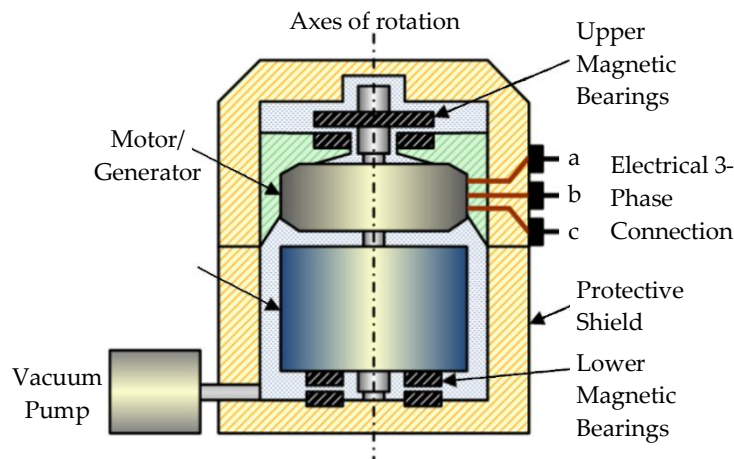


Figure 2.20 Flywheel structure(adapted from [65])

The kinetic energy of a rotating flywheel is

$$E = \frac{1}{4}M\omega^2 r^2 \tag{2.8}$$

where $E$ is the kinetic energy stored within the flywheel, $r$ is the radius of the motor, $M$ is the mass of the flywheel and $\omega$ is the rotational speed of the flywheel. Flywheels are designed with a maximum rotational speed in mind. Flywheels with a high rotational speed are more attractive for automotive applications seeing that they have a smaller form factor and the kinetic energy is directly

equal to the square of the rotational speed of the flywheel [29]. Flywheel energy storage systems are normally operated in a partial vacuum to reduce the losses within the system caused by aerodynamic resistance. Some flywheels also make use of noncontact magnetic bearings to reduce the losses in the system. Flywheels are somewhat dangerous due to the high amount of kinetic energy stored within these devices. Flywheels utilize containments vessels in the case of a mechanical failure of the rotor in the system. Flywheels have a long service life compared to batteries and do not suffer from capacity loss [29], [65]. Flywheels also do not suffer from depth-of-discharge effects as experienced in batteries. Flywheels have a high efficiency which is usually in the range of 90-95% [48]. Flywheel systems are typically used as a power quality device to provide energy during a shift from one power source to another [48]. The maximum power a flywheel system can deliver depends on the power rating of the electric motor connected to the flywheel system. Flywheel systems can be used as a short-term energy storage method, whilst being able to provide high specific power. The Oerlikon Engineering Company in Switzerland made a passenger bus that used a flywheel that weighs 1500 kg which rotated at a speed of 3000 rpm [66]. The passenger bus was recharged at each bus stop, using the available electrical supply to accelerate the flywheel to its maximum speed.

In order to compare the electrical energy storage systems as discussed in this section, the different characteristics of these systems are summed up and compared in table 2.2 below.

Table 2.2: Electrical Energy Storage Comparison (adapted from [49], [54], [66], [67])

| Energy Storage Type | Gravimetric Energy Density (Wh/kg) | Specific Power (W/kg) | Cycle Life |
|---|---|---|---|
| Lead Acid | 30-50 | 180-400 | 1000-3000 |
| Ni-Fe | 30-60 | 25-150 | 1200-4000 |
| Ni-Cd | 40-80 | 150-350 | 2000-3000 |
| Ni-MH | 70-95 | 200-300 | 500-3000 |
| Lithium-ion | 110-250 | 200-430 | 1500-3500 |
| LiPo | 130-225 | 260-450 | >1200 |
| Ultracapacitors | 5-15 | 1000-10 000 | 1 000 000 |
| Fuel Cells* | 250 -1 000 | 50-200 | 1 000 - 5 000 hours |
| Flywheel | 10 - 150 | 2 000 – 10 000 | > 100 000 |

* These values are highly dependent on the type of fuel cell used. The cycle life of the fuel cell is also dependent on the type of membrane used as well as the amount of power generated by the fuel cell.

# 2.4 Battery Characteristics

This section discusses some of the important characteristics of batteries that are applicable to this project. Figure 2.21 shows an overview of the battery characteristics that were investigated.
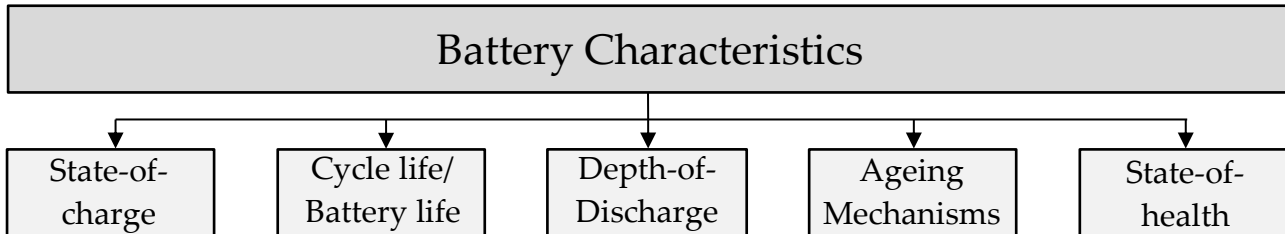


Figure 2.21: Battery characteristics section overview

## 2.4.1 State-of-Charge (SoC)

The state-of-charge of a battery or EES device is defined as the ratio of the current capacity $Q_t$ of the battery to the nominal capacity $Q_n$ of the battery. The nominal capacity of the battery is normally given by the manufacturer. The SoC is defined as

$$SoC = \frac{Q_t}{Q_n}. \tag{2.9}$$

Four main SoC estimation methods are used in the literature, which are [68]:

i. Direct measurement – The measurement method uses the physical battery properties to determine the SoC of the battery. A commonly used property that is used is the internal resistance of the battery.

ii. Adaptive systems – The adaptive systems make use of adaptive methods such as a Kalman filter or neural networks to determine the SoC of the battery.

iii. Book-keeping estimation – This method involves monitoring the current flowing into or out of the battery and integrating this current over time to determine the SoC of the battery.

iv. Hybrid methods – The hybrid methods make use of multiple estimation methods to further improve the accuracy of the SoC estimation.

The SoC estimation methods are described more thoroughly below:

1. *Direct measurement* [69]: Many different methods are used to approximate the SoC of the battery. This includes the open-circuit voltage method, impedance measurement method, impedance spectroscopy method and the terminal voltage measurement method.

   1.1 *Open-circuit voltage method:* There is a somewhat linear relationship between the open-circuit voltage and the SoC of the battery. This relationship varies for every battery and depends on the battery type used. This method requires the battery to be disconnected from the load for a certain period of time to accurately determine the SoC.

   1.2. *Terminal voltage method:* Seeing that the EMF of a battery is approximately linearly proportional to the SoC of a battery, the terminal voltage of the battery is also approximately

proportional to the SoC. This method can be inaccurate seeing that the terminal voltage has a non-linear characteristic when the battery is close to the end of its discharge.

*1.3. Impedance method:* The impedance measurement method measures the internal impedance of the battery. The relationship between the SoC of a battery and the impedance is not unique for all battery types and is normally not linear.

*1.4. Impedance Spectroscopy method:* This method measures battery impedance over a wide range of ac frequencies. This is done at different current and discharge currents and these measured impedance measurements are used to correlate the measured impedance with the current impedance of the battery to determine its SoC.

2. *Book-keeping Estimation* [61]: This method measures the current flowing into or out of the battery. The characteristics of the battery are used in this method to take into account the loss within the battery, capacity-loss and discharge efficiency. Two methods are commonly used, the Coulomb counting method and the modified Coulomb counting method.

   2.1. *Coulomb counting method:* This method measures the battery current and integrates over time and uses this information to estimate the SoC of the battery according to

$$SoC(t) = SoC(0) - \int_{\tau=0}^{t} \frac{I_b(\tau)}{Q_b} d\tau, \tag{2.10}$$

   where $I_b(\tau)$ is the instantaneous current measured and $Q_b$ is the nominal battery capacity.

   2.2. *Modified Coulomb counting method:* This method is similar to the previously mentioned method but uses the corrected current to improve the accuracy of the method. The corrected current is a function of the instantaneous current and is given as

$$I_c(t) = k_2 I(t)^2 + k_1 I(t) + k_0, \tag{2.11}$$

   where $k_0$, $k_1$ and $k_2$ are constants that are experimentally determined.

3. *Adaptive systems* [68]: Adaptive systems make use of neural networks, fuzzy logic, fuzzy neural networks and Kalman filters. These systems adapt and change their parameters automatically. Seeing that the performance of the battery is affected by multiple chemical factors, the SoC is typically nonlinear and these methods estimate the SoC better than other methods. Some of the neural networks used in the adaptive system is

   3.1. *BP Neural Network:* The backpropagation neural network is one of the most commonly used neural networks. The neural network is a multi-layer feedforward network that makes use of backpropagation to train the neural weights of the network.

   3.2. *RBF Neural Network:* The radial basis function is a neural network that has three layers namely the input, hidden and output layer. In an RBF neural network, each input node is connected to all the hidden layer nodes. The output of the neural network is a linear combination of the hidden layer functions.

   3.3. *Fuzzy logic method:* The fuzzy logic method makes use of fuzzy logic to approximate the SoC of the battery by using input parameters such as the impedance and voltage of the

battery. Fuzzy logic requires a thorough understanding of the influence of these parameters on the SoC of the battery.

4. *Hybrid Methods* [68]: Hybrid methods combine two of the methods discussed in the above sections. Hybrid methods benefit from the advantages of each method but results in a more complex method/algorithm. The hybrid methods are not discussed in detail, instead only some combinations that have been used in the literature are given below:

   *4.1. Coulomb counting and EMF combination*

   *4.2. Kalman filter and Coulomb counting*

   *4.3. Extended Kalman filter and per-unit system.*

## 2.4.2 Cycle life/Battery life

The cycle life of a battery is defined as the number of discharge-charge cycles that can be performed by the battery before the battery fails to meet a certain performance criteria. It is important to distinguish between the calendar life and the cycle life of a battery. The calendar life of the battery refers to the calendar aging that occurs as the battery ages, whether or not the battery is in use. Cyclic aging is related to the usage of the battery [70].

The cycle of batteries is usually tested using three methods, namely [71]

- A standardised cycle life test in which the battery is discharged at a constant current using the full battery capacity at a constant temperature.

- A specialised evaluation of a battery's performance for a specific application, which includes applying load cycles to the battery that matches that of its intended application.

- An accelerated test in which one of the battery aging mechanisms is manipulated to drastically decrease the cycle life and therefore the time required to test the battery. The temperature of the battery is typically elevated to simulate battery aging [72].

These test methodologies are difficult to compare seeing that battery aging mechanisms are highly non-linear [71].

These tests that are used to evaluate the cycle life of a battery typically consist of three steps:

1. Measurement of the battery's initial performance.

2. A series of cycle life tests are performed.

3. Measurement of the battery's cell performance and cell degradation at the end of the battery's life.

## 2.4.3 Depth-of-Discharge (DoD)

The depth-of-discharge of the battery refers to the percentage of the battery capacity that has been discharged as a percentage of the total battery capacity [73]. The depth-of-discharge value to which a battery is discharged typically affects the cycle life of the battery [74]. A relationship exists between the battery capacity, cycle life and depth-of-discharge experienced by the battery. Increasing the depth-of-discharge reduces the number of charge/discharge cycles that the battery can endure before losing capacity. This relationship is shown in figure 2.22.
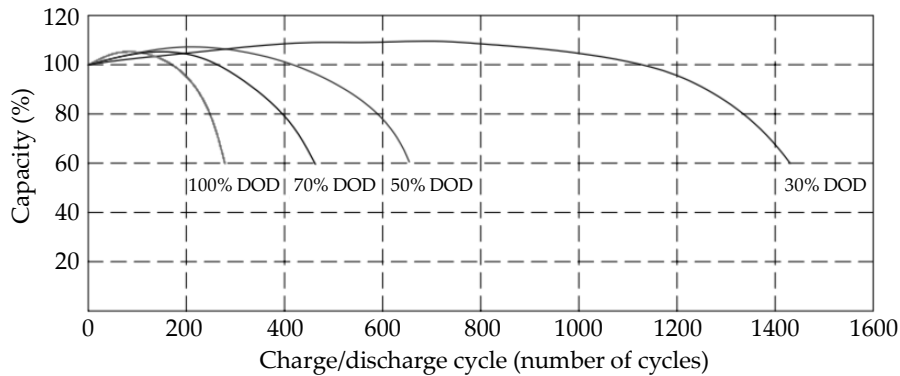


Figure 2.22: Capacity versus Cycle life at different DoD's (adapted from [74])

## 2.4.4 Ageing Mechanisms

Batteries degrade and lose capacity as they age. The capacity loss within the battery can be attributed to various factors that negatively affect the battery such as high operating temperature, high discharge/charging rate and high SoC levels. Each battery chemistry type also experiences aging due to the specific chemistry and electrochemical reactions used in the battery. The capacity loss is linked to the degradation of the electrolyte used in the battery, as well as the degradation of the electrodes [75]. The electrodes degrade in the battery by varies means but are normally caused by the loss of active material in the electrode, surface area reduction and loss of conductivity [71]. The different chemical compounds used in the various battery chemistries result in different aging processes for each battery chemistry type. The battery cells also degrade even if the cells are not used. The following components or aging mechanisms are [70]:

- *Aging of the anode*

- *Aging of the cathode*

- *Aging of the electrolyte and separator*

- *Aging of exterior cell components*

The main causes of anode aging in Li-ion batteries are as follow [70]:

1. *Current collector corrosion*:        Corrosion increases the contact resistance and contact loss of the collector.

2. *Change in morphology:* The morphology of the anode can be negatively altered due to either mechanical stresses or morphological changes at the surface of the anode due to solvent co-intercalation [76].

3. *Lithium plating:* Lithium plating, which is the formation of metallic lithium around the anode, occurs when the $Li^+$-ions cannot intercalate fast enough into the anode and Li deposits form around the anode. This usually occurs when high charging currents are experienced at low temperatures.

4. *SEI layer:* The SEI (Solid Electrolyte Interphase) layer is used to protect the particle surface. Any defect in this layer results in lithium corrosion which reduces the energy available in the battery [70].

The aging of the cathode in the Li-ion batteries are caused by [75] :

1. *SPI Formation:* Solid Permeable Interphase (SPI) is a film layer formed on the cathode particles due to electrolyte reactions and undergoes changes during the battery's lifetime.

2. *Loss of Active Material:* The loss of active material is due to structural damage, particle cracking and insufficient contact.

3. *Metal dissolution:* Metal dissolution results in capacity loss and results in higher contact resistance.

## 2.4.5 State of Health

The state of health (SoH) of a battery is used to characterize the current condition of the battery. The factors determining the SoH of the battery is the internal resistance of the battery and the capacity of the battery [70]. The two most commonly used SoH definitions used are:

- *SoH$_C$ – Capacity Rated*: The capacity of the battery is the most important determining factor and compares the initial capacity of a fresh battery to the actual capacity of the battery.

- *SoH$_R$ – Impedance Rated*: The battery's ability to provide power to the system is the most important factor and is strongly related to the impedance of the battery.

It is difficult to define the SoH of a battery as there are multiple definitions of the SoH in the literature and no unified definition [77]. The state-of-health of the battery is as stated above related to the number of cycles endured by the battery as well as the temperature experienced by the battery. Figure 2.23 shows this relationship [78].
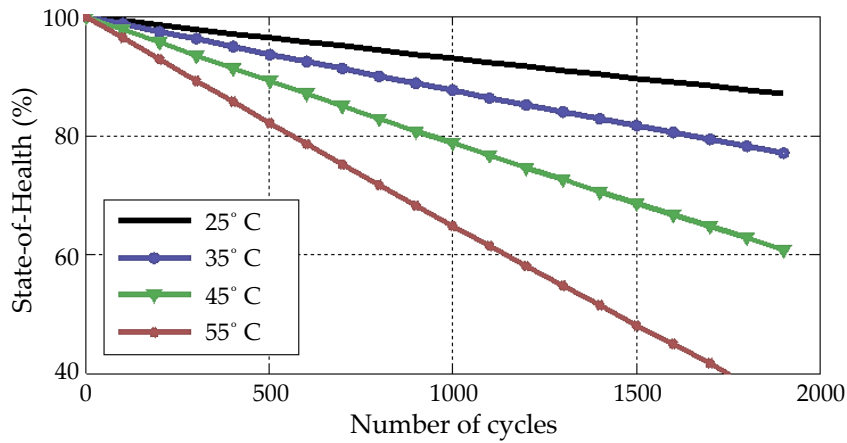
Figure 2.23: SoH versus Cycle Life (adapted from [78])

# 2.5 Control Topology

This section documents some of the control topologies that were applicable to this thesis. Figure 2.24 shows the control topologies that were investigated in this section.
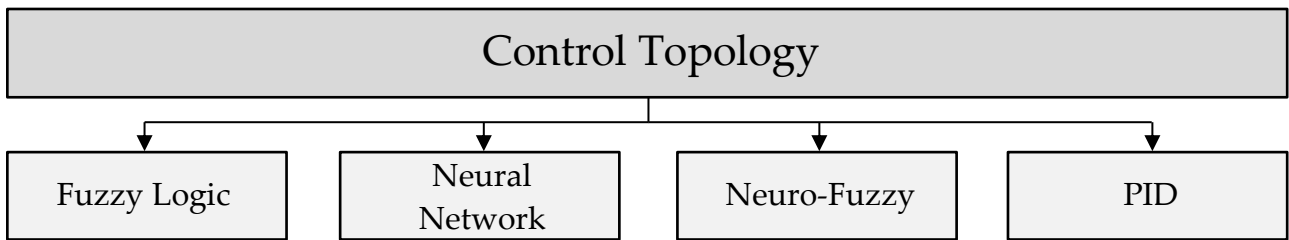


Figure 2.24: Control topology section overview

A control system is a system that controls the behaviour of different components in the system so that the system will provide a desired system response [79]. Control systems can be divided into two categories: open-loop and closed-loop [80], [81]. Both open-loop and closed-loop controllers aim to maintain a variable at a desired value. Open-loop control systems have no feedback and thus cannot modify the input to control the output of the system [79]. A closed-loop control system attempts to maintain the desired output by comparing the desired output to the actual output of the system and adjusts the systems controlling functions accordingly [79]. A closed-loop control system is shown in figure 2.25.
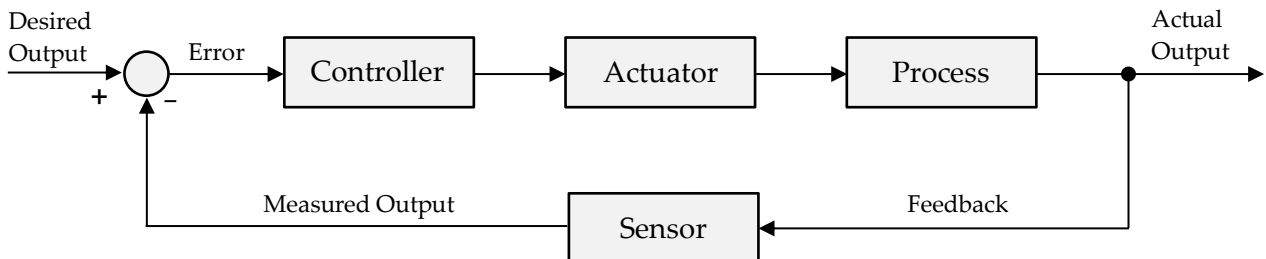


Figure 2.25: Closed-loop control system (adapted from [81])

Closed-loop control systems have many advantages over open-loop control systems, such as being able to better reject external disturbances and noise [79]. Closed-loop control systems also tend to more accurate [82].

A set of standard test signals are used to compare the performance of different competing controllers. The step response of a system in the time domain is the output of the system over time when a step input is applied [83]. The step response of a system is shown in figure 2.26.
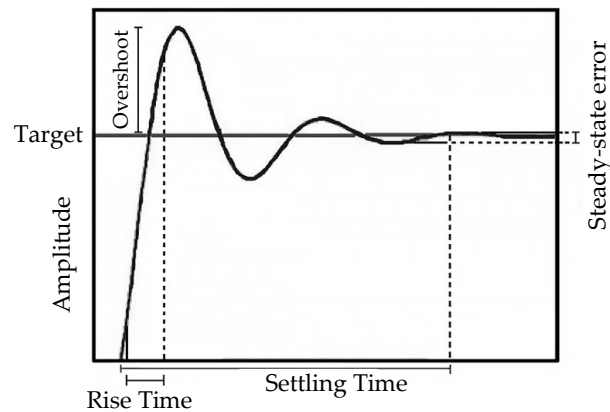


Figure 2.26: Step response of a system (adapted from [83])

The following characteristics are of importance when comparing the step response of controllers [83]:

- **Rise time** – Is the time taken for the output signal to rise from a specified lower threshold value (typically 10%) to a specified higher threshold (typically 90%) after the step input is applied.

- **Peak time** – The time taken for the output signal to reach its maximum value.

- **Overshoot** – The percentage by which the output exceeds the steady-state value.

- **Settling time** – The time taken for the response of the system to settle within a certain range of the steady-state value.

- **Steady state error** – The difference between the steady-state output signal and the referenced signal.

## 2.5.1 Fuzzy Logic

Fuzzy logic is based on fuzzy sets, which is in turn a generalization of classical set theory [84]. In standard or binary logic, a condition is either true false (a degree of truth of 0.0) or true (a degree of truth of 1.0). Fuzzy logic allows partially true conditions that have a degree of truth ranging from 0.0 to 1.0. Fuzzy logic is aimed at providing a formalized method of reasoning which is approximate rather than exact. This allows one to characterize and control a system whose model and characterizing functions are ill-defined or not known [85]. Fuzzy logic is able to handle vague and imprecise terms and data [86]. Fuzzy logic makes use of four sub-systems which are the fuzzifier,

defuzzifier, rule base and membership functions. Figure 2.27 shows the components of a fuzzy logic controller.
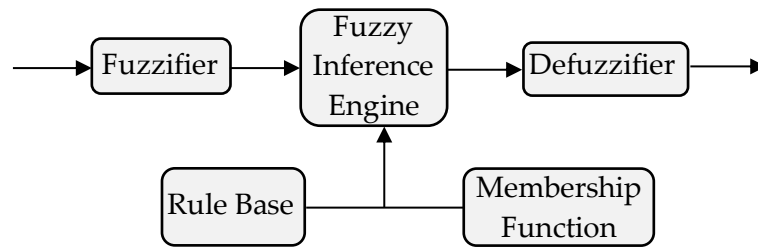


Figure 2.27: Fuzzy Logic System [87]

The fuzzifier converts the crisp numeric input received to a linguistic variable using the membership functions and rule base [87]. The fuzzy inference is a method that interprets the values of the fuzzy input vector to the output vector, based on the rules set in the rule base [88]. The defuzzifier then converts the fuzzy quantity or linguistic variables to a precise quantity that can be used in the real world. The fuzzifier and defuzzifier both make use of membership functions to map the non-fuzzy inputs to fuzzy linguistic values and vice versa [89]. Membership functions are curves that define how each input vector is mapped to a membership value between 0 to 1. Various types of membership functions exist, with the most commonly used functions as follow:

- Trapezoidal function

- Triangular function

- Gaussian function

- Generalised Bell function

Membership functions can be any arbitrary curve. A more complex curve increases the computational time required to evaluate the curve. Although the shape of the membership function influences how the input is mapped to a membership value, the number of membership functions used and the overlap between these functions has a big influence on the output of the fuzzy system.

Fuzzy logic controllers have the following advantages:

- It does not require a transfer function or a precise mathematical model of the system [90].

- Fuzzy logic is tolerant of imprecise data [88].

- Fuzzy logic does not require training sets like neural networks, but can be created from the expert knowledge of the system [88].

- It is easy to interpret the results of a fuzzy system because of the linguistic variables and methods used [91].

Fuzzy logic has the following disadvantages:

- Changes in the system that alter the topology of the system require that the rule base of the system be adapted [91].

- In order to define the inference logic rules, the designer requires a thorough understanding of how the system works [91].

- Trail-and-error is often used to optimize the system.

- There are several tuning parameters (defuzzification, inference and fuzzification) that need to modified whilst optimizing system performance.

S. T. Sisakat *et al.* (2015) utilised a fuzzy logic controller to implement an energy management strategy for a hybrid energy storage system that utilised a battery and an UC. The fuzzy logic controller was deployed to three different HESS topologies [92].

Z. Shengzhe *et al.* (2017) also utilised a fuzzy logic-based control structure to implement power management in a hybrid energy storage system. The controller utilises a Kalman filtering algorithm to estimate the SOC of the battery and the state-of-power of the system and calculates the power flow accordingly [93].

## 2.5.2 Neural Network

Neural networks are adaptive networks that are composed of simple processing elements, also called neurons that operate in parallel [94]. Various networks exist and they resemble the brain in two regards [95]:

1. The processing elements obtain information from the environment through some learning methods.

2. The connection strength between the simple processing units or neurons, known as the synaptic weights, is used to store the acquired knowledge.

The learning method entails that a learning algorithm is used, which modifies the synaptic weights between the neurons. Advanced learning methods also exist in which the topology of the neural network changes and modifies itself, similar to how neurons in the human brain die and new synaptic connections are made. Neurons as referred to in neural networks are information-processing units that are central to neural networks. Figure 2.28 shows the basic non-linear model of a neuron.

Three basic components form the model of the neuron in figure 2.28. These components are:

1. The connecting links, also called synapses, have a synaptic weight which is multiplied by the input signal $x_k$. The synaptic weight of an artificial neuron can range from negative to positive values [95].

2. An adder block sums the input signals after the synaptic weight has been multiplied. Linear or non-linear adder blocks are used.

3. The output of the neuron has to be limited to a permissible amplitude or range. This is done through the activation function. Different types of activation functions are used to limit the output of the neuron to permissible levels. The most commonly used functions are the threshold function and the sigmoid function.
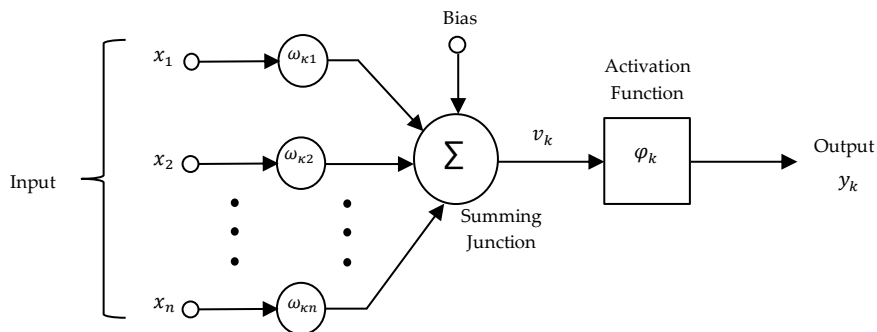


Figure 2.28: Non-linear neuron model (adapted from [95])

The neural network structure is linked with the learning algorithm used by the neural network. There are three main different types of neural networks [95]:

1. Single-layer Feedforward Networks – A network in which the input layer of nodes are directly connected to the output layer of neurons as shown in figure 2.29a. This network is strictly feedforward and is called a single-layer feedforward network seeing that there is only a single-layer of computational nodes.

2. Multilayer Feedforward Networks – Multilayer feedforward network differs from a single-layer network by using multiple computational layers. The computational layers that are not connected directly to the output of the network are called hidden layers, as is shown in figure 2.29b. Adding hidden layers adds to the amount of information that the network is able to process.

3. Feedback Networks – Feedback networks differ from feedforward networks by utilizing at least one feedback loop. Feedback loops in neural networks improve on the learning ability of the neural network [95].

Artificial neural networks have the following advantages:

• After an ANN has been trained, the ANN is able to produce output with incomplete information [96].

- If one or more of the cells in an ANN gets corrupted the ANN is still able to generate output. [97].

- ANN process information in a parallel way, increasing throughput [97].
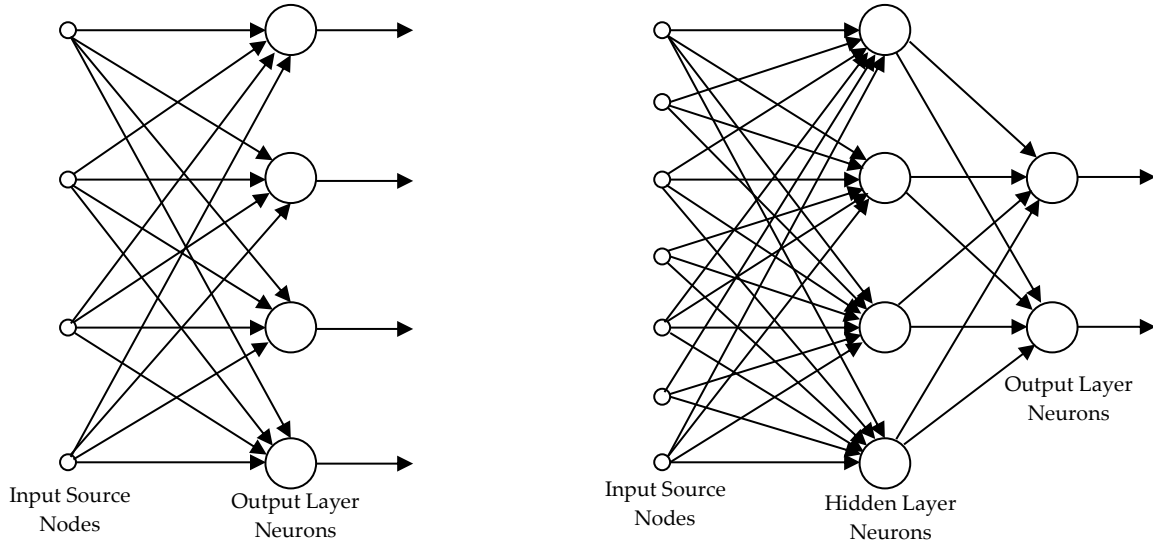


Figure 2.29: **a**) Single-layer feedforward network (adapted from [95]); **b**) Multi-layer feedforward network (adapted from [95])

Artificial neural networks have the following disadvantages:

- Artificial neural networks require excessive training times [98].

- The neural network depends on the quality and accuracy of the data set [98].

- Neural networks require processors with parallel processing power, due to their parallel nature.

## 2.5.3 PID Controller

PID control is one of the most commonly used closed-loop control structure [99]. The mnemonic *PID* refers to the individual terms in the controller, namely Proportional for P, Integral for I and Derivative for D. The PID controller consists out of a Proportional controller (PC), Integral controller (IC) and a Derivative controller (DC), as is shown in figure 2.30.
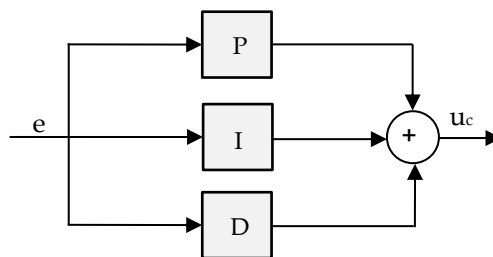


Figure 2.30: PID (adapted from [99])

### 2.5.3.1 Proportional controller (PC)

The proportional controller changes the controlled variable proportionally and is dependent on the present error of the system. Proportional control is widely used and the steady-state error in the system is inversely proportional to the proportional gain. As the proportional gain constant increases so does the steady-state error of the system, but if the gain becomes too large, the system can become unstable [100]. If the proportional gain constant is too small, then the corrective action of the system may be too small when system disturbances occur. The proportional gain alone can never be used to eliminate the steady-state error. The time-domain representation of the proportional gain is given as:

$$u_c(t) = k_p e(t) \tag{2.12}$$

### 2.5.3.2 Integral controller (IC)

The integral controller is used to correct the steady-state error produced by the proportional controller. The integral controller's output is proportional to both the duration of the error and the magnitude of the error. The integral in the integral controller sums the instantaneous error over time. The integral controller corrects the steady-state error of the proportional control system, but it may worsen the transient response of the system [100]. The time-domain representation of the integral controller is given as:

$$u_c(t) = k_I \int e(\tau)d\tau \tag{2.13}$$

### 2.5.3.3 Derivative controller (DC)

The derivative controller uses the derivative of the error (rate of change of the error) signal and multiplies this rate of change with the derivative gain. The derivative controller has the effect that it slows the rate of change of the controller [100]. Derivative control has the effect of increasing the stability and reducing the overshoot of the system [100]. It also improves the transient response of the system. The time-domain representation of the system is given as follows:

$$u_c(t) = k_D \frac{de}{dt} \tag{2.14}$$

### 2.5.3.4 Proportional integral controller (PI)

The proportional integral controller integrates the proportional and integral controllers as can be deducted from the name. PI controllers eliminate forced oscillations and reduce the steady-state error of the system, but have a negative effect on the transient response. The time-domain representation of the system is as follows:

$$u_c(t) = k_p e(t) + k_I \int e(\tau)d\tau \tag{2.15}$$

## 2.5.3.5 Proportional derivative controller (PD)

The derivative controller alone may in some circumstances produce no control signal. This could occur when there is no change in the error signal as might occur in steady-state circumstances. The controller would thus not be able to rectify the steady-state error. The derivative term is thus always used in conjunction with the proportional term, in order to prevent the controller from entering this inactive state [99]. The time-domain representation is as follows:

$$u_c(t) = \ k_p e(t) + k_D \frac{de}{dt} \tag{2.16}$$

## 2.5.3.6 Proportional Integral Derivative controller (PID)

The PID controller integrates the three different control types and is the most commonly used controller type in the industry [101]. Two methods are commonly used in order to determine the constants and tuning parameters of the PID controller. Firstly, a process model can be derived for the system to be controlled. P, I and D constant values can then be chosen based on the dynamic model of the system. Secondly, a manual tuning method can be used to tune the parameters of the system. The effect of the parameters on the performance of the system is given in table 2.3. The time-domain structure of the PID controller is as follows:

$$u(t) = \ k_p e(t) + k_D \frac{de}{dt} + \ k_I \int e(\tau) d\tau \tag{2.17}$$

Table 2.3: PID Parameter influence (adapted from [100], [102])

| PID Parameter | Overshoot | Steady-State Error | Rise Time | Settling Time |
|---|---|---|---|---|
| $k_p$ | Increase | Decrease | Decrease | Small Change |
| $k_D$ | Minor decrease | No effect | Minor decrease | Minor decrease |
| $k_I$ | Increase | Decrease significantly | Decrease | Increase |

# 2.5.4 Neural-Fuzzy

A neuro-fuzzy system is based on a fuzzy logic system and uses some neural network to train the fuzzy logic system [103]. The fuzzy logic systems are easy to understand and interpret, providing clarity whilst the addition of a neural network adds the ability to learn and adjust the parameters of the fuzzy system [104]. Fuzzy logic systems require prior knowledge of the system, whilst neural networks learn and adjust the model parameters using previous observed examples and available results [105]. A neuro-fuzzy system has the characteristics that the system can be represented as a set of fuzzy rules during the learning process, with or without initialization of prior knowledge [105]. A neuro-fuzzy system can be represented as a three-dimensional neural network as is shown in figure 2.31 [106].
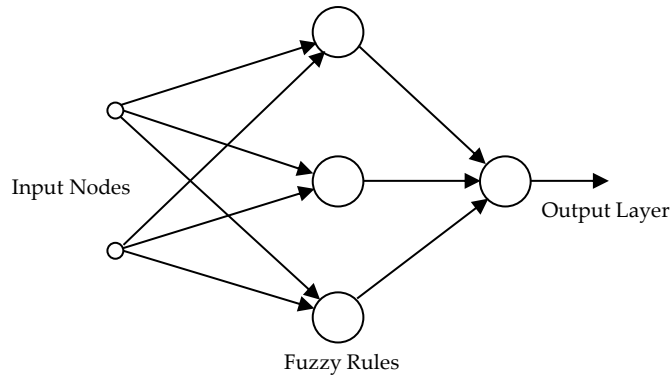
Figure 2.31: Neuro-fuzzy system (adapted from [106])

The first layer in the three-dimensional network is the input layer; the second layer represents the fuzzy rules whilst the third layer represents the output layer. There can mainly be distinguished between three types of fuzzy neural networks (FNNs), namely:

*Cooperative Fuzzy Neural Network:* In this fuzzy neural network the neural network is employed as a pre-processing block to the fuzzy block/set. The sub-blocks of the fuzzy system are determined by the neural network, which makes use of training data to define these sub-blocks [91]. The fuzzy system/blocks are then executed after its sub-blocks are calculated. The structure of a cooperative fuzzy neural network is shown in figure 2.32.
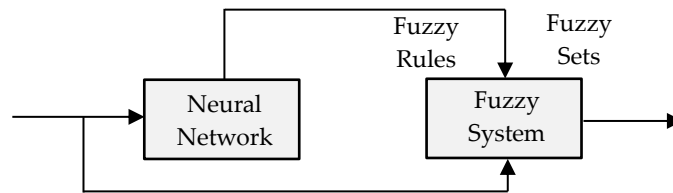


Figure 2.32: Cooperative Fuzzy Neural Network (adapted from [91])

*Concurrent Fuzzy Neural Network:* In the concurrent fuzzy neural network the neural network and fuzzy system continuously work together to process the inputs of the system [91]. In such a system the fuzzy system processes the inputs and then the neural network produces the output values from the fuzzy systems output, or the other way around in which the neural network handles the inputs and the fuzzy system produces the output. The concurrent FNN is shown in figure 2.33.
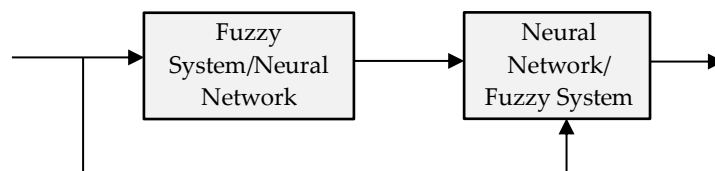


Figure 2.33: Concurrent fuzzy neural network (adapted from [91])

*Hybrid Fuzzy Neural Network:* The hybrid FNN is a fuzzy system that uses a learning algorithm (NN) to determine its parameters. The hybrid FNN is a fully fused fuzzy logic system and NN [105]. The hybrid FNN has the advantage that the NN does not have to transmit data to the fuzzy system seeing that the two different systems are fused into one structure. Researchers

have developed different hybrid neuro-fuzzy architectures, such as FALCON, ANFIS, GARIC and EFuNN. These hybrid FNN's are briefly described below:

- **FALCON (Fuzzy Adaptive Learning Control Network)**: It is a multi-layered network that has two linguistic nodes for each output variable [107]. The first hidden layer is responsible for the fuzzification of the input to the network. Each node in the hidden layer can represent a single membership function or a complex set of membership functions. FALCON uses a hybrid learning algorithm to determine the initial rule base of the fuzzy system and a gradient learning descent to optimally change the parameters of the membership functions.

- **ANFIS (Adaptive Neuro-Fuzzy Interference System)**: This hybrid FNN also makes use of a fuzzy interference system and is a multi-layered feedforward network, as is shown in figure 2.29 [108]. The learning method of the neural network in the ANFIS system is based on the gradient descent and the chain rule [108]. The first hidden layer in the multi-layered network maps the input layer to the relative membership function. The second hidden layer makes use of the T-norm operator to calculate the antecedent values of the fuzzy rule set. The third hidden layer is used to normalize the rule strengths, whilst the fourth layer is used to determine the output of the rule sets.

- **GARIC (Generalized Approximate Reasoning based Intelligence Control)**: This hybrid FNN makes use of two neural network systems, namely the Action State Evaluation Network (ASEN) and the Action Selection Network (ASN). The ASEN evaluates the actions of the ASN [107]. The ASN is a five layered feedforward network in which the connections between networks are not weighted. The first hidden layer in the ASN is used to store the linguistic values of the input variables. The second hidden layer determines the degree of truth of the inputs by making use of the fuzzy rules. The third hidden layer outputs the linguistic values produced by the second layer. GARIC makes use of the local mean-of-maximum method in order to compute the rule outputs.

- **EFuNN (Evolving Neural Fuzzy Network)**: The nodes in this NN are created during the learning phase [109]. The first hidden layer of nodes represents the fuzzy quantification of the input variables [95]. Each neuron in the layer can have its own membership function. The second hidden layer contains nodes that change/evolve through supervised and unsupervised learning. The third hidden layer determines the degree of truth of the inputs to the output membership functions, whilst the last layer defuzzifies this information and produces the numerical output for the output variable [91].

# 2.6 Control boards

This section discusses the control boards that were considered for this study. Figure 2.34 shows an overview of the control boards that were investigated.
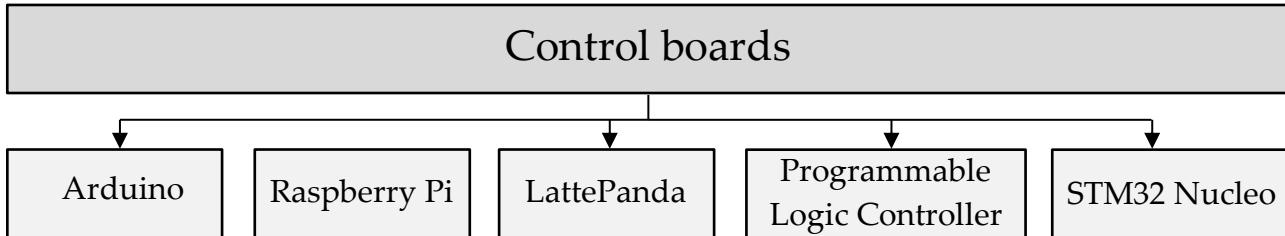


Figure 2.34: Control boards section overview

## 2.6.1 Arduino

Arduino is an open-source development board with digital and analog input/output ports [110]. The Arduino boards typically feature an Atmel ATmega328 microcontroller, RAM, EEPROM and flash memory. The Arduino boards also contain an Analog-to-Digital Converter and a convenient to use USB connector to easily interface with a host computer. The programming language used is a simplified version of C/C++ [110]. Different types of Arduino boards exist, with most boards being able to interface with MATLAB®/Simulink®. An Arduino IO Package exists in MathWorks® to handle the interface between Simulink® and the supported Arduino board [111]. This package allows real-time communication between the Arduino board and Simulink®. Using the control logic created in Simulink® can easily be deployed to the Arduino using the Arduino Hardware Support Package.

Simulink®/MATLAB® provide support for the Arduino boards, for example the Arduino Uno, the Mega 2560 and the Arduino 101. The boards mentioned above are considered to be some of the Arduino boards with the most functionality and processing power/memory out of the range of Arduino boards. Table 2.4 compares the three mentioned boards.

Table 2.4: Arduino comparison (adapted from [112])

|  | Arduino Uno | Arduino Mega 2560 | Arduino 101 |
|---|---|---|---|
| **CPU Clock Speed (MHz)** | 16 | 16 | 32 |
| **Digital I/O Pins** | 14 | 54 | 14 |
| **Analog I/O Pins** | 6 | 16 | 6 |
| **SRAM (KB)** | 2 | 8 | 24 |
| **EEPROM (KB)** | 1 | 4 | - |
| **Flash Memory (KB)** | 32 | 256 | 196 |

Arduino boards have a strong and active community that provides support for the boards. The Arduino boards also have multiple analog and digital input/pins and they also have a relatively

small form factor compared to some of the other controllers discussed in the chapter. The SRAM and flash memory available in the boards limit the complexity of the Simulink®/MATLAB® programs that can be deployed to the boards.

## 2.6.2 Raspberry Pi

The Raspberry Pi is a general-purpose small factor single-board computer developed by the Raspberry Pi Foundation in the United Kingdom. The board makes use of a quad-core CPU, a built-in Broadcom GPU, RAM and level 1 and 2 cache. MathWorks® provides a Simulink® Support Package for the Raspberry Pi. A library of Simulink® blocks is included in the Support Package, allowing one to access the I/O peripherals and other communication interfaces [113]. Various versions of the Raspberry Pi have been developed. Table 2.5 shows the specifications of some of the Raspberry Pi models [114].

Table 2.5: Raspberry Pi comparison (adapted from [114])

|  | Raspberry Pi 2 Model B | Raspberry Pi 3 Model B | Raspberry Pi Zero W |
|---|---|---|---|
| **CPU Clock Speed** | Quad Core @ 900MHz | Quad Core @ 1.25GHz | Single Core @ 1GHz |
| **RAM** | 1 GB | 1 GB | 512 MB |
| **GPIO** | 40 Pins | 40 Pins | 40 Pins |
| **Wi-Fi** | No | Built in | No |
| **Ethernet Port** | Yes | Yes | No |
| **GPU** | Videocore IV | Videocore IV | BCM 2835 |

The Raspberry Pi boards usually use some variation of Linux as an operating system, but other operating systems such as Windows 10 IoT core are used. The various Raspberry Pi models all use a HDMI interface to provide a digital video output.

The Raspberry Pi series of boards are widely used, especially in IoT applications. With a relatively large amount of RAM available, coupled with a quad-core processor, the Raspberry Pi is capable of executing more complex programs. The board also has a built-in Ethernet port and controller. The general I/O ports can be used to generate a PWM signal with a frequency range from 0 to 8 kHz, through Simulink®, but other frequencies can be generated within the native programming interface of the Raspberry Pi.

The Raspberry Pi could therefore be used as a closed-loop controller; for example Miguel Molina *et al.* (2015) implemented a fuzzy controller for environmental energy control indoors whilst Feidias Ioannidis *et al.* (2014) used Raspberry Pi to implement a PID controller to control the temperature of high power laboratory power supply [115], [116].

## 2.6.3 Programmable Logic Controller

The programmable logic controller is a micro-processor based controller that performs logic, timing and arithmetic to control machines and processes [117]. The PLC uses programmable memory to store instructions and functions to be executed. PLCs have the following basic functional components such as the central processing unit, power supply, input/output interface, memory and a communication interface. The typical arrangement of these components is shown in figure 2.35.
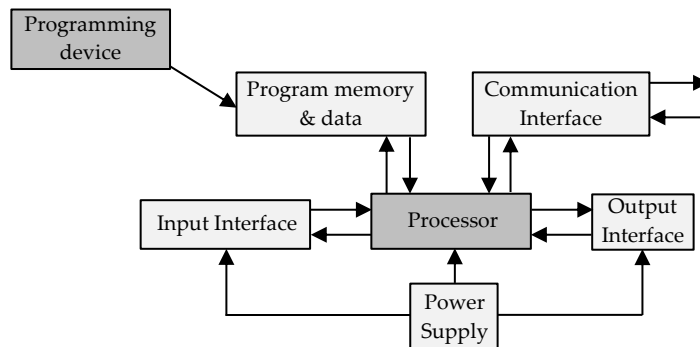
Figure 2.35: PLC Functional Units (adapted from [118])

Five commonly used programming methods are used to program PLC's, these are [118]:

- Ladder Diagram  -  Graphical programming language which is derived from wired relay circuits.

- Function Block Diagram  -  Functional blocks and functions are interconnected into networks and are graphically represented.

- Instruction List  -  Textual assembler language.

- Structured Text  -  High-level language.

- Sequential Function Chart  -  Graphical programming language that depicts the sequence of steps that is monitored and executed.

Most PLCs are rugged and are designed to withstand temperature variations, vibrations and humidity. PLCs have modular I/O modules and other cards that are easy to integrate and to add to existing systems. The main difference between PLCs and other computing devices is that PLCs are designed to operate in severe conditions. Simulink® PLC Coder also allows one to easily deploy a simulated system to a PLC, without the user having to generate the necessary ladder diagrams or structured text.

## 2.6.4 dSpace Controller

dSpace (Digital signal and control engineering) is a company that produces electronic control units. These electronic control units are composed of real-time processors with a large array of input/output boards. dSpace has a strong tie with MATLAB® and Simulink®, with Simulink® and

MATLAB® providing support packages for real-time interfacing and simulation of the dSpace controller. The DS1104 R&D controller is one of the controller boards developed by dSpace, containing a real-time processor, comprehensive I/O and PCIe interface [119].

The Real-Time workshop software included in MATLAB® together with Simulink® allows one to use the analog and digital I/O channels [120]. The Real-Time interface provides the different functional blocks to Simulink®. The compiler makes the Simulink® model and code compatible with that of the dSpace controller. The ControlDesk software allows real-time management of the running process on the dSpace controller.

T. He *et al.* made use of a dSpace controller operating in conjunction with MATLAB®/Simulink® to implement a neuro-adaptive PID controller for a DC motor control system. The developed system was used to adjust the parameters of the controllers whilst the control system was active and utilised the system to monitor the motor [121].

R. Silva-Ortigoza *et al.* used a DC/DC buck converter as a smooth starter for a DC motor using a hierarchical control structure implemented on a dSpace controller. The DS1104 board was used in conjunction with Simulink® to experimentally track the performance of the controller and the DC/DC converter [122].

## 2.6.5 LattePanda

The LattePanda is a single-board computer, comparable to the Raspberry Pi. The first LattePanda was developed in 2015 and utilized an Intel Atom x5-Z8300 CPU with an x86 instruction set [123]. This Intel CPU has 4 cores and operates at a clock frequency of 1.44 GHz. It also has 2/4 GB of RAM. The board also has an Ethernet port as well as WiFi and Bluetooth 4.0. Similarly to the Raspberry Pi, this board has multiple GPIO pins. What is unique about this board is the fact that it also integrates an ATmega32u4 processor. This board thus incorporates the superior CPU processing power of a higher clocked multi-core Intel CPU and the functionality of the ATmega32u4 processor.

The board has 20 GPIO pins that directly interface with the ATmega chip. The board thus has 12 analog inputs, which can be used for digital I/O. These analog pins have a 10-bit resolution. The board is also able to generate an 8-bit PWM output on 6 of the GPIO pins. The board is also there able to use SPI and I2C to communicate.

The LattePanda board is usually distributed with windows 10, but support is available for other operating systems such as Linux, Android for x86 and MacOS [124]. The newest iteration, named the LattePanda Alpha, utilizes an 8th Gen Intel CPU operating at a clock rate of 3.4 GHz, 8 GB of RAM and utilizes the ATmega32u4 processor. This board is shown in figure 2.36.

Simulink does not provide support packages for the LattePanda, but seeing as the LattePanda has enough processing power, Simulink®/MATLAB® can be executed on the LattePanda whilst using Windows 10 or Linux as the OS. Simulink could then be used together with the Arduino support package to interface with the ATmega32u4 processor on the LattePanda.
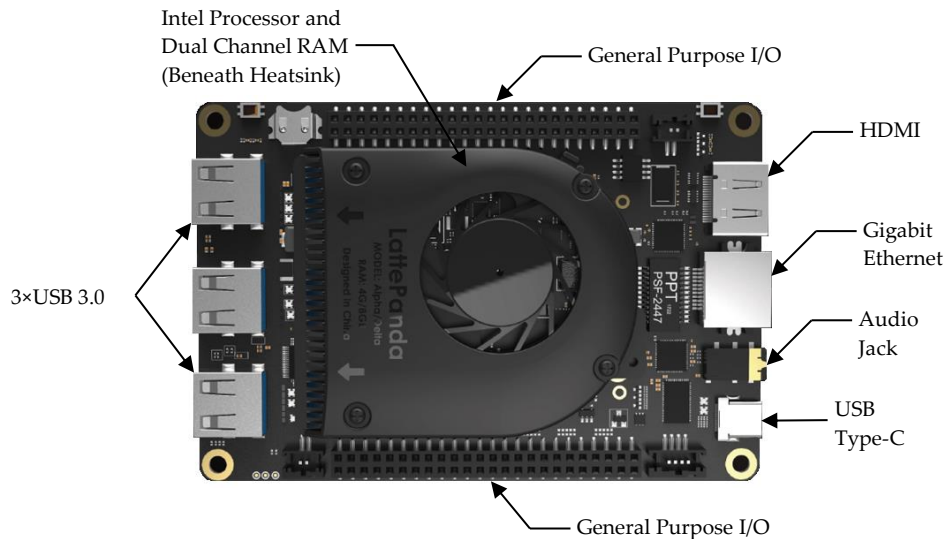
Figure 2.36: LattePanda Alpha (adapted from [123] )

## 2.6.6 STMicro Nucleo board

The STMicro Nucleo development boards are low cost microcontrollers developed by STMicroelectronics. These boards use an ARM Cortex processor, operating at 32 MHz to 100 MHz depending on the board [125]. The Nucleo boards are designed in such a way as to allow easy integration with Arduino extension boards, adding functionality such as Ethernet ports, motor drivers and Bluetooth and Wi-Fi capability to name a few [125]. These boards integrate the ST-Link debugger and programmer and do not require an external programming board. The STMicro32 boards have pin compatibility to the Arduino Nano whilst the STMicro64 has a similar pinout to the Arduino Uno boards. The Arduino boards and the Nucleo range of boards are similar in their pinouts and board size, but the Nucleo range of boards have faster processing speeds and more memory than the Arduino boards [126]. The STMicro32 Nucleo 64 board is shown in figure 2.37.

The Nucleo series of boards have a higher core clock frequency, more flash memory, more SRAM and more I/O output pins compared to that of the Arduino boards. Simulink®/MATLAB® also has support packages available for the Nucleo series of boards. Due to the increase core clock frequency and memory, the Nucleo boards can execute more complex programs generated in Simulink® compared to the Arduino.

O. Setyawati *et al.* used a STM32 microcontroller to implement a fuzzy logic controller to control the output voltage of a buck converter. In this study the performance of the fuzzy logic controller was compared to the performance of a PID controller. The study showed that the fuzzy logic controller had a higher steady-state error, but had no overshoot whilst also reducing the settling time of the system compared to the PID controller [127].

M. Thamma *et al.* utilised a STM32 microcontroller to implement a self-tuning fuzzy PID controller for a first order linear system with a time delay. The self-tuning fuzzy PID controller was experimentally deployed to the microcontroller by using Simulink and utilised various sensors and pumps to control the water level in a system [128].
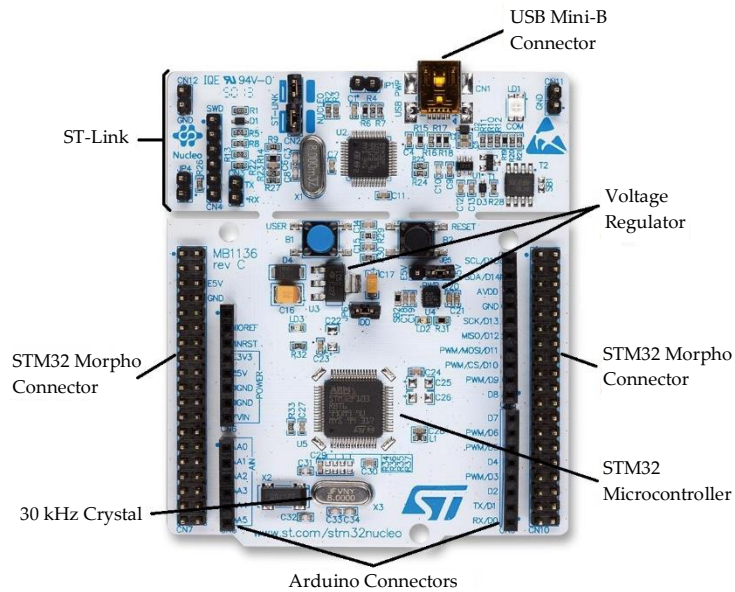
Figure 2.37: Nucleo STM32 (adapted from [125])

# 2.7 Software

## 2.7.1 MATLAB®/Simulink®

MATLAB® is an interactive environment for performing technical computations. MATLAB® stands for Matrix Laboratory and has been commercially available from 1984 [129]. MATLABs® core consists out of C-coded routines used for numerical analysis, matric computation and manipulation and graphics. MATLAB® utilizes sophisticated data structures and contains built-in, debugging and editing tools and supports object-oriented programming. MATLAB® provides powerful routines for numerical matrix algebra; as well as application-specific packages for fields such as applied science and engineering. MATLAB® also has easy to use graphic commands to be able to easily visually represent the results. All MATLAB® variables are multidimensional arrays, no matter what type of data.

MATLAB® provides build-in support for some serial port devices, but support packages for other third-party hardware such as webcams, Arduino and Raspberry Pi are available. Third-party support packages are available for all the controllers listed in section 2.6. MATLAB® provides packages for parallel computing, math and statistics, control systems, signal processing and communication, image processing and data acquisition, to name a few.

Simulink® is a MATLAB® based block diagram environment for model-based design and multi-domain simulation. It provides a graphical interface, with customizable model blocks, with additional block libraries available. Simulink® is able to simulate dynamic systems and seeing that Simulink® is integrated into MATLAB®, one is able to utilize MATLAB® algorithms and export simulation results to MATLAB® for additional analysis [130]. Simulink supports linear and non-linear systems, as well as simulating these systems in continuous or discrete-time.

Third-party support packages are available for various microcontrollers and single-board computers, such as Arduino, Raspberry Pi, STM32 and even FPGAs. PLCs can also be programmed

through Simulink PLC Coder® that generates the hardware-independent code for the PLCs. Simulink® allows one to easily deploy algorithms and control topologies to these hardware devices. For example, the Fuzzy Logic Controller block or the PID block used in the model can easily be executed on the hardware device. Simulink® translates and compiles these blocks into the specified hardware-dependent code for the specific device connected to the target computer.

## 2.7.2 LTspice®

LTspice® is a high-performance SPICE simulation package. SPICE simulators are powerful tools for circuit analysis. LTspice® is freeware produced by the semiconductor manufacturer Linear Technology, which is a part of Analog Devices [131]. LTspice® is used to simulate electronic circuits, for example the frequency response of an analog filter can be simulated. It features the SPICE simulation software as well as waveform viewer. LTspice® by default includes a library of macromodels for general electronic devices and integrated circuits, such as switching regulators and amplifiers [131]. All the most commonly used passive components are included, as well as circuit models developed for power MOSFETs that accurately exhibit the gate-charge behaviour without using sub-circuits or additional nodes. Reducing the number of nodes in the model reduces the computational time required to simulate the circuit.

LTspice® is one of the most popular SPICE simulation packages and claims to be able to simulate switching regulators extremely fast compared to other SPICE simulation packages [132]. LTspice® also has no limit on the number of nodes that can be used in the schematic editor used to create the simulated circuit. LTspice® allows one to create models for electronic devices or use the SPICE files created by the manufactures of the electronic devices.

LTspice® can be used to determine the transient response, steady-state response, DC transfer function of the circuit. It can even be used to view the Fourier response of the circuit. The waveform viewer in LTspice® can be used to view the current and voltage waveforms [122]. The waveform viewer can also be used to view the power absorbed by a component and therefore the heat generated by that component. LTspice® is therefore an effective and efficient method of simulating analog circuits, such as power electronic circuits and passive/analog frequency filters, as applicable to this project.

# 2.8 Drive Cycles

In various countries all new light-duty ICE vehicles are required by law to undergo emission tests. Vehicle exhaust emissions are inherently variable, thus these standardized drive cycles were developed to be able to conduct an emission test under reproducible conditions [133]. Drive cycles are used to define a test profile that attempts to represent the velocity at which a vehicle would move on an urban road in a certain environment. Drive cycles are also used to determine the durability of the drive train and the engine of the vehicle. Drive cycles are usually defined in terms of the

vehicle speed at a specific gear selection as a function of time [134]. Some drive cycles also define the drive cycle in terms of the vehicle speed at a specific gear selection as a function of distance.

The emission levels for a vehicle are dependent on various parameters, such as the vehicle type, engine type, engine displacement, vehicle size to name a few as well as the operational factors such as the speed, road gradient, acceleration and gear selection [133]. Unsurprisingly various drive cycles exist for different vehicle types and that represent different environmental driving, such as urban city driving versus highway travel [134]. Emission testing usually occurs in a laboratory environment with the vehicle positioned on a chassis dynamometer.

Drive cycles can also be broadly divided into two drive cycle types, namely transient drive cycles and steady-state drive cycles. Steady-state drive cycles are designed such that it consists out of a sequence of constant engine speeds and loads. These cycles are mainly used to test diesel-powered trucks which often travel at constant speeds for long durations. Various transient drive cycles exist and they are designed to represent a particular scenario. Some are representative of real-world driving conditions whilst other are designed to stress the drive train and engine of the vehicle. Other drive cycles are used in legislation for type approval. For example the New European Driving Cycle (NEDC) is used in the European Union for type approval of light-duty vehicles [135]. Some of the common drive cycles are shortly discussed below.

## 2.8.1 NYCC Drive Cycle

US EPA New-York City Cycle was developed for chassis dynameter testing for light-duty vehicles. The test simulates a vehicle moving at slow speeds in an urban city environment with frequent stops. The NYCC drive cycle has a duration of 598 seconds and has an average speed of 11.4 km/h and a maximum speed of 44.6 km/h. The speed profile versus time is shown below in figure 2.38.
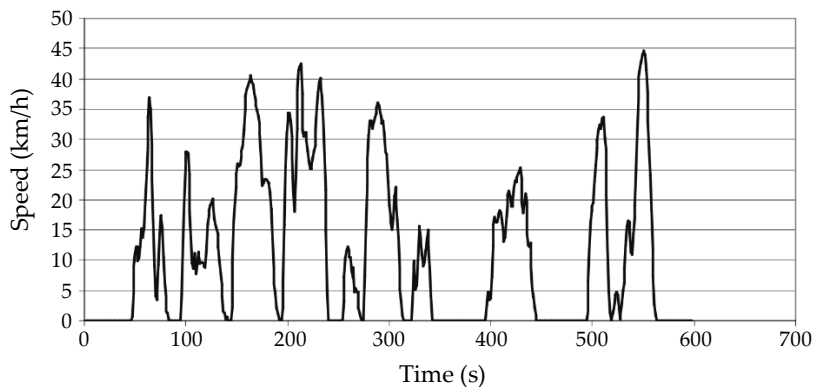


Figure 2.38: NYCC Drive Cycle  (adapted from [133])

## 2.8.2 WLTC Class 2 Drive Cycle

The Worldwide harmonized Light vehicle Test Cycles (WLTC) was developed for chassis dynameter testing for light-duty vehicles. The United Nations Economic Commission for Europe (UNECE) developed the WLTC drive cycle to replace the ageing New European Driving Cycle (NEDC) which at that point in time was used for European type approval [136]. The final version of the WLTC test

was finalized in 2015 and aims to provide a harmonized test procedure that can be used internationally. The test procedure is used by European countries as well as India, Japan and South Korea. The WLTC has three different test profiles/classes for different power-to-weight ratio vehicles. Class 3 is used to test vehicles with a high power-to-weight ratio is representative of vehicles driven in Japan and Europe. The Class 3 drive cycle is shown in figure 2.39, illustrating the different power draw stages in the profile.
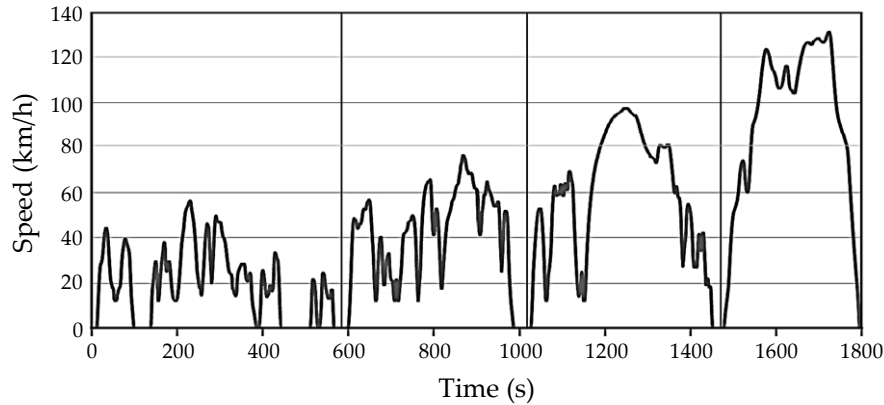


Figure 2.39: WLTC Class 3 Drive Cycle (adapted from [133])

Class 2 is used to test vehicles with a lower power-to-weight ratio and is representative of low power vehicles driven in India, Japan and Europe. Class 1 is used to test the vehicles with a low power-to-weight ratio.

## 2.8.3 ECE 15 Drive Cycle

An example of a drive cycle with a more constant speed profile and fewer accelerations and decelerations is the ECE 15 profile that was used to form the NEDC profile. The NEDC profile consisted out of four repetitions of the ECE 15 cycle and one cycle of the followed by one EUDC segment. The ECE 15 is an urban driving cycle and it was devised to represent the city driving conditions for example in Rome or Paris. The profile is characterized by low speed, low exhaust gas temperatures and low engine load. The ECE 15 profile is shown below in figure 2.40
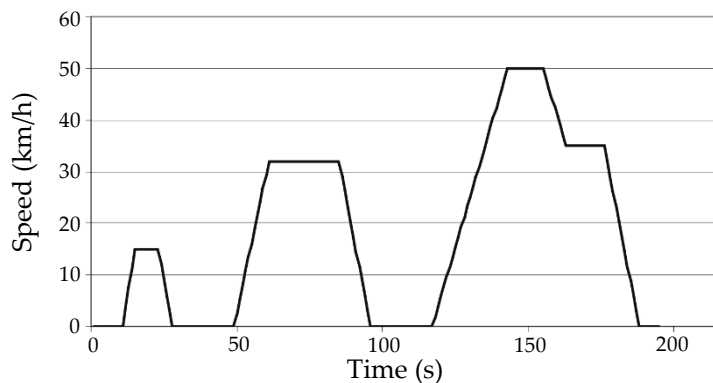


Figure 2.40: ECE 15 Drive Cycle (adapted from [133])

There are more than 250 defined drive cycles in existence [133]. The fact there are so many defined drive cycles indicates that there is a need for a more standardised and representative drive cycle that

could be used universally. One universally applicable drive cycle would never exist, just because there are different vehicle classes and different characteristics that need to be tested. Attempts are being made by researchers to create more realistic drive cycles, especially for electric vehicles [137], [138].

# 2.9 Conclusion

The literature study was done in order to gain an understanding of the different topics pertaining to this study. HESS, EES devices, battery characteristics, control boards and control mechanisms were investigated and documented in this chapter. The drive cycles were briefly discussed and will be used in later chapters to analyse the performance of the HESS.

The literature study also included a case study section, that documented and briefly discussed the work that was done by other researchers regarding passive and active HESS topologies. This was done to investigate the potential benefits and drawbacks of the different HESS topologies. It was noticed from these case studies that the hybridization of batteries and ultracapacitors usually resulted in a reduced power requirement from the battery seeing that the ultracapacitor absorbs the transient power impulses. The case studies also provided information that could be used in later chapters for verification and validation purposes.

The literature study that was done provided the knowledge required to enable the study to progress to the design phase. The literature study was also used in later chapters to verify and validate the results obtained in these chapters. The next chapter discusses the conceptual design of the overhead controller and the control topology used that was used for the HESS. The functional units are also specified and created in this chapter. A detailed design was also done for each functional unit. The DC/DC converters are designed in the next chapter as well as the controllers used to control these DC/DC converters.

# Chapter 3 - Design

*This section describes the overhead control scheme and functional units. The design of the DC/DC converters as well as the overhead controller are discussed and documented in this chapter. The calculations that were done for the functional units are also shown and discussed in this section. Figure 3.1 shows an overview of the points that are discussed in this chapter.*
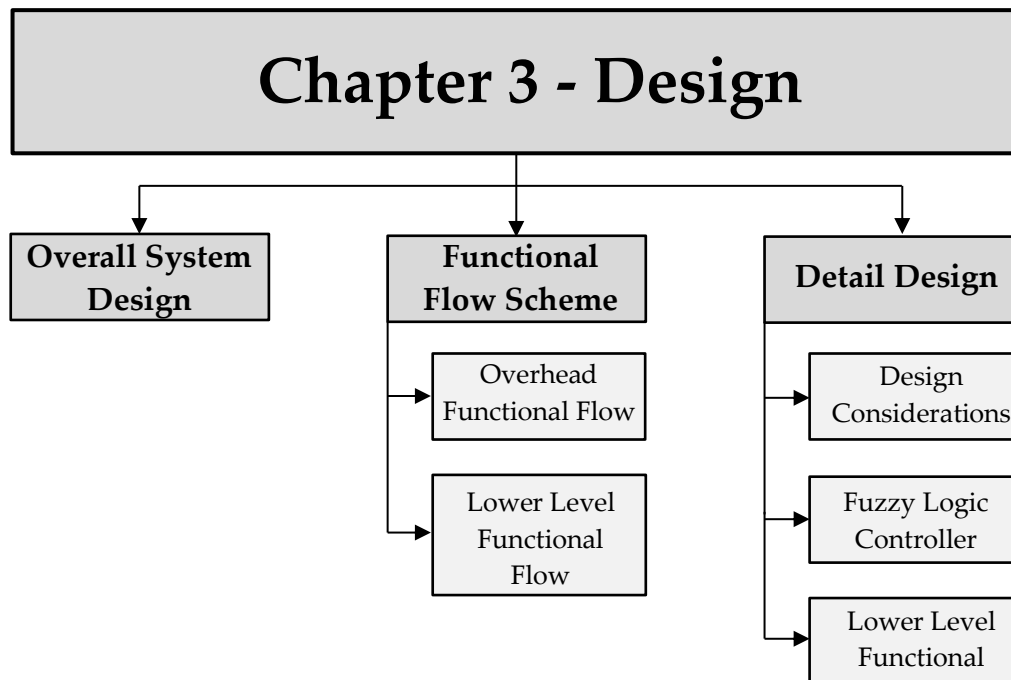
Figure 3.1: Design Chapter Overview

## 3.1 Overall System Design

This section discusses the overall design and layout of the system. The overall control scheme is illustrated in figure 3.2. The overall system consists out of two DC/DC converters and a switch, which are used to control the flow of energy from the battery/UC throughout the system. The overhead controller measures the SoC of the battery and UC as well as the load power, DC/DC converters power and the switch power and controls the duty cycle of the DC/DC converters and the state of the switch.
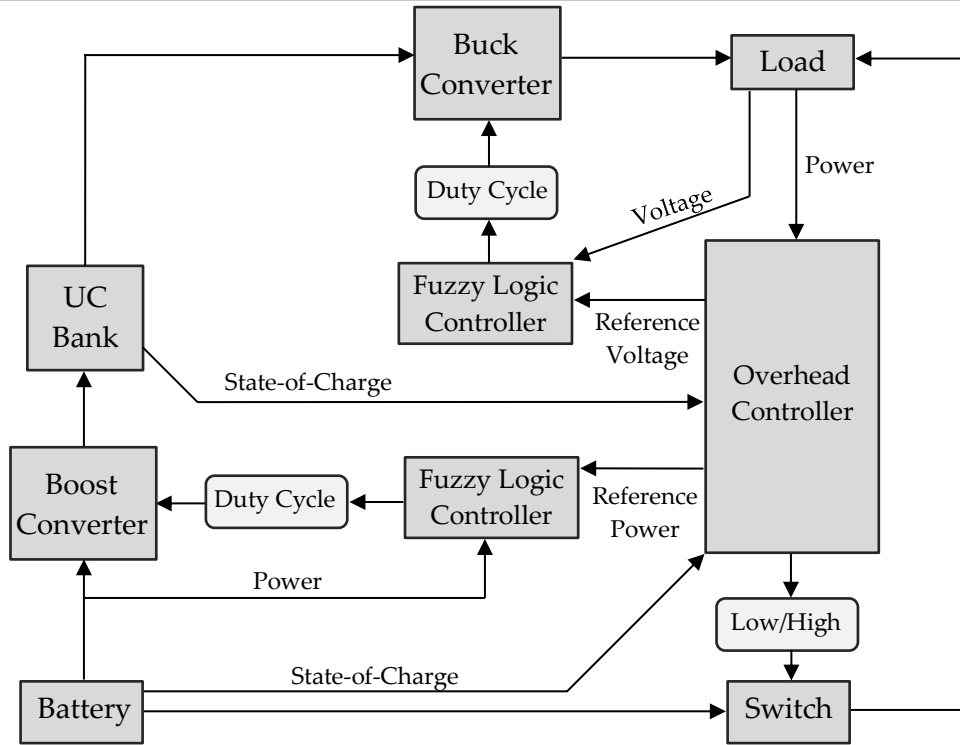
Figure 3.2: Overhead system design

The DC/DC converters used in the topology are unidirectional. The system voltages were selected in such a way that the output voltage of the buck converter is equal to that of the battery. This was done to reduce the power/voltage spikes when the system switches between modes, e.g. when the battery is directly connected to the load via the switch and the system disconnects the battery from the load and provides power through the buck converter to the load. The topology utilizes a switch to able to connect the battery directly to the load, instead of a DC/DC converter, to reduce the power losses associated with a DC/DC converter and to reduce the overall system complexity.

The fuzzy logic controller that interfaces with the boost converter is used to control the amount of power being transferred from the battery to the ultracapacitor. The fuzzy logic controller that interfaces with the buck converter is used to operate the buck converter in constant voltage mode, where the reference voltage is the voltage of the battery.

The overhead controller measures the SoC of the battery and the UC to determine in which control mode the system should operate. The control modes are discussed more thoroughly in the next section. The voltage levels of the battery and the UC was selected in such a manner that the output voltage of the buck converter would be equal to that of the battery. The voltage of UC whilst operating in a SoC range from 25% - 100% should therefore be at a higher voltage than that of the battery, so that a boost converter can be used to charge the UC from the battery and a buck converter can be used to provide power to the load at a voltage level equal to that of the battery. An argument can be made that the voltage level ranges of the battery and UC can be swapped and the boost converter replaced with a buck converter and the buck converter replaced with a boost converter. The DC/DC converter connected to the load needs to be rated to deliver a much higher amount of power than the DC/DC converter connecting the battery to the UC. From the designer's own

anecdotal experience, it is easier to design a high-power buck converter compared to a boost converter, thus the topology and voltage levels were chosen in such a way that a buck converter would be used to provide power to the load.

# 3.2 Control Conditions

The HESS controller attempts to minimize the power spikes experienced by the EES device with the higher energy density and the lower power density, which in this case are the batteries. The controller limits the power drawn from the battery to a user-defined limit and thus indirectly averages the power drawn from the load, if the user-defined limit is chosen such that it supplies the average amount of power drawn by the load, as well as accounting for any DC/DC converter losses. This user-defined limit should be chosen in such a manner as to limit the power drawn from the battery to its nominal discharge rate. The idea is that for an electric vehicle, the vehicle would for example be designed for normal city commuting or let's say high-performance track racing, the manufactures of the vehicle would choose a battery type and size that would be able to provide the average amount of power to the load.

This would allow the manufacturers to choose a battery type with a higher energy density and a lower power density, seeing that the battery only needs to be able to supply the average power drawn by the load. The controller tries to average the power of the load as experienced by the battery. The controller allows a system to utilize batteries that are more energy-dense, instead of batteries that have a higher power density, but sacrifice on energy density in turn. The overhead control rules that were used for the active HESS controller to limit the power drawn from the battery are shown in figure 3.3.
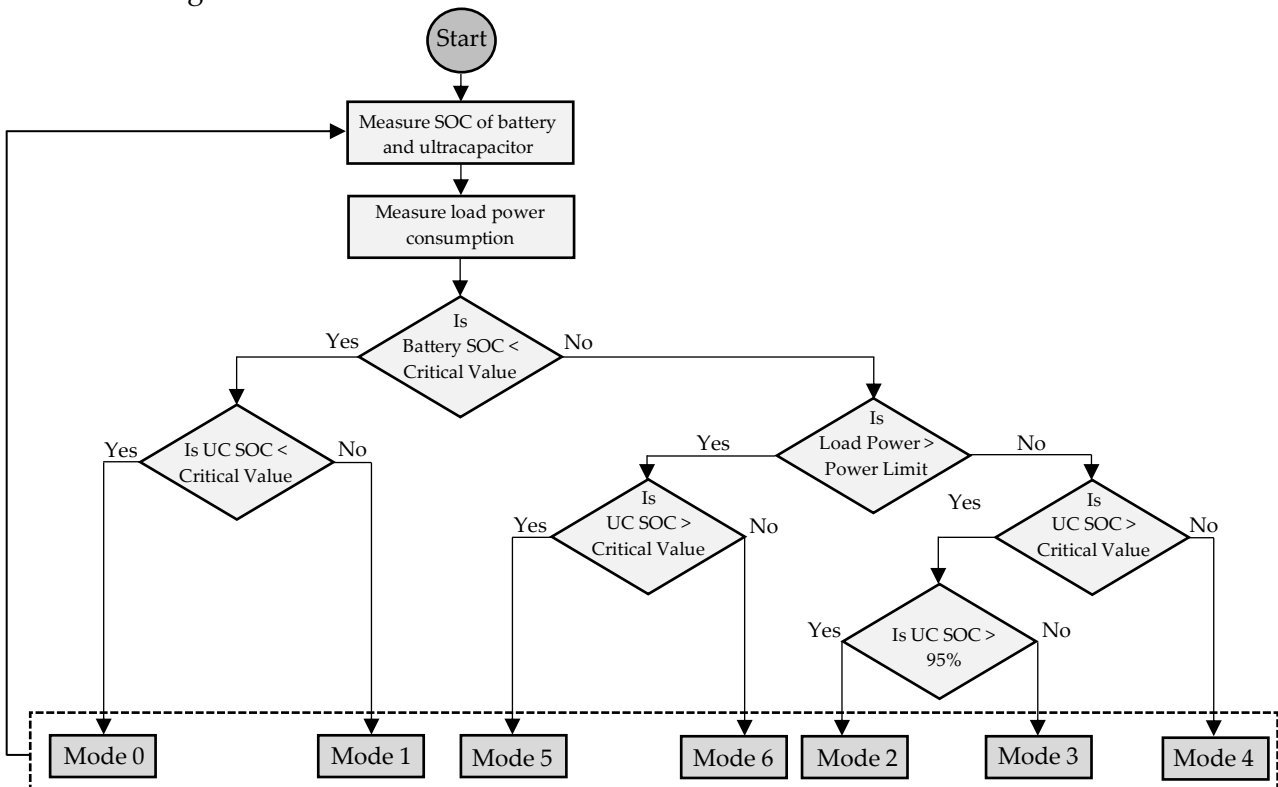


Figure 3.3: Overhead control rules

The critical values in the figure are 10% for the battery and 25% for the UC. The controller has 7 modes of operation; these modes are described below. Mode switching is implemented by controlling the state of the switch as well as the reference power for the DC/DC converters.

## Mode 0

This mode is activated when the state-of-charge (SoC) of the battery is below 10% and the SoC of the ultracapacitor is below 25%, i.e. both the battery and the ultracapacitor are depleted. This mode pulls the switch low to disconnect the battery from the load and zero power is transferred by either DC/DC converters. The ultracapacitor is also electrically isolated by driving a switch low. This is done because otherwise the diode in the boost converter could become forward biased when the voltage of the ultracapacitor drops below that of the battery, which would further deplete the battery, possibly damaging it and there is no control over the amount of power being transferred in this case. The system is therefore in shutdown. This switch is not shown in the overhead control topology diagram, seeing that the switch was simply a MOSFET added in series to the input of the boost converter.

## Mode 1

When the SoC of the battery is below 10% and the SoC of the ultracapacitor is above 25% the ultracapacitor provides power to the load, irrelevant of how much power the load draws, until the ultracapacitors SoC reaches 25%. After the SoC of the ultracapacitor reaches below 25% mode 0 will be triggered. The flow of power throughout the system in this mode is shown in figure 3.4a.

## Mode 2

This mode is activated when the load power is below the user-defined power limit for the battery pack and the state-of-charge (SoC) of the battery is above 10% and the SoC of the ultracapacitor is above 95%, the battery only provides power to the load. The controller drives the state of the switch high, in order to directly connect the battery to the load, bypassing the DC/DC converters. No power is transferred by the DC/DC converters, as depicted in figure 3.4b.
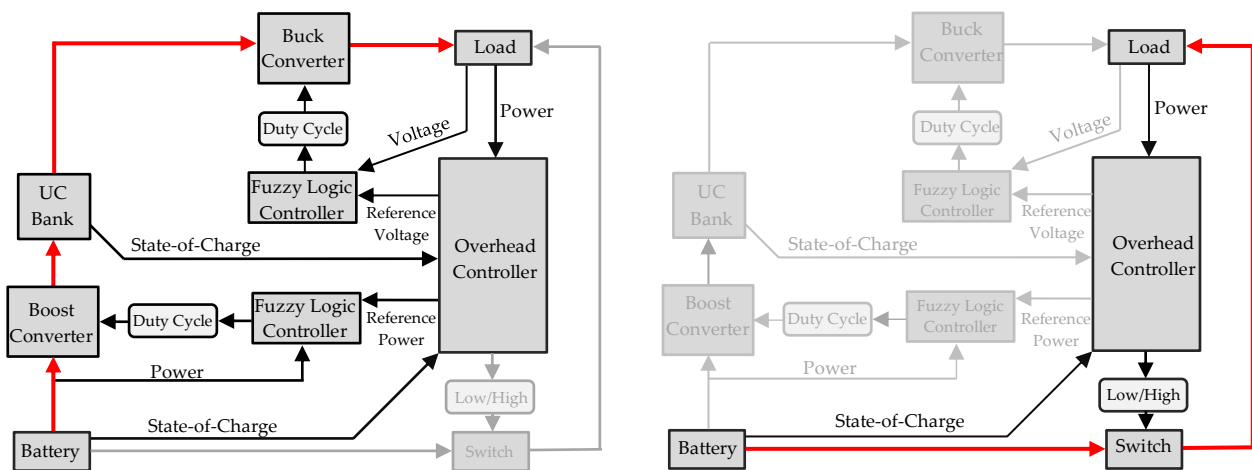


Figure 3.4: a) Mode 1 Power Flow; b) Mode 2, 4 & 6 Power Flow

## Mode 3

If the load power is below the user-defined power limit and the SoC of the ultracapacitor is between 25% and 95%, the battery provides power to both the load and to the ultracapacitor so that the following holds true,

$$P_{load} + P_{UC} \leq Battery\ Power\ Limit, \tag{3.1}$$

where $P_{load}$ is the power drawn by the load and $P_{UC}$ is the power provided to the ultracapacitor by the battery. The flow of power in this mode is shown in figure 3.5a. The battery charges the ultracapacitor to ensure a high SoC of the ultracapacitor so that if the load power drastically increases, the ultracapacitor has sufficient energy to be able to supply power to the load.

## Mode 4

If the load power is below the user-defined power limit and the SoC of the ultracapacitor is below 25% the battery provides power to the load and no power is transferred through the boost converter to the ultracapacitor. The ultracapacitor is also isolated by driving a switch low as in mode 0, to prevent the diode in the boost converter from becoming forward biased when the ultracapacitor voltage falls below that of the battery's voltage. This mode's power flow is similar to that of mode 2s power flow. The power flow of this mode is shown in figure 3.4b.

## Mode 5

This mode is activated when the load power is higher than the defined power limit for the battery pack. If the SoC of the ultracapacitor is higher than 30% and SoC of the battery is above 10% the ultracapacitor provides power to the load through the buck converter as illustrated in figure 3.5b. The battery provides power to the ultracapacitor at the user-defined power limit.

## Mode 6

When the load power is higher than the defined power limit, but the SoC of the ultracapacitor is lower than 25%, i.e. the ultracapacitor is unable to provide power to the load and the batteries are directly connected to the load through the switch, as illustrated in figure 3.4b.
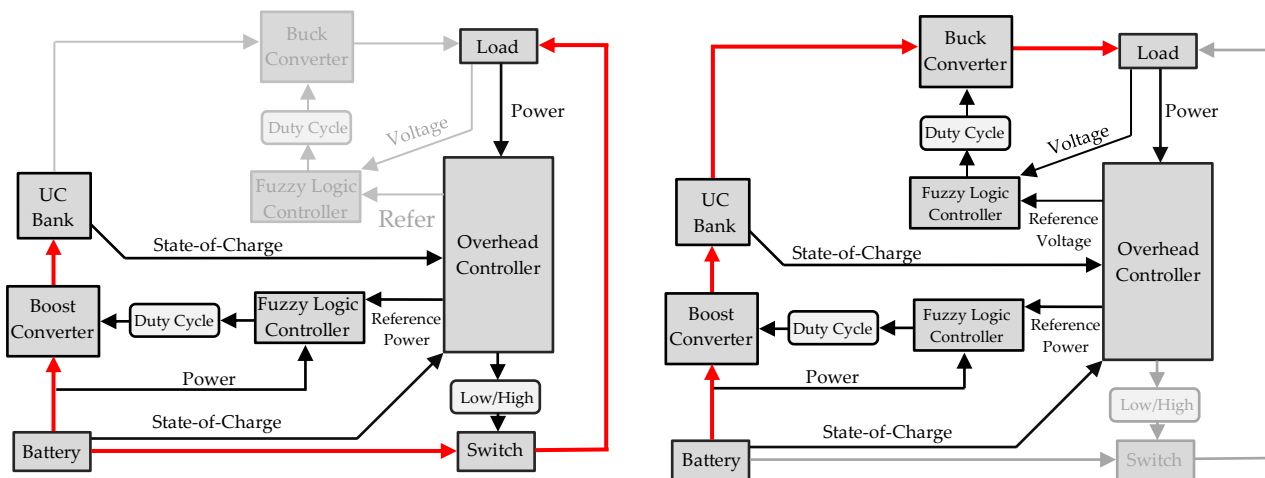


Figure 3.5: a) Mode 3 Power Flow; b) Mode 5 Power Flow

Directly connecting the battery to the load during high power draw is not ideal and reaching this mode indicates that the user-defined power limit is below the average power draw of the load or the ultracapacitor bank is undersized and is not able to supply power to the load through a series of high power peaks, draining the ultracapacitor bank below 25% before the battery is able to recharge the ultracapacitor bank.

# 3.3 Detail Design

In the section the design considerations are discussed first, followed by the detailed design of the functional units. This includes the design calculations that were done for the DC/DC converters as well as some of the other functional units.

## 3.3.1 Design considerations

This section briefly discusses the design decisions that were made regarding the system topology, control topology, controllers and the electrical energy storage devices that were used.

### 3.3.1.1 Hybrid energy storage system topology

The topology that was chosen was a topology that was not commonly used by other researchers in the field. The topology as shown in figure 3.2 utilises two DC/DC converters as well as a switch. This topology was also implemented by Z. Song *et al.* and C. Xiang *et al.* with success [33], [139]. The topology is able to control the flow of power between the two EES devices and the power flowing to the load, whilst being able to bypass the losses associated with the DC/DC converters to connect the battery directly to the load.

### 3.3.1.2 Control topology

As can be noted from figure 3.2 the system utilizes a total of three controllers. The overhead controller is used to determine the reference power/voltage for the two fuzzy logic controllers. The overhead controller makes use of conditional control to determine in which operating mode the controller should operate. Fuzzy logic was used for the control of the DC/DC converters as it was found in the literature that fuzzy logic is a sufficient control technique and does not require the designer to generate a complex mathematical model characterising the DC/DC converters to determine the parameters of the controller.

### 3.3.1.3 Controller

The controller that was used for this study was the STM32 Nucleo F767ZI. This controller was chosen firstly because it was available at the time of the study at the research facility and the performance of the controller was sufficient. The controller is more suited for this study compared to the Arduino, due to its higher core clock frequency, 32 bit RISC core and 12-bit ADCs.

### 3.3.1.4 Electrical energy storage systems

The two EES devices that were used were an ultracapacitor and battery. The ultracapacitor bank that was used consisted out of six 3000 F cells in series. Each cell has a maximum voltage of 2.7 V, resulting in a UC bank capacitance of 500 F with a voltage rating of 16.2 V. An integration kit from Maxwell was used to interconnect the UC cells in series. The integration kit balances the voltages across the cells, to prevent individual cells from becoming overcharged and subsequently damaging the cells. The batteries that were used were the NCR 18650b Lithium-ion batteries from Panasonic. Each battery cell has a rated capacity of 3200 mAh and a nominal voltage of 3.6 V. These batteries have a stated gravimetric energy density of 243 Wh/kg. Two of these battery cells were used in series resulting in a battery pack with a nominal voltage of 7.2 V and a capacity of 3200 mAh.

# 3.4 Overhead functional unit

The overhead functional unit is shown in figure 3.6. The only external functional unit is the load, FU 8. The controller interfaces to the power converters, FU 5 and FU 7, through FU 3 which serves to isolate the controller from the power electronics. FU 4 and FU 6, which are the electrical energy storage devices, are interfaced to one another and to the load FU 8, through the power converters.
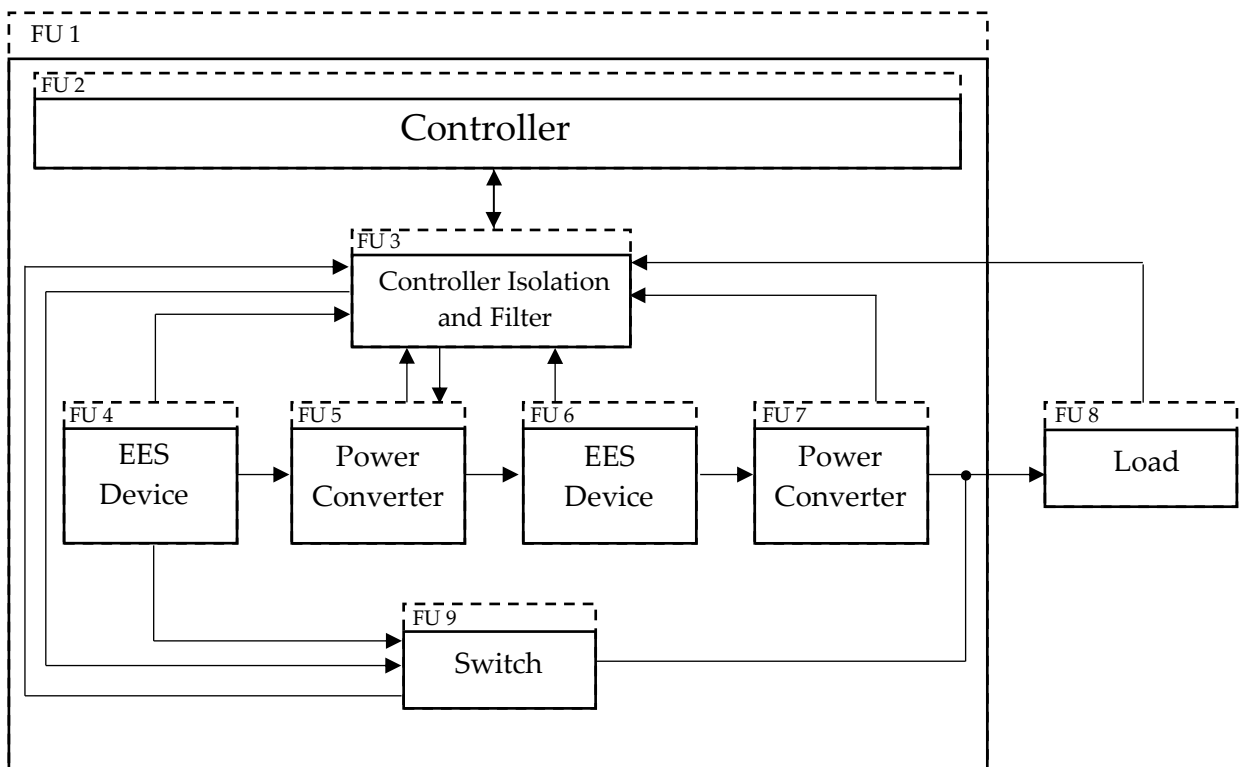


Figure 3.6: Overhead functional unit

# 3.5 Lower Level Functional Units

The lower level FUs are discussed in this section. Functional units 2 through functional units 9 are discussed.

## 3.5.1 Functional Unit 2

Functional unit 2 is the controller unit of the proposed hybrid energy storage system. FU 2 consists out of three controlling units FU 2.1 is the overhead controller, whilst FU 2.2 and FU 2.3 are the fuzzy logic controllers responsible for controlling the power transferred by each power converter, or FU 5 and FU 7. The lower level functional units for FU 2 are shown below in figure 3.7.
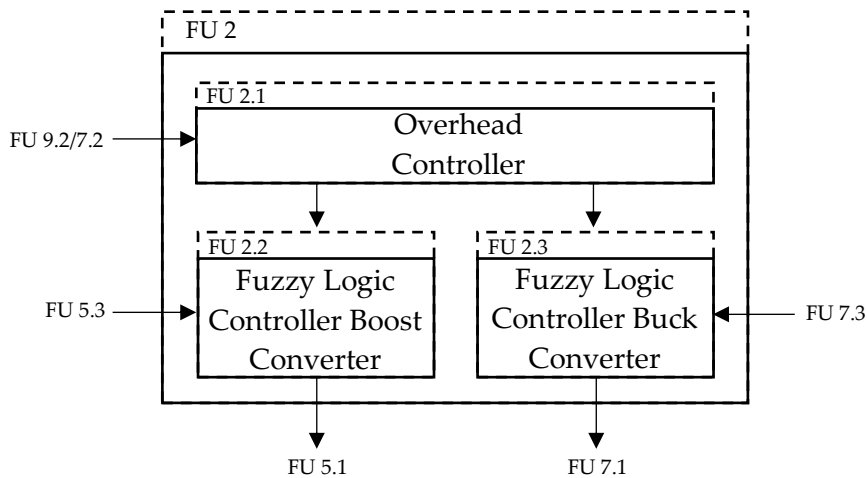


Figure 3.7: Functional Unit 2

The overhead controller, FU 2.1, receives the voltage and current measurements from FU 4, 6 and 8 to determine the load power as well as the SoC of FU 4 and 6. FU2.1 passes the desired power levels for each power converter to the respective fuzzy logic controllers according to the power distribution scheme discussed in section 3.2. FU 2.2 and FU 2.3 measure the voltage and current of FU 5 and 7 respectively, and alter the duty cycle as required to reach the desired power level. This duty cycle is passed to FU 5.1 and FU 7.1 through FU 3.2.

It is important to note that FU 2 was implemented as a whole on the STM32 Nucleo F767ZI microcontroller. The fuzzy logic control units, together with the overhead controller are compiled into the necessary instructions/code through Simulink® so that these functional units execute concurrently on the microcontroller.

## 3.5.2 Functional Unit 3

Functional Unit 3 was added to the system to ensure that the controller was firstly isolated from the power electronics in the project and secondly to filter the output signals from the sensors. The lower level functional unit diagram is shown below in figure 3.8.
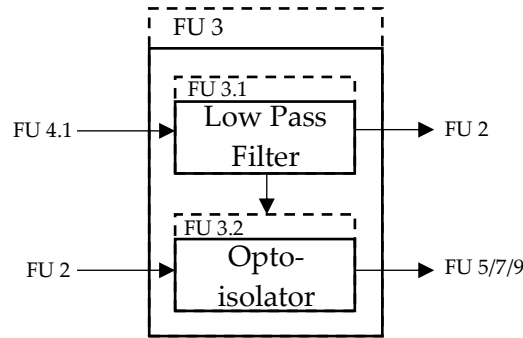
Figure 3.8: Functional Unit 3

FU 3.1 consists out of an array of low pass filters used to filter noise from the sensor signals. The filtered signals are passed to FU 2, to the respective lower level functional units. FU 3.2 consists out of an array of opto-isolators that are used to electrically isolate the controller from the driver ICs used in the DC/DC converters (FU 5 and 7) and the MOSFET switch (FU 9).

## 3.5.3 Functional Unit 4

Functional unit 4 is one of the EES devices in the HESS. Functional unit 4 consists out of the Li-ion battery, FU 4.1, and the power measurement sensor, FU 4.2 as shown in figure 3.9. The power measurement unit consists of a current and voltage sensor, in order to calculate the power delivered by FU 4.1. Texas Instruments INA 126 shunt current sensor was utilised to accurately measure the current, whilst a simple voltage divider circuit was used to measure the voltage. FU 4.2 interfaces with FU 3.1, which filters the output signal and passes the filtered signal to FU 2.1. The battery interfaces with both the boost converter, FU 9.2, and the MOSFET, FU 5.2.
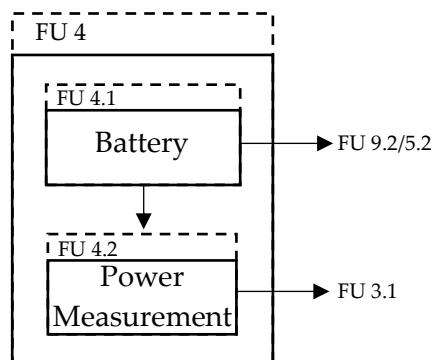


Figure 3.9: Functional Unit 4

## 3.5.4 Functional Unit 5

Functional unit 5 is the power converter that is used to charge the ultracapacitor (FU 6.1). Three functional unit blocks are utilized. FU 5.1 is the MOSFET driver IC, which interfaces with the opto-isolator as well as the switching device within the boost converter in FU 5.2, which are shown in figure 3.10. The boost converter interfaces with the battery in FU 4 and outputs the power to the ultracapacitor in functional unit 6.1. The power measurement block is similar to FU 4.2 as discussed above.
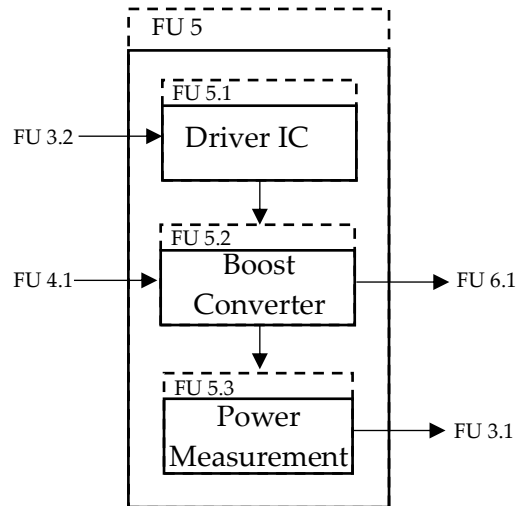
Figure 3.10: Functional Unit 5

## 3.5.5 Functional Unit 6

Functional unit 6 is similar to FU 4, the battery is only replaced by an ultracapacitor, FU 6.1. FU 6.2 is similar to the power measurement blocks in the previously discussed blocks. The ultracapacitor is connected to the boost converter and the buck converter, FU 7.2. The power flow into/out of the ultracapacitor is measured by FU 6.2 and the output signal from the measurement sensors is filtered by FU 3 and passed to FU 2.1. Functional unit 6 is shown in figure 3.11.
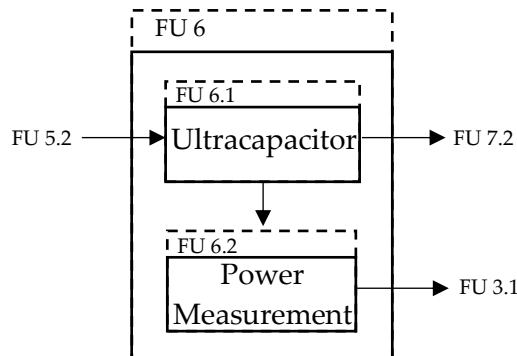


Figure 3.11: Functional Unit 6

## 3.5.6 Functional Unit 7

Functional unit 7 consists out of the buck converter, FU 6.1, the driver IC, FU 7.1, and the power measurement block, FU 7.3 as shown in figure 3.12. The buck converter connects with the ultracapacitor and is used to control the amount of power that can be transferred to the load, FU 8.
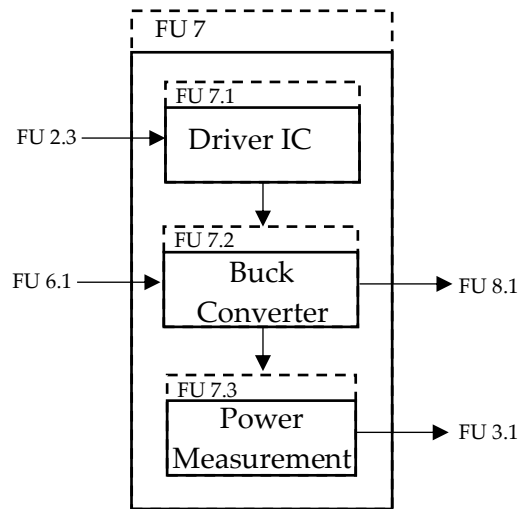
Figure 3.12: Functional Unit 7

## 3.5.7 Functional Unit 8

Functional unit 8 is the only external functional unit in the system and is shown in figure 3.13. FU 8 represents the load block, which consists out of the programmable load, FU 8.1, and a power measurement block, FU 8.2. The programmable load is connected to both the buck converter and the switch, FU 9. The power measurement block interfaces with the programmable load and the output of the block is connected to the low pass filter.
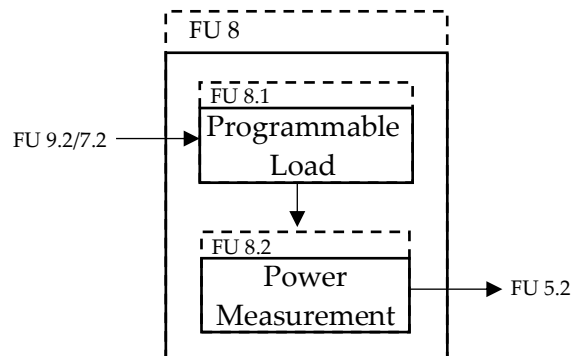
Figure 3.13: Functional unit 8

## 3.5.8 Functional Unit 9

The last functional unit is FU 9, which contains the MOSFET and driver IC that is used to directly connect the battery to the load, as illustrated in figure 3.14. The MOSFET is connected to the battery, FU 4.1, and the programmable load FU 8.1. FU 9.3 measures the power flowing through the MOSFET. The FU is shown below in figure 3.14.
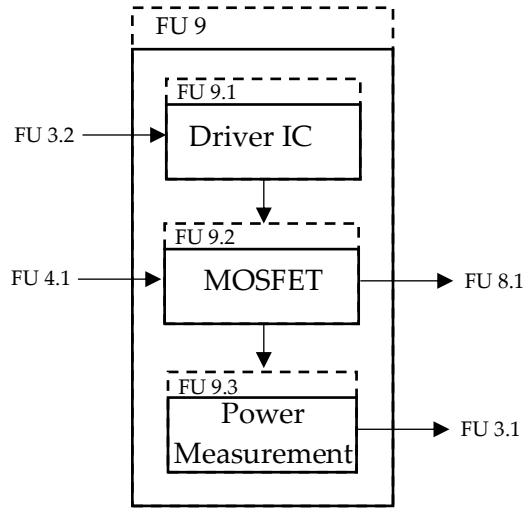
Figure 3.14: Functional Unit 9

# 3.6 Buck Converter

The buck converter is used to provide power to the load from the ultracapacitor. The feedback controller determines the required duty cycle for a certain power level. The buck converter topology is shown in figure 3.15. As the user may note, a non-synchronous buck converter topology was chosen, due to its simplicity.



Figure 3.15: Buck converter diagram

The electrical requirements for the buck converter are tabulated in table 3.1.

Table 3.1: Buck converter electrical requirements

| Input voltage range | 10 V – 16 V |
|---|---|
| Nominal output voltage | 7.4 V |
| Maximum output power | 100 W |
| Maximum output current | 13.5 A |

The buck converter is designed such that it is to operate in continuous conduction mode (CCM). The first step is to calculate the maximum duty cycle the converter will operate at, to determine the maximum switching current throughout the converter. The maximum duty cycle is calculated using the equation,

$$D = \frac{V_{out}}{V_{in(max)} \times \eta} \tag{3.2}$$

where $D$ is the maximum duty cycle and $\eta$ is the converter efficiency. The converter efficiency is estimated for calculation purposes at 85%. The maximum duty cycle is then,

$$D = \frac{7.4}{16 \times 0.85} = 0.544. \tag{3.3}$$

The inductor can now be calculated if the desired inductor ripple current is known. An inductor ripple current of 20% was chosen. The inductor ripple current is then,

$$\Delta I_L = 0.2 \times I_{out} = 2.7\text{A} \tag{3.4}$$

where $\Delta I_L$ is the inductor ripple current.

The following equation gives a good estimate for the value of the inductor,

$$L = \frac{V_{out} \times (V_{in} - V_{out})}{\Delta I_L \times f_s \times V_{in}}. \tag{3.5}$$

where $f_s$ is the switching frequency. Choosing a switching frequency of 10 kHz and using $V_{in}$ as 13V and substituting those values into equation 3.5 results in

$$L = \frac{7.4 \times (16 - 7.4)}{2.7 \times 10\,000 \times 16} = 147.31\ \mu\text{H}. \tag{3.6}$$

The requirements for the rectifier diode can be calculated by noting from the topology that the forward current rating is equal to the maximum output current. The average forward current rating for the diode is thus

$$I_F = I_{OUT(\text{max})} \times (1 - D), \tag{3.7}$$

where $I_F$ is the average forward current of the diode. This results in an average forward current rating of

$$I_F = 13.5 \times (1 - 0.544) = 6.156\ \text{A}. \tag{3.8}$$

A Schottky diode with a lower forward voltage should be used to reduce losses. The diode should also be able to dissipate the power losses associated with the forward voltage drop, which is equal to

$$P_D = I_F \times V_F. \tag{3.9}$$

Using a $V_F$ of 0.6V, which is typical for Schottky diodes with a high average forward current in equation 3.9 results in a diode power dissipation of

$$P_D = 6.156 \times 0.6 = 3.6936\ \text{W}. \tag{3.10}$$

The minimum value for the output capacitor can be calculated for a desired output voltage ripple using the following equation

$$C_{out(\text{min})} = \frac{\Delta I_L}{8 \times f_s \times \Delta V_{out}}. \tag{3.11}$$

With a desired output voltage ripple of 5%, the capacitor value is

$$C_{out(\text{min})} = \frac{2.7}{8 \times 10\,000 \times 0.05 \times 7.4} = 91.21\ \mu\text{F}. \tag{3.12}$$

The ESR of the capacitor also adds to the voltage ripple, so it is important to choose a capacitor with a low ESR and/or increase the capacitance of the chosen capacitor to compensate for the additional voltage ripple.

The maximum switching current which the MOSFET should withstand during full load is calculated by using equation 3.13.

$$I_{SW} = \frac{\Delta I_L}{2} + I_{OUT(\max)} \tag{3.13}$$

By substituting the calculated values into equation 3.13, we find that

$$I_{SW} = \frac{2.7}{2} + 13.5 = 14.85 \text{ A}. \tag{3.14}$$

To sum up the above calculations, the calculated values for the buck converters components are given below:

- An inductor with an inductance so that $L > 147.31$ µH and it should be able to conduct an average current of at least 13.5 A.

- $C > 91.21$ µF

- Diode with an $I_F$ of at least 6.156 A, a suitable package and heatsink to be able to dissipate 3.69 W of power and a forward voltage as low as possible.

- A MOSFET with a low $R_{DS(on)}$ and suitable switching characteristics.

- The MOSFET should be able to switch 14.85 A of current.

## 3.7 Boost Converter

The boost converter is used to charge the ultracapacitor from the battery. The basic topology of a boost converter is shown in figure 3.16. A non-synchronous converter topology was utilized due to its simplicity.
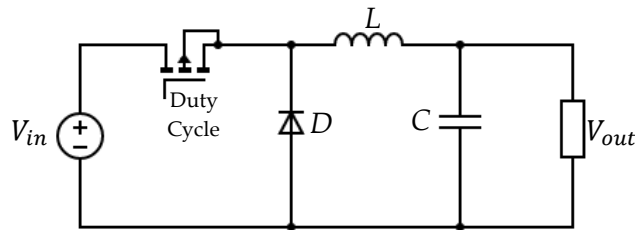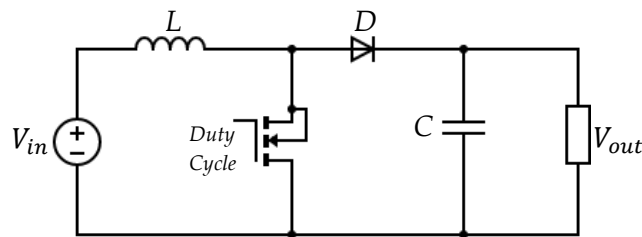


Figure 3.16: Boost converter

The electrical requirements for the boost converter are tabulated in table 3.2.

Table 3.2: Boost converter electrical requirements

| | |
|---|---|
| Input voltage range | 5 V – 8 V |
| Nominal output voltage | 13 V |
| Maximum output power | 25 W |
| Maximum output current | 1.92 A |

The following equation gives a good estimate of the value of the inductor if the inductor ripple current is known,

$$L = \frac{V_{IN(min)} \times (V_{out} - V_{IN(min)})}{\Delta I_L \times f_s \times V_{out}}, \tag{3.15}$$

where $f_s$ is the switching frequency and $\Delta I_L$ is the inductor ripple current. Using a desired inductor ripple current of 20%, equation 3.15 can be used to calculate the value for the inductor,

$$\Delta I_L = 0.2 \times I_{OUT(max)} \times \frac{V_{out}}{V_{in}} = 0.998 \tag{3.16}$$

Using equation 1 to calculate the required inductance of the inductor whilst using a switching frequency of 10 kHz is

$$L = \frac{5 \times (13 - 5)}{0.988 \times 10000 \times 13} = 311.43 \text{ μH.} \tag{3.17}$$

The maximum forward current rating for the rectifier diode used is simply

$$I_F = I_{OUT(max)} = 1.92 \text{ A} \tag{3.18}$$

where $I_F$ is the average forward current of the diode. The power that the diode should be able to dissipate is

$$P_D = I_F \times V_F \tag{3.19}$$

where $V_F$ is the diodes forward voltage. A Schottky diode should be used to reduce the power losses as defined by equation 3.19. The power that the diode needs to be able to dissipate is

$$P_D = 1.92 \times 0.6 = 1.152 \text{ W} \tag{3.20}$$

if a diode with a $V_F$ of 0.6V is used.

In order to calculate the value of the output capacitor, the maximum duty cycle at which the boost converter would operate needs to be calculated. The maximum duty cycle occurs when the minimum input voltage is applied to the boost converter. The maximum duty cycle is thus

$$D = 1 - \frac{V_{IN(min)} \times \eta}{V_{out}} \tag{3.21}$$

where $D$ is the switching duty cycle and $\eta$ is the converter efficiency. Using an estimated efficiency of 85% the maximum duty cycle is

$$D = 1 - \frac{5 \times 0.85}{13} = 0.673. \tag{3.22}$$

The minimum value for the capacitance of the output capacitor can be calculated using

$$C_{out(\text{min})} = \frac{I_{OUT(\text{max})} \times D}{f_s \times \Delta V_{out}}. \tag{3.23}$$

where $C_{out(\text{min})}$ is the minimum output capacitance and $\Delta V_{out}$ is the desired output voltage ripple. An output voltage ripple of 5% was chosen. The minimum output capacitance is then

$$C_{out(\text{min})} = \frac{1.92 \times 0.673}{10\,000 \times 0.05 \times 13} = 198.79\ \mu\text{F}. \tag{3.24}$$

A capacitor with a low ESR should be used, seeing that the ESR of the capacitor adds to the output voltage ripple.

The maximum switching current which the MOSFET should be able to withstand during full load is calculated by using equation 3.25.

$$I_{SW} = \frac{\Delta I_L}{2} + \frac{I_{OUT(\text{max})}}{1 - D}. \tag{3.25}$$

By substituting the calculated values into equation 3.25, we find that

$$I_{SW} = \frac{0.998}{2} + \frac{1.92}{1 - 0.673} = 6.73\ \text{A}. \tag{3.26}$$

To sum up the above calculations, the calculated values for the boost converters components are given below:

- An inductor with an inductance so that $L > 311.31\ \mu\text{H}$ and be able to conduct an average current of at least 5 A.

- A capacitor with a capacitance so that $C > 198.79\ \mu\text{F}$ and which has a low ESR.

- Diode with an $I_F$ of at least 1.92 A, a suitable package and heatsink to be able to dissipate 1.152 W of power and a forward voltage as low as possible.

- A MOSFET with a low $R_{DS(on)}$ and suitable switching characteristics.

- The MOSFET should be able to switch at least 6.73 A.

# 3.8 Fuzzy Logic Controller

## 3.8.1 Fuzzy logic control scheme

The DC/DC converters in the system, FU 5 and 7, are used to transfer power between the EES devices in the system and the load. The power being transferred by the boost converter from the battery to the ultracapacitor needs to be controlled. The output voltage of the buck converter also needs to be controlled. A closed-loop control structure is used to control the amount of power being transferred. Figure 3.17 depicts the closed-loop control structure used for the DC/DC converters.
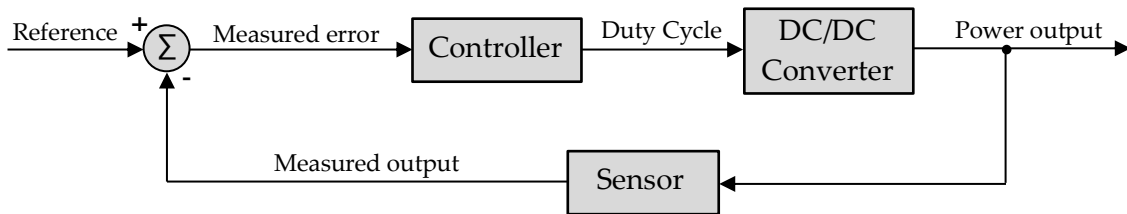


Figure 3.17: Closed-loop controller

The reference power for the boost converter is set by the overhead controller (FU 2.1). The controller then calculates the difference between the set-point and the desired output and increases or decreases the duty cycle accordingly. Fuzzy logic, which accommodates expert knowledge in controller design, was used as the control topology. The fuzzy logic controller structure is shown in figure 3.18.
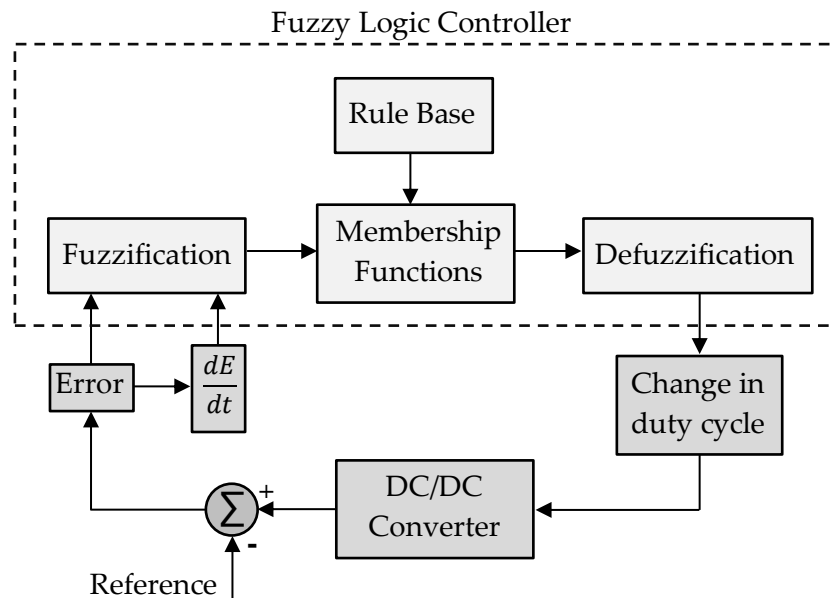


Figure 3.18: Fuzzy logic control structure

The error is equal to the difference between the reference point set by the overhead controller and the measured output value. As we can note from figure 3.18 the error and rate of change of the error are supplied as inputs to the fuzzy controller. The controller outputs the amount with which the duty cycle should change from the previous set duty cycle. The input values are passed to the

fuzzification block of the controller. Fuzzification is the process of converting the input values into the required linguistic variables.

After the input values have been fuzzified the membership functions determine the degree of truth of the input values to the rules in the rule base. The defuzzification block converts the fuzzy set into a crisp value, which is the change in the duty cycle.

Fuzzy logic does not require a mathematical model of the system, the designer of the fuzzy logic system only requires a thorough understanding of the relation between the input and output variables of the system. The important system characteristic to keep in mind for both the DC/DC converters used is that increasing the duty cycle, increase the output voltage/power increases. This forms the basic rule set for the fuzzy logic controller. The fuzzy logic controller subsystem as implemented in MATLAB®/Simulink® is shown in figure 3.19. A saturation block limits the maximum and minimum output duty cycle of the controller.
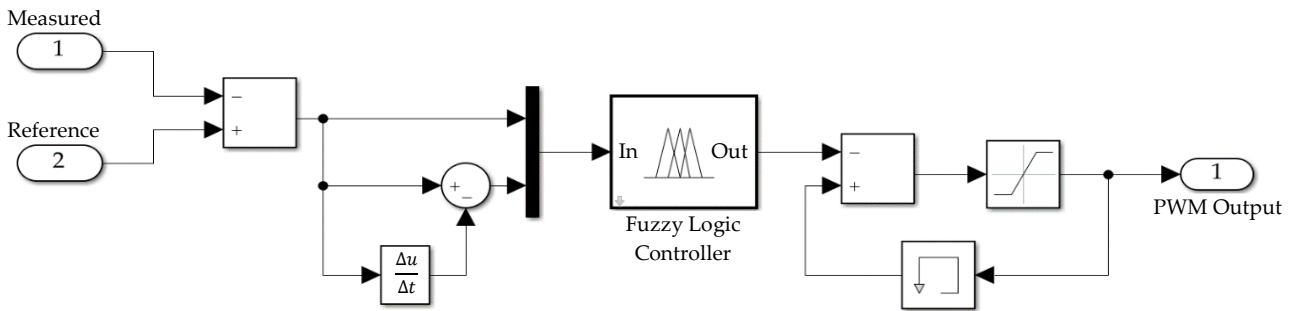


Figure 3.19: Fuzzy logic controller subsystem

The fuzzy logic controller has two inputs, i) error between the controlled value and the reference value and ii) the rate of change of the error. The error and rate of change of the error is mathematically defined in equations 3.27 and 3.28.

$$e(k) = V_{ref} - V_{o(ADC)} \tag{3.27}$$

$$ce(k) = e(k) - e(k-1) \tag{3.28}$$

where $V_{ref}$ is the desired reference voltage and $V_{o(ADC)}$ is the converted digital value of the output voltage. It is important to note that the boost converter operates in a current-controlled mode, whilst the buck converter operates in a voltage-controlled mode. $V_{ref}$ and $V_{o(ADC)}$ in equation 3 would thus be $I_{ref}$ and $I_{o(ADC)}$.

A saturation block is used in Simulink® to prevent the controller from outputting a duty cycle of 0% which would cause the inductor in the boost converter to saturate, whilst a duty cycle of 100% would cause the inductor in the buck converter to saturate. The previous value of the outputted duty cycle is stored in a memory block and the change in duty cycle value outputted by the controller is added to this value. A differential block was used to determine the rate of change of the error.

## 3.8.2 Membership functions

Two input membership functions are required for the two different inputs into the controller. The membership functions are simple curves that define how each input value is mapped to a specific value, or the degree of truth that that value has. The first membership function, as shown in figure 3.20 is the error in the set-point and the controlled value.
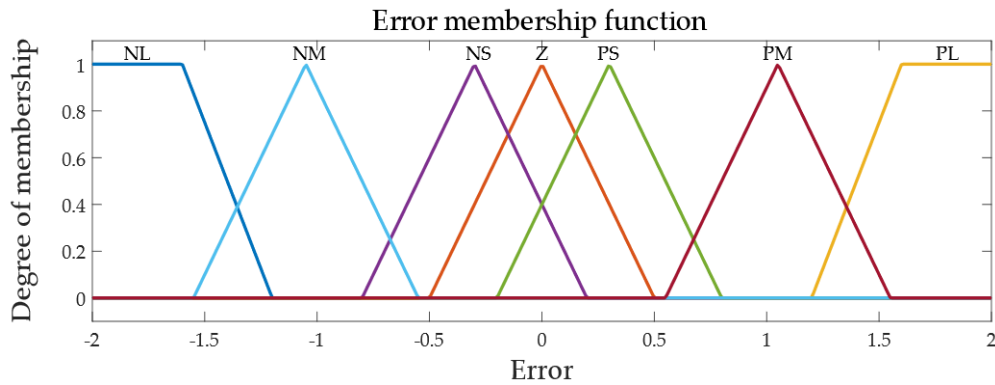


Figure 3.20: Error membership function

The second membership function, as shown in figure 3.21, is the rate of change of the error membership function. This function is used to determine if the error is reduced at a satisfactory rate.
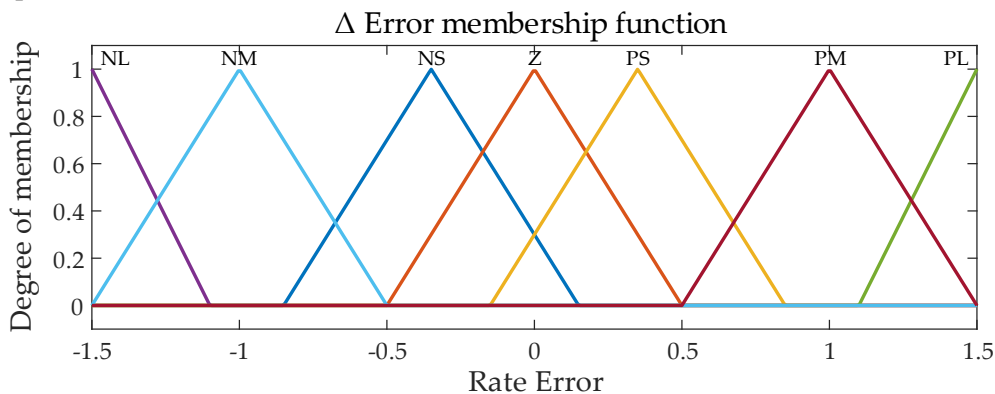


Figure 3.21: Δ Error membership function

Each membership function has 7 functions, which are abbreviated as NL (Negative Large), NM (Negative Medium), NS (Negative Small), Z (Zero), PS (Positive Small), PM (Positive Medium) and PL (Positive Large). The fuzzy logic controller only requires one output membership function seeing that it only has one output, which is the change in duty cycle. The output membership function is shown in figure 3.22.

The input range of the membership functions were changed and varied during the simulation process until the controller performed satisfactorily. Adjusting the input range of the membership functions adjusts the gain and inversely the sensitivity of the input functions.
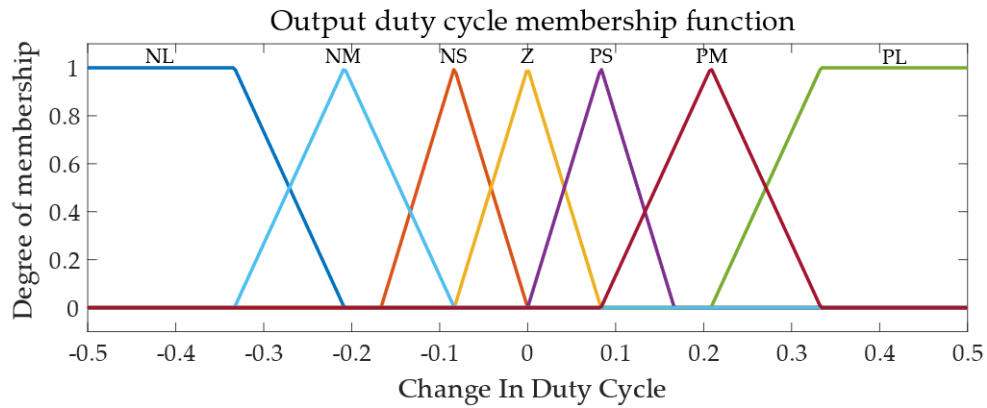
Figure 3.22: Output duty cycle membership function

The rule base of the fuzzy logic controller contains the if-then rules for the input values applied to the fuzzy logic controller. The fuzzy rules employed for the fuzzy logic controller are shown in table 3.3.

Table 3.3: Fuzzy rules

|  |  | $\Delta$ Error | | | | | | |
|---|---|---|---|---|---|---|---|---|
|  |  | **NL** | **NM** | **NS** | **Z** | **PS** | **PM** | **PL** |
|  | **NL** | NL | NL | NL | NM | NM | NS | Z |
|  | **NM** | NL | NM | NM | NS | NS | Z | PS |
|  | **NS** | NB | NM | NS | NS | Z | PS | PM |
| **Error** | **Z** | NM | NS | NS | Z | PS | PS | PM |
|  | **PS** | NM | NS | Z | PS | PS | PM | PL |
|  | **PM** | NS | Z | PS | PS | PM | PM | PL |
|  | **PL** | Z | PS | PM | PM | PL | PL | PL |

where:

**N** - Negative        **Z** – Zero        **P** – Positive

**S** - Small        **M** – Medium        **L** - Large

An example of one of the rules described in table I is:

*If ("**Error**") is (NS) AND ("$\Delta$ **Error**") is (NM) then output is (NL).*

The output of each rule needs to be combined into a single fuzzy set and this is done by aggregating these outputs. The aggregation method used was the maximum method, which returns the maximum value of a set. The defuzzification method that was used was the centroid calculation method. The Mamdani inference system was used. The resultant rule surface generated from the rules in table 3.3 is shown below in figure 3.23.
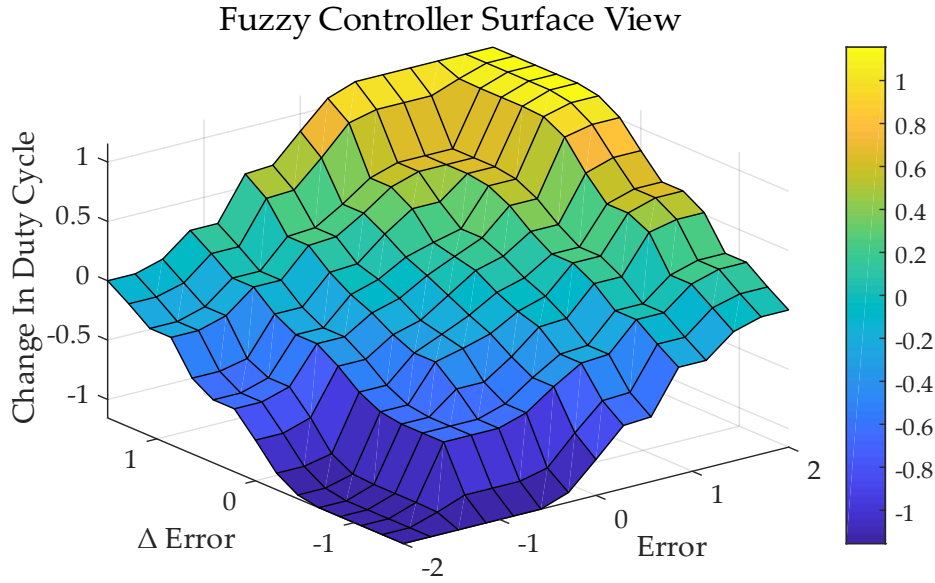
Figure 3.23: Fuzzy controller surface view

The rules resulting from the rule table can be summed up as follow:

- If the error is zero and the change in the error is also zero, keep the duty cycle the same.
- If the error is negative and the change in error is negative, the duty cycle decreases.
- If the error is negative and the change in error is positive, the duty cycle increases.
- If the error is positive and the change in error is negative, the duty cycle decreases.
- If the error is positive and the change in error is positive, the duty cycle increases.

# 3.9 Drive Cycle

In various countries all new light-duty ICE vehicles are required by law to undergo emission tests. Vehicle exhaust emissions are inherently variable, thus standardized drive cycles were developed to be able to conduct an emission test under reproducible conditions [133]. Drive cycles are also used to determine the engine or drive train durability [133]. A model of an electric vehicle's powertrain was used to calculate the power that needs to be developed from the speed profile.

The resistive forces on the vehicle can be calculated by using 3.29:

$$F_d(v(t)) = \frac{1}{2}\rho_a c_D A_f v(t)^2 + gm_t \sin\varphi(t) + F_r(v(t)) \tag{3.29}$$

where $c_R$ is the coefficient of rolling resistance, $m$ is the mass of the vehicle, $g$ is the gravitational constant, $\rho_a$ is the density of air, $c_D$ is the drag coefficient, $A_f$ is the frontal surface area of the vehicle and $V$ is the vehicle velocity. $F_d(v(t))$ is the resultant force of the summation of the aerodynamic drag, grading resistance and the rolling resistance $F_r(v(t))$.

The rolling resistance is described by a fifth-order polynomial function of the vehicle speed i.e.

$$F_r(v(t)) = gm_t \cos\varphi(t)\{a_0 + a_1 v(t) + a_2 v(t)^2 + a_3 v(t)^3 + a_4 v(t)^4 + a_5 v(t)^5\} \tag{3.30}$$

where $a_0, ..., a_5$ are experimentally determined coefficients. In this paper, the coefficients determined in the work of Sciarretta *et al.* was used [140].

The torque at the wheels required to accelerate the vehicle is calculated as

$$\tau_{wh} = r_{wh}F_d(t) + \frac{\theta_v}{r_{wh}}\frac{dv(t)}{dt} \tag{3.31}$$

where $\theta_v$ is the inertia of the vehicle and $r_{wh}$ is the radius of the wheels. The rotational speed of the wheels is simply calculated as

$$\omega_{wh}(t) = v(t)/r_{wh}. \tag{3.32}$$

When the vehicle utilizes a gearbox, the rotational torque ($\tau_m$) and speed ($\omega_m$) of the motor inverter is calculated as

$$\tau_m(t) = \tau_{wh}(t)/G_r \tag{3.33}$$

$$\omega_m(t) = \omega_{wh}(t)/G_r. \tag{3.34}$$

where $G_r$ is the reduction ratio of the gearbox.

The input power of the motor-inverter is then

$$P_m = \begin{cases} \tau_m(t)\omega_m(t)/\eta_{inv}, & for \ \tau_m(t) > 0 \\ \tau_m(t) \ \omega_m(t) \ \eta_{inv}, & otherwise \end{cases} \tag{3.35}$$

where $\eta_{inv}$ is the motor inverter efficiency, which is a function of $\omega_m(t)$ and $\tau_m(t)$.

Table 3.4 shows the values and assumptions that were used to calculate the power required to move the vehicle at the speed as defined in the specific drive cycle.

Table 3.4: Vehicle Parameters

| | | |
|---|---|---|
| $c_D$ | Drag coefficient | 0.29 |
| $A_f$ | Frontal area (m²) | 2.09 |
| $\theta_v$ | Total vehicle inertia (kg.m²) | 145 |
| $\rho_a$ | Air density (kg/m³) | 1.2 |
| $m_t$ | Vehicle mass (kg) | 1 200 |
| $a_0$ | Rolling resistance coefficient | 8.8e-3 |
| $a_1$ | Rolling resistance coefficient | -6.42e-5 |
| $a_2$ | Rolling resistance coefficient | 9.27e-6 |
| $a_3$ | Rolling resistance coefficient | -3.30e-7 |
| $a_4$ | Rolling resistance coefficient | 6.68e-9 |
| $a_5$ | Rolling resistance coefficient | -4.46e-11 |
| $r_{wh}$ | Wheel radius (m) | 0.29 |
| $G_r$ | Gear ratio | 6.45 |
| $\eta_{inv}$ | Motor-inverter efficiency (%) | 91 |

# 3.10 Shunt Current Sensor

This section briefly discusses the design and values chosen for the shunt current sensor. In order to monitor the power flow throughout the system, the current needs to be measured as well as the voltage at certain points. Various methods for measuring the flow of current exist, with the two most commonly used methods are shunt current monitoring and by making use of the Hall effect. The shunt current monitoring simply uses a low Ohmic value resistor in series with the conduction path to be measured and measures the voltage across the resistor. Ohm's law is then used to calculate the current through the resistor. This method has the disadvantage that the shunt resistor dissipates some power and also creates a voltage drop, which could influence some circuits if the shunt resistor is used for low side current monitoring, introducing a drift/difference between the actual reference ground point and the load.

The Texas Instruments INA 169 was chosen as the current shunt monitors. This IC has a high precision operational amplifier and has a wide input voltage range. Figure 3.24 shows the basic connection of the IC.
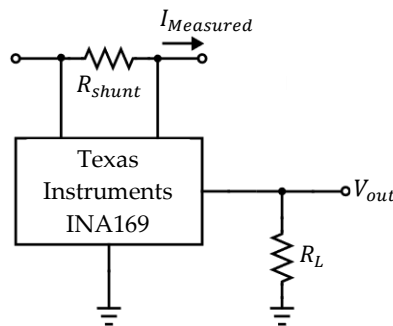


Figure 3.24: Shunt current sensor

The calculation of the shunt resistor's parameters is not shown here, as these calculations are somewhat trivial and is easily calculated using Ohm's law. The maximum differential voltage that the IC can measure is 500 mV, which was taken into account whilst determining the shunt resistor's parameters.

# 3.11 Low Pass Filter

The design of the low pass filter (FU 3.1) is discussed below. A passive low pass RC filter was used, seeing that they are easy to design, implement and make use of only two components. The layout of the low pass RC filter is shown below in figure 3.25.
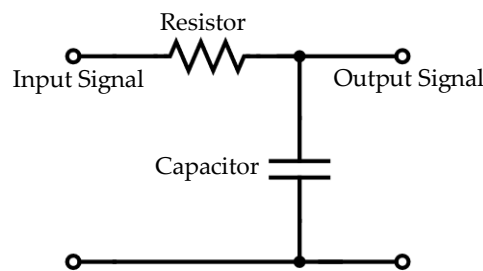


Figure 3.25: Low pass filter

The values for the resistor and capacitor can be calculated using the transfer function that relates the input voltage to the voltage over the capacitor, which is expressed as

$$H_c(s) = \frac{V_c(s)}{V_{in}(s)},$$

(3.36)

where $V_c(s)$ is the voltage over the capacitor and $V_{in}(s)$ is the input voltage.

The gain across the capacitor is equal to

$$G_c = |H_c(jw)| = \left| \frac{V_c(jw)}{V_{in}(jw)} \right| = \frac{1}{\sqrt{1 + (wRC)^2}}.$$

(3.37)

The cutoff frequency of the filter is defined as the point in the frequency response of the filter at which the output power is half of the nominal input power, or where the gain is equal to $\frac{1}{\sqrt{2}}$. Substituting the value of $\frac{1}{\sqrt{2}}$ into equation 3.37 results in

$$\frac{1}{\sqrt{2}} = \frac{1}{\sqrt{1 + (wRC)^2}}$$

(3.38)

$$\therefore w = \frac{1}{RC}$$

(3.39)

$$\therefore f_c = \frac{1}{2\pi RC}$$

(3.40)

Equation 3.40 can then be used to calculate the required values for R and C if we choose a cutoff frequency of 1 kHz and a resistance value of 10 Ω for R, then C is

$$1\,000 = \frac{1}{2\pi(10)C}$$

(3.41)

$$\therefore C = 15.9 \ \mu F$$

A 16 $uF$ capacitor was therefore chosen.

## 3.12 Validation and Verification

Validation was done in this chapter by utilising the conceptual design and the functional flow units to ensure that all the required sub-systems were included in the system, to ensure that the system would meet the objectives as described in chapter 1. The hybrid energy storage structure topology was verified by comparing it to the work done Z. Song *et al.* and C. Xiang *et al.* seeing that they made use of a similar topology [33], [139]. The design calculations that were used to calculate the values of the DC/DC converters were similar to those described in the power electronics handbook of N. Mohan *et al.* and the design guidelines presented by Texas Instruments [141]- [143].

Verification of this chapter was done by means of simulation to ensure that the sub-systems and the overall system operated as designed. The simulation of these sub-systems was done in chapter 4 and is omitted from this chapter. The verification of this chapter is therefore discussed in chapter 4.

# 3.13 Conclusion

The design chapter stared with the conceptual design of the overall system. The conceptual design showed all the required sub-systems for the system. The overhead control of the controller for the HESS was discussed. The different operating modes were also developed and discussed. Functional unit diagrams were created for the system as a whole as well as the various sub-systems. The functional unit diagrams were used to ensure that each sub-system had the required interfaces so that the different sub-systems successfully integrated with another.

A detailed design was done for the DC/DC converter and some of the other sub-sections. The simulation parameters were determined in this chapter and will be used in chapter 4. The work done by Sciarretta *et al.* was used to define equations which would be used to create the power profiles from the speed profiles of the three different drive cycles that were discussed in chapter 2 [140].

The design of the PCB for the system was also done in this chapter. Recommendations and guidelines on the optimal layout of the components in a DC/DC converter were taken into account. The PCB design can be seen in Appendix B of this document.

The next chapter discusses the simulations that were done in MATLAB®/Simulink®. The sub-systems were simulated as well as the overall system. The behaviour of the overhead controller was verified and the performance of the fuzzy logic controllers was also simulated. These results were used to verify that the sub-systems were correctly designed.

# Chapter 4 - Simulation

*This chapter discusses the simulation parameters and results that were obtained after the functional units and the overall active HESS were simulated. The results of the simulations are discussed in detail as well as the software that was used for the simulations. The performance of the passive and active HESS is compared. Figure 4.1 shows an overview of this chapter.*
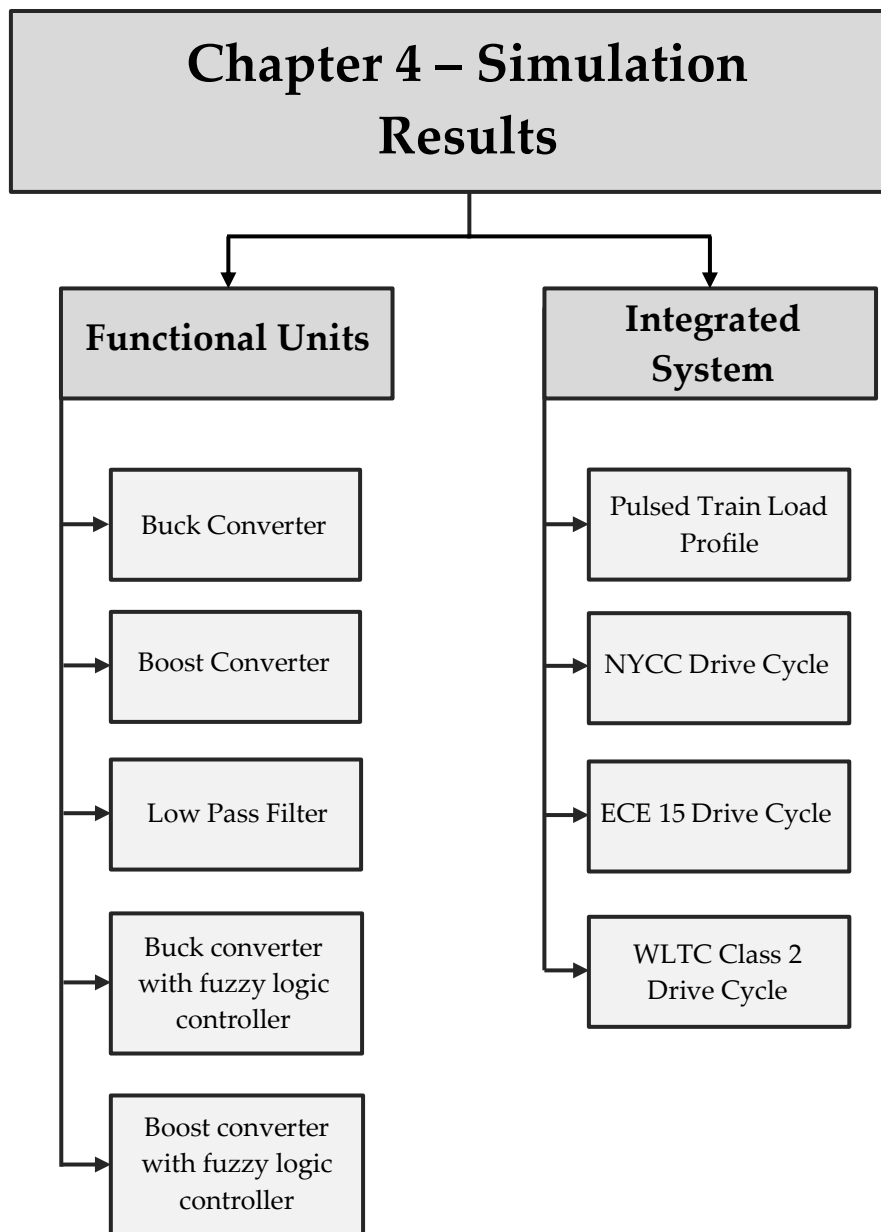
Figure 4.1: Simulation Chapter Overview

# 4.1 Functional Unit Simulation

The simulation results of some of the functional units as described in chapter 3 are discussed in this section. MATLAB®/Simulink® and LTspice® were used to simulate and verify the functional units. The buck converter, boost converter, low pass filter and the performance of the fuzzy logic controllers are simulated in this chapter. The first functional unit that was simulated was FU 7, which is the buck converter.

## 4.1.1 Buck Converter

In order to verify the design calculations as shown in chapter 3, the buck converter was simulated in Simulink®. The simulated circuit is shown in figure 4.2. As calculated in chapter 3 the simulated inductor has an inductance of 150 μH and the output capacitor has a capacitance of 460 μF.



Figure 4.2: Simulated buck converter

As stated in the design section, the switching frequency of the buck converter is 10 kHz. Table 4.1 contains the parameters used for the components in the simulation.

Table 4.1: Buck converter simulation parameters

| Component | Characteristic | Value |
|---|---|---|
| MOSFET | $R_{DS(on)}$ | 20 mΩ |
| Inductor | Inductance | 150 μH |
| Diode | Forward Voltage | 0.6 V |
| | Peak Reverse Voltage | 100 V |
| Capacitor | Capacitance | 460 μF |
| | ESR | 52 mΩ |

Figure 4.3 shows the buck converter's output voltage over a 1 Ω resistive load as the duty cycle is swept from 0% to 95%. As we can note from the figure, the output voltage relationship to the duty cycle is linear as we would expect from the equations given in chapter 3.
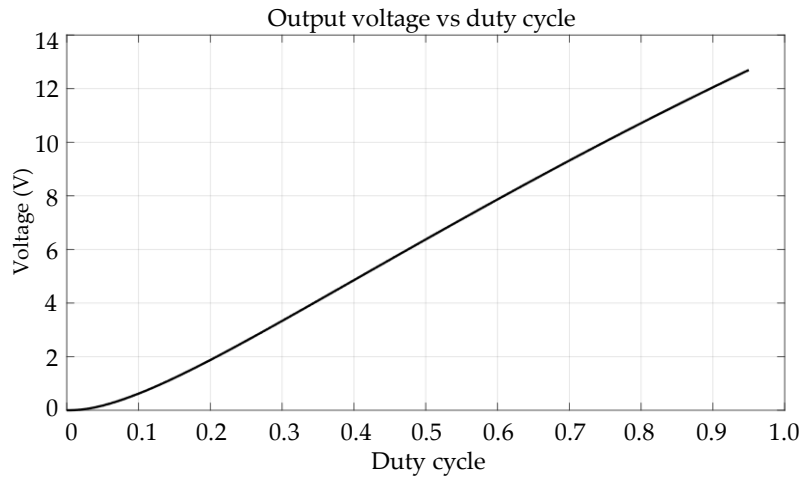
Figure 4.3: Buck converter output voltage vs duty cycle

The estimated efficiency of the converter at different power levels was also simulated. The efficiency of the converter at 10 W and 100 W is shown in figures 4.5 and 4.6 respectively. These estimated efficiency plots were simply created by plotting the power delivered to the load over the power provided by the voltage source. The estimated efficiency at a certain load power can be estimated from the graphs when they reach steady-state. The transient response should be ignored of the graphs should be ignored.
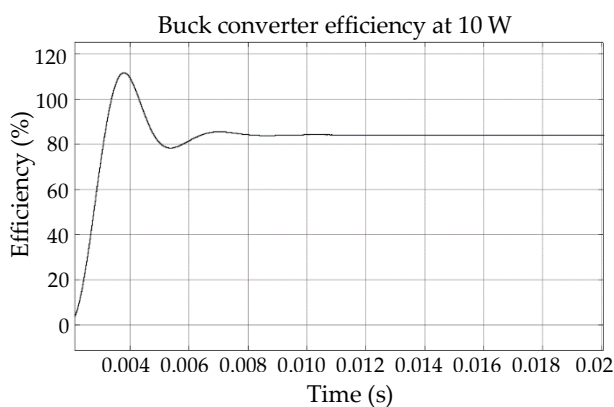


Figure 4.4: **a**) Buck converter efficiency at 10W          **b**) Buck converter efficiency at 100W
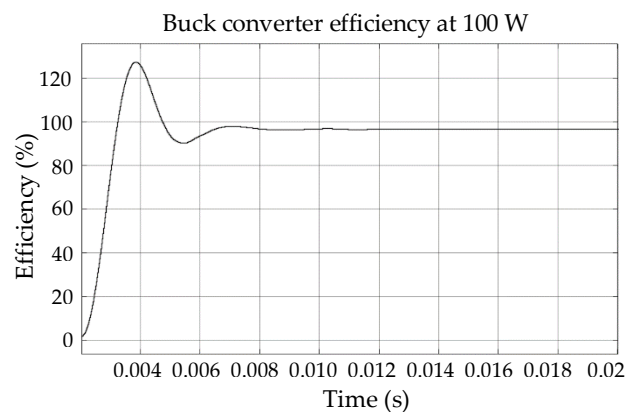
Using a diode with a forward voltage of 0.6V, the estimated converter efficiency for a load of 10W is about 90%, whilst the estimated efficiency for a load of 100W is about 95%. These estimated efficiency values are somewhat optimistic for an asynchronous converter. The Simulink® model does not take into account stray inductance, resistance and capacitance in the printed circuit board, the capacitor and the inductor. The Simulink® simulations were also used to verify that the buck converter operated in CCM. This was done by verifying that the current flowing through the inductor does not drop to zero during the normal operating conditions of the buck converter.

# 4.1.2 Boost Converter

Simulink® was also used to simulate the boost converter in order to verify the calculated values for the design of the boost converter. The simulated circuit is shown in figure 4.5. As calculated in the previous chapter, the simulated inductor has an inductance of 330 µH and the simulated capacitor has a capacitance of 460 µF.
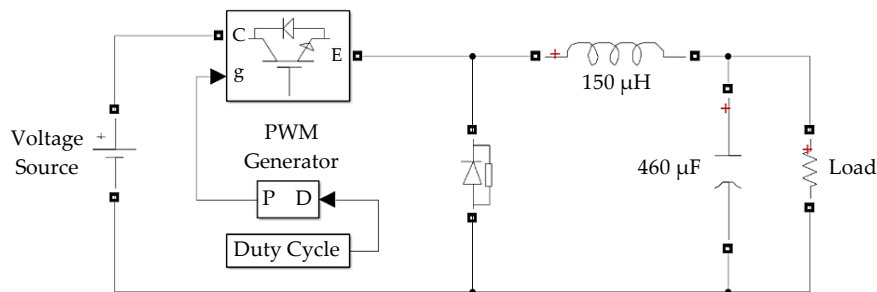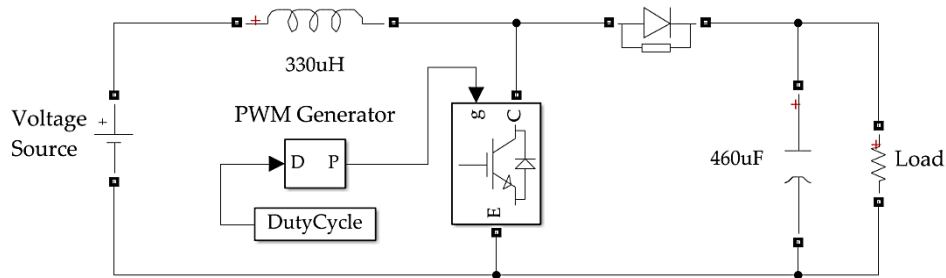


Figure 4.5: Simulated boost converter

As stated in the design section the switching frequency of the boost converter is 10 kHz. Table 4.2 contains the parameters used for the components in the simulation.

Table 4.2: Boost converter simulation parameters

| Component | Characteristic | Value |
|-----------|---------------|-------|
| MOSFET | $R_{DS(on)}$ | 8 mΩ |
| Inductor | Inductance | 330 µH |
| Diode | Forward Voltage | 0.6 V |
| | Peak Reverse Voltage | 100 V |
| Capacitor | Capacitance | 470 µF |
| | ESR | 52 mΩ |

Figure 4.6 shows the output current of the boost converter as the duty cycle is swept from 0% to 95%. A battery was used as the input source at a voltage of 7 V and an ultracapacitor at a voltage of 14 V was used at the load side.
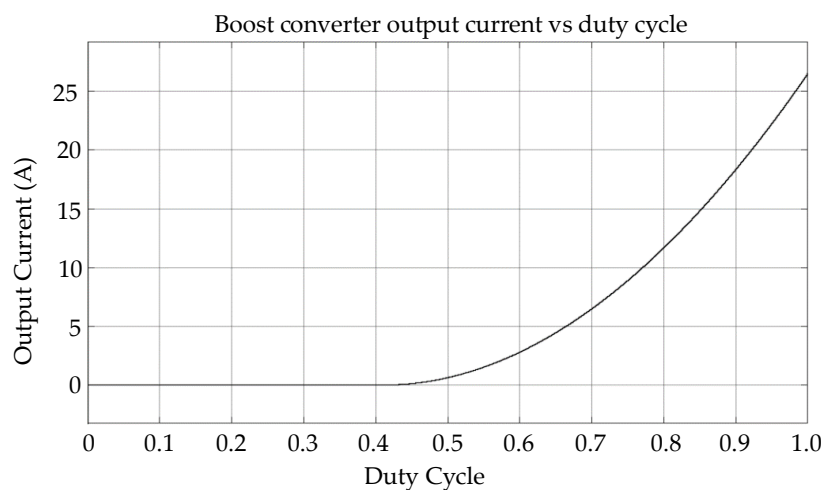


Figure 4.6: Boost converter output current vs duty cycle

As we can note from the figure, the boost converter only starts to transfer power to the ultracapacitor after the duty cycle increases sufficiently so that the boost converter output voltage is higher than that of the ultracapacitor. The estimated efficiency of the boost converter at different power levels was also simulated. The efficiency of the converter at 10 W and 25 W is shown in figures 4.7a and 4.7b respectively. These estimated efficiency plots were simply created by plotting the power delivered to the load over the power provided by the voltage source. The estimated efficiency at a certain load power can be estimated from the graphs when they reach steady-state.
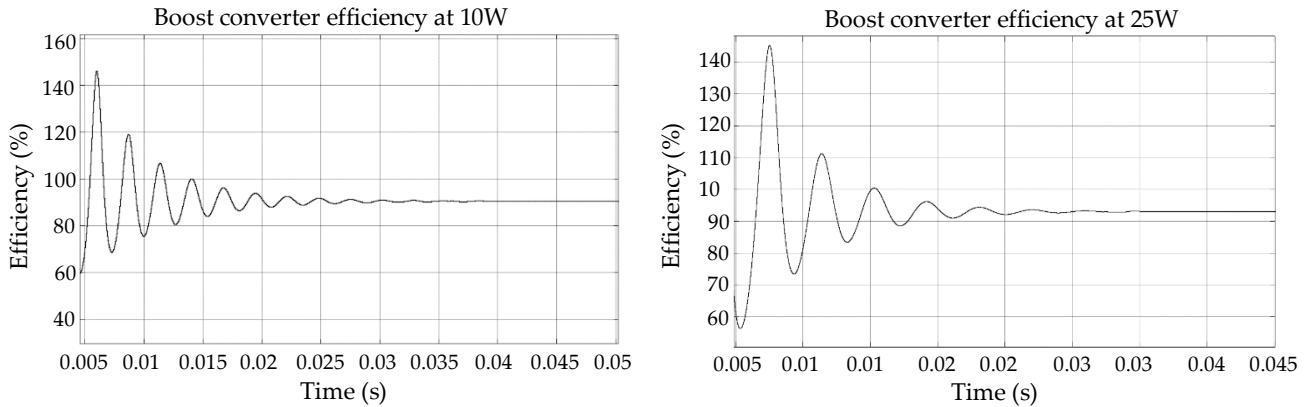


Figure 4.7: **a**) Boost converter efficiency at 10W  **b**) Boost converter efficiency at 25 W

The estimated efficiency of the boost converter at 10 W is 89% and the estimated efficiency at 25 W is about 92%. The Simulink® model does not take into account the losses associated with stray inductance and capacitance as the circuit would contain when practically implemented.

## 4.1.3 Low pass filter

The low pass filter (FU 3.1) was simulated in LTSpice® to verify that the cut-off frequency was as designed. Figure 4.8 shows a bode plot of the frequency response of the filter. The solid black line represents the magnitude response of the filter, whilst the dotted line represents the phase response of the filter. We can see that at 1 kHz the filter attenuates the input signal 3dB as designed.
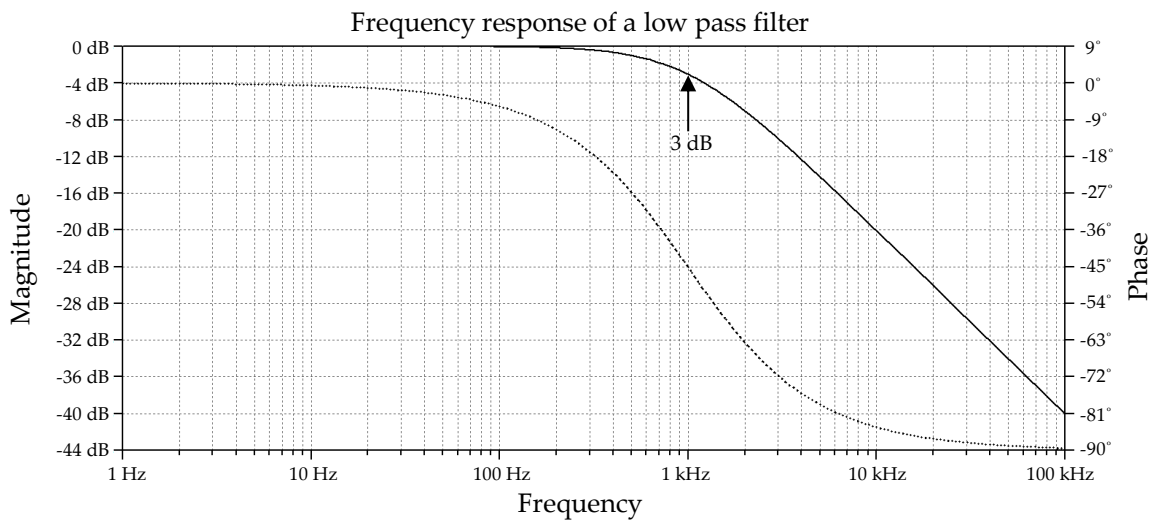


Figure 4.8: Bode plot of low pass filter

## 4.2 Fuzzy Logic controller performance

This section documents how the fuzzy logic controllers were simulated as well as the performance of the fuzzy logic controllers. The performance metrics that were used to verify their performance was the rise time, settling time and the overshoot of the controlled value.

### 4.2.1 Fuzzy logic controller – buck converter

As indicated in previous sections, there are two fuzzy logic controllers, F.U. 2.2 and F.U. 2.3, that controls the operation of the buck and boost converter respectively. This section shows the simulated performance of the controllers for a step-change in the reference point. The boost converter is current-controlled whilst the buck converter is voltage-controlled.

The performance of the buck converter was simulated first. Figure 4.9 shows the Simulink® model used to simulate the fuzzy logic controller and the buck converter. A battery is used as the voltage source of the buck converter at a voltage of 16V. A resistor with a resistance of 1 Ohm was used as the load in the model. The fuzzy logic controller block receives as input the reference/set-point voltage and the actual measured voltage over the resistor and then uses the difference between these two values to alter the duty cycle outputted to the buck converter. The monitoring block simply contains the Simulink® scope used to capture the output voltage and reference voltage versus time.
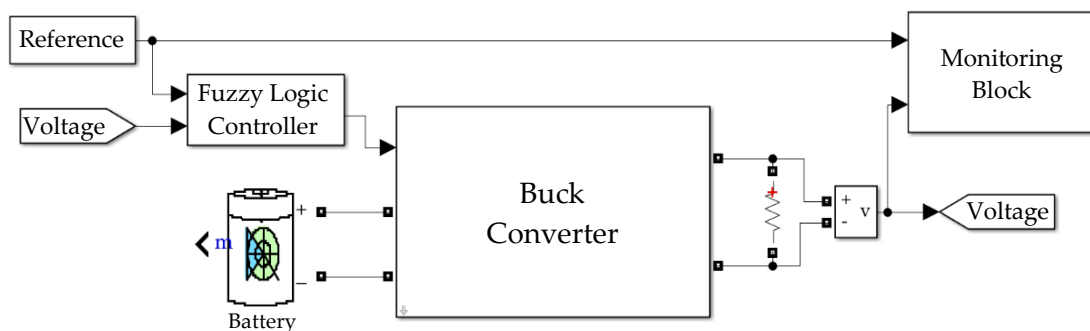


Figure 4.9: Fuzzy logic controller and buck converter simulation setup

The fuzzy logic controller block is shown in figure 4.10 below. The fuzzy logic controller receives as input the difference between the measured voltage and the set-point voltage as well as the derivative of this error. Seeing that the fuzzy logic controller outputs the amount that the duty cycle should increase or decrease, the previous outputted duty cycle value needs to be stored. The memory block is used to store the current duty cycle. The value of change in duty cycle outputted by the fuzzy logic controller is then added/subtracted from the previous value. The saturation block is used to limit the output duty cycle of the controller to a value between 0% and 95%.
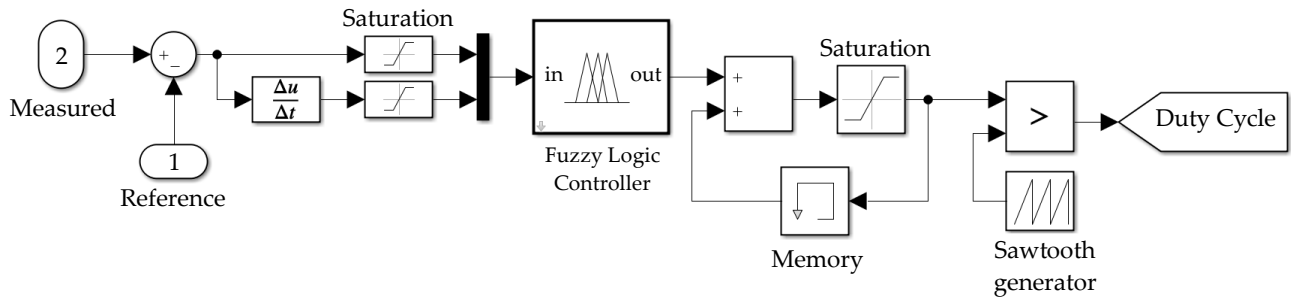
Figure 4.10: Fuzzy logic controller subsystem

The saturation blocks used for the inputs of the fuzzy logic controller are used to limit the input values to the input range defined for the fuzzy membership functions. If the input value is outside the defined input range, the fuzzy logic controller outputs an erroneous value. Figure 4.11 shows the step-response of the buck converters output voltage.
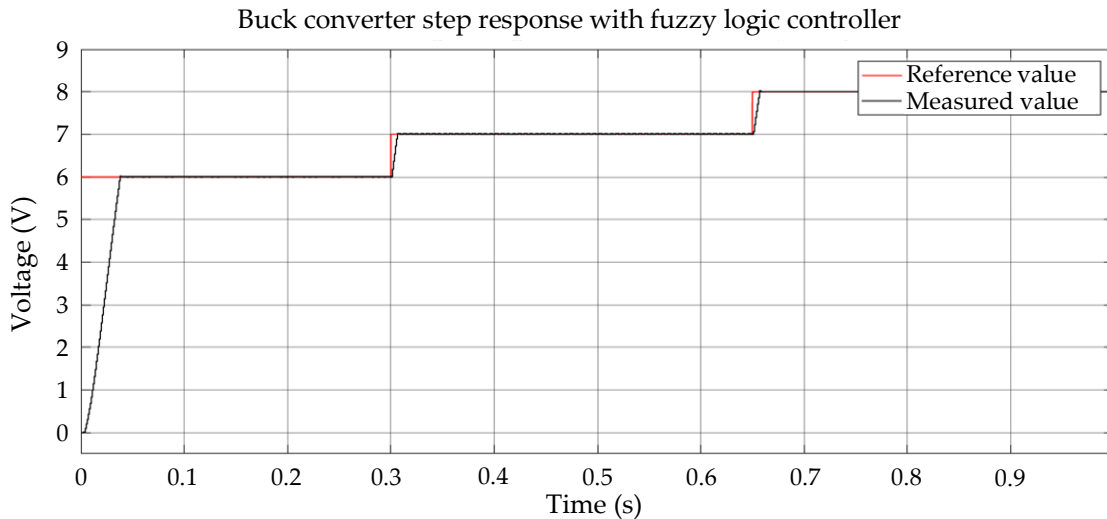


Figure 4.11: Buck converter step response with fuzzy logic controller

At 0.3s the reference voltage steps from 6 V to 7 V and at 0.65s the voltage steps from 7 V to 8 V. The reference voltage ranges from 6 V to 8 V and this range was chosen as this would be within the nominal voltage range of the battery bank. Figure 4.12 shows a zoomed-in portion of the step response of the converter from 7 V to 8 V.

We can note from the figure that the fuzzy logic controller adequately controls the output voltage of the buck converter. The rise time for the step change from 7 V to 8 V is 4.8ms. The controlled signal also only exhibits an overshoot of 2.4%, with a satisfactory settling time and zero steady-state error. The settling time for the output voltage was 8.1ms using an error band of 1%.

Buck converter zoomed in step response with fuzzy logic controller
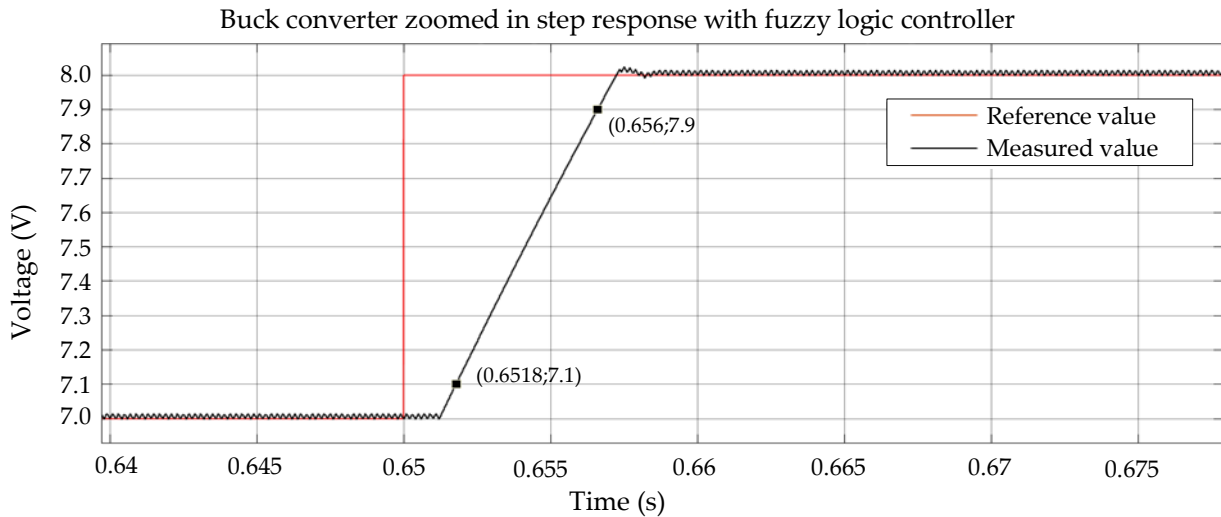


Figure 4.12: Buck converter step response from 7 V to 8 V

## 4.2.2 Fuzzy logic controller – boost converter

The performance of the fuzzy logic controller controlling the boost converter as simulated in Simulink® is discussed in this section. The model simulated as shown in figure 4.13, the boost converter is used to transfer power from the battery, which is the input source, to the ultracapacitor.
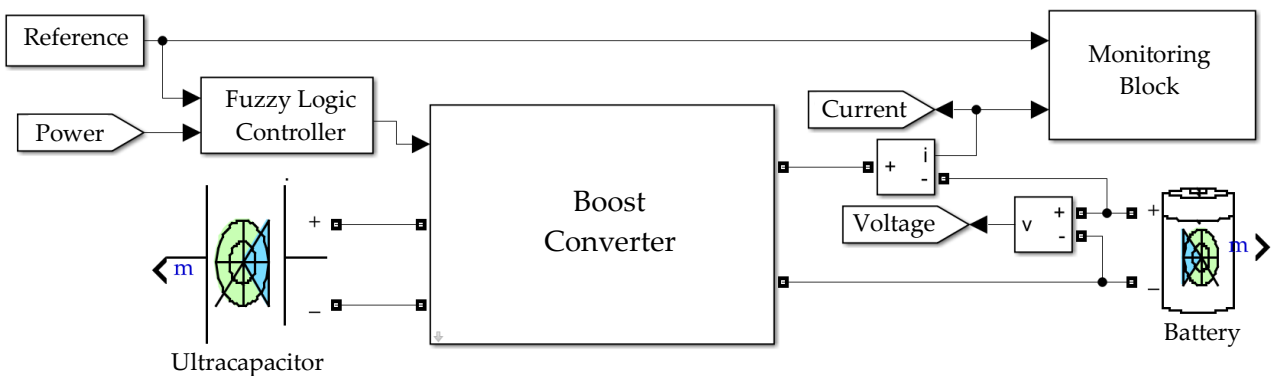


Figure 4.13: Fuzzy logic controller and boost converter simulation setup

The monitoring block as shown is used to log the data obtained in the simulation. The fuzzy logic controller block and implementation in Simulink® for the boost converter is similar to the block used for the buck converter as was shown in figure 4.10. The voltage and current measurements were used to calculate the power transferred from the battery to the ultracapacitor. The boost converter is used to regulate the power transferred from the battery to the ultracapacitor. The boost converters reference power is stepped at 0.2s from 7 W to 14 W and then at 0.4s from 14 W to 21 W. The boost converters step response whilst controlling the output power is shown in figure 4.14.
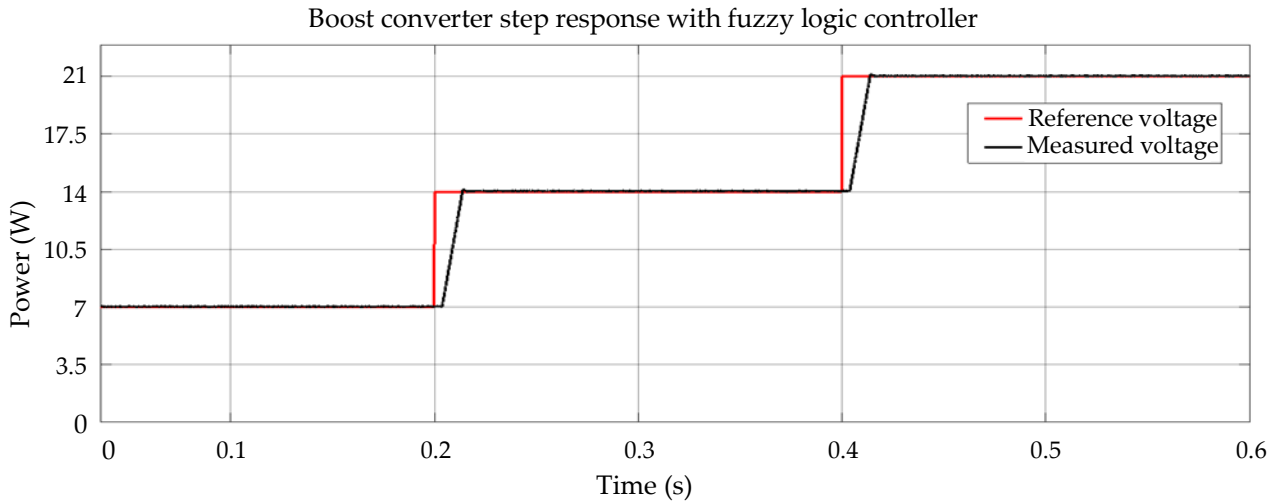
Figure 4.14: Boost converter step response with fuzzy logic controller

Figure 4.15 shows a zoomed-in portion of the step response of the boost converter when the reference power steps from 7 W to 14 W. The rise time is 8ms with an overshoot of only 2.1% and no steady-state error. With an error band of 1%, the settling time is 15.1ms.
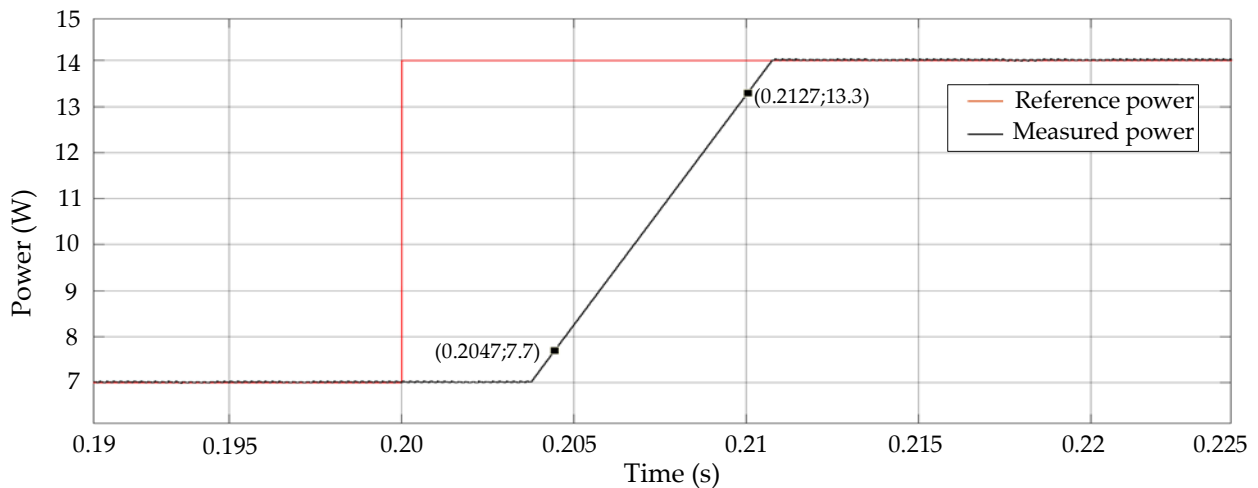


Figure 4.15: Boost converter zoomed-in step response with fuzzy logic controller

## 4.3 Drive cycle simulation

This section discusses the resultant power profiles that were created using the equations and parameters given in section 3.9. The three drive cycles that were used were the NYCC, ECE 15 and the WLTC drive cycles and their uses and origin were shortly discussed in the literature section. These three drive cycles were used in order to test the system using a range of different types of profiles.

MATLAB®/Simulink® was used to calculate the power that the electric motor in the vehicle needs to generate to move the vehicle according to the speed profile. The calculations that were done in order to calculate the power were discussed in section 3.9. Figure 4.16 shows the resultant power profile generated for the NYCC drive cycle.

**NYCC speed profile**
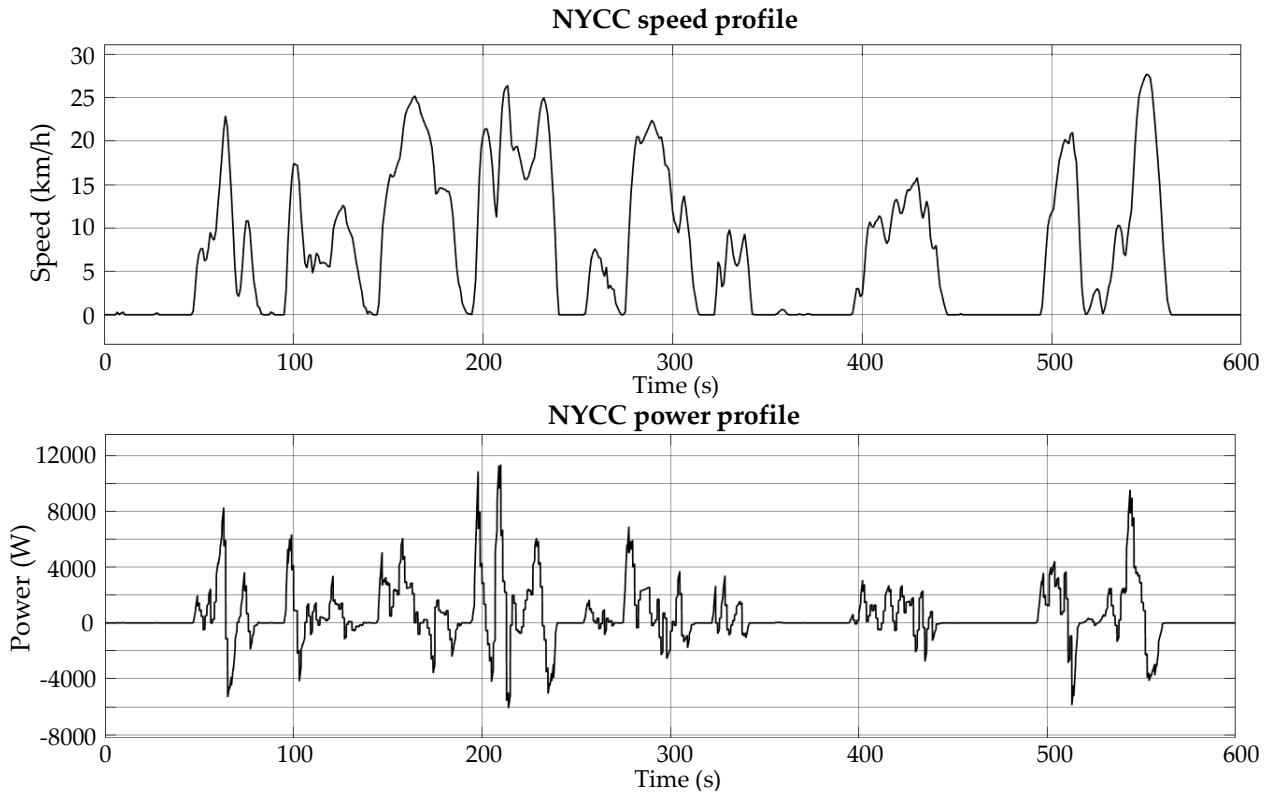


**NYCC power profile**



Figure 4.16: NYCC speed and power profile

The ECE 15 profile is an example of a steady-state drive cycle with speed plateaus. The power profile generated for this profile is shown in figure 4.17. The resultant power profile has high, sharp peaks caused by the transitions from acceleration/deceleration to a constant speed.

**ECE 15 speed profile**



**ECE 15 power profile**
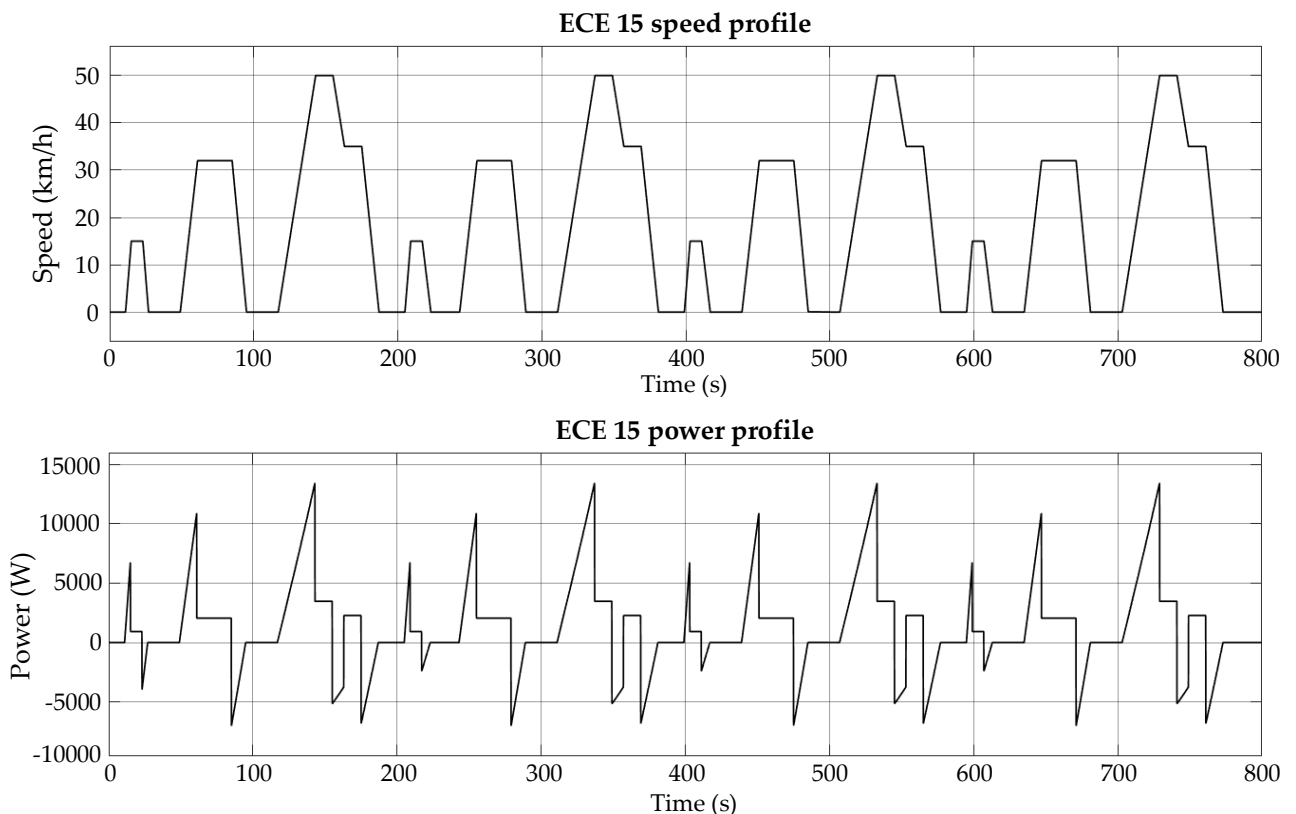


Figure 4.17: ECE 15 speed and power profile

In reality, a vehicle would not accelerate to a certain speed and suddenly maintain a constant speed, but would taper off to the constant speed. The speed profile would have rounded edges whilst the resultant power profile would have more gradual transitions.

The WLTC drive cycle was finalized in 2015 and was designed to provide a harmonized test procedure that can be used internationally. The Class 2 profile was used and is shown in figure 4.18. The Class 2 profile is used test vehicles with a lower power-to-weight ratio and is representative of vehicles driven in Europe, Japan and India.
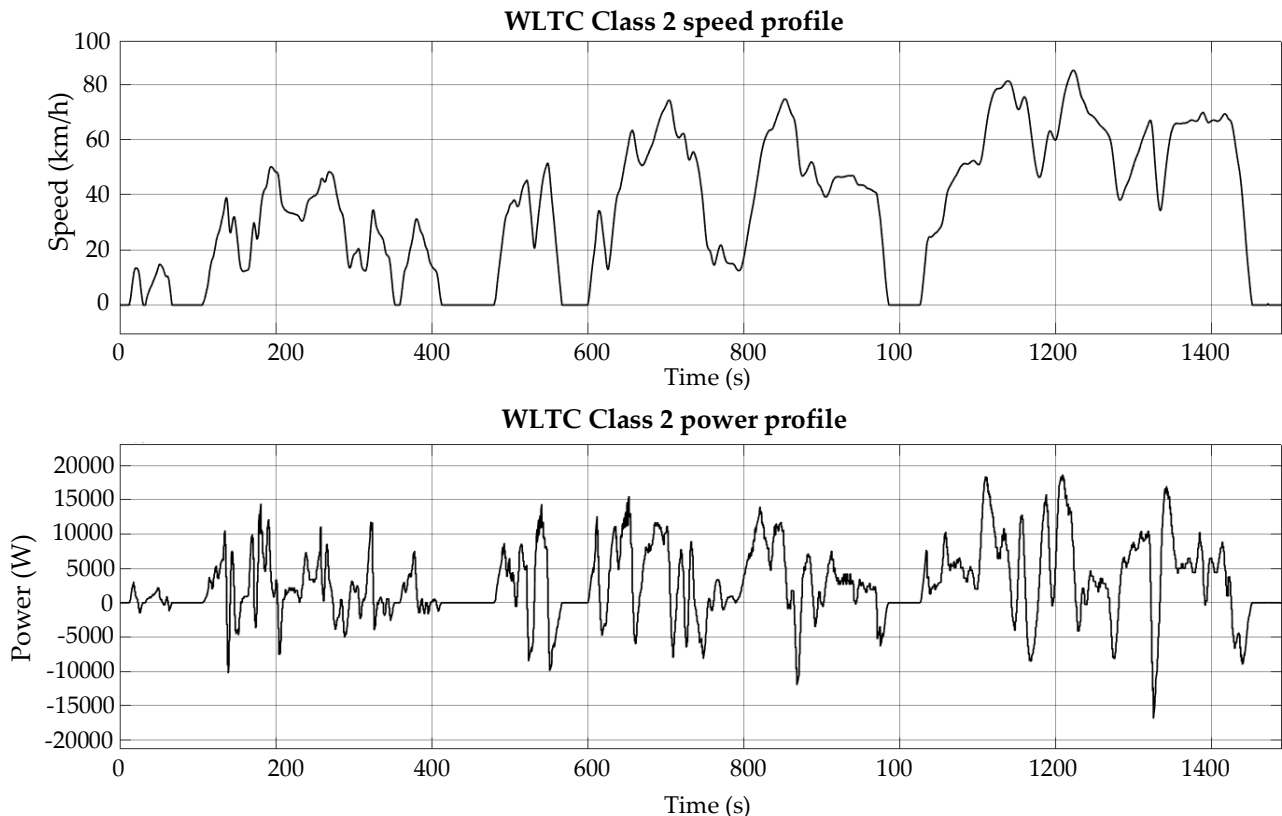


Figure 4.18: WLTC Class 2 speed and power profile

As can be seen in figures 4.16, 4.17 and 4.18 the resultant power profiles have both a positive and negative section. The negative part of the profile represents the power that is absorbed by the vehicle, be it through the normal disk/drum or regenerative brakes, to decelerate the vehicle according to the speed profile. The active HESS that was designed utilizes unidirectional DC/DC converters and is therefore unable to absorb this regenerative power. The power profiles that were used to simulate and evaluate the performance of the designed HESS only consist of the positive part of the profile.

## 4.4 Integrated System

This section discusses the simulated performance of the designed hybrid energy storage system as was done in MATLAB®/Simulink®. The performance of the designed HESS system is compared to a passive HESS consisting out of a battery and ultracapacitor in parallel. The ultracapacitor and battery used in both the passive HESS and the designed active HESS have the same capacity and

characteristics. Various load profiles were used in the simulations to compare the performance of the designed system to that of the passive system. A repeating pulsed load sequence was used as one of the load profiles.

The calculated power profiles for the different drive cycles as shown in the previous section were used to represent a realistic load that would be experienced by an electric vehicle. The results of these simulations are presented below. The load profiles that were used were scaled down so that the peak power that needs to be delivered by the DC/DC converters is below the designed limit. The profiles were also scaled in such a way that the average power required from the battery in the active system is below the nominal battery power limit. Figure 4.19 shows the complete overall system simulation model. The buck converter and boost converter block includes the fuzzy logic controllers. The power measurement block measures the voltage, current and calculates the state-of-charge of the battery/ultracapacitor.

The overhead controller measures the state-of-charge of the battery and ultracapacitor and the power delivered to the load. The controller then sets the reference power, which is the power that the boost converter should transfer from the battery to the ultracapacitor. The controller also sets the reference voltage for the buck converter. The controller also controls the state of the switch, either connecting/disconnecting the battery to/from the load.

The monitoring block is simply used to log the power transferred by the DC/DC converters and the power drawn from the battery and ultracapacitor, as well as the operating mode of the controller. The monitoring block contains a scope block to log this data.
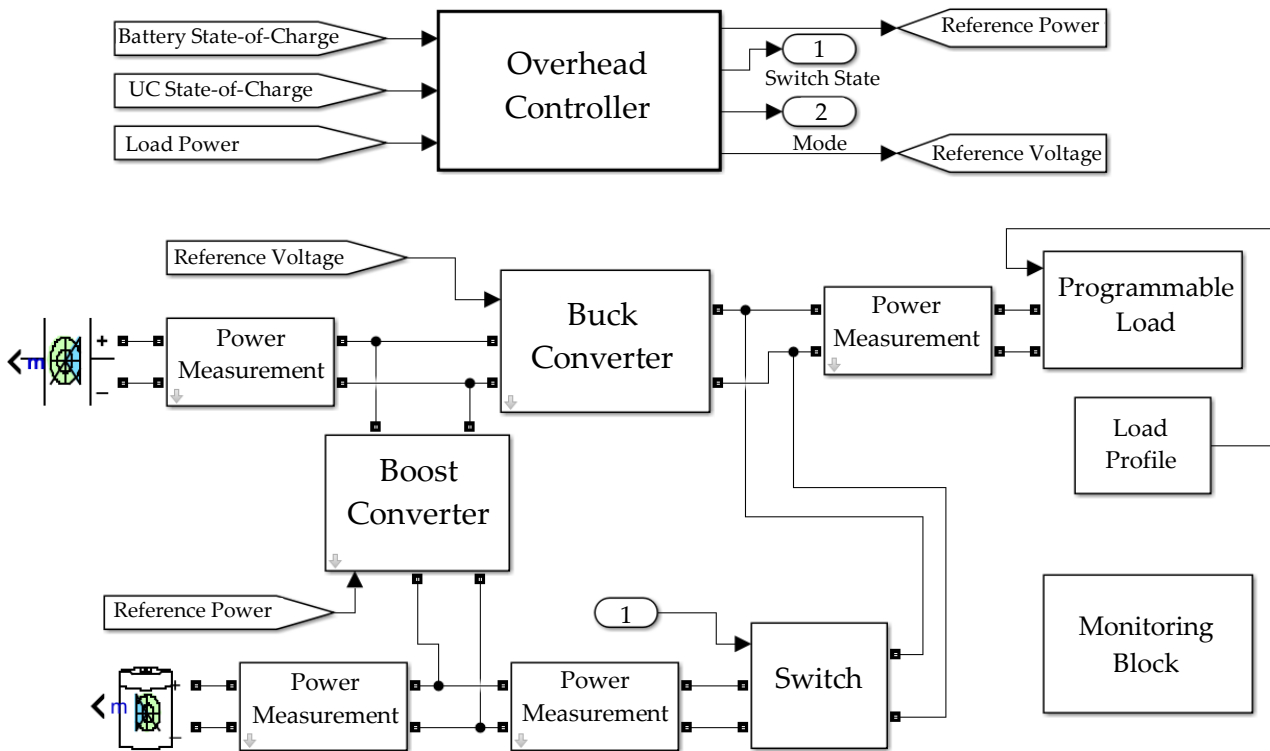


Figure 4.19: Complete system simulated model in Simulink®

# 4.4.1 Pulsed Load

This section discusses the simulation results for a pulsed load profile. Two different pulse train load profiles were used to evaluate and compare the performance of the system. The one profile has a lower amplitude and a higher duty cycle, whilst the other profile has a higher amplitude and a lower duty cycle. The first profile has a maximum amplitude of 38 W and a minimum amplitude of 6.6 W and a duty cycle of 36%. The second profile has a maximum amplitude of 62 W and 9 W with a duty cycle of 20%. These load profiles were applied to the passive HESS and active HESS. The values for these load profiles were arbitrarily chosen, with the only constraint being that the peak power in the profile should be less than the power that the buck converter can transfer whilst the average power for the profile should be less than the power that the boost converter can transfer.

The state-of-charge of the battery and the ultracapacitor was set to 80% during the simulations, so that for the active system, it operates in its nominal conditions and does not trigger any of the other modes as discussed in section 3.2. The average power of the load profile was used as the user-defined power limit for the battery. This ensured that the state-of-charge of the ultracapacitor at the end of the simulation was at the same level as at the beginning of the simulation.

## 4.4.1.1 Passive HESS performance for pulsed load with 38 W peak

Figure 4.20 shows the performance of the simulated passive system. The passive HESS does reduce the peak power impulses experience by the battery. As stated in the literature chapter, in the passive HESS the ultracapacitor serves as a low pass filter, averaging the power that the battery needs to provide. We can see that the passive system almost halves the peak power that the battery needs to provide to the load.
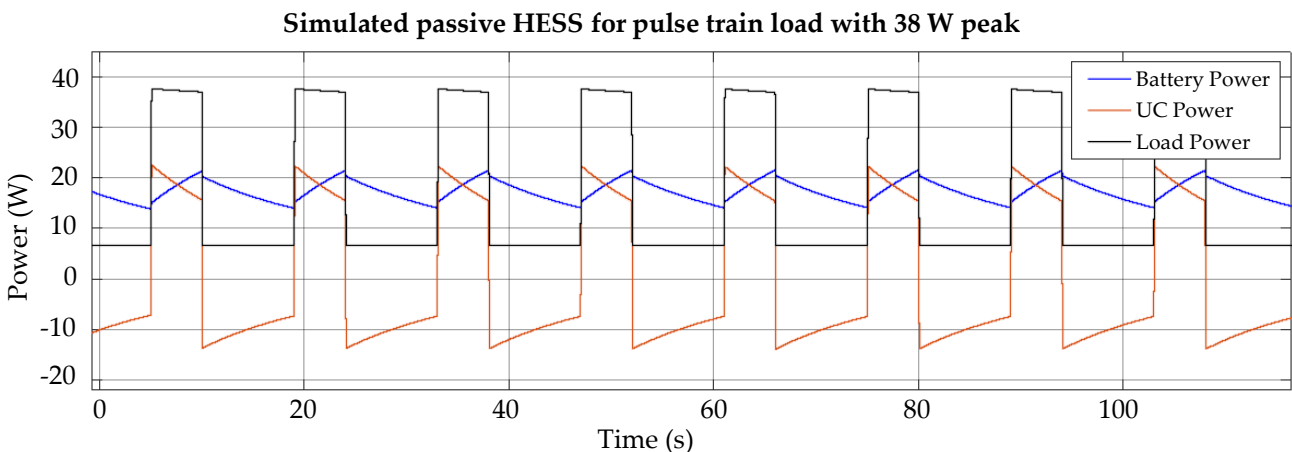


Figure 4.20: Passive HESS results for low pulse train profile

## 4.4.1.2 Active HESS performance for pulsed load with 38 W peak

The performance of the active HESS is shown in figure 4.21. The first graph in the figure shows power drawn by the load and the power provided by both the battery and the ultracapacitor. As we can note from this graph the power provided by the battery is equal to the average power for the load profile plus the losses associated with the DC/DC converters. The second graph shows the

power flowing through the switch to the load from the battery. The third graph shows the power provided by the boost converter to the ultracapacitor from the battery. The last graph just shows the current operating mode of the overhead controller.

As shown by the red portion in figure 4.21 the load power is higher than the user-defined power limit for the battery, which was 19 W. According to the control scheme as defined in figure 3.3, when the SoC of the battery is higher than 10% and the SoC of the UC is between 25% and 95% and the load power is above 19 W the controller operates in mode 5. The UC provides power to the load through the buck converter, whilst the battery provides power to the UC at the user-defined power limit rate. As we can see from the graph showing the boost converters power, 19 W of power is being transferred to the UC. We can also see that no power flows through the switch, seeing that the switch is disconnected in this mode.
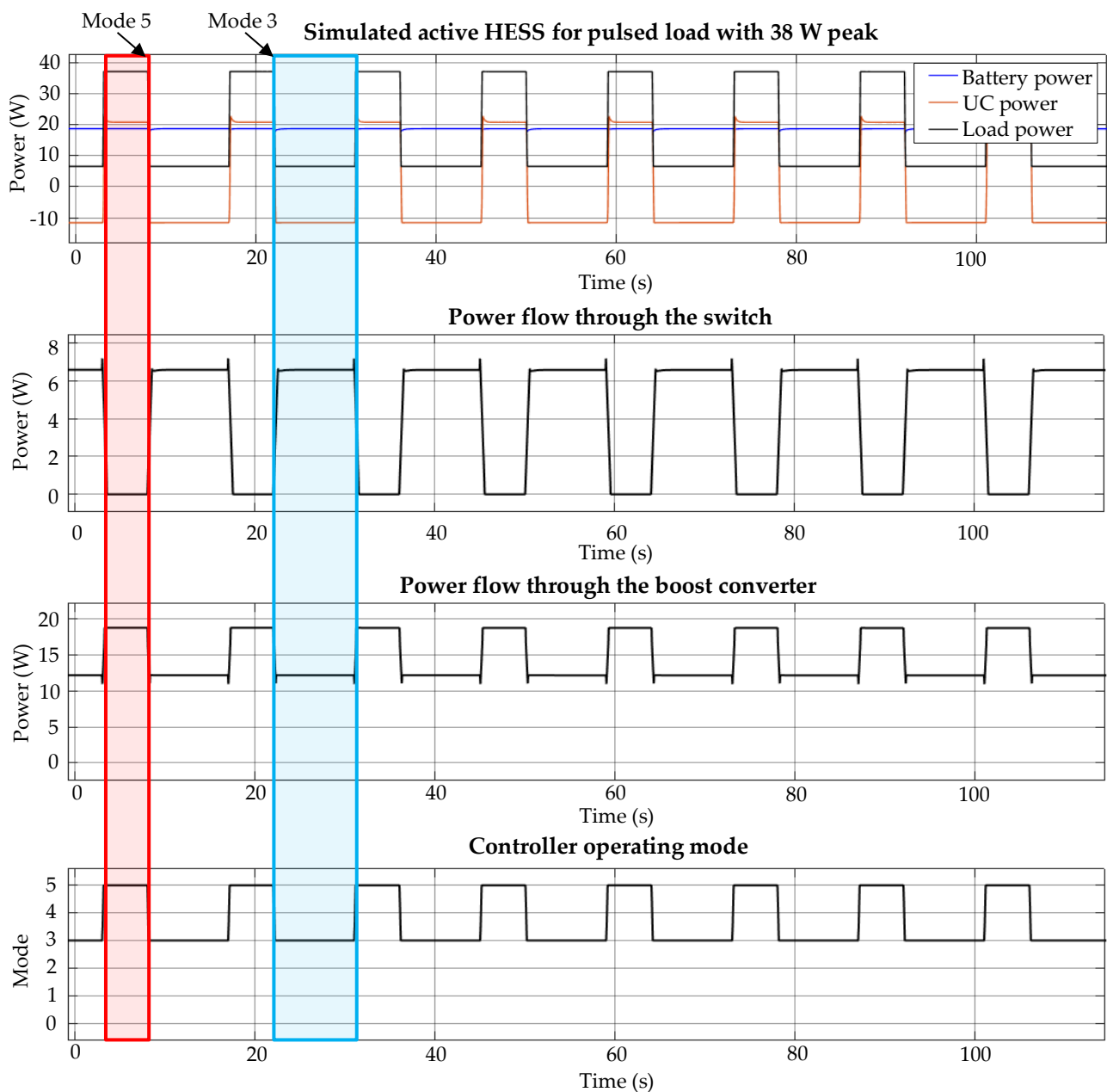


Figure 4.21: Simulation results for the low pulse train

The blue portion in figure 4.21 shows the operation of the overall controller in mode 3. The power drawn by the load is less than the user-defined battery power limit in this portion. According to the overall control scheme, when the SoC of the battery is above 10% and the SoC of the UC is between 10% and 95% and the load power is less than the defined limit, the system operates in mode 3. In this mode the battery directly provides power to the load through the switch, whilst power is provided from the battery through the boost converter to the UC so that the sum of the power drawn from the battery is equal to the defined limit. As can be seen from the second graph, the power drawn by the load through the switch is 6.8 W, which is equal to the power drawn by the load minus the power losses through the switch. The power transferred through the boost converter is approximately 12 W, which is equal to the battery power limit (19 W) minus the load power (6.6 W).

### 4.4.1.3 Passive HESS performance for pulsed load with 62 W peak

The second profile has a maximum amplitude of 62 W and a minimum amplitude of 9 W and a duty cycle of 20%. Figure 4.22 shows the results of the simulation for the passive HESS. We can note from the figure that the passive HESS reduces the peak power that the battery needs to provide. The peak power that the battery needs to provide is about 25 W, reduced from the 62 W drawn by the load. The peak power provided by the ultracapacitor is about 44 W.
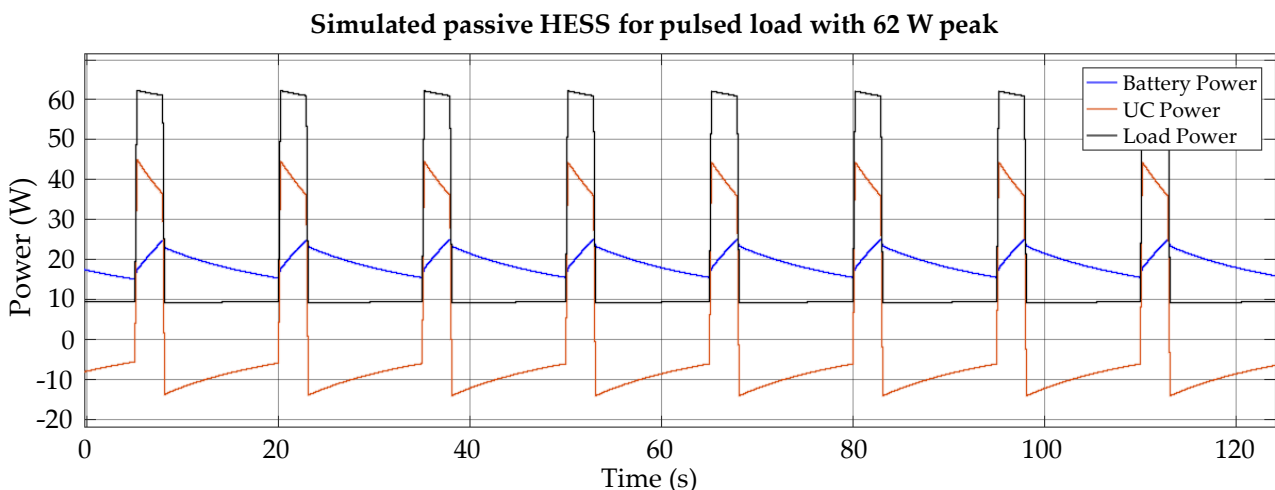


Figure 4.22: Passive HESS simulation for high pulse train

The peak power-sharing factor for this load profile between the UC and the battery is about 2:1. Comparing this factor to that of the other load profile, we can note that the peak power-sharing factor between the UC and the battery is dependent on the load profile. This factor is dependant on the duty cycle, frequency and amplitude of the load as noted in the literature study.

### 4.4.1.4 Active HESS performance for pulsed load with 62 W peak

The performance of the active HESS as simulated is shown in figure 4.23. As we can see from the figure below, the active HESS limits the power provided by the battery to the defined power limit for the battery. The power drawn from the battery is about 21 W, whilst the peak power drawn from

the UC is about 48W. As we can note from this graph the power provided by the battery is equal to the average power for the load profile plus the losses associated with the DC/DC converters.
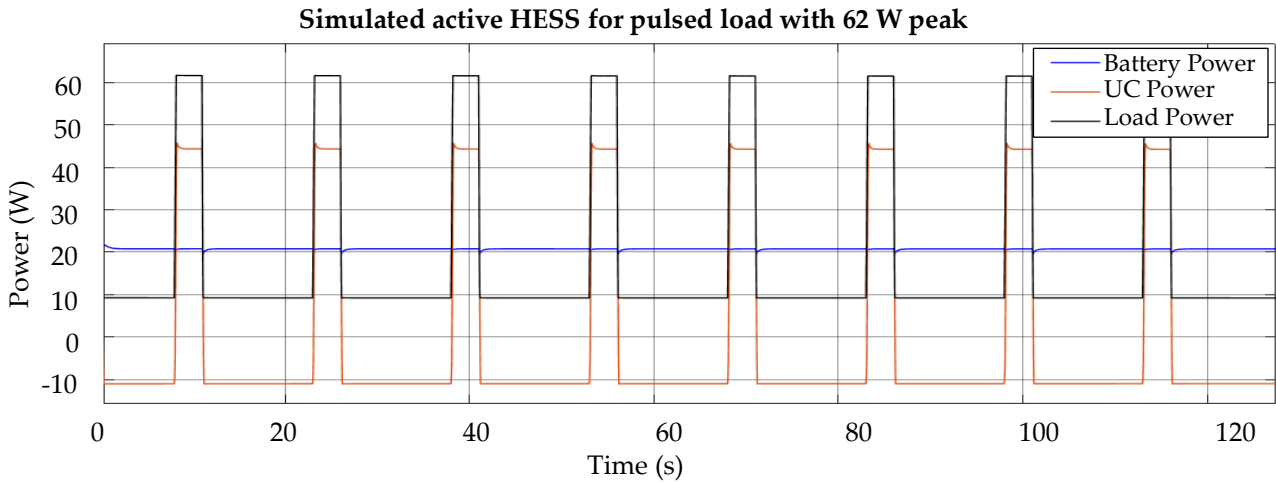


Figure 4.23: Active HESS simulated for high pulse train

The other graphs showing the boost converter power, power flowing through the switch and the operating mode of the controller is not shown, to avoid being redundant, seeing that this profile and operating modes is the same as that shown in figure 4.21, except for the first graph in that figure.

## 4.4.2 Drive cycles

In order to compare the performance of the passive and designed active HESS to a more realistic load profile, the NYCC, ECE 15 and WLTC class 2 drive cycle were used. The results of simulating the passive and active HESS are shown and discussed below.

### 4.4.2.1 NYCC Drive Cycle – Passive HESS

The results of the simulated passive HESS are shown below in figure 4.24. As we can see from the figure, the passive system reduces the peak power impulses experienced by the battery. The peak power drawn from the battery is 22.75 W, whilst the peak power provided by the ultracapacitor is 63 W.
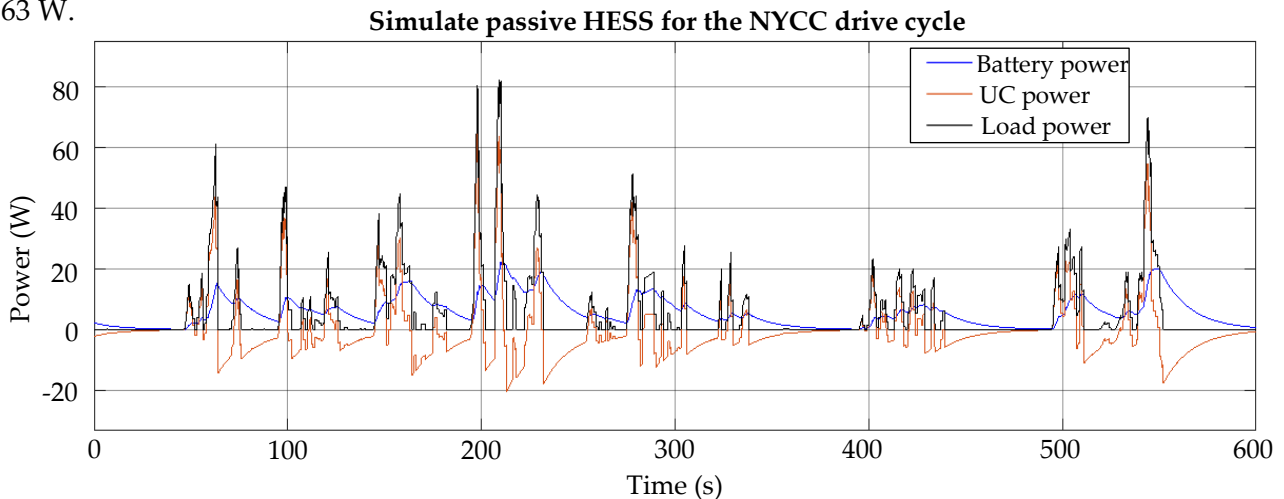


Figure 4.24: Simulated passive HESS for NYCC drive cycle

As previously stated, the UC functions as a low pass filter in the passive HESS and this is evident from figure 4.24. The power-sharing ratio between the ultracapacitor and the battery is dependent each devices' internal resistance.

## 4.4.2.2 NYCC Drive Cycle – Active HESS

Figure 4.25 shows the simulated performance of the active HESS. The active topology limits the power drawn from the battery to a defined limit of 10 W. This limit of 10 W was chosen so that the SoC of the UC is the same at the start and end of the cycle, therefore this limit is equal to the average power drawn by the load plus the losses associated with the DC/DC converters.

A zoomed-in portion of figure 4.25 is included in the figure to show the power flowing through the boost converter and the switch, as well as the operating mode of the controller. The red portion shown in figure 4.25 shows when the load power is higher than the user-defined power limit for the battery. The system operates in mode 5 according to the control rules for the overhead controller. The UC provides power to the load through the buck converter, whilst power is provided from the battery through the boost converter to the UC.

The blue portion shows the operation of the controller in mode 3. Seeing that the load power is lower than the battery limit, the battery is directly connected to the load. The battery also provides power to the UC through the boost converter at a rate equal to the difference in the defined power limit and the load power. As we can note from figure 4.26 the sum of the power provided by the boost converter and the switch at any point in time is equal to the defined limit of 10 W.
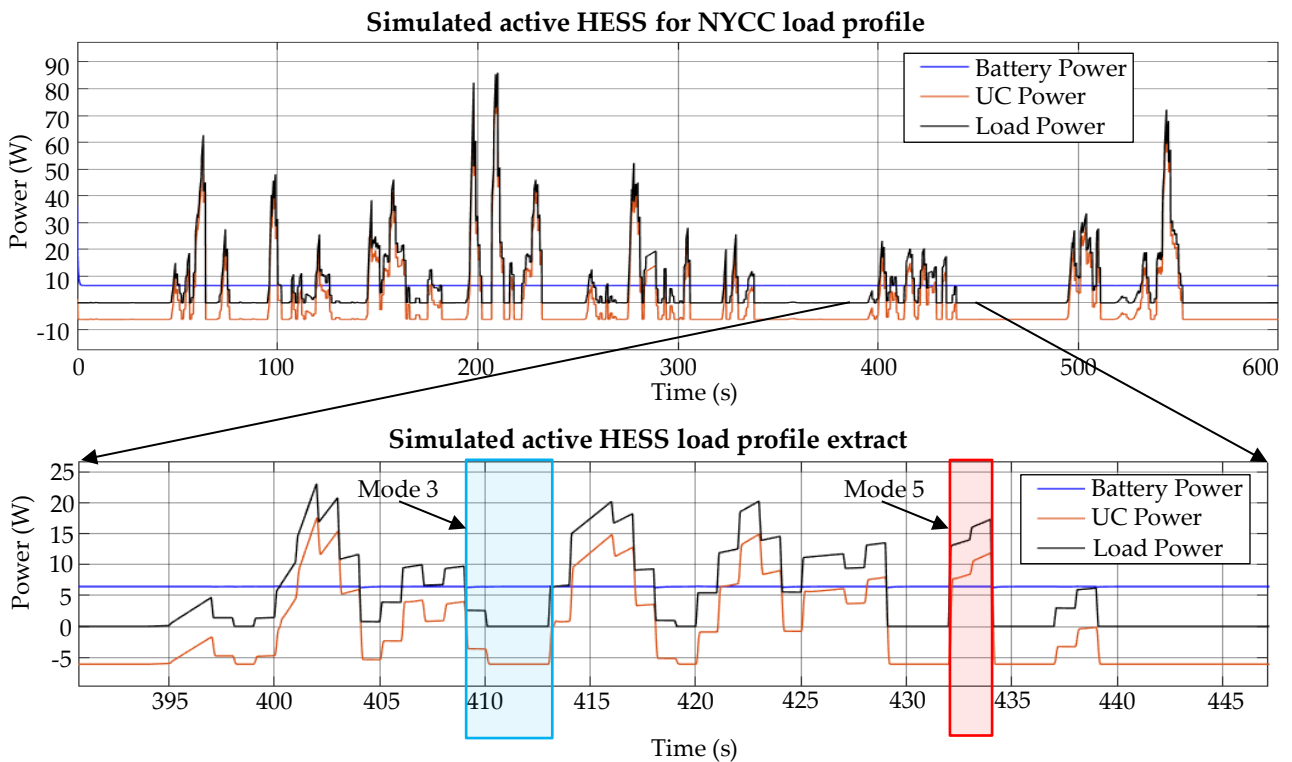


Figure 4.25: Simulated active HESS for NYCC load profile
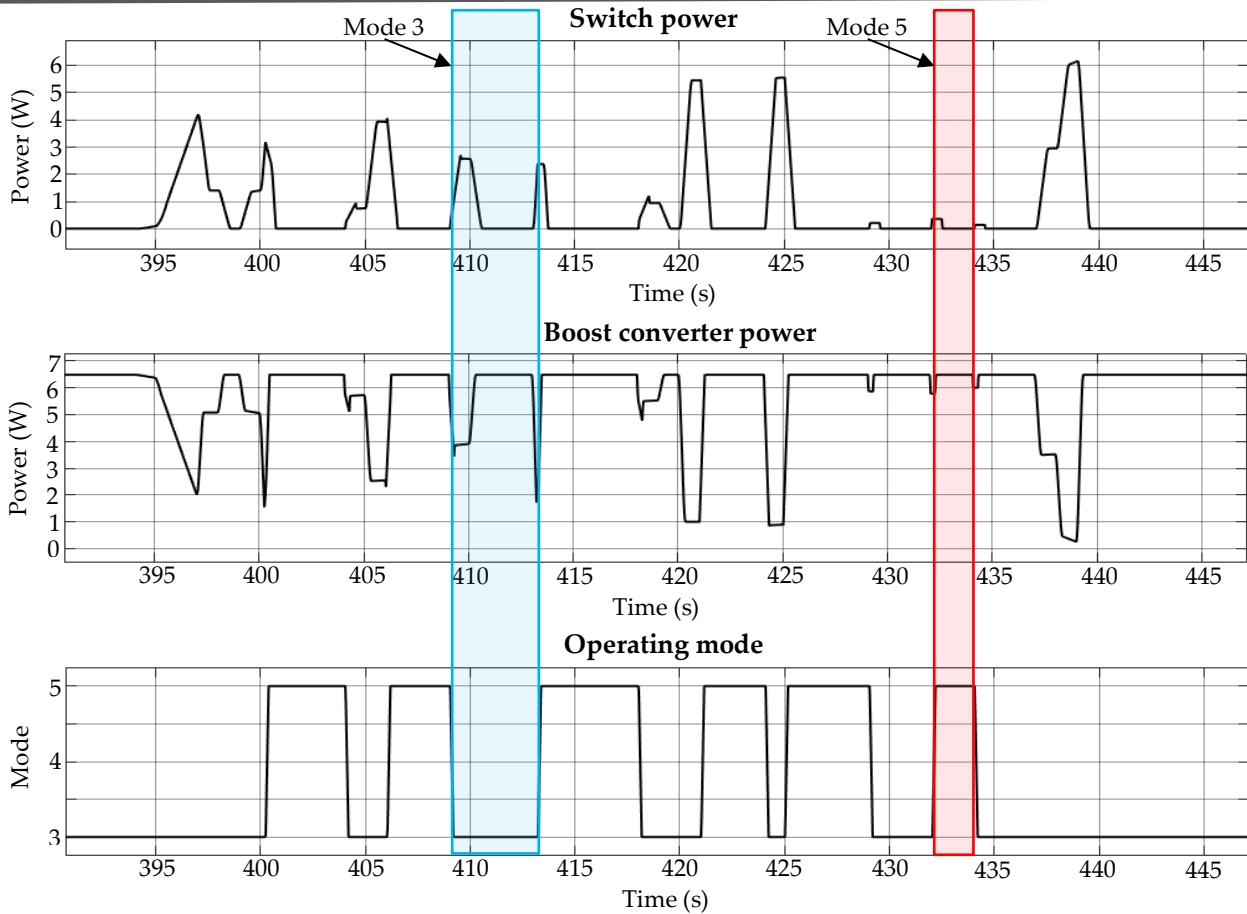
Figure 4.26: Simulated active HESS for NYCC load profile (continued)

### 4.4.2.3 ECE 15 Drive Cycle – Passive HESS

The performance of the passive HESS for the ECE 15 drive cycle was simulated and is shown below in figure 4.27. The ECE 15 profile has power-peaks with a higher sustained power draw than some of the other profiles, as highlighted by the red square in the figure. We can note from the profile that the UC provides power during the first part of these higher peaks, thereafter the battery starts to provide power to the load.
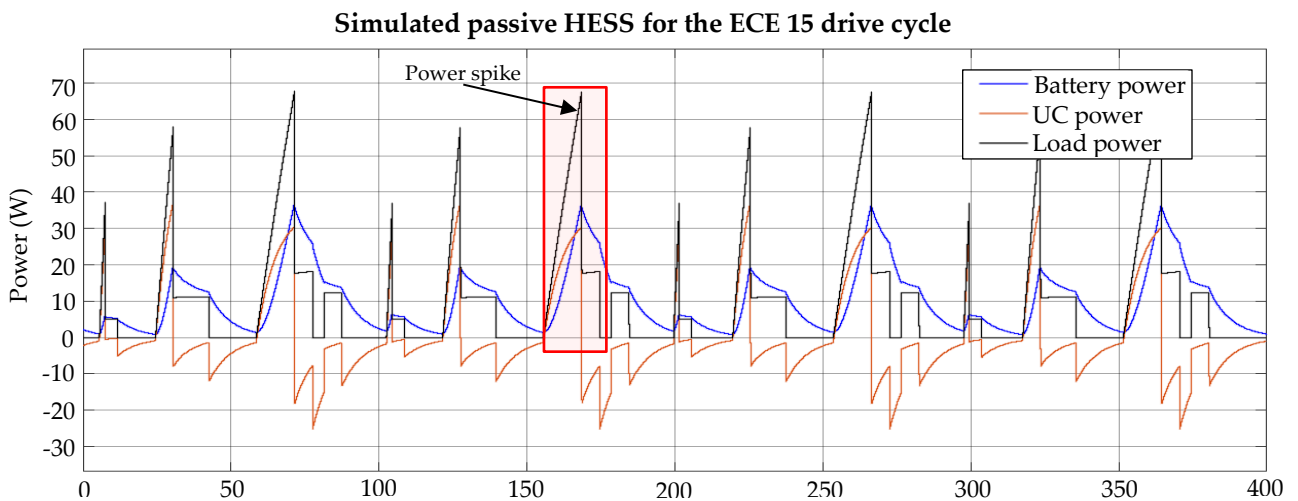


Figure 4.27: Simulated passive HESS for ECE 15 drive cycle

The peak power drawn from the battery by this load profile was 37.4 W, whilst the maximum power drawn by the load was 68 W. The passive topology does significantly reduce the peak-power requirements for the battery.

## 4.4.2.4 ECE 15 Drive Cycle – Active HESS

The power limit for the active topology was set to 10.44 W for the ECE 15 profile. As stated earlier, this power limit was chosen such that the SoC of UC is the same at the start and the end of the cycle, so that the cycle can, for example, be repeated until the battery is depleted. The simulated performance of the active HESS is shown in figure 4.28.
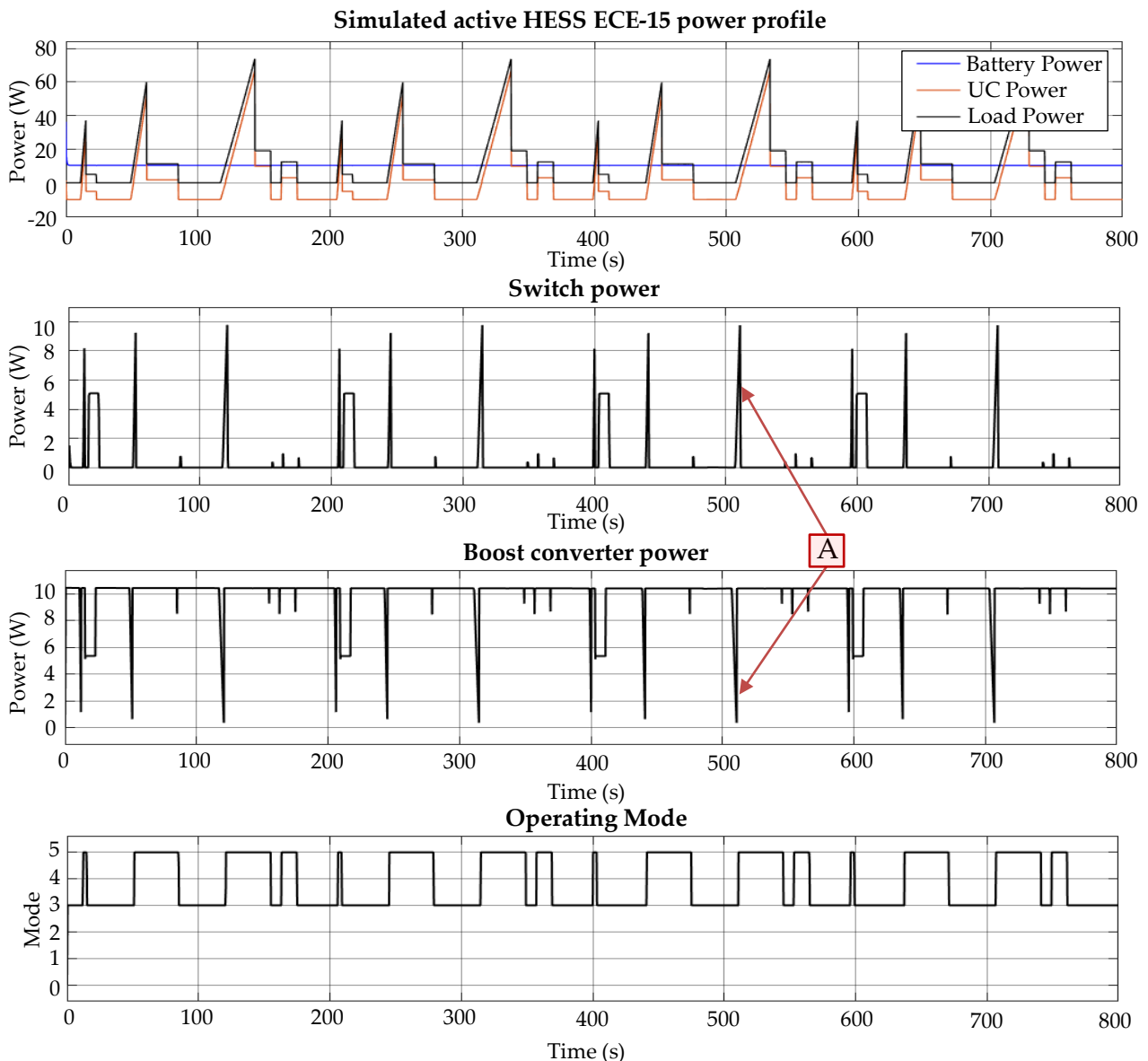


Figure 4.28: Simulated active HESS for ECE 15 drive cycle

The power transferred through the boost converter and switch as shown in the second and third graphs in figure 4.28 has some sharp short power spikes as noted by point A in the figure. This is simply due to the nature of the profile, the power of the load increases linearly and this power is provided by the switch, until the load's power draw is below the defined limit, at which point the

switch is disconnected and the boost converter provides power to the load. As has been discussed earlier, the ECE 15 profile is a synthetic drive cycle with more steady-state conditions compared to the NYCC and WLTC drive cycles. This profile is more representative of the load that for example a diesel truck may experience whilst driving from traffic light to traffic light in a city.

### 4.4.2.5 WLTC Class 2 Drive Cycle – Passive HESS

The simulated performance of the passive HESS for the WLTC class 2 drive cycle is shown in figure 4.29. The passive topology reduces the peak power drawn from the battery and reduces the power ripple experienced by the battery, but the battery still has to provide a large portion of the power, for example at point A in the figure. The battery provides 40 W of power to the load at the peak.
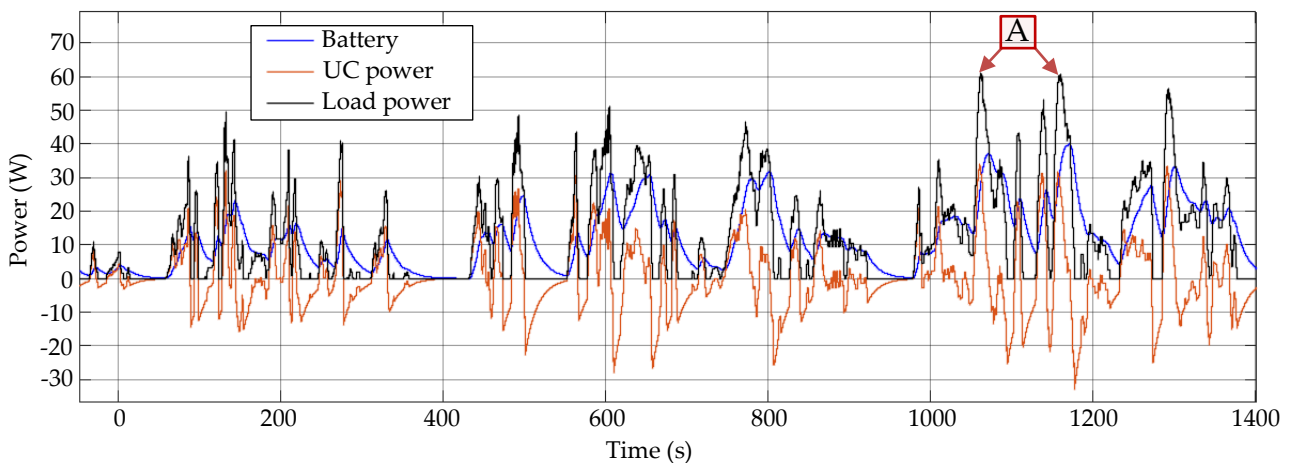


Figure 4.29: Simulated passive HESS performance for WLTC class 2 drive cycle

### 4.4.2.6 WLTC Class 2 Drive Cycle – Active HESS

The defined limit for the active topology was set to 9.2 W for this profile and the resultant power profile is shown in figure 4.30. We can note that the active topology drastically reduces the peak power that is drawn from the battery compared to the passive topology. The other graphs showcasing the power flow through the switch and the boost converter are not shown for this drive cycle just to reduce redundancy seeing that the two other drive cycles, as well as the pulse train load profiles, have shown how the power flows through the system.
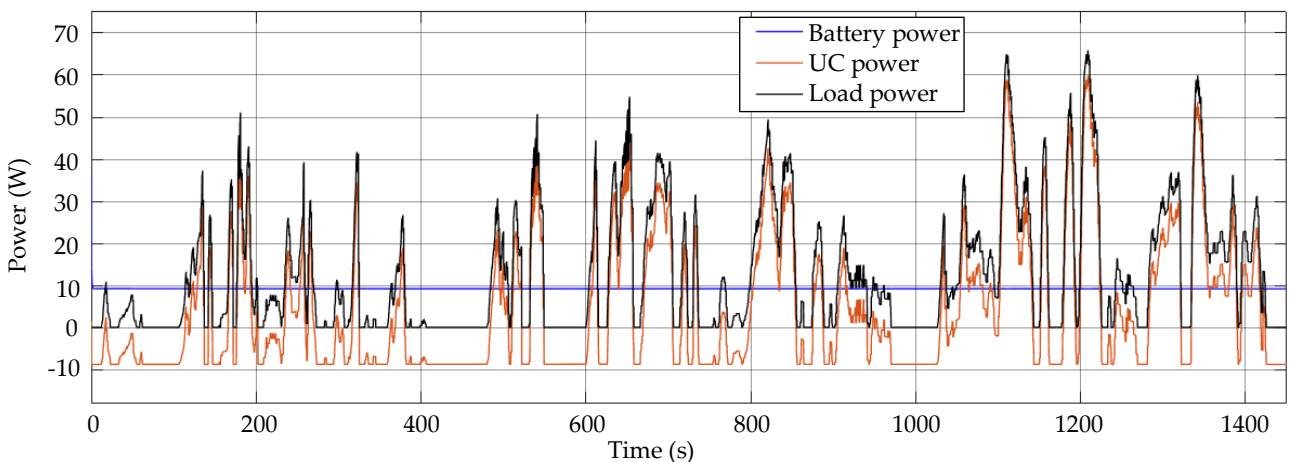


Figure 4.30: Simulated active HESS performance for WLTC class 2 drive cycle

## 4.5 Comparison

The performance of the passive and the designed active HESS is shortly compared in this section. The peak-power shaving of the passive and active topology was used to compare the systems performance to one another. Table 4.3 shows the comparison between the battery-only, the passive and active topology.

Table 4.3: Comparison of performance between battery-only, passive and active system

| | Battery-only | Passive HESS | | Active HESS | |
|---|---|---|---|---|---|
| | Peak power | Peak power | Percentage peak power reduction | Peak power | Percentage peak power reduction |
| **Pulse train 38 W** | 38 W | 21.4 W | 43.7% | 19 W | 50.0% |
| **Pulse train 62 W** | 62 W | 25.1 W | 59.5% | 21 W | 66.1% |
| **NYCC drive cycle** | 84.9 W | 22.75 W | 73.2% | 5.6 W | 93.4% |
| **ECE 15 drive cycle** | 74 W | 37.4 W | 49.5% | 10.44 W | 85.9% |
| **WLTC 2 drive cycle** | 65.2 W | 40 W | 38.7% | 12.4 W | 80.9% |

Figure 4.31 shows the peak-power that the battery needs to provide for each system. The battery-only system is shown in dark blue; the passive HESS is shown in red whilst the active HESS is shown in grey. We can note from the figure and the table that the passive HESS and active HESS reduces the peak power impulses, as we would expect. The passive and active HESS had the greatest improvement on the NYCC profile, reducing the peak-power experienced by the battery by 73.2% and 93.4%.
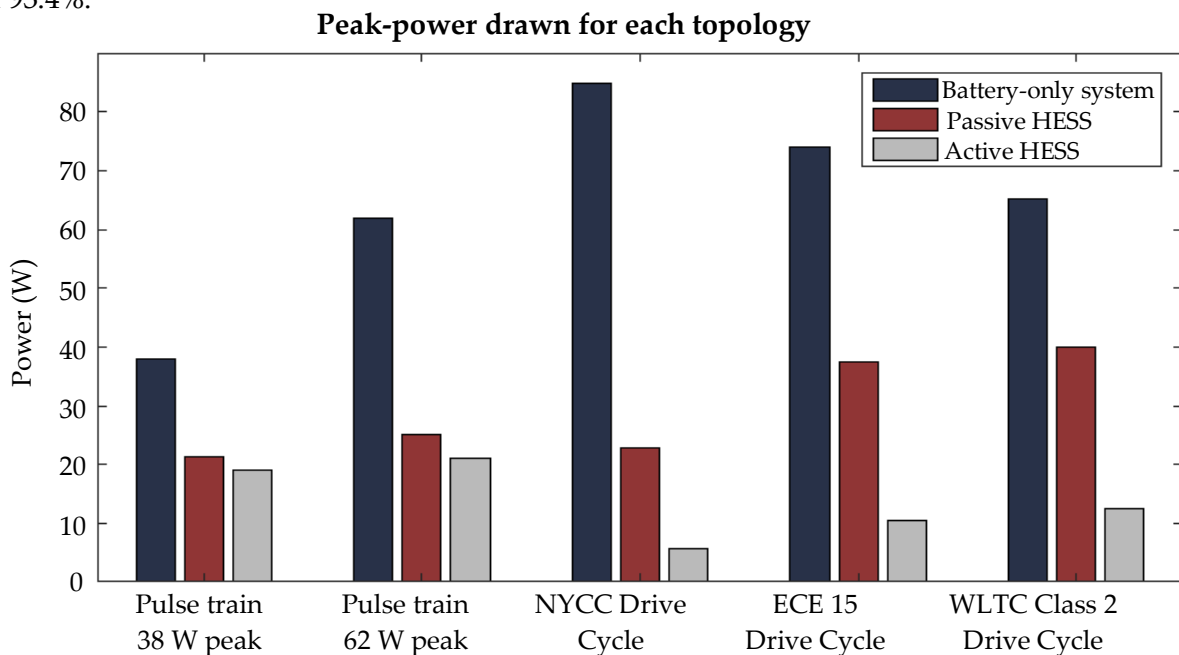


Figure 4.31: Peak-power drawn from the battery for the different topologies

The active HESS had the least peak-power reduction on the pulse train with the larger duty cycle and 38 W amplitude. The passive HESS had the least peak-power reduction on the WLTC class 2 load profile. Figure 4.32 compares the percentage peak-power reduction for the passive and active HESS for the different load profiles that were used. We can note that for the WLTC class 2 load profile that the active topology has a peak-power shaving percentage more than double that of the passive topology.
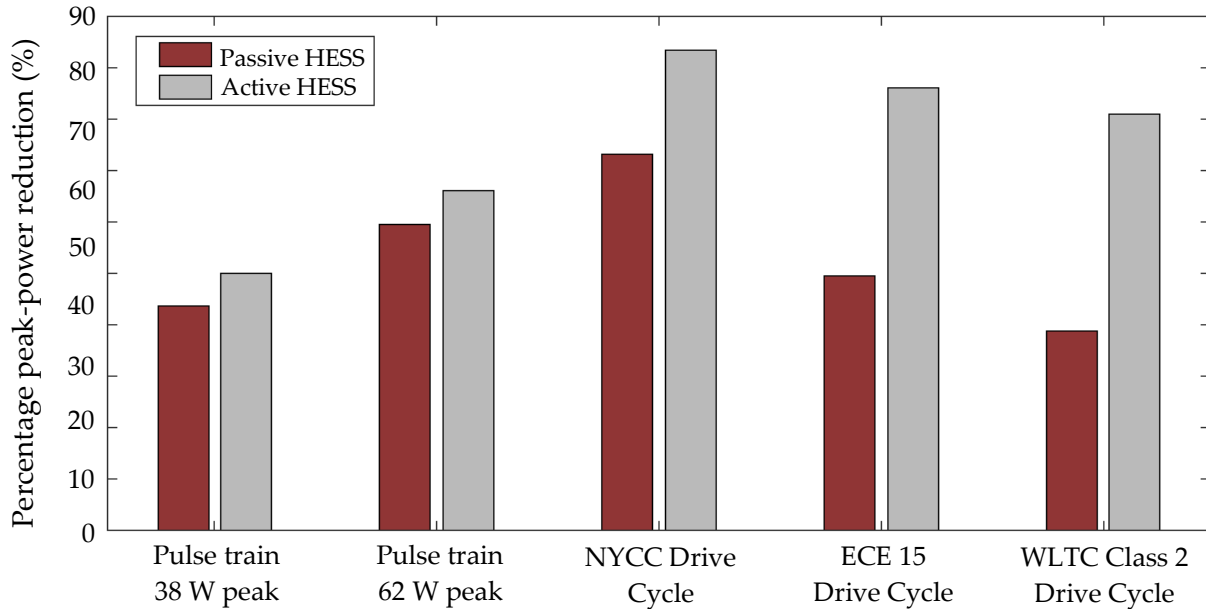


Figure 4.32: Percentage peak-power reduction (%)

For the pulse train loads, the active topology only improved on the peak-power reduction over the passive topology by 6.3% and 6.6% respectively.

# 4.6 Verification and validation

This chapter was used to verify the design calculations as was done in chapter 3. The design of the functional units was verified. The buck converter, boost converter and low pass filter were simulated and their designed parameters were verified. The fuzzy logic controllers that are used to control the buck and boost converter were also simulated to firstly verify the control layout of the controllers. The simulations were also used to verify that the designed fuzzy logic membership functions and rules were correctly chosen and defined.

The equations that were given in chapter 3 to calculate the power profiles from the drive cycles were also verified by comparing the power calculated for a specific profile to that calculated by other researchers for that specific profile [46], [144]. The overall design of the system was also verified in this chapter through simulation by verifying that the different sub-systems correctly interfaced with another and that the systems worked as designed.

The overall design of the system was also validated in this chapter. The goal of the designed active HESS is to reduce the peak-power drawn from the battery. This goal was validated by the simulation

of the overall system where the different load profiles were simulated. As shown throughout section 4.4 above, the simulated active topology reduces the peak-power drawn from the battery. The simulated overall system is validated in chapter 5 by comparing the simulated system and the practically implemented system.

# 4.7 Conclusion

The purpose of this chapter was to simulate the different functional units and the overall system in order to verify their design. These different functional units and the overall system were simulated in MATLAB®/Simulink®. The results of these simulations were documented in this chapter. The design of the buck and boost converter as well as the fuzzy logic controllers were verified. The performance of the passive HESS was compared to that of the designed active HESS. Different load profiles were used such as a pulse train load profile and the NYCC drive cycle.

The simulation results showed that the passive HESS reduces the peak-power drawn from the battery during these load profiles. The simulations showed that in the passive HESS topology, the UC functions as a low pass filter, reducing the power ripple and spikes on the battery. The power--sharing ratio between the UC and the battery is dependent on the internal resistance of each source and can therefore not be dynamically controlled. The active HESS improves on this by being able to control the power flow throughout the system. We can note from the simulations that the active HESS drastically reduces the peak-power drawn from the battery for the tested load profiles. We can note from the figures that included the power transferred through the boost converter and the switch that there is no delay in switching between different modes and the DC/DC converters instantaneously start to provide power.

Practically this would not be the case, as well as the system may oscillate between different modes seeing that the practically measured values for the SoC of the battery/UC and the power drawn by the load may not be that accurate. It is therefore important to implement some form of hysteresis control in the practical system. The next chapter discusses the practical implementation of the active HESS. The performance of the fuzzy logic controllers is documented in this chapter, as well as the performance of the practically implemented system. The simulated and experimental results are compared to one another in the next chapter.

# Chapter 5 – Experimental implementation

*This chapter discusses the experimental implementation of the designed active HESS. The physical setup of the active HESS is shown and discussed. The performance of the experimental system is documented in this chapter and briefly compared to the performance of the simulated system. Figure 5.1 gives an overview of what was done in this chapter.*
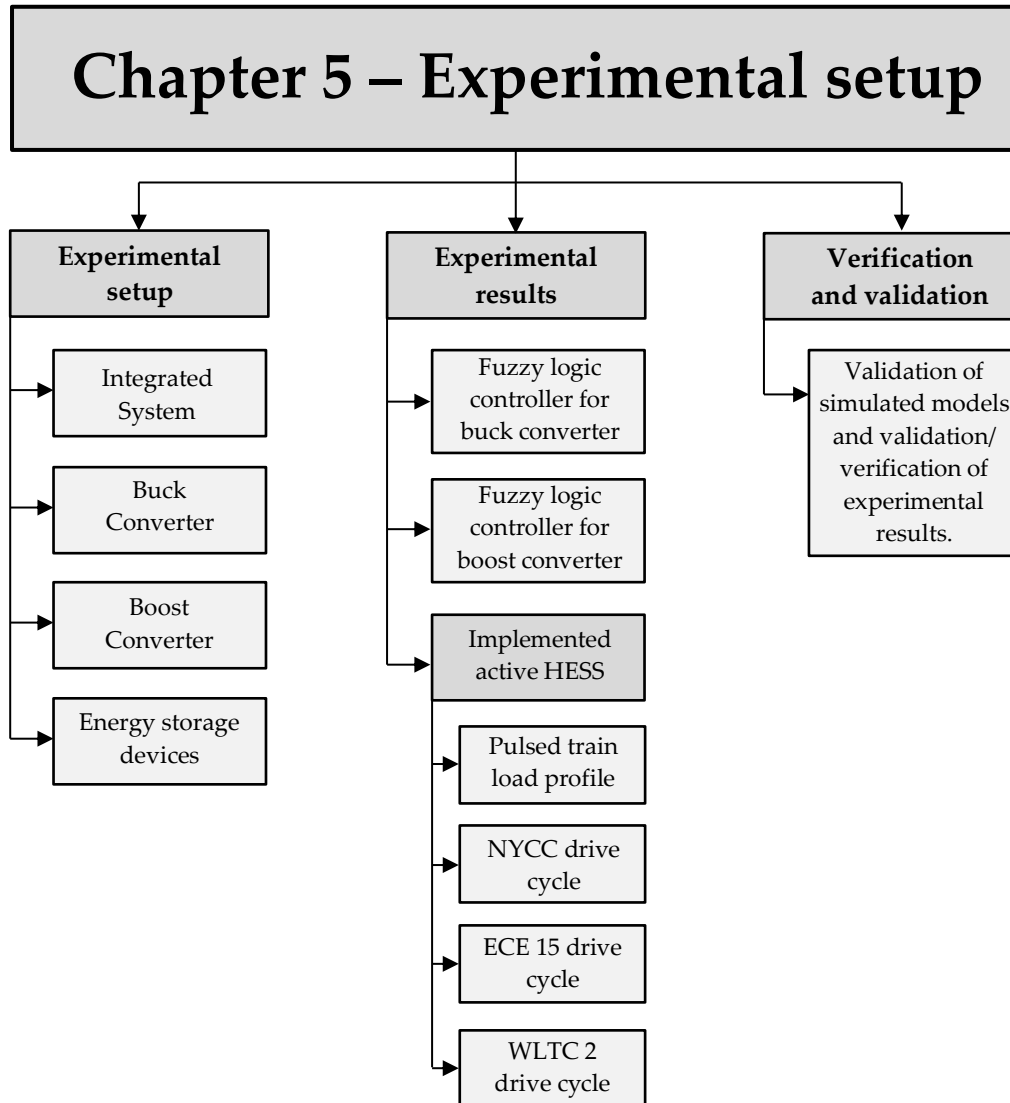


Figure 5.1: Chapter 5 overview

## 5.1 Experimental setup

This section documents the experimental setup used to further verify the design calculations of chapter 3 and to validate and verify the results obtained for the simulated model. As was stated in chapter 3, a PCB was designed to house most of the functional units in this project. All the functional units were first experimentally implemented on "protoboards" and breadboards to verify that they

were working correctly, before the functional units were implemented on the PCB containing all the functional units.

## 5.1.1 Integrated system

The integrated PCB used to interconnect all the functional units is shown below in figure 5.2. The buck converter, boost converter, current and voltage sensors, MOSFET drivers, voltage regulators and the low pass filter array are housed on the PCB. The PCB uses four phoenix screw terminals to interface with the programmable load, the battery, the ultracapacitor and to receive power from the 15 V bench power supply. The bench power supply is used to provide power to the MOSFET drivers as well as the LM 7805 voltage regulator which supplies a regulated 5 V output that is needed to power the shunt current monitor ICs. The IRF3205 MOSFET was used as the switch that connects the battery to the programmable load.
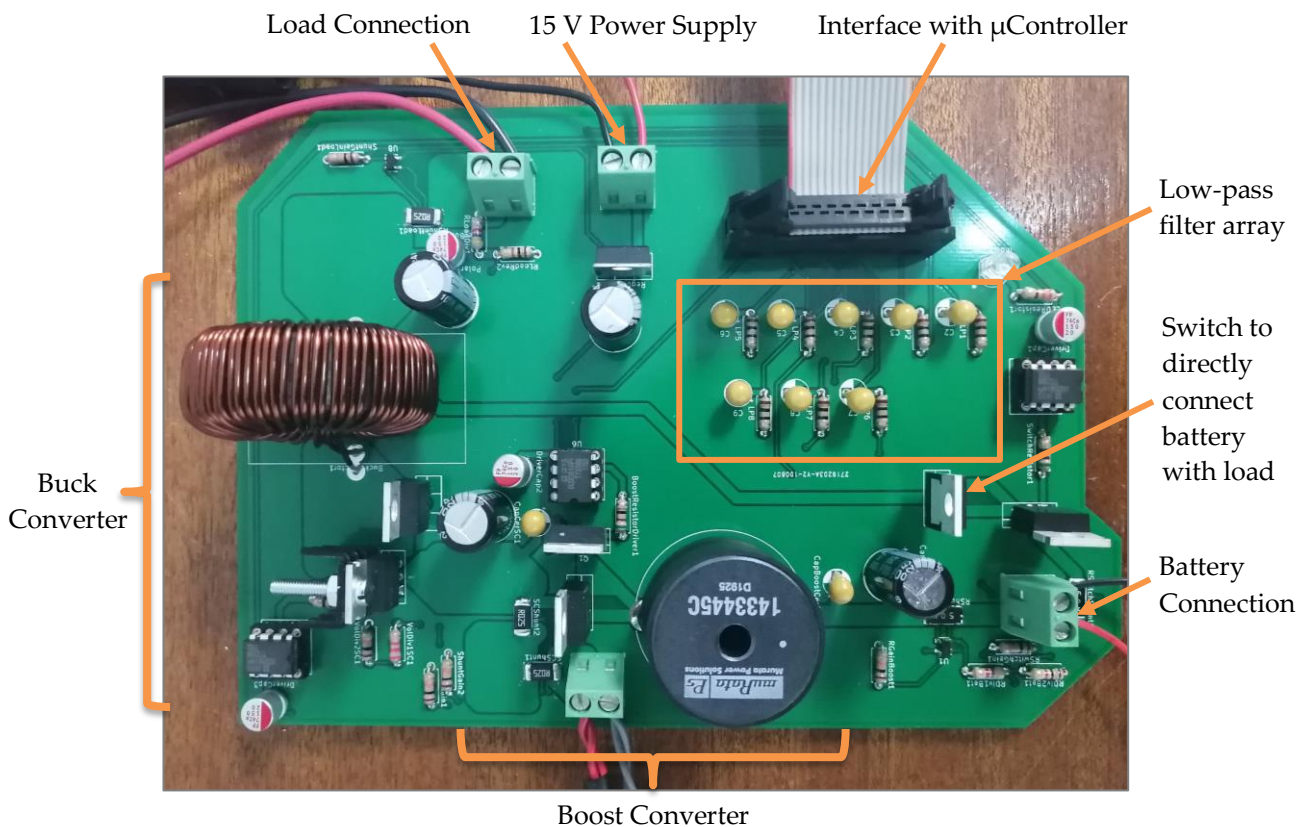


Figure 5.2: Implemented system on the PCB

## 5.1.2 Buck converter

The implemented buck converter section is shown below in figure 5.3. After the designed component values were practically implemented on a "protoboard" to verify that the values were correctly calculated, they were transferred to the PCB. As shown in the figure, a 150µH inductor was used, whilst the IRF4905 MOSFET was used as the switching device in the converter. The SBR40U switching diode was used seeing as this was an asynchronous buck converter.
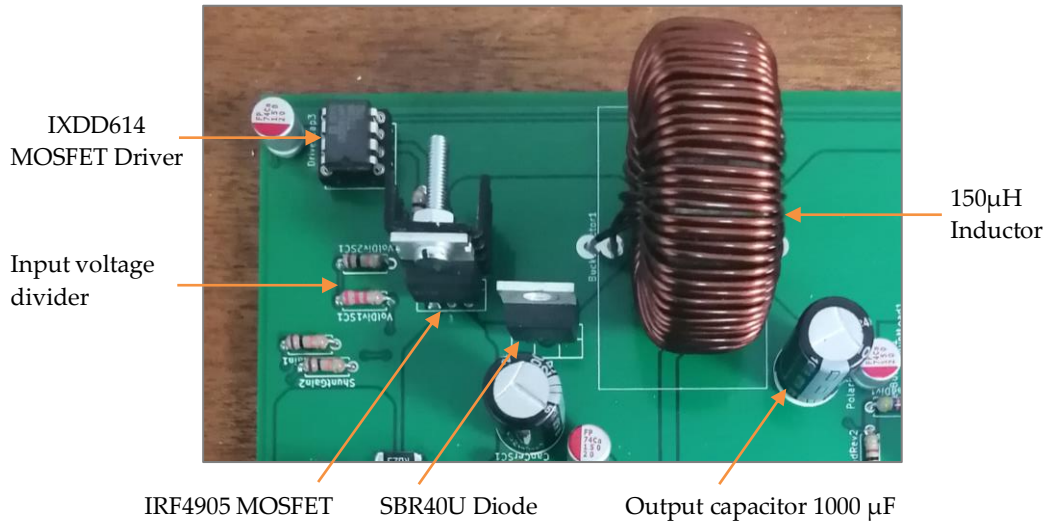
Figure 5.3: Implemented buck converter

The IXDD614 MOSFET driver was used to drive the IRF4905 MOSFET. An output capacitor with a capacitance of 1000 μF was used, compared to the simulated 470 μF capacitor, to reduce the output voltage ripple.

## 5.1.3 Boost converter

The boost converter as implemented on the PCB is shown in figure 5.4. Similarly to the buck converter, the boost converter was first implemented on a "protoboard". After verifying that the boost converter worked as designed, the components were soldered to the PCB.
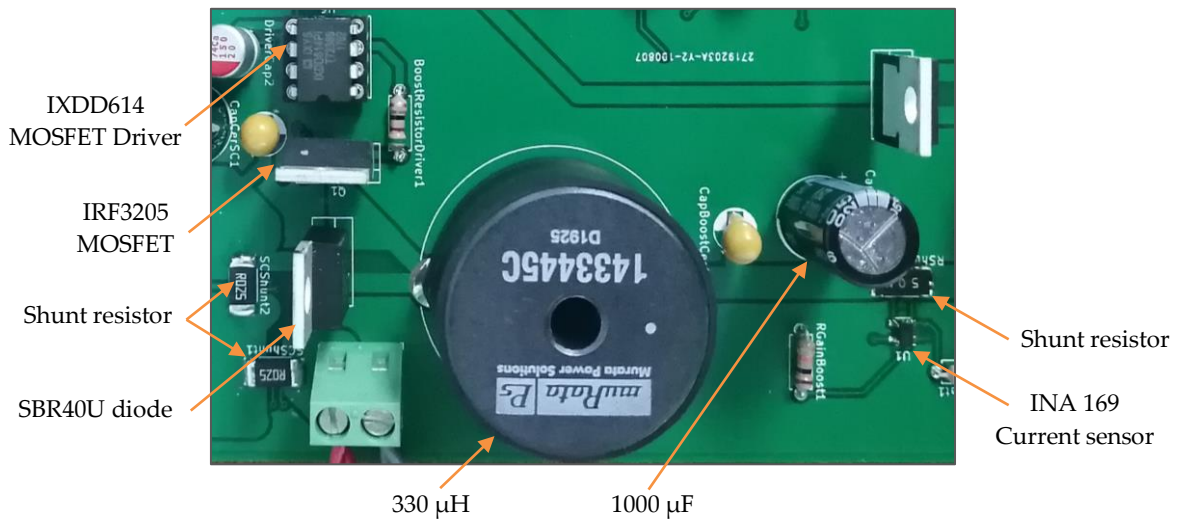


Figure 5.4: Implemented boost converter

An output capacitor with a capacitance of 1000 μF was used. The shunt resistors were used in conjunction with the INA 169 current sensors to measure the current flowing into the boost converter. The two shunt resistors on the left-hand side were used to measure the current flowing into and out of the ultracapacitor. The INA 169 is only capable of measuring unidirectional current flow, two INA 169 ICs and two shunt resistors were therefore required to measure the current bidirectionally. These two INA 169 ICs were mounted on the underside of the PCB due to layout constraints.

# 5.1.4 Complete system setup

The completed system setup used to experimentally implement and test the active HESS is shown in figure 5.5. As shown in the figure a laptop executing Simulink's Real-Time® environment is directly connected to the target hardware via a micro-USB cable. The target hardware was the STM 32 Nucleo F767ZI microcontroller.
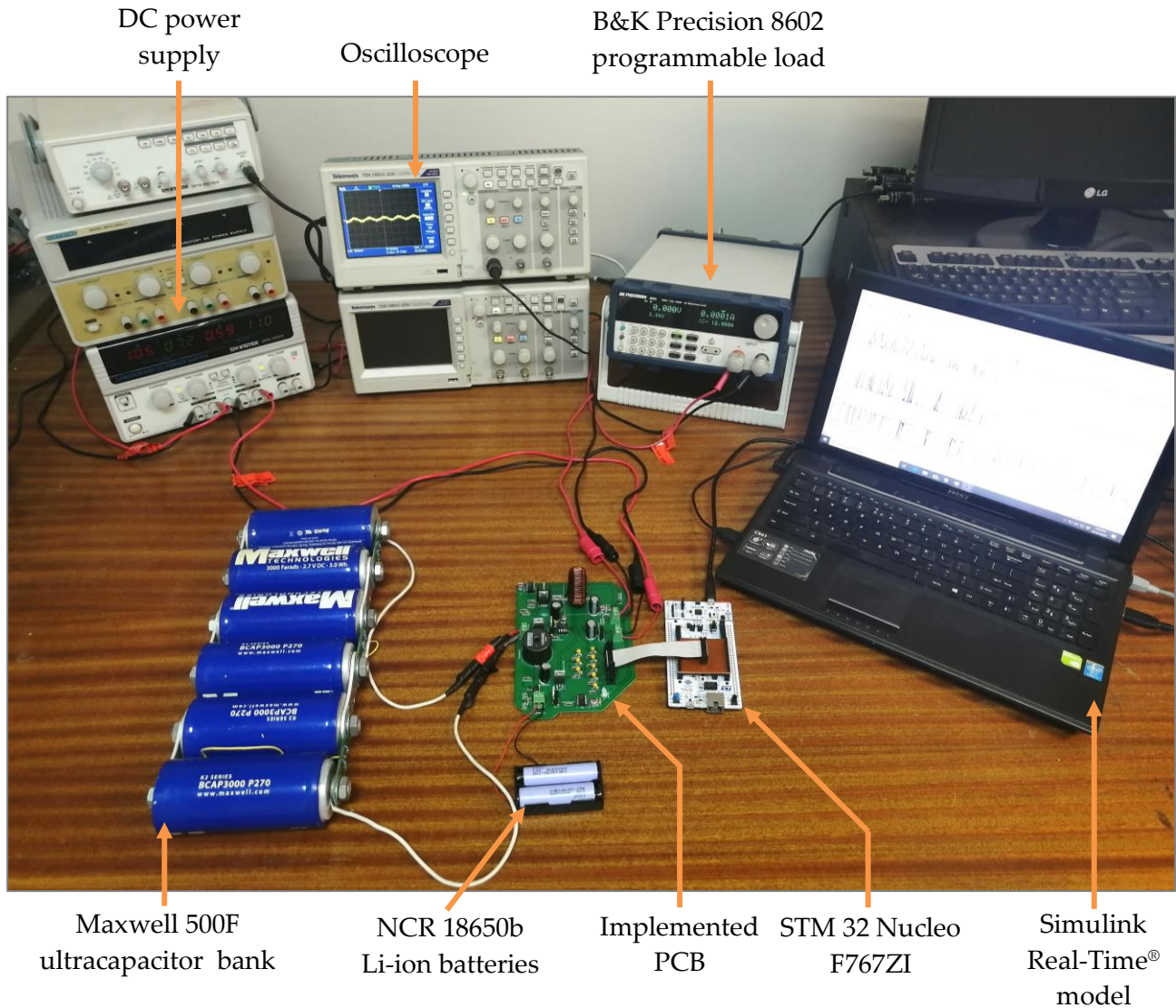


Figure 5.5: Complete system setup

As was discussed in chapter 3, two NCR 18650b batteries from Panasonic were used, each with a capacity of 3200 mAh and a nominal voltage of 3.6 V. The 18650 Li-ion batteries were used seeing that they are similar to the batteries that were first used in production electric vehicles, such as the Tesla Roadster and the Tesla Model S. Tesla has since switched over to a 21700 battery cell, which has a slightly larger volume. These batteries also utilize different lithium chemistries, with improved energy and power density. Nonetheless, the NCR 18650b batteries were used, seeing that they are widely available.

The UC bank from Maxwell that was used had a capacitance of 500 F with a voltage rating of 16.2 V. The UC bank consists out of 6 cells connected in series, each with a capacitance of 3000F and a maximum voltage of 2.7 V. The size of the UC bank also doesn't have a big influence on the performance of the active HESS, seeing that the SoC of the UC should be the same at the start and end of each load cycle. The UC bank should be sufficiently sized that it is able to store enough energy to provide power when the controller operates the system in mode 5 so that the SoC of the UC does not drop below 25% during any point in the load cycle. A capacitor bank with a lesser capacitance could have been used, but this size UC bank was used seeing that it was already available at the research laboratory.

The Simulink® model used to experimentally implement the active HESS is shown in figure 5.6. The sensor input blocks utilize the add-on package for the Nucleo F767ZI in Simulink® to utilize the analog-to-digital converters in the Nucleo. The look-up tables that are connected to the output of the analog-to-digital blocks are used to convert the measured values to the actual value, for example to a current or voltage value.

The fuzzy logic controllers as shown in the red blocks, control the duty cycle of the PWM signal applied to the buck and boost converter. The overhead controller outputs the reference voltage for the buck converter and the reference power for the boost converter. The buck and boost converter enable output ports in the overhead controller are used to drive the output PWM signal to zero to disenable the buck and boost converters, depending on the operating mode.

The B&K Precision 8602 programmable load was used to practically emulate the load profiles that were simulated in chapter 4. B&K Precision provides software to interface with the programmable load. The software provided can unfortunately only store 100 data points, which was not enough data points to accurately represent some of the load profiles. In order to accurately emulate these load profiles, the external analog port was utilised. This port allows one to control the electronic load from zero to full-scale rating with a 0 – 10 V input signal. This was implemented by using a MOSFET driver and MOSFET connected to pin D6 as shown in figure 5.6 to control the load via this input signal. This MOSFET driver and MOSFET were implemented on a breadboard, but are not shown in figure 5.5.

The time block was used to implement a delay during the start-up of the system wherein both the buck converter and boost converter are disabled. The time block was also utilised to implement hysteresis control to prevent the system from oscillating between different modes. A hysteresis delay of 200 ms was implemented before the system is allowed to switch between operating modes. This delay was found practically to be sufficient and prevented the system from oscillating between operating modes.
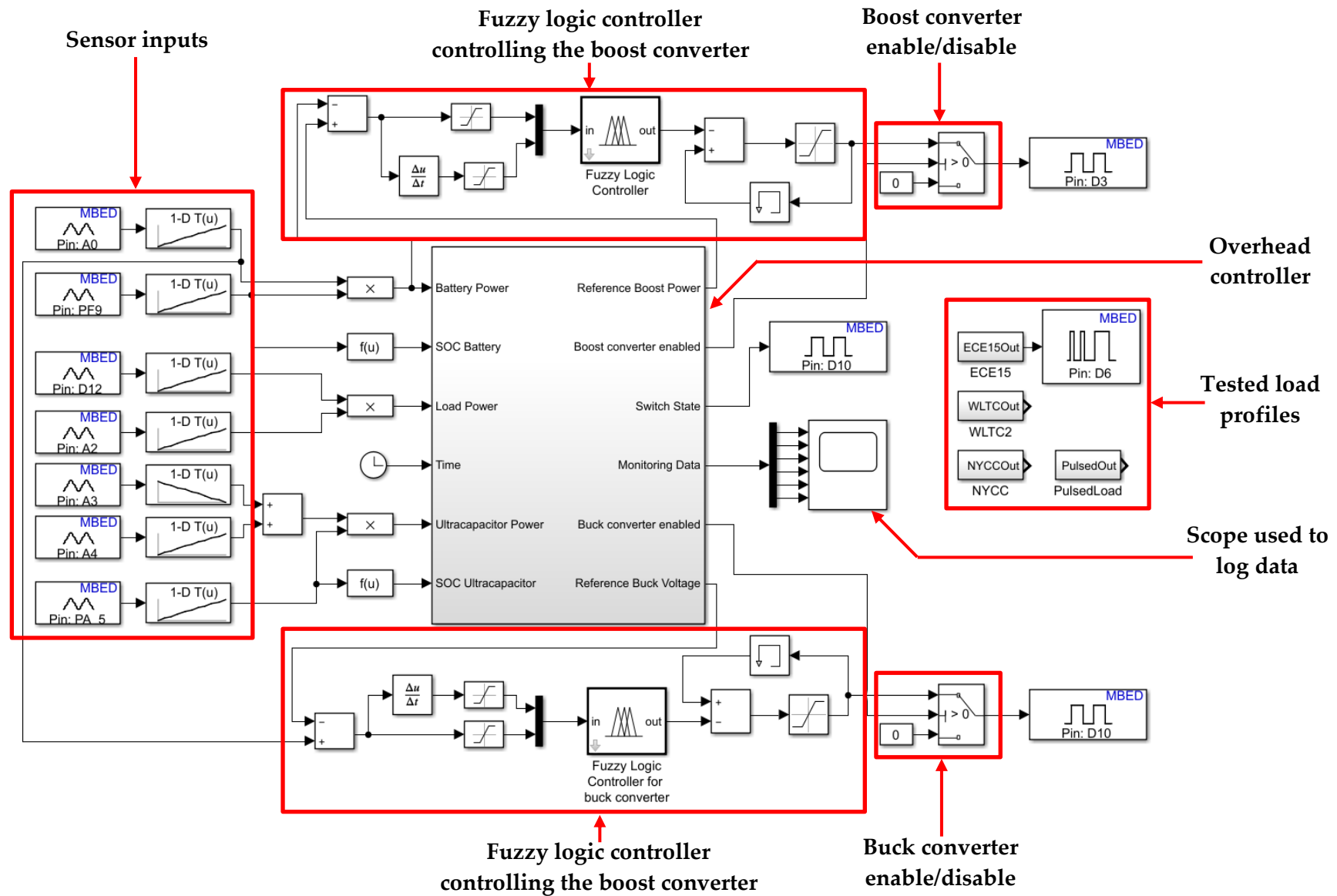
Figure 5.6: Experimental MATLAB®/Simulink® Model

# 5.2 Functional unit testing

## 5.2.1 Buck converter

The experimentally implemented buck converter as shown in figure 5.3 was practically tested to verify the performance of the converter. Figure 5.7 compares the analytical, simulated and experimental output voltage of the buck converter against the duty cycle.
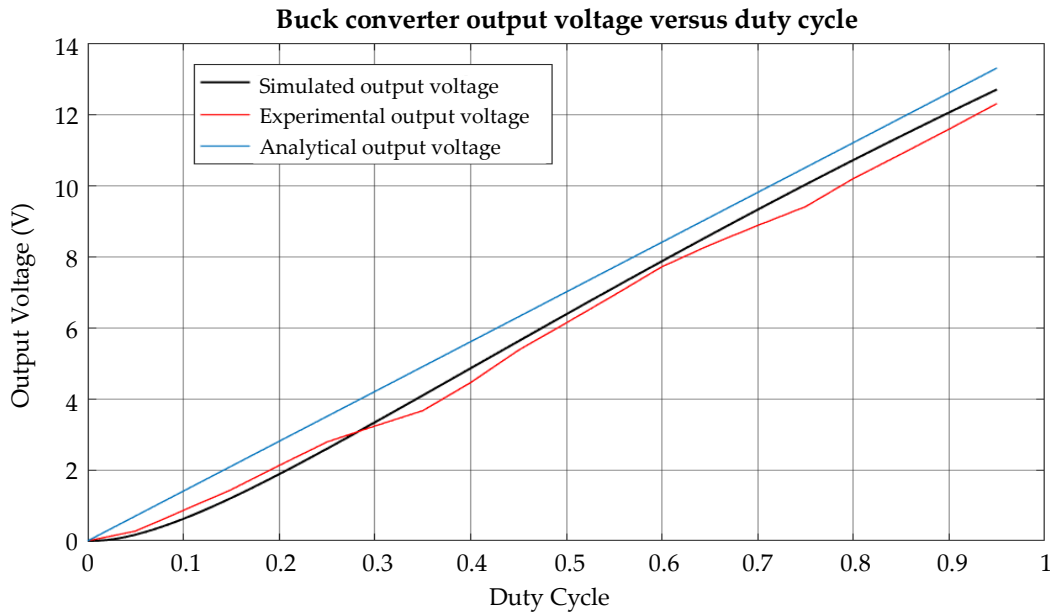


Figure 5.7: Buck converter output voltage versus duty cycle

As we can see the output voltage of the experimentally implemented buck converter was approximately equal to that of the simulated buck converter. Figure 5.8 shows an oscilloscope screenshot of the voltage over the inductor relative to ground in orange. The blue waveform shows the input current going into the buck converter.
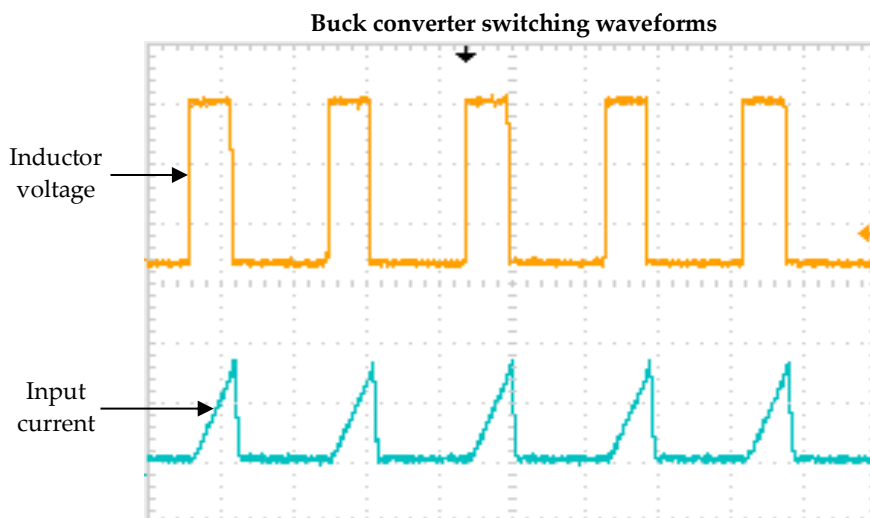


Figure 5.8: Buck converter switching waveform as measured on oscilloscope

## 5.2.2 Boost converter

The performance of the boost converter was verified by experimentally comparing the performance of the boost converters output current to the simulated values. Figure 5.9 gives a comparison of the analytical, simulated and experimental performance of the boost converter.
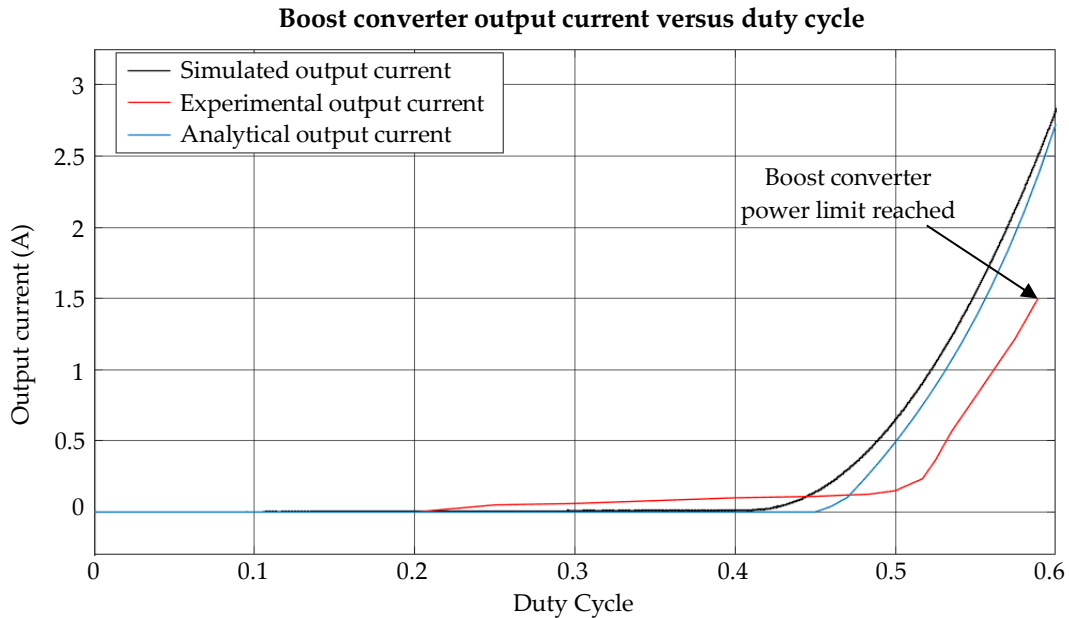


Figure 5.9: Boost converter output voltage versus duty cycle

Figure 5.10 shows an oscilloscope screenshot of both the switching waveform to the gate of the MOSFET and the second waveform shows the current through the inductor at full load. This was done to verify that the value for the inductor was correctly calculated so that the inductor operated in continuous conduction mode at full load. As we can note from the waveform, the inductor current never drops to zero.
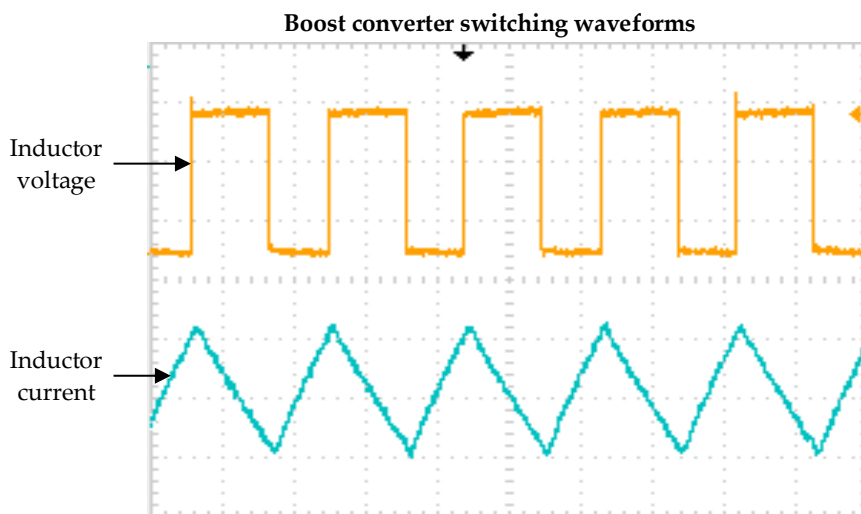


Figure 5.10: Boost converter switching waveform as measured on oscilloscope

## 5.2.3 Fuzzy logic controller for buck converter

The fuzzy logic controller controlling the buck converter was the first functional unit that was tested. The physical implementation of the buck converter is shown in figure 5.2. As discussed in previous sections, the buck converter operates in a constant voltage mode, keeping the output voltage equal to that of the battery's voltage. In order to verify that the fuzzy logic controller is able to control the output voltage of the buck converter, the reference voltage was set to step from 6 V to 7 V and then from 7 V to 8 V. The range of 6 V- 8 V was chosen seeing that the nominal voltage operating range is within these two values. The output voltage versus the reference voltage of the buck converter is shown in figure 5.11. The programmable load was set to a certain resistance value, to sink the power outputted by the converter.
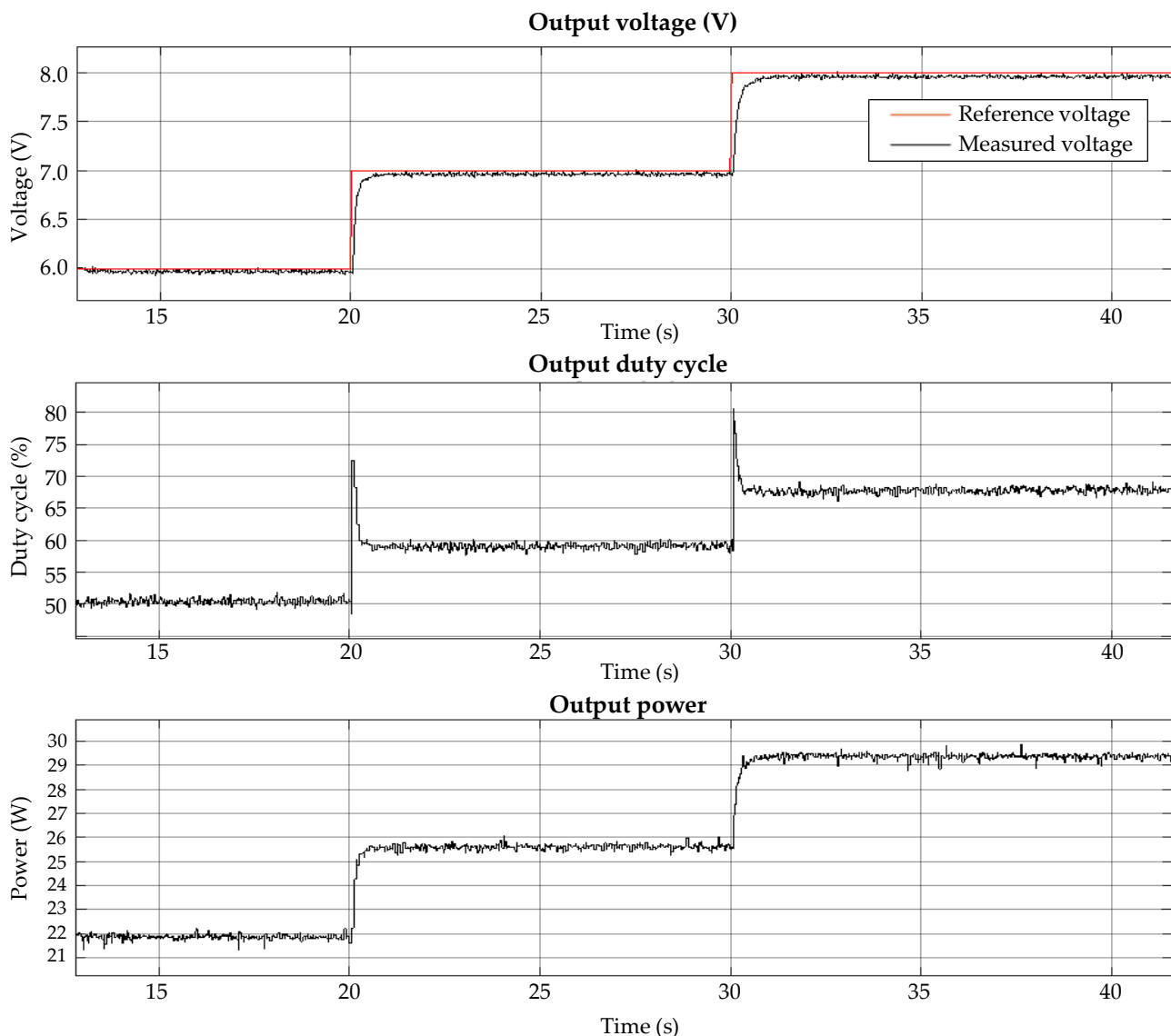


Figure 5.11: Practical buck converter voltage step response

The rise time for the output voltage to step from 6 V to 7 V is 240 ms. The signal has a steady-state voltage of about 6.97 V, resulting in a steady-state error of 0.43%, which is within acceptable limits and exhibits no overshoot. This steady-state error could simply be the result of an inaccurate

measurement or that the defined range for the error membership function in the fuzzy logic controller responding to "zero change" was set too wide.

Nonetheless, the fuzzy logic controller is able to adequately control the output voltage of the buck converter. The reader may also note that the output voltage has a somewhat slow rise as it nears the reference voltage. The output gain block associated with the fuzzy logic controller block was adjusted in order to attempt to reduce overshoot in the output voltage. The second graph shows how the fuzzy logic controller changes the output duty cycle as the reference voltage changes. The third graph just shows the power drawn from the buck converter at the different reference voltages, as the programmable load was set to sink an arbitrary current of 3.6A during the test.

Although the above test showed that buck converter is able to control the voltage of the buck converter, the buck converter would normally maintain the output voltage at the same voltage as that of the battery, but the load on the buck converter would change.
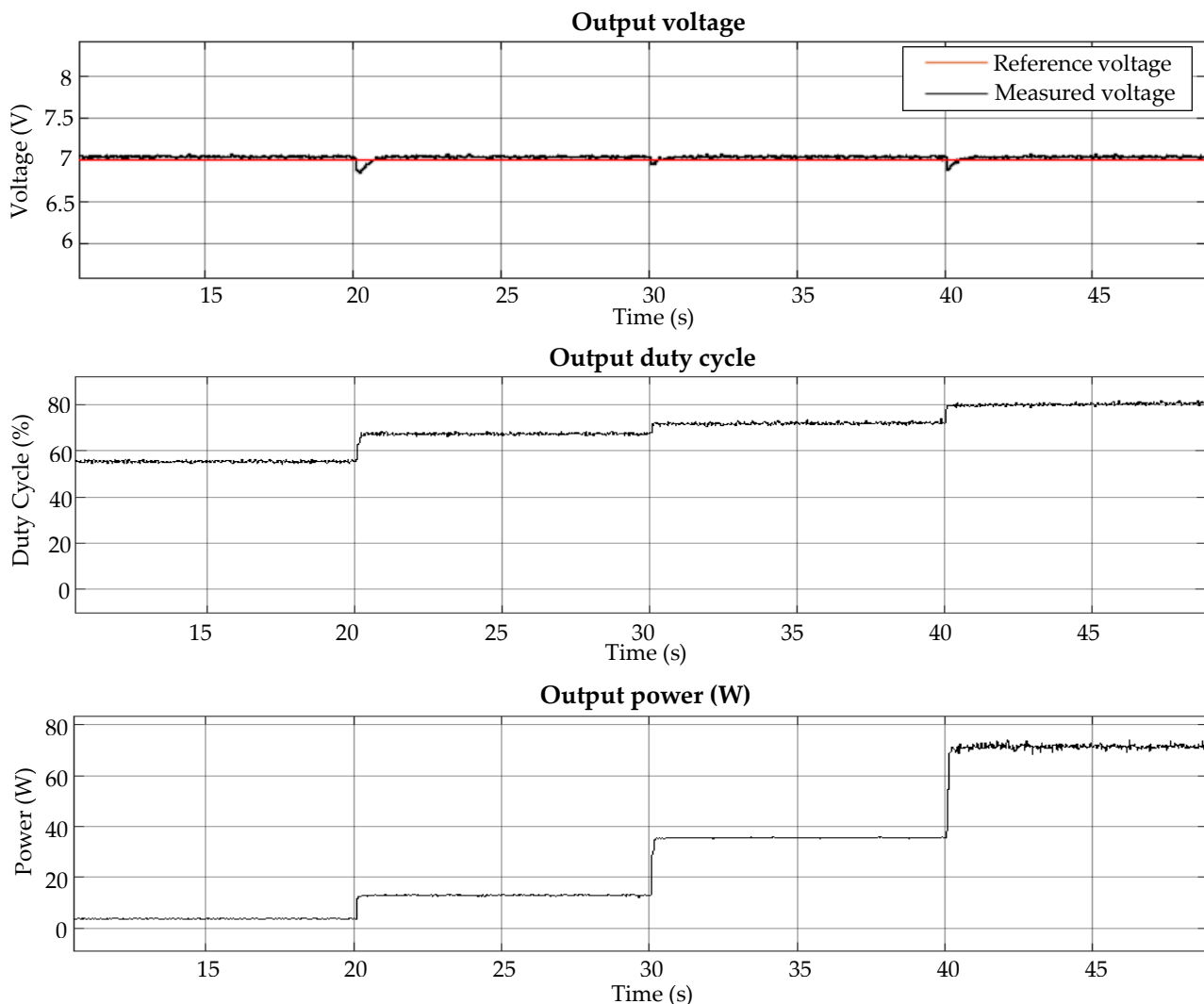


Figure 5.12: Practical buck converter response for step in output power

To verify this, the buck converters output was set to a constant voltage, whilst the power drawn by the load was stepped by an arbitrary value. The results of this test are shown in figure 5.12. The

load power steps from 4 W to 13 W at t = 20 s; 13 W to 36 W at t = 30 s and then from 36 W to 73 W at t = 40 s, whilst the reference voltage was set to 7 V.

## 5.2.4 Fuzzy logic controller for boost converter

The performance of the fuzzy logic controller controlling the boost converter was tested. The location of the boost converter on the designed PCB is shown in figure 5.3. Seeing that the boost converter is used to control the flow of power from the battery to the UC, the reference power was stepped to test the performance of the fuzzy logic controller. The reference power was stepped from 2.8 W to 7 W at t = 20 s and then from 7 W to 14 W at t = 30 s. Figure 5.13 shows the performance of the boost converter. The second graph shows how the duty cycle changes as the required power throughput changes.
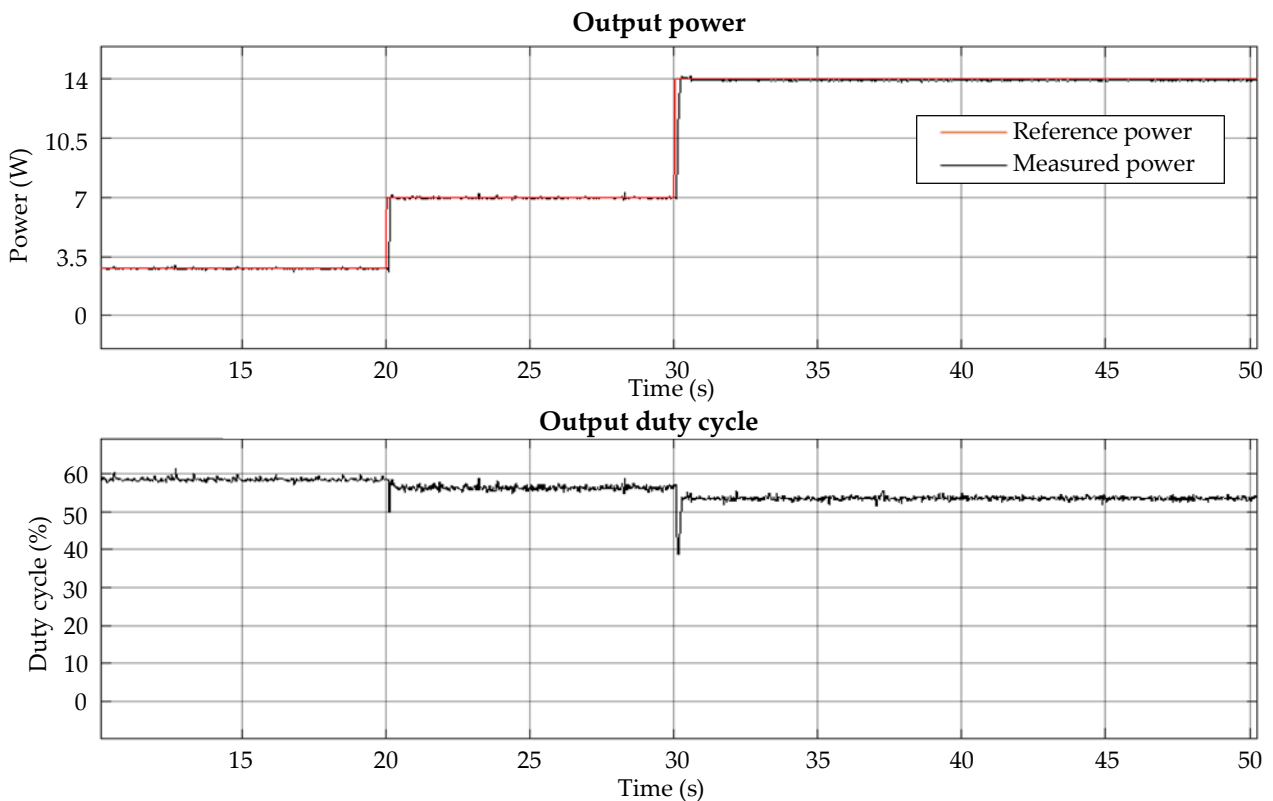


Figure 5.13: Practical boost converter step response

We can note from the above figure that the boost converter is more sensitive to changes in the duty cycle compared to the buck converter. The boost converter requires a higher resolution of control than the buck converter. The overshoot when the reference power steps at t = 30 s is 2.4% with a steady-state error of 0%. The rise time for the output power was 110 ms. Using an error band of 1%, the settling time for the output power was 400 ms.

## 5.2.5 Fuzzy logic controller comparison

This section comparers the performance of the simulated and practically implemented fuzzy logic controllers. The different performance values such as the rise time, overshoot and settling time are shown in table 5.1. As we can note from table 5.1, the experimental implementation of the fuzzy logic controller had a longer rise time and settling time compared to the simulated fuzzy logic controller. The overshoot of the experimentally implemented system was comparable to the simulated system.

Table 5.1: Fuzzy logic controller comparison

|  | Simulated boost converter | Experimental boost converter | Simulated buck converter | Experimental buck converter |
|---|---|---|---|---|
| **Rise Time** | 8 ms | 110 ms | 4.8 ms | 240 ms |
| **Overshoot** | 2.1% | 2.4% | 2.4% | 0% |
| **Settling Time** | 15.1 ms | 400 ms | 8.1 ms | 870 ms |

The large difference between the simulated controller and the results obtained for the practical system was found to be caused by the sampling time of the STM32 F767ZI as practically implemented in Simulink®. The sampling time of the microcontroller through Simulink® was found to be approximately 2.5 ms. The simulated model used a discrete-time model, with a sampling rate for the simulation model of 2 us. It was also experimentally found that as the complexity of the simulated model increased, the performance of the controller degraded, as one would expect.

The performance of the fuzzy logic controllers controlling the boost and buck converters practically could be improved on by increasing the sampling time. It is thought that the slow sampling time for the microcontroller is either caused by complexity of the Simulink® model, which apart from requiring the microcontroller to execute the model, requires the microcontroller to communicate the measured values to the Simulink® target computer or this slow-down is caused by a software limit in the STM32 ADC blocks. The source code for these blocks is unfortunately closed-source and cannot easily be viewed/altered.

Although the performance of the practically implemented systems was not as good as the performance of the simulated system, the practically implemented fuzzy logic controllers were still able to control the output voltage and output power respectively. The same microcontroller was therefore used as it would be able to control the flow of power throughout the system, although not as effective as the simulated system.

## 5.3 Overall system implementation

This section documents the performance of the experimentally implemented active HESS. This section shows the performance of the system tested against the different load profiles. The different operating modes described in chapter 3 were also tested.

### 5.3.1 Pulse train load

The pulse train with an amplitude of 38 W and duty cycle of 36% was tested first. This was the same pulse train load profile that was used during the simulation process. The results of the test are shown in figure 5.14. Figure 5.14 contains three different graphs. The first graph shows the power flow from the battery to/from the UC to the load. The second graph shows the power flowing through the switch whilst the third graph shows the power supplied by the load.
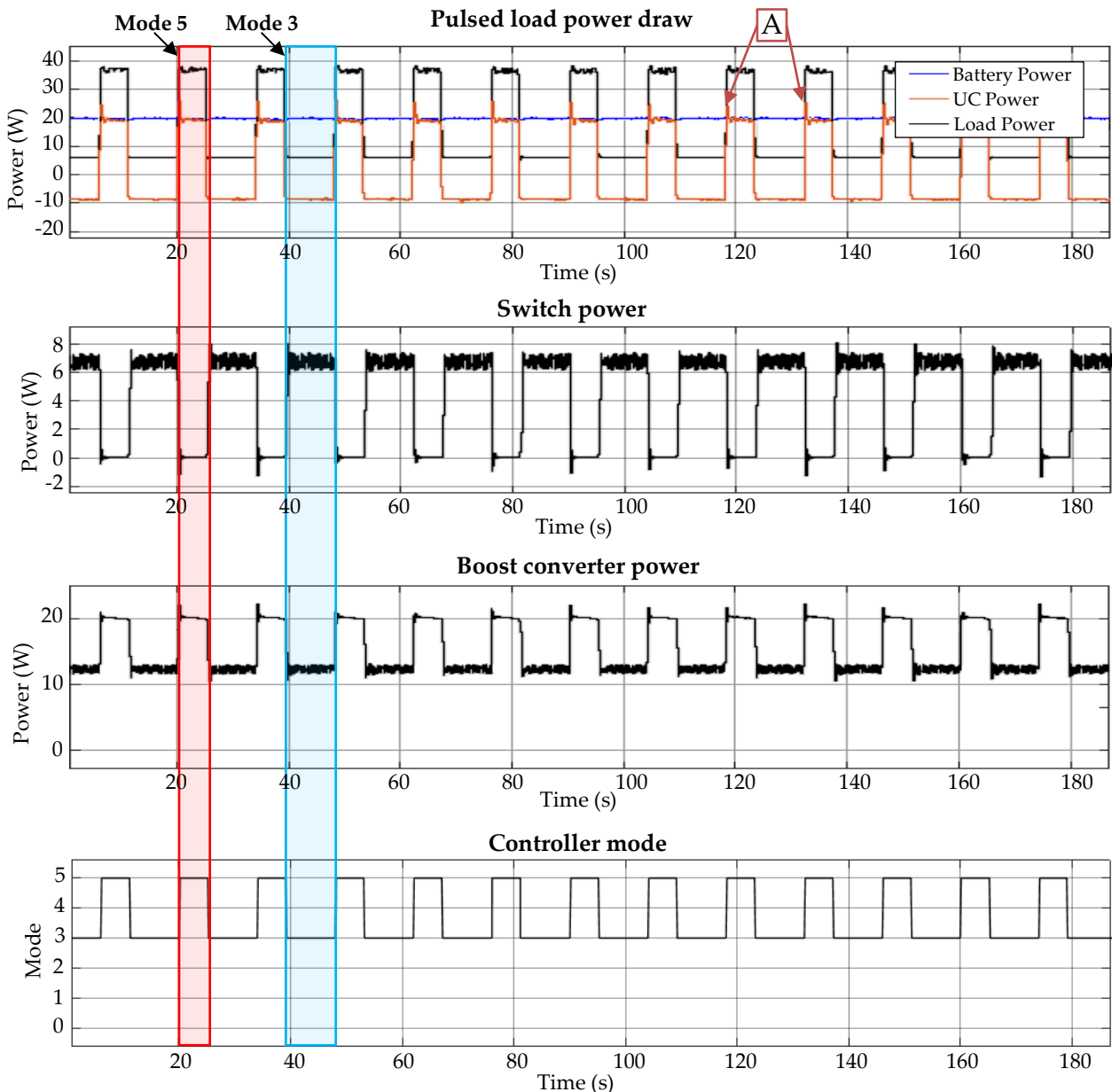


Figure 5.14: Experimental system results for pulse train load with 38W peak

We can firstly note from the figure that the designed system is able to control the power flow throughout the system and limits the power provided by the battery to the user-defined limit. We can also note how the overhead controller switches between the different modes of operation, depending on the load's power draw. As shown by the red portion, when the load's power draw is above the defined limit, the system switches to mode 5 in which the UC provides power through the buck converter to the load. The boost converter transfers power from the battery to the UC at the defined power limit, which in this case was 20.5 W. This power limit was required to ensure that the SoC of the UC was the same at the start and end of the cycle, which would allow the system to provide power to the load profile until the battery is depleted. No power is provided through the switch to the load.

When the load power drops below the defined limit, as shown in the blue portion, the system switches to operating mode 3 in which the battery provides power directly to the load. In this mode, the battery provides power to the load and if the SoC of the UC is between 25% and 95%, the battery charges the UC so that the total power drawn from the battery is equal to the power limit.

The reader may note that the power provided by the UC to the load has a high peak as pointed out by point A in figure 5.14. This is the result of the overshoot caused by the fuzzy logic controller controlling the buck converter. The buck converter's duty cycle is set to zero during mode 3 when no power is to be transferred from the UC through the buck converter to the load. When the system then switches to mode 5, the fuzzy logic controller changes the duty cycle so that the output voltage of the buck converter is equal to that of the battery. This large step-change results in the overshoot as observed in figure 5.14. Comparing the performance of the fuzzy logic controller in this case to that as discussed above in section 4.2.1, we note that the controller did not exhibit any overshoot when first tested.

This variance was found to be a result of a slowdown in the performance of the controller as implemented on the STM32 Nucleo. The tests that were done in section 5.2 only deployed the fuzzy logic controller, ADC and the necessary logging block to the microcontroller. Once the additional fuzzy logic controller block was added for the boost converter, the other ADC converter blocks, DSP blocks as well as all the required scope blocks to log the data, the performance of the fuzzy logic controller degraded, due to the increased overall computational load on the microcontroller. Although the fuzzy logic controller block did not perform as well as it did when it was first tested, the performance was still deemed satisfactory, seeing that it was still able to adequately control the flow of power. The overshoot could also be exaggerated by the programmable load, which at the same time is attempting to sink the specified amount of power, as the output voltage of the buck converter changes from 0 V to the reference voltage.

The second pulse train load profile was tested next and the results are shown below in figure 5.15. The user-defined power limit for the battery was set to 23.5 W. The controller sufficiently controls the power flow throughout the system and limits the power drawn from the battery. The UC provides power through the buck converter to the load when the loads power draw is above the

defined limit. The battery provides power to the load through the switch when the load's power draw is below the defined limit.
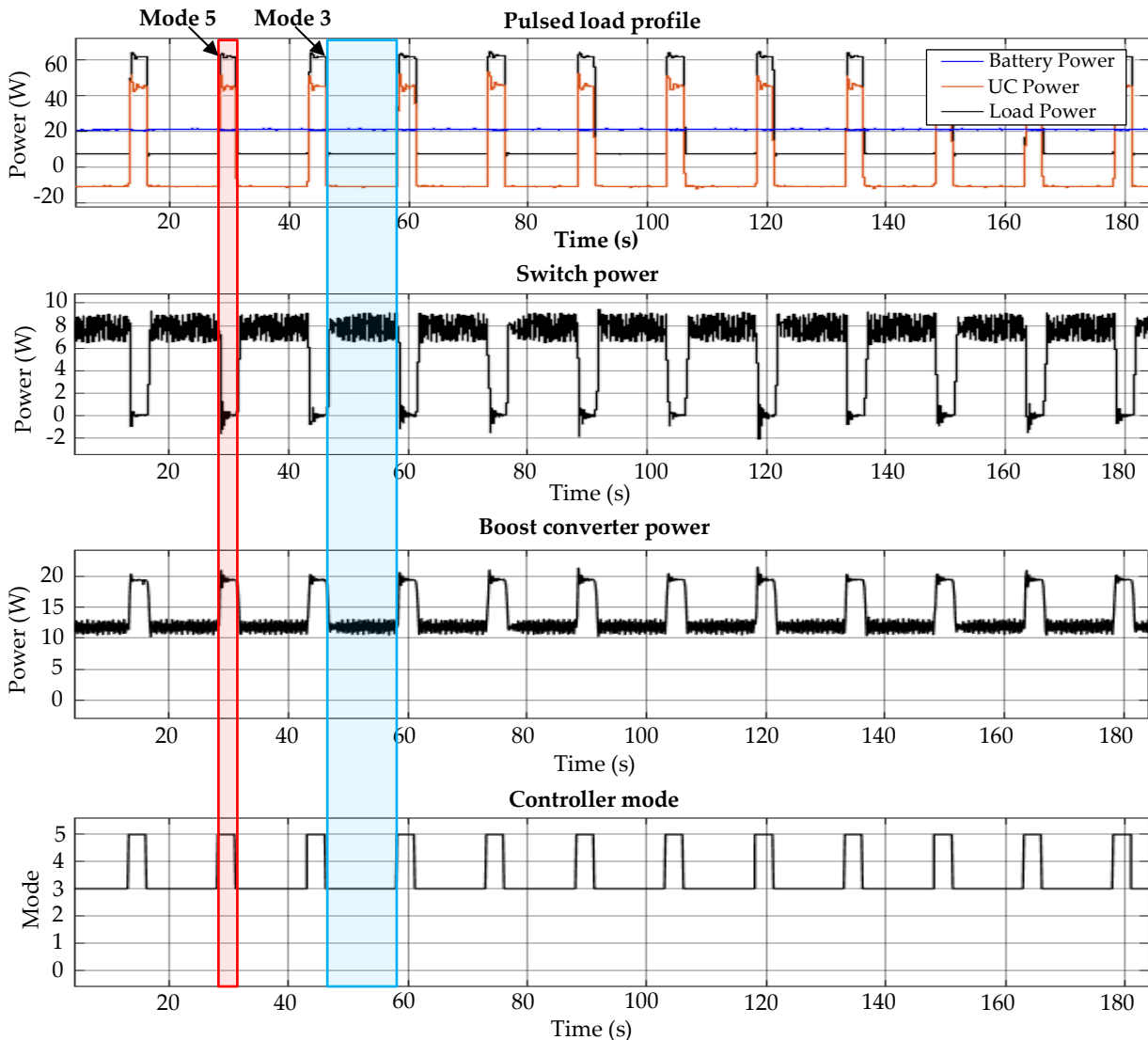


Figure 5.15: Experimental system results for pulsed train load with 62 W peak

As has been shown for the previous load profiles, the blue portion in figure 5.11 shows when the system operates in mode 3, with the battery providing power to the load and the UC. The red portion shows when the system operates in mode 5, providing power to the load from the UC through the buck converter, whilst the battery charges the UC.

## 5.3.2 NYCC drive cycle

The power profile developed from the NYCC drive cycle was also used to test the performance of the practically implemented system. The user-defined power limit was set to 8.4 W. This power limit was chosen such that after the duration of the drive cycle, which is 600 s, the SoC of the UC is at the same level at the start and the end of the profile. Figure 5.16 also shows the SoC of the UC during this load profile, to illustrate the statement made above.

As we can note from the results, the defined power limit had to be increased when compared to the limit used in the simulations. This was due to the losses associated with the DC/DC converters in the topology. The power limit that was required for the experimental system was 8.4 W whilst the power limit utilized for the simulated system was 5.6 W.
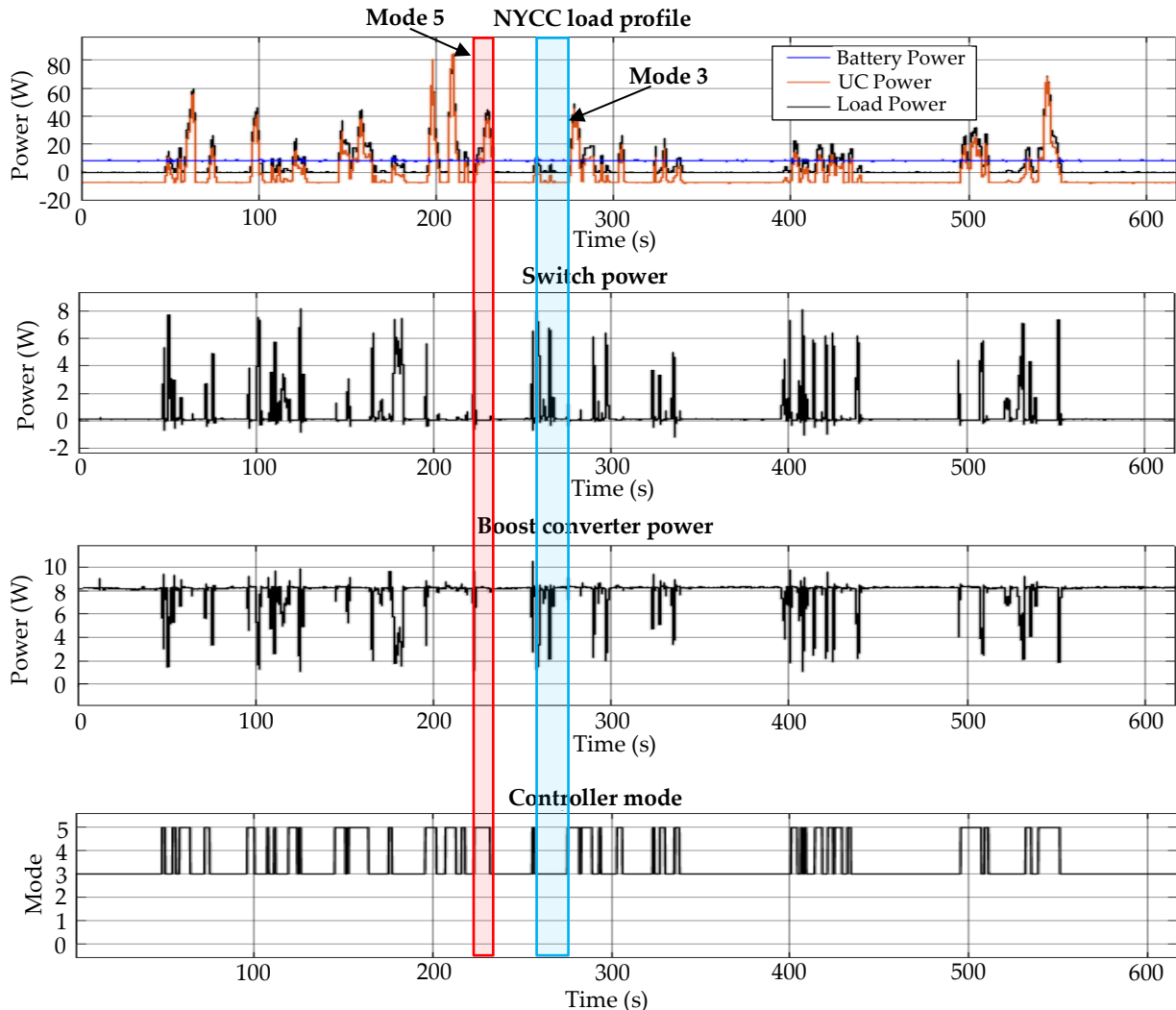


Figure 5.16: Experimental system results for NYCC drive cycle

### 5.3.3 ECE 15 drive cycle

The resultant power flow throughout the system is shown in figure 5.17 after the ECE 15 drive cycle was tested. The power draw from the battery was limited to 11.93 W, whilst the average power required for the simulated model was 10.44 W. We can note from figure 5.17 that the system is able to limit the power drawn from the batteries.

The red portion in the figure, as has been explained for the other load profiles, shows when the system operates in mode 5 when the load's power draw is above the defined limit. The blue portion shows when the overhead controller operates in mode 3.
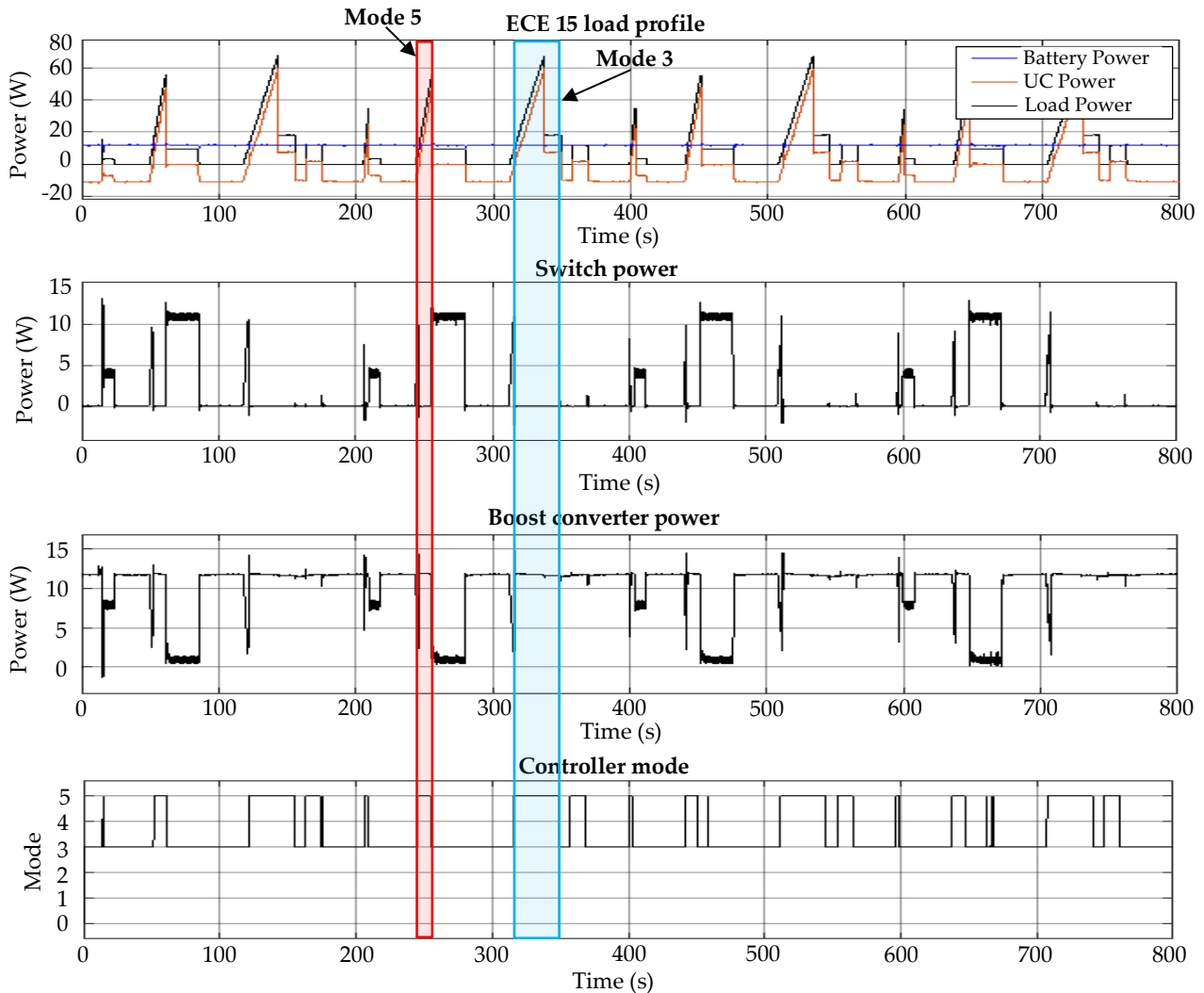
Figure 5.17: Experimental system results for the ECE 15 drive cycle

## 5.3.4 WLTC 2 drive cycle

The WLTC 2 drive cycle was the last profile that was tested and the resultant power flow is shown in figure 5.18. A power limit of 13.8 W was required to ensure that the SoC of the UC was the same at the start and the end of the cycle. The simulated system required a power limit of 12.4 W. The SoC of the UC during this profile is also shown. We can see that the SoC of the UC is at the same level at the end of the cycle as it was at the beginning of the cycle.

When the system operates in mode 3, we can see that the SoC of the UC increases, seeing that the battery charges the UC. In mode 5 the SoC of the UC decreases as it provides power to the load through the buck converter.
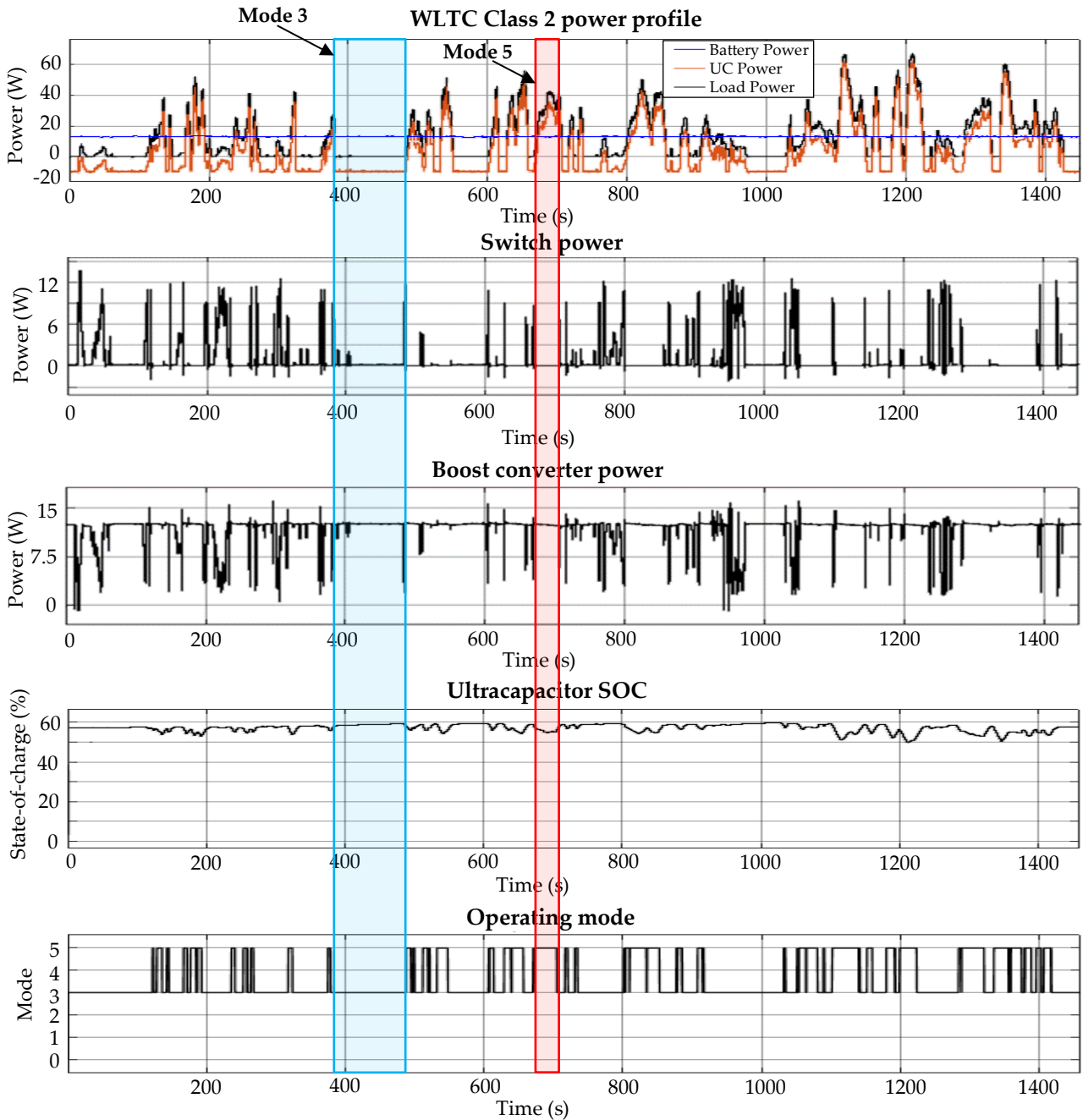
Figure 5.18: Experimental system results for WLTC 2 drive cycle

# 5.4 Mode testing

The different operating modes of the overhead controller were practically tested, to verify that the controller altered the flow of power depending on the control conditions. The pulsed load was used to test the different operating modes, seeing as the power flow for the pulsed load is easy to analyse. The NYCC test profile was also used to show how the controller switches between modes when the defined power limit for the battery was incorrectly set.

As the reader may have noted from the results of the previous sections, the system would be able to provide power to the load whilst limiting the power drawn from the battery until the battery would eventually be depleted for a certain profile. But a vehicle would rarely complete the same drive cycle over and over in real-world conditions. It is also difficult to predict what the vehicles power

draw would be and is the subject of much research [145]- [148]. This issue is discussed more thoroughly in the next chapter. In order to illustrate the control of power through the system when the power limit was set to a higher value than the average power for the specific load profile, the NYCC load profile was retested. The results of this test are shown in figure 5.19.
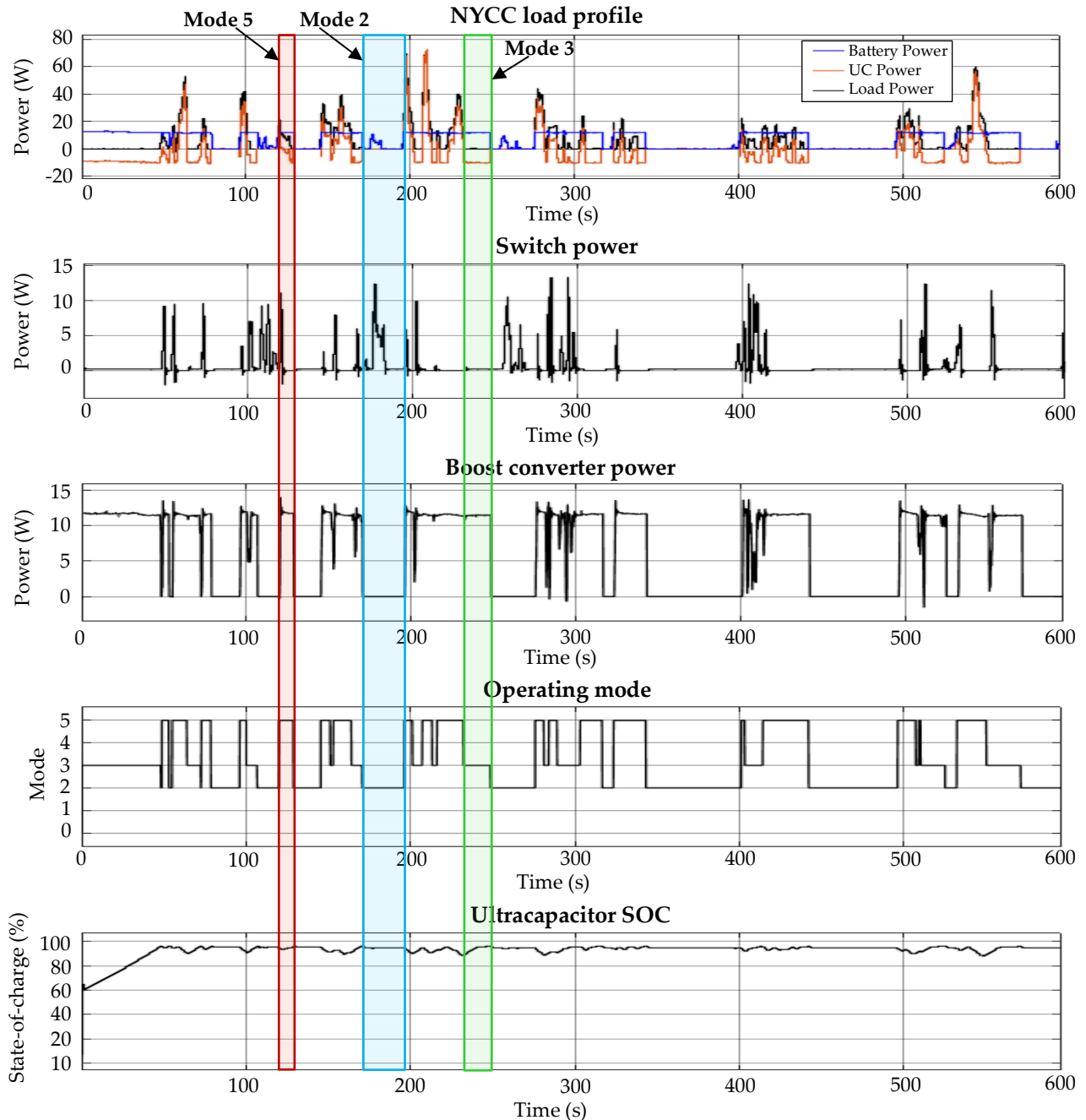


Figure 5.19: Experimental system results for NYCC drive cycle – retested with higher power limit

The defined power limit was set to 11.6 W, whilst the average power draw for this profile is only 8.4 W. As we can note from the graph in figure 5.19 showing the SoC of the UC, the controller starts in mode 3, because the load power is below the limit, but the UC is not fully charged, so the UC is charged until a SoC of 97% is reached. When the load power increases above the defined limit, the controller switches to mode 5 as shown by the red portion of the figure.

The controller switches back to mode 3 and charges the UC and once the SoC of the UC reaches 97%, the controller switches to mode 2 shown by the blue portion in the figure. In this mode the battery is directly connected to the load, whilst no power is transferred through the boost converter to the UC. Hysteresis control was implemented to prevent the mode controller from oscillating between modes 2 and 3 when the SoC of the UC reaches a certain level. The upper limit for the SoC was set to 97% whilst the lower limit was set to 93%.

Figure 5.20 is used to show that the controller is able to switch from the normal operating modes, which would be modes 3 and 5, to mode 4 and 6, in which the battery is directly connected to the load when the UC is depleted and its SoC is below 30%. We can see from the load profile that the battery provides all the power to the load through the switch, whilst no power is transferred from the UC. The only two operating modes that are not shown is modes 0 and 1. Mode 0 simply disconnects both the UC and the battery, seeing that both devices are depleted. Mode 1 provides power to the load through the buck converter to the load from the UC when the battery is depleted. Once the UC is also depleted, this system will enter mode 0.
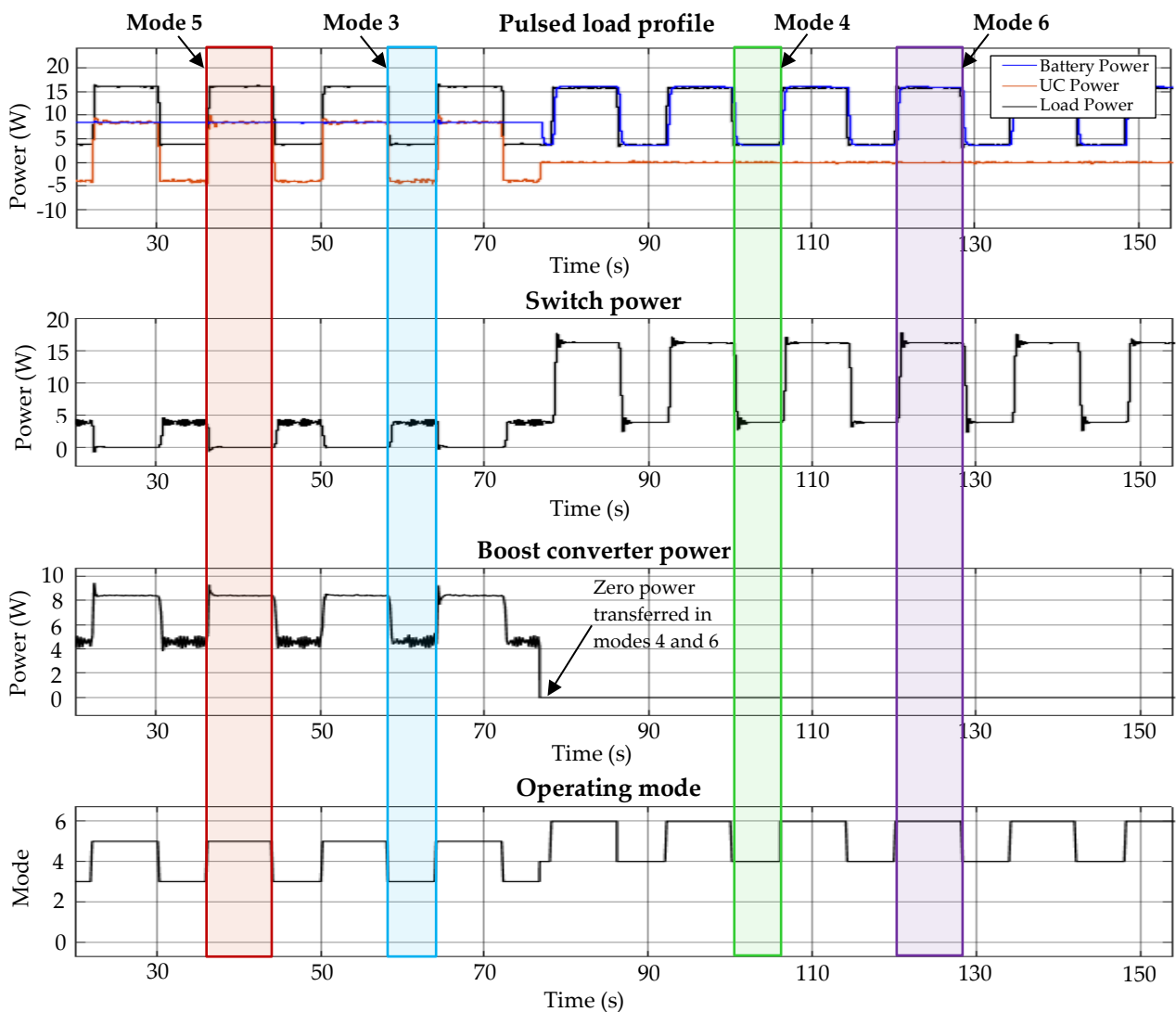


Figure 5.20: Experimental system results for Mode 4 and 6 testing

# 5.5 Comparison

This section briefly compares the performance of the experimentally implemented active HESS to that of the simulated active HESS. The average power that was required for the drive cycles are shown in table 5.2. The average power drawn by each load profile is given in the first column. The second column shows the average power that had to be drawn from the battery to ensure that the SoC of the UC was the same at the start and end of the load cycle. The increased power required for the simulated system compared to the average power for the load is due to the losses associated with the DC/DC converters. The average power required for the experimentally implemented system is also shown in the table.

We can note that the average power that was required for the experimental system was higher than the simulated system. This is due to the fact that the efficiency of the buck and boost converters were set to 92% for the simulation model, whilst the practically implemented buck and boost converters had a lower efficiency than this.

Table 5.2: Comparison

|  | Average power for drive cycle | Simulated required power | Experimental power required |
|---|---|---|---|
| **Pulsed Load 38 W Peak** | 18.07 W | 19.05 W | 20.5 W |
| **Pulsed Load 62 W Peak** | 20.4 W | 21.47 W | 23.58 W |
| **NYCC Drive Cycle** | 5.09 W | 5.6 W | 8.40 W |
| **ECE-15 Drive Cycle** | 9.12 W | 10.44 W | 11.93 W |
| **WLTC Class 2 Cycle** | 10.86 W | 12.4 W | 13.8 W |

Figure 5.21 compares the peak-power drawn for the battery-only system to the peak-power drawn from the active HESS topology. The battery-only system was not practically implemented, seeing that the load profiles that were tested could damage the batteries, as some of them would exceed the maximum discharge rating of the batteries. The peak-power that would have been drawn for the battery-only system was therefore estimated by using the peak-power point in each load profile. The peak-power drawn from the battery for the active HESS is equal to the battery power limit that was set. We can note that the experimentally implemented system reduces the peak-power drawn from the battery and is capable of managing the flow of power throughout the system.
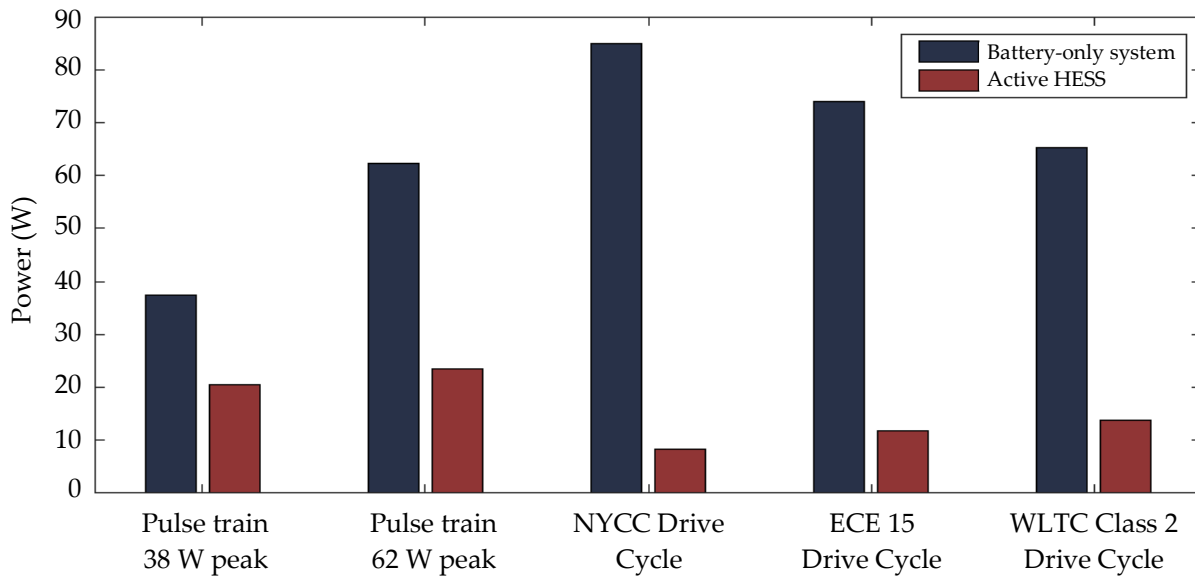
Figure 5.21: Comparison between peak-power drawn from battery-only system and active HESS

# 5.6 Verification and validation

The experimental results given and discussed in this chapter were verified and validated against the simulated results obtained in chapter 4. The performance of the different functional units was compared to the simulated performance of these functional units in chapter 4. The performance of the fuzzy logic controllers controlling the buck converter and the boost converter respectively were compared and the results of the comparison are tabulated in table 5.1. The difference between the performance of the simulated and experimental implementation was also discussed. The validation that was done for the fuzzy logic controllers was done by checking that the fuzzy logic controller controlling the buck converter was able to operate in a voltage-controlled mode and that the fuzzy logic controller controlling the boost converter was able to operate in a power-controlled mode. This ensured that the overall controller would be able to control the flow of power throughout the system through the fuzzy logic controllers, according to the control scheme as developed in chapter 3.

The experimental implementation of the buck and boost converters were verified against the simulated results as well as the analytical design calculations that were done in chapter 3. The results of the verification that was done is shown in figure 5.22 and figure 5.23. We can see that that the analytical, simulated and experimental results are closely related, thus validating the design and implementation of the two DC/DC converters. The overhead control scheme that was designed in chapter 3 and simulated in chapter 4 was also verified in this chapter. This was done by practically implementing the overall control system together with the fuzzy logic controllers. The integrated system was practically tested by utilising a programmable load to emulate the load profiles that were tested in chapter 4. The results obtained for the practical system was verified by comparing these results to the simulated results in section 4.3.

**Buck converter output voltage versus duty cycle**
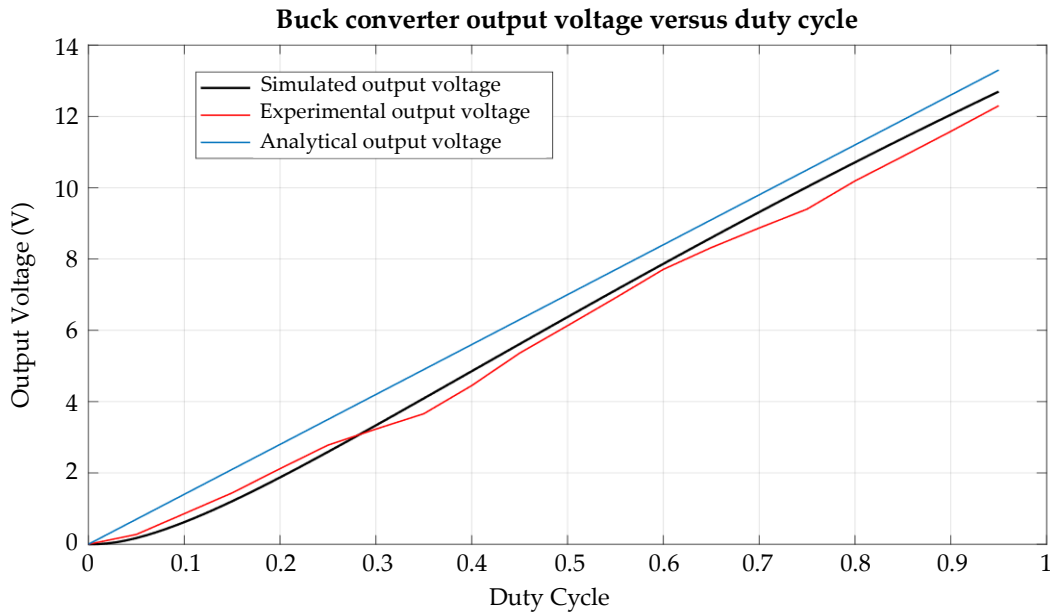


Figure 5.22: Buck converter output voltage versus duty cycle

**Boost converter output current versus duty cycle**
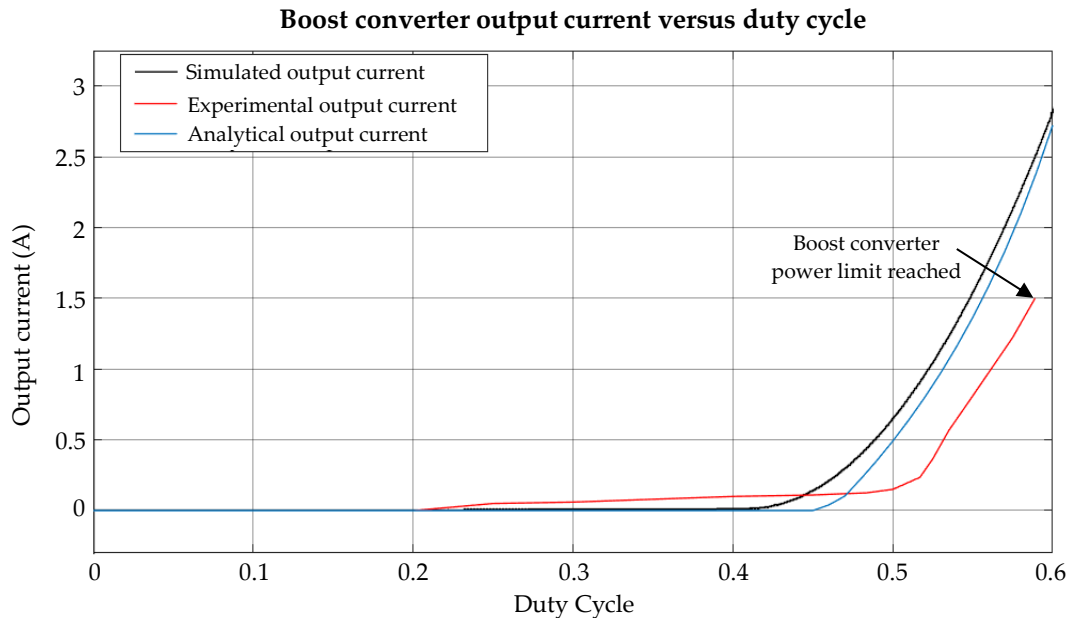


Figure 5.23: Boost converter output voltage versus duty cycle

Another way of verifying the performance of the experimentally implemented HESS was by comparing the average power that the active HESS had to deliver for each load profile. The results of this comparison were discussed in section 5.5 and are shown in table 5.2. As we can note from the table, the experimental system had highest average power requirement, due to the practical losses associated with DC/DC converters, resistance of the PCB tracks as well as stray inductance and capacitance. The average values were however within margin of error for a practically implemented system.

To ensure the validity of the calculations that were used to create the power profiles from the real-world speed profiles that a vehicle may experience; the created power profiles were compared to the results obtained by Barlow *et al.* and of Sciarretta *et al.* [133], [140]. The topology that was used

was also validated in this chapter seeing that the topology was able to manage the power flow throughout the system and successfully integrated the different EES devices.

## 5.7 Conclusion

This chapter was used to document the practical implementation of the simulated active HESS to verify that the controller can in a practical application control the flow of power between two EES devices, in order to reduce the peak-power drawn from one the devices. This chapter discussed and documented the results obtained for some of the functional units and the overall integrated system. The active HESS was tested against the load profiles that were defined in chapter 3. As was documented in this chapter, the HESS was able to actively manage the flow of power throughout the system in order to provide power to the load whilst limiting the power drawn from the battery.

The simulated performance of the fuzzy logic controllers controlling the buck and boost converters were compared to the performance of the practically implemented fuzzy logic controllers. The practically implemented fuzzy logic controllers did not perform as well as the simulated controllers. The difference was given in table 5.1 and it was discussed that the degraded performance of the practical system was due to the limited sampling frequency of the microcontroller whilst connected as an external target in Simulink®. The limited sampling frequency of the microcontroller was caused by either the computational complexity of the Simulink® model that was deployed to the microcontroller or by a software limitation in the add-on package provided by STMicroelectronics® for Simulink® to be able to sufficiently utilize the microcontroller's ADCs. Nonetheless, the microcontroller was still able to adequately control the output voltage of the buck converter, as well as the power transferred through the boost converter to the load.

The experimentally implemented system reduced the peak-power drawn from the battery by 90.1% for the NYCC drive cycle, whilst only reducing the peak-power drawn from the battery by 46.05% for the pulsed load profile with the 38 W peak. The experimental system showed that:

- The overhead control scheme that was developed was able to adequately control the active HESS topology that was utilised in this project.
- Fuzzy logic was a sufficient closed-loop control structure for controlling DC/DC converters.

The next chapter is the closing chapter of the dissertation. A summary of the results obtained during the research project are presented. Recommendations for future work as well as the shortfalls of this project are discussed. The verification and validation that was done throughout the study and the research questions are also addressed in the next chapter.

# Chapter 6 – Conclusion and recommendations

*This chapter is the closing chapter of the dissertation. The chapter firstly discusses the main topics discussed in the previous chapters and focusses on the simulation and experimental results that were obtained. The key research questions are also discussed in this chapter. Recommendations for future work are also discussed. The chapter is concluded after the discussion on how the project was continuously verified and validated.*

## 6.1 Discussion

This section summarises and discusses the work done throughout the study. The introductory chapter provided background information surrounding hybrid energy storage systems and the reasons for hybridization. Battery life and capacity are negatively affected by spikes of high-power draw and electric vehicle designers combat this by utilising power-dense batteries, sacrificing on the energy-density of the system. The research project was based on this problem and was addressed by developing an active HESS that would focus on reducing the peak-power drawn from the battery. The abstracts and citations of the articles that were generated from this research project were also given in the first chapter. Two articles were written; the first article described the design and simulation of the HESS. This article was accepted and presented at the IEEE International Multidisciplinary Information Technology and Engineering Conference (IMITEC). The second article that was written summarised the practical implementation and the results obtained from this active HESS and was submitted to the World Electric Vehicle Journal (WEVJ). These two articles can be found in Appendix A of this document.

The literature chapter discussed the relative literature pertaining to the problem as defined in the first chapter. The different HESS topologies that exist and their benefits/drawbacks were documented. The different energy storage devices that were most commonly used in the industry were also discussed. A case study was also done surrounding the results that were obtained by other researchers for different topologies. Seeing that the study focussed on electric vehicles, the most commonly used energy storage devices in this sector were batteries and ultracapacitors. Batteries and ultracapacitors were thus chosen as the energy storage devices that should be hybridized, due to their complementary characteristics.

A study was also briefly done for the different system controllers that could be used. Different single-board based computers, microcontrollers and PLCs were considered. It was decided that the SMT32 Nucleo F767ZI was to be used, seeing that this microcontroller has multiple ADC/DAC's, a relatively fast processor and much more static and dynamic memory compared to some more commonly used microcontrollers. The microcontroller also easily integrates with Simulink® and the microcontroller was already available at the research facility. The chapter also documented some of the aging-methods in batteries, which explain why batteries are damaged/aged by high currents and why peak-power reduction is advantageous.

The design chapter utilised the information gathered in the literature study to create a concept and detail design. Functional units were created and the interface between the different functional units was defined in this chapter to minimize the risk that the different sub-systems would not correctly interface with one another.

The topology that was chosen made use of two DC/DC converters as well as a switch to control the flow of power through the system. Unidirectional converters were utilised to reduce the complexity of the designed system. The control rules to control the state of each DC/DC converter as well as the switch were also developed in this chapter. The control rules were designed in such a manner that the system tries to limit the power drawn from the battery to a user-defined power limit.

This user-defined power limit was set to the average power that the load profile would consume plus the losses associated with the DC/DC converters. This would allow the system to provide power for that load profile. The average power used by a vehicle during a drive cycle on an average commute is highly variable and is dependent on various factors such as traffic, weather, the route and even the state-of-mind of the driver. Setting a predefined power limit for the batteries, in this case, could be detrimental to the vehicle's performance seeing that the power limit could have been set too low, which would either limit the performance of the vehicle or the power drawn from the batteries could damage/shorten the lifespan of the batteries.

To overcome this an advanced predictive control method could be developed, which dynamically adjusts the power drawn from the battery, for example by using a sliding window that calculates the average power drawn by the load. With the advent of intelligent, autonomous vehicles wherein the user could enter the route that the vehicle needs to travel or the vehicle could calculate the route by providing the destination location, the vehicle could calculate the average power that would be required for the route profile. The vehicle could measure the weight of the vehicle, know the defined speed limits for the specific route, has a predefined maximum acceleration/deceleration, total route ascent and descent together with the route length and use this information to calculate the average power for each segment of the route. This information can then be used to dynamically adjust the power limit so that the UC is able to provide power when the vehicle accelerates and is depleted to be able to absorb power during regenerative braking. Although the developed system in this project does not take into account all of this information, it provides a platform for future work to implement some of these predictive control techniques. This brief digression was made to describe to the reader the reasoning behind why the system has a controllable power limit.

After the design of the overhead controller was defined, a detailed design was done for the buck and boost converter. A control topology was required to be able to control the power flow through the boost converter and the output voltage of the buck converter. Different control topologies were considered, with fuzzy logic being chosen due to the information gathered in the literature study indicating that fuzzy logic has comparable performance to PID controllers but doesn't require a transfer function/mathematical model to develop the controller and it is usually less susceptible to disturbances when compared to PID controllers. The membership functions and accompanying

rules were developed and discussed in this chapter. The designs of some of the other functional units were also done in this chapter.

Chapter 4 was used to simulate the performance of the different sub-systems as well as the performance of the overall system. The design calculations as were done in chapter 3 for the DC/DC converters were verified by the simulations that were done in Simulink®. The membership functions used for the fuzzy logic controller were also verified and adjusted during the simulation process. The performance of the fuzzy logic controllers controlling the buck and boost converters were also verified.

The overall control system was tested in this chapter against the different load profiles. Three different real-world driving cycles were used to create a realistic load representative of the power that a vehicle would draw. The simulations verified and showed that the system was able to control the flow of power throughout the system so that the power drawn from the battery was limited to the user-defined power limit. The simulation results showed that the active topology was able to drastically reduce the peak-power drawn from the battery and improve over the performance of the passive topology.

Chapter 5 discussed the practical implementation of the system. The step response of the fuzzy logic controllers was practically tested to verify that the controllers were able to control the power and voltage of the boost and buck converters respectively. The completely integrated system was also tested. The practically implemented system was able to reduce the peak-power drawn from the battery and limit the power drawn to the average power required for that specific load profile.

It can be noted that the designed system is not only suitable for the hybridization of batteries and ultracapacitors, but any EES devices with complementary characteristics could be used. This could include for example the hybridization of fuel cells and batteries, with a constant amount of power being drawn by the fuel cells whilst the batteries provide the large changes in output power. Fuel cells and ultracapacitors could also be hybridized; any combination of EES devices could have been utilized.

# 6.2 Key Research Questions

- Could a controller be developed that is able to control the flow of power in a HESS so that the power impulses experienced by the battery is minimized?

  *The results obtained from the simulated and practically implemented system as documented in section 4.4 and section 5.3 showed that a controller that could control the flow in such a manner was designed and implemented. The designed system and control strategy were able to control the flow of power between the battery and ultracapacitor in such a way that the system was still able to provide the required power to the load, whilst minimizing the power drawn from the battery to the average power required for the load profile.*

- Are there any benefits to using an active HESS compared to a passive HESS or a standalone battery?

*The active HESS was able to minimize the power drawn from the battery and reduced the peak-power drawn from the battery. Compared to the passive HESS the active system further reduced the peak-power drawn from the battery. The active HESS would firstly increase battery life by reducing these power spikes. The system secondly allows the designer to utilise batteries optimised for energy density, instead of having to utilise batteries that trade energy density for power density in order to provide power to the load in a battery-only system. The active topology also increases the peak-power that the system is able to deliver, limited only by the power rating of the DC/DC converter interfacing the ultracapacitor and the load, and the duration of the load peak.*

## 6.3 Future Work and Recommendations

This section describes the possible areas for future research and improvements that could be made to the developed system based on the findings of this thesis.

- The design of the DC/DC converters can be altered and improved on by firstly implementing bidirectional DC/DC converters. Bidirectional DC/DC converters would allow the system to absorb power from the load, for example when the regenerative braking is utilised in an electric vehicle. This would widely increase the power management ability of the topology.

- Although Simulink® provides an easy to use software platform to deploy algorithms and control to embedded hardware, it resulted in the degradation in the performance of the microcontroller due to the computational complexity of the model. In order to improve on the performance of the practically implemented fuzzy logic controllers, it is recommended that in future work that the model is deployed to embedded hardware with a faster processor and more dynamic/static memory when used in conjunction with Simulink®, or the control algorithm and fuzzy logic lookup table should be written in the embedded software for the specific control board that is used.

- In this study a rule-based strategy was used as the power management strategy, but improvements can be made by utilising predictive optimising algorithms for the power management strategy. Some of the algorithms that for example could be considered are the dynamic programming optimisation algorithm (DP), an artificial neural network working in conjunction with Pontryagin's Minimum Principle (PMP) or a driving pattern recognition (DPR)-based power management strategy, to name a few.

# 6.4 Validation and verification

This section discusses the verification and validation process that was carried out to ensure that the project met the objectives of the project as well as answer the research questions that were formulated in Chapter 1. The verification and validation process that was undertaken is shown in figure 6.1. In section 1.4.7 in Chapter 1, the verification and validation process that needed to be carried out was discussed in detail. The literature study that was done in chapter 2 was utilised in the succeeding chapters for the verification and validation process. The case studies done surrounding similar projects carried out by other researchers were documented and were compared to this study to ensure that the objectives of the research were feasible.

The design of the DC/DC converters were verified by comparing the designed component values to that of other projects. The design of the control scheme that was implemented was also compared to the work done by other researchers that also implemented rule-based strategies for active HESS. The load profiles that were used were verified by comparing the power profile calculations for these profiles to that of other researchers. These load profiles were validated by using industry-standard drive cycles that are used to test the performance of vehicles.
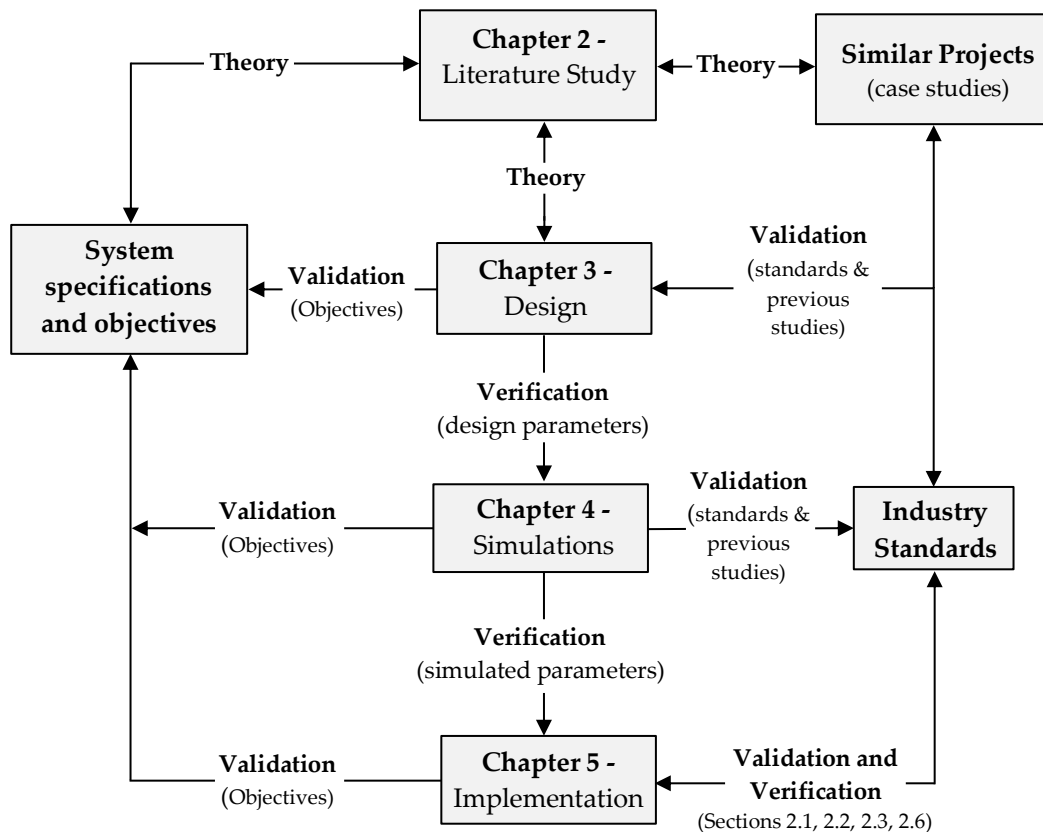


Figure 6.1: Verification and validation of the dissertation

The simulations done in Chapter 4 made use of industry-standard software and was used to firstly verify the designed sub-systems in Chapter 3. The overhead controller was also verified during the simulation process by testing the response of the controller and comparing that to the designed

response rules. It was also verified that the simulated system met the system requirements and the objectives of the project.

The experimental implementation of the system was verified and validated firstly by using the industry-standard measuring equipment to verify that the data collected by the system was correct. The experimental results closely matched the simulated results, validating the results and further verifying that the implemented system functioned as designed. The experimental system's results were compared to the objectives of the thesis in order to validate that the right system to answer the research questions was developed and implemented and to verify that the system was built correctly.

# 6.5 Conclusion

This research project was undertaken to investigate if a controller could be developed for an active HESS that reduces the peak-power impulse experienced by a battery in a battery/ultracapacitor hybrid system. A control topology to control the DC/DC converters as well as the overall power flow in the system, was developed, simulated and experimentally implemented. From the results obtained it is clear that an active topology with the correct control could successfully integrate different electrical energy storage devices and utilise their complementary characteristics. The designed active HESS topology could be implemented in electric vehicles, micro-grids or any system that would benefit from the hybridization of two electrical energy storage devices.

# Bibliography

[1]     F. Watson, "December global electric vehicles sales set new record: S&P Global Platts data," S&P Global, 11 Feb 2019. [Online]. Available: https://www.spglobal.com/platts/en/market-insights/latest-news/electric-power/021119-december-global-electric-vehicle-sales-set-new-record-sampp-global-platts-data. [Accessed 3 June 2019].

[2]     Z. Song, H. Hoffman, J. Li, X. Han, X. Zhang and M. Ouyang, "A comparison study of different semi-active hybrid energy storage system topologies for electric vehicles," *Journal of Power Sources*, vol. 274, pp. 400-411, 2015.

[3]     M. Choi, J. Lee and S. Seo, "Real-Time Optimization for Power Management Systems of a Battery/Supercapacitor Hybrid Energy Storage System in Electric Vehicles," *IEEE Transactions on Vehicular Technology*, vol. 63, no. 8, pp. 3600-3611, 2014.

[4]     M. Hannan, M. Hoque, A. Mohamed and A. Ayob, "Review of energy storage systems for electric vehicle applications: Issues and challenges," *Renewable and Sustainable Energy Reviews*, vol. 69, pp. 771-789, 2017.

[5]     T. Amietszajew, E. McTurk, J. Fleming and R. Bhagat, "Understanding the limits of rapid charging using instrumented commercial 18650 high-energy Li-ion cells," *Electrochimica Acta*, pp. 346-352, 2018.

[6]     P. V. Braun, J. Cho, J. H. Pikul, W. P. King and H. Zhang, "High power rechargeable batteries," *Current Opinion in Solid State and Materials Science*, vol. 16, no. 4, pp. 186-198, 2012.

[7]     J. Cao and A. Emadi, "A New Battery/UltraCapacitor Hybrid Energy Storage System for Electric, Hybrid, and Plug-In Hybrid Electric Vehicles," *IEEE Transactions on Power Electronics* , vol. 27, no. 1, pp. 122-132, 2012.

[8]     M. E. Choi, S. W. Kim and S. W. Seo, "Energy Management Optimization in a Battery/Supercapacitor Hybrid Energy Storage System," *IEEE Transactions on Smart Grid*, vol. 3, no. 1, pp. 463-472, 2012.

[9]     Y. Bai, H. He, J. Li, S. Li, Y.-x. Wang and Q. Yang, "Battery anti-aging control for a plug-in hybrid electric vehicle with a hierarchical optimization energy management strategy," *Journal of Cleaner Production*, vol. 237, pp. 1-3, 2019.

[10]    B. S. Lee, Z. Wu, V. Petrova, X. Xing and H. D. Lim, "Analysis of Rate-Limiting Factors in Thick Electrodes for Electric Vehicle Applications," *Journal of The Electrochemical Society*, vol. 165, no. 3, pp. 525-533, 2018.

[11]    W. Du, A. Gupta, X. Zhang, A. M. Sastry and W. Shyy, "Effect of cycling rate, particle size and transport properties on lithium-ion cathode performance," *International Journal of Heat and Mass Transfer*, vol. 53, no. 17-18, pp. 3552-3561, 2010.

[12]    Y. W. Ang Yang, F. Yang, D. Wang, Y. Zi, K. L. Tsui and B. Zhang, "A comprehensive investigation of lithium-ion battery degradation performance at different discharge rates," *Journal of Power Sources*, vol. 443, pp. 1-11, 2019.

[13]    J. Du, Y. Liu, X. Mo, Y. Li, J. Li, X. Wu and M. Ouyang, "Impact of high-power charging on the durability and safety of lithium batteries used in long-range battery electric vehicles," *Applied Energy*, vol. 255, pp. 3-10, 2019.

[14] J. M. Miller, T. Bohn, T. J. Dougherty and U. Deshpande, "Why hybridization of energy storage is essential for future hybrid, plug-in and battery electric vehicles," in *2009 IEEE Energy Conversion Congress and Exposition*, San Jose, pp. 2614- 26220, 2009.

[15] A. Kuperman, "Battery - Ultracapacitor hybrids for pulsed current loads," *Renewable and Sustainable Energy Reviews,* vol. 15, no. 2, pp. 981-992, 2011.

[16] R. A. Dougal, S. Liu and R. E. White, "Power and life extension of battery-ultracapacitor hybrids," *IEEE Transactions on Components and Packaging Technologies,* vol. 25, no. 1, pp. 120-131, 2002.

[17] M. Ehsani and Y. Gao, "Ultracapcitors," in *Modern Electric, Hybrid Electric, and Fuel Cell Vehicles*, Florida, CRC Press, 2005, pp. 314-315.

[18] K. Fic, A. Platek, J. Piwek and E. Frackowiak, "Sustainable materials for electrochemical capacitors," *Materials Today,* vol. 21, no. 4, pp. 437-454, 2018.

[19] A. Hausmann and C. Depcik, "Expanding the Peukert equation for battery capacity modeling through inclusion of a temperature dependency," *Journal of Power Sources,* vol. 235, pp. 148-158, 2013.

[20] J. Larmine and J. Lowry, "Batteries," in *Electric Vehicle Technology Explained*, Chichester, John Wiley & Sons, Ltd, 2003, pp. 57-58.

[21] J. Moreno, "Ultracapacitor-Based Auxiliary Energy System for an Electric Vehicle: Implementation and Evaluation," *IEEE Transactions on industrial electronics,* vol. 54, no. 4, pp. 2147-2156, 2007.

[22] L. Gao, R. Dougal and S. Liu, "Power enhancement of an actively controlled battery/ultracapacitor hybrid," *IEEE Transactions on Power Electronics,* vol. 20, no. 1, pp. 236-243, 2005.

[23] S. Liu, X. Zhang, H. Guo and J. Xie, "Multiple Input Bidirectional DC/DC Converter for Energy Supervision in Fuel Cell Electric Vehicles," in *International Conference on Electrical and Control Engineering*, Wuhan, pp. 3890-3893, 2010.

[24] S. Bluhm, "Improving Mine Ventilation Electricity Consumption," Mining Review Africa, 26 September 2008. [Online]. Available: https://www.miningreview.com/improving-mine-ventilation-electricity-consumption/. [Accessed 12 March 2018].

[25] Eskom, "The Energy Efficiency series: Towards an energy efficient mining sector," [Online]. Available: http://www.eskom.co.za/sites/idm/Documents/121040ESKD_Mining_Brochure _paths.pdf. [Accessed 12 March 2018].

[26] Z. Ristovski, B. Miljevic and L. Morawska, "Respiratory health effects of diesel particulate manner," *Respirology,* vol. 17, pp. 201-212, 2012.

[27] D. A. Wetz, B. Shrestha, P. M. Novak and S. Donahue, "Capacity fade of a high power battery when evaluated for use within a prime power supply„," in *2014 17th International Symposium on Electromagnetic Launch Technology*, La Jolla, pp. 1 -7, 2014.

[28] X. Han, L. Lu, Y. Zheng, X. Feng, Z. Li, J. Li and M. Ouyang, "A review on the key issues of the lithium ion battery degradation among the whole life cycle," *eTransportation*, vol. 1, pp. 1-18, 2019.

[29] S. M. Lukic, J. Cao and R. C. Bansal, "Energy Storage Systems for Automotive Applications," *IEEE Transactions on Industrial Electronics,* vol. 55, no. 6, pp. 2258-2267, 2008.

[30]  A. C. Baisden and A. Emadi, "ADVISOR-based model of a battery and an ultra-capacitor energy source for hybrid electric vehicles," *IEEE Transactions on Vehicular Technology,* vol. 53, no. 1, pp. 199-205, 2004.

[31]  P. Golchoubian, "Real-time Energy Management of a Battery Electric Vehicle Hybridized with Supercapacitor," UWSpace, Waterloo, 2017.

[32]  D. Hoelscher, A. Skorcz, Y. Gao and M. Ehsani, "Hybridized Electric Energy Storage Systems for Hybrid Electric Vehicles," in *IEEE Vehicle Power and Propulsion Conference*, Windsor, pp. 1-6, 2006.

[33]  C. Xiang, Y. Wang and S. Hu, "A New Topology and Control Strategy for a Hybrid Battery-Ultracapacitor Energy Storage System," *Energies,* vol. 7, pp. 2874-2896, 2014.

[34]  Y. Kim and N. Chang, Design and Management of Energy-Efficient Hybrid Electrical Energy Storage Systems, Cham: Springer, 2014.

[35]  P. B. Bobba and K. R. Rajagopal, "Modeling and analysis of hybrid energy storage systems used in Electric vehicles," in *2012 IEEE International Conference on Power Electronics, Drives and Energy Systems (PEDES)*, Bengaluru, pp. 1-6, 2012.

[36]  X. Liu, Q. Zhang and C. Zhu, "Design of battery and ultracapacitor multiple energy storage in hybrid electric vehicle," in *IEEE Vehicle Power and Propulsion Conference*, Dearborn, pp. 1395-1398, 2009.

[37]  J. M. Miller and G. Sartorelli, "Battery and ultracapacitor combinations — Where should the converter go?," in *2010 IEEE Vehicle Power and Propulsion Conference*, Lille, pp. 1-7, 2010.

[38]  L. H. Seim, "Modeling, Control and Experimental Testing of a Supercapacitor/Battery Hybrid System - Passive and Semi-Active Topologies," Norwegian University of Life Sciences - Department of Mathematical Sciences and Technology, Ås, Norway, 2011.

[39]  I. Aharon and A. Kuperman, "Design of semi-active battery-ultracapacitor hybrids," in *IEEE 26-th Convention of Electrical and Electronics Engineers in Israel*, Eliat, pp. 593-597, 2010.

[40]  D. Haifeng and C. Xueyu, "A Study on Lead Acid Battery and Ultra-capacitor Hybrid Energy Storage System for Hybrid City Bus," in *2010 International Conference on Optoelectronics and Image Processing*, Haiko, pp. 154-159, 2010.

[41]  C. Zhao, H. Yin and Z. Yang, "A quantitative comparative study of efficiency for battery-ultracapacitor hybrid systems," in *IECON 2014 - 40th Annual Conference of the IEEE Industrial Electronics Society*, Dallas, Texas, pp. 3076-3082, 2014.

[42]  Z. Yingchao, G. Zhen, Z. Yongchang and Z. Tianwen, "Active battery/ultracapacitor hybrid energy storage system based on soft-switching bidirectional converter," in *2013 International Conference on Electrical Machines and Systems (ICEMS)*, Busan, pp. 2177-2182, 2013.

[43]  H. Min, C. Lai, Y. Yu and T. Zhu, "Comparison Study of Two Semi-Active Hybrid Energy Storage Systems for Hybrid Electric Vehicle Applications and Their Experimental Validation," *Energies,* vol. 10, no. 3, p. 279, 2017.

[44]  J. Shen, "Energy management of a battery-ultracapacitor hybrid energy storage system in electric vehicles," University of Maryland, Maryland, 2016.

[45]  M. Michalczuk, L. Grzesiak and B. Ufnalski, "A lithium battery and ultracapacitor hybrid energy source for an urban electric vehicle," *Przeglad Elektrotechniczny,* vol. 88, no. 4, pp. 158-162, 2012.

[46] R. Carter, A. Cruden and P. J. Hall, "Optimizing for Efficiency or Battery Life in a Battery/Supercapacitor Electric Vehicle," *IEEE Transactions on Vehicular Technology,* vol. 61, no. 1, pp. 1526-1533, 2012.

[47] M. Ehsani and Y. Gao, "Energy Storages," in *Modern Electric, Hybrid Electric, and Fuel Cell Vehicles*, Florida, CRC Press, 2005, pp. 309-314.

[48] H. Chen, T. N. Cong and W. Yang, "Progress in electrical energy storage system: A critical review," *Progress in Natural Science ,* vol. 19, pp. 291-312, 2019.

[49] I. Hadjipaschalis, A. Poullikkas and V. Efthimiou, "Overview of current and future energy storage technologies for electric power applications," *Renewable and Sustainable Energy Reviews,* vol. 13, no. 6-7, pp. 1513-1522, 2009.

[50] G. L. Kyriakopoulos and G. Arabatzis, "Electrical energy storage systems in electricity generation: Energy policies, innovative technologies, and regulatory regimes," *Renewable and Sustainable Energy Reviews,* vol. 56, pp. 1044-1067, 2016.

[51] F. Diaz-Gonzalez and A. Sumper, "A review of energy storage technologies for wind power applications," *Renewable and Sustainable Energy Reviews,* vol. 16, no. 4, pp. 2154-2171, 2012.

[52] M. A. Fetchenko, S. R. Ovshinsky and B. Reichman, "Recent advances in NiMH battery technology," *Journal of Power Sources,* vol. 165, no. 2, pp. 544-551, 2007.

[53] E. Karden, S. Ploumen and B. Fricke, "Energy storage devices for future hybrid electric vehicles," *Journal of Power Sources,* vol. 168, no. 1, pp. 2-11, 2007.

[54] X. Shen, H. Liu, X.-B. Cheng, C. Yan and J.-Q. Huang, "Beyond lithium ion batteries: Higher energy density battery systems based," *Energy Storage Materials,* vol. 12, pp. 161-175, 2018.

[55] L. Lu, X. Han, J. Li and J. Hua, "A review on the key issues for lithium-ion battery management in electric vehicles," *Journal of Power Sources,* vol. 226, pp. 272-288, 2013.

[56] Y. Miao, P. Hynan, A. v. Jouanne and A. Yokochi, "Current Li-ion Battery Technologies in Electric Vehicles and Opportunities for Advancements," *Energies,* vol. 12, p. 1074, 2019.

[57] J. M. Miller, "Energy storage system technology challenges facing strong hybrid, plug-in and battery electric vehicles," in *2009 IEEE Vehicle Power and Propulsion Conference*, Dearborn, pp. 1-10, 2009.

[58] A. M. Aris and B. Shabani, "An experimental study of a lithium ion cell operation at low temperature conditios," in *1st International Conference on Energy and Power*, Melbourne, pp. 128-135, 2016.

[59] A. B. Cultura and Z. M. Salameh, "Modeling, Evaluation and Simulation of a Supercapacitor Module for Energy Storage Application," in *International Conference on Computer Information Systems and Industrial Applications*, pp. 876-882, 2015.

[60] P. Kokkotis, C. S. Psomopoulos and G. Loannidis, "Hierarchical classification of supercapacitors; stroke degradation and their enviromental issues in the End-of-Life phase," in *13th International Conference on Protection and Restoration of the Environment (PRE 13)*, Greece, pp. 374-382, 2016.

[61] A. Venkataraman, "Pseudocapacitors for Energy Storage," Portland State University, Portland, 2015.

[62] Y. Zhang, H. Feng, X. Wu, L. Wang, A. Zhang and T. Xia, "Progress of electrochemical capacitor electrode materials: A review," *International Journal of Hyrdrogen,* vol. 34, no. 11, pp. 4889-4889, 2009.

[63]    Y. P. Huang and P. F. Tsai, "Improving the Output Power Stability of a High Concentration Photovoltaic System with Supercapacitors: A Preliminary Evaluation," *Mathematical Problems in Engineering,* vol. 2015, pp. 1-7, 2015.

[64]    Maxwell, "BC Series Ultracapasitors," [Online]. Available: https://www.maxwell.com /images/documents/bcseries_ds_1017105-4.pdf. [Accessed 9 September 2019].

[65]    M. G. Molina, Dynamic Modelling and Control Design of Advanced Energy Storage for Power System Applications, San Juan: CONICET, Instituto de Energía Eléctrica, 2010.

[66]    M. Ehsani and Y. Gao, "Ultrahigh-Speed Flywheels," in *Modern Electric, Hybrid Electric and Fuel Cell Vehicles*, Florida, CRC Press, 2005, pp. 322-326.

[67]    M. Amiryar and K. Pullen, "A Review of Flywheel Energy Storage System Technologies and Their Applications," *Applied Sciences,* vol. 7, no. 3, p. 286, 2016.

[68]    W. Y. Chang, "The State of Charge Estimating Methods for Battery: A Review," *ISRN Applied Mathematics,* vol. 2013, p. 7, 2013.

[69]    R. Zhang, B. Xia, B. Li, L. Cao, Y. Lai and W. Zheng, "State of the Art of Lithium-Ion Battery SOC Estimation for Electrical Vehicles," *Energies ,* vol. 11, p. 1820, 2018.

[70]    C. Schlasza, P. Ostertag and D. Chrenko, "Review on the aging mechanisms in Li-ion batteries for electric vehicles based on the FMEA method," in *2014 IEEE Transportation Electrification Conference and Expo (ITEC)*, Dearborn, pp. 1-6, 2014.

[71]    J. Groot, "State-of-Health Estimation of Li-ion Batteries: Cycle Life Test Methods," Chalmers University of Technology, Göteborg, 2012.

[72]    K. Amine, J. Liu and I. Belharouak, "High-temperature storage and cycling of C-LiFePO4/graphite Li-ion cells," *Electrochemistry Communications,* vol. 7, no. 7, pp. 669-673, 2005.

[73]    M. E. V. Team, "Massachusetts Institute of Technology," 12 December 2008. [Online]. Available: http://web.mit.edu/evt/summary_battery_specifications.pdf. [Accessed 23 June 2019].

[74]    T. Guena and P. Teblanc, "How Depth of Discharge Affects the Cycle Life of Lithium-Metal-Polymer Batteries," in *Twenty-Eighth International Telecommunications Energy Conference*, Providence, Rhode Island, pp. 1-8, 2006.

[75]    E. Wikner, "Lithium ion Battery Aging: Battery Lifetime Testing and Physics-based Modeling for Electric Vehicle Applications," Chalmers University of Technology, Göteborg, 2017.

[76]    J. Vetter, P. Novak and M. Wagner, "Ageing mechanisms in lithium-ion batteries," *Journal of Power Sources,* vol. 147, no. 1-2, pp. 269-281, 2005.

[77]    L. Lu, X. Han and J. Li, "A review on the key issues for lithium-ion battery management in electric vehicles," *Journal of Power Sources,* vol. 226, pp. 272-288, 2013.

[78]    Q. Xie, "Research Projects," USC, [Online]. Available: http://sportlab.usc.edu/~qingxie /subpagge_research.htm. [Accessed 23 June 2018].

[79]    R. C. Dorf and R. H. Bishop, "Introduction to Control Systems," in *Modern Control Systems, 12th*, California, Pearson, 2011, pp. 1-4.

[80]    D. S. Omirou, "Open and Closed-Loop Control Systems," Frederick University Cyprus, Nicosia, Accessed: 2018.

[81]    D. Bishop, "Introduction to Control Systems," in *Modern Control Systems*, Harlow, Pearson, 2014, pp. 1-50.

[82] D. Ghose, "Introduction to Control Systems," 2012. [Online]. Available: http://nptel.ac.in/courses/101108056/module7/lecture13.pdf. [Accessed 5 April 2018].

[83] D. Corrigan, "Characterising the Response of a Closed Loop System," 24 November 2012. [Online]. Available: http://www.mee.tcd.ie/~corrigad/3c1/control_ho2_2012_students.pdf. [Accessed 5 April 2018].

[84] F. Dernoncourt, "Introduction to fuzzy logic," January 2013. [Online]. Available: http://aisii.azc.uam.mx/mcbc/Cursos/IntCompt/Lectura15.pdf. [Accessed 5 April 2018].

[85] A. H. Kurdi and J. L. Granter, "Fuzzy Logic Based Hardware Accelerator with Partially Reconfigurable Defuzzification Stage for Image Edge Detection," *International Journal of Reconfigurable Computing,* vol. 2017, p. 13, 2017.

[86] A. Q. Ansari, "The Basics of Fuzzy Logic: A Tutorial Review," *Computer Education -Stafford-Computer Education Group,* no. 88, pp. 5-9, 1998.

[87] R. M. Mateo, I. Yoon and J. Lee, "Cooperation Model for Object Group using Load Balancing," *International Journal of Computer Science and Network Security,* vol. 6, no. 12, pp. 1-10, 2006.

[88] MATLAB, "PDF Documentation for Fuzzy Logic Toolbox," [Online]. Available: https://www.mathworks.com/help/pdf_doc/fuzzy/fuzzy.pdf. [Accessed 9 April 2018].

[89] T. J. Ross, "Defuzzification to scalars," in *Fuzzy Logic with Engineering Applications*, New Mexico, Wiley and Sons Ltd, 2010, pp. 98-100.

[90] D. Pattnaik, B. Sahu and D. Samantaray, "Microcontroller based implementation of a fuzzy knowledge based controller," National Institute of Technology, Rourkela, Odisha, pp. 16- 34, 2013.

[91] J. Viera, F. Morgado-Dias and A. Mota, "Neuro-Fuzzy Systems: A Survey," *WSEAS Transactions on Systems,* no. 3, pp. 414-419, 2004.

[92] S. T. Sisakat and S. Barakati, "Fuzzy Energy Management in Electrical Vehicles," *2015 4th Iranian Joint Congress on Fuzzy and Intelligent Systems (CSIS),* vol. 4, pp. 1-6, 2015.

[93] Z. Shengzhe, W. Kai and X. Wen, "Fuzzy logic-based control strategy for a battery/supercapacitor hybrid energy storage system in electric vehicles," *2017 Chinese Automation Congress (CAC),* pp. 5598-5601, 2017.

[94] H. Atmaca, B. Cetisli and H. Serhan, "The Comparison of Fuzzy Inference Systems and Neural Network Approaches with ANFIS Method for Fuel Consumption Data," Osmangazi University, Osmangazi, pp. 1-4, 2001.

[95] S. Haykin, "What is a Neural Network," in *Neural Networks and Learning Machines*, Ontario, Pearson Prentice Hall, 2009, pp. 1-3.

[96] Y. Singh and A. S. Chauhan, "Neural networks in data mining," *Journal of Theoretical and Applied Information Technology,* vol. 5, pp. 37-42, 2009.

[97] P. Prashar, "Neural Networks in Machine Learning," *International Journal of Computer Applications,* vol. 105, no. 14, pp. 1-3, 2014.

[98] S. Vlad, "On the Prediction Methods Using Neurla Networks," in *6th International Symposium of Hungarian Researchers on Computational Intelligence*, Budapest, pp. 1-6, 2005.

[99] M. Johnson and M. Moradi, PID Control: New Identification and Design Methods, London: Springer, 2005.

[100] K. A. Tehrani and A. Mpanda, "PID Control Theory," in *Introduction to PID Controllers - Theory, Tuning and Application to Frontier Areas*, Amiens, Intec Open, pp. 213 -216.

[101] K. J. Astrom and R. M. Murray, Feedback Systems, Princeton and Oxford: Princetion University Press, 2010.

[102] K. S. Rao and R. Mishra, "Comparative study of P, PI and PID controller for speed control of VSI-fed induction motor," *International Journal of Engineering Development and Research,* vol. 2, no. 2, pp. 2740-2744, 2014.

[103] D. Nauck and R. Kruse, "Neuro-fuzzy systems for function approximation," *Fuzzy Sets and Systems,* vol. 101, no. 2, pp. 261-271, 1999.

[104] J. Vieira, F. M. Dias and A. Mota, "Neuro-Fuzzy Systems: A Survey," *WSEAS Transactions on Systems,* vol. 3, no. 2, pp. 414-419, 2004.

[105] R. Kruse, "Fuzzy neural network," Scholarpedia, 2008. [Online]. Available: http://www.scholarpedia.org/article/Fuzzy_neural_network. [Accessed 23 June 2018].

[106] J. J. Buckley and H. Yoichi, "Neural nets for fuzzy systems," *Fuzzy Sets and Systems,* vol. 71, no. 3, pp. 265-276, 1995.

[107] A. Abraham, "Neuro Fuzzy Systems: State-of-the-Art Modeling Techniques," in *International Work-Conference on Artificial Neural Networks*, Heidelberg, 2001.

[108] J. R. Jang, "ANFIS: Adaptive-Network-Based Fuzzy Inference System," *IEEE Transactions on Systems, Man and Cybernetics,* vol. 23, no. 3, 1993.

[109] N. Kasabov, "Evolving fuzzy neural networks for supervised/unsupervised online knowledge-based learning," *IEEE Transactions on Systems, Man, and Cybernetics, Part B (Cybernetics),* vol. 31, no. 6, pp. 902-918, 2001.

[110] W. Durfee, "Arduino Microcontroller," 2011. [Online]. Available: http://www.me.umn.edu /courses/me2011/arduino/arduinoGuide.pdf. [Accessed 18 April 2018].

[111] B. Messner, R. Hill and J. Taylor, "Simulink ArduinoIO Package," [Online]. Available: http://ctms.engin.umich.edu/CTMS/index.php?aux=Activities_IOpack. [Accessed 18 April 2018].

[112] Arduino, "Compare board specs," Arduino, [Online]. Available: https://www.arduino.cc/en /Products.Compare. [Accessed 17 October 2019].

[113] MathWorks, "Simulink Support Package for Raspberry Pi Hardware," MathWorks, [Online]. Available: https://www.mathworks.com/help/supportpkg/raspberrypi/. [Accessed 23 April 2018].

[114] Maker Shed, "Raspberry Pi Comparison Chart," [Online]. Available: https:// www.makershed.com/pages/raspberry-pi-comparison-chart. [Accessed 24 November 2018].

[115] M. Molina-Solana, M. Ros and M. Delgado, "Unifying fuzzy controller for IEQ: implementation in a Raspberry Pi," in *9th Conference of the European Society for Fuzzy Logic and Technology (EUSFLAT)*, Gijón, 2015.

[116] F. Ioannidis, "Intelligent controller based on Rapsberry Pi," University of Manchester, Manchester, pp. 72-98, 2014.

[117] W. Bolton, Programmable Logic Controllers, Burlington: Elsevier, 2006.

[118] M. Z. Haq, "Programmable Logic Controller," Bangladesh University of Engineering and Technology, Bangladesh,

https://pdfs.semanticscholar.org/presentation/bdee/f34f07a9e3b66aff7da7cc8605a9b9410ac5.pdf.

[119] dSPACE, "DS1104 R&D Controller Board," dSPACE, [Online]. Available: https://www.dspace.com/en/pub/home/products/hw/singbord/ds1104.cfm. [Accessed 7 July 2018].

[120] ADINE: Active Distribution Network, "D37 Technical description of RTDS / dSPACE simulation enviroment," 1 October 2007. [Online]. Available: http://www.tut.fi/eee/adine/ADINE_D37.pdf. [Accessed 12 July 2018].

[121] T. He and L. Peng, "Application of Neuron Adaptive PID on DSPACE in Double Loop DC Motor Control System," in *2010 International Conference on Computing, Control and Industrial Engineering*, Wuhan, pp. 257-260, 2010.

[122] R. Silva-Ortigoza, V. M. Hernández-Guzmán, M. Antonio-Cruz and D. Muñoz-Carrillo, "DC/DC Buck Power Converter as a Smooth Starter for a DC Motor Based on a Hierarchical Control," *IEEE Transactions on Power Electronics,* vol. 30, no. 2, pp. 1076-1084, 2015.

[123] DFRobot, "LattePanda Alpha vs LattePanda Original," LattePanda, [Online]. Available: https://www.lattepanda.com/blog-2446.html. [Accessed 14 August 2018].

[124] LattePanda, "Operating System," LattePanda, [Online]. Available: http://docs.lattepanda.com/content/alpha_edition/os/. [Accessed 23 July 2018].

[125] STMicroelectronics, "STM32 Nucleo Boards," [Online]. Available: https://www.farnell.com/datasheets/1801183.pdf. [Accessed 12 July 2018].

[126] STMicroelectronics, "STM32F3 Series," [Online]. Available: https://www.st.com/en/microcontrollers/stm32f3-series.html?querycriteria=productId=SS1576. [Accessed 12 July 2018].

[127] O. Setyawati, H. Suyono, H. M. Himawan, N. Sulistiyanto and M. Rif'an, "Prototype of buck converter using fuzzy logic control for LED driver," in *2018 5th International Conference on Electrical and Electronic Engineering (ICEEE)*, Istanbul, pp. 27-30, 2018.

[128] M. Thamma and K. Homchat, "Real-time implementation of self-tuning fuzzy PID controller for FOPDT system base on microcontroller STM32," in *2017 2nd International Conference on Control and Robotics Engineering (ICCRE)*, Bangkok, pp. 130-134, 2017.

[129] F. Gustafsson and N. Bergman, MATLAB for Engineers Explained, Linkoping: Springer Science & Business Media, 2012.

[130] MathWorks Simulink, "PDF Documentation for Simulink," 2019. [Online]. Available: https://www.mathworks.com/help/pdf_doc/simulink/index.html. [Accessed 24 October 2018].

[131] Analog Devices, "LTspice," [Online]. Available: https://www.analog.com/media/en/simulation-models/spice-models/LTspiceGettingStartedGuide.pdf?modelType=spice-models. [Accessed 26 September 2018].

[132] P. Mathys, "ECEN 1400 - Introduction to Digital and Analog Electronics," May 2014. [Online]. Available: https://ecee.colorado.edu/~mathys/ecen1400/pdf/scad3.pdf. [Accessed 27 September 2018].

[133] T. J. Barlow, S. Latham, I. S. McCrae and P. G. Boulter, "A reference book of driving cycles for use in the measurement of road vehicle emissions," TRL Limited, Department for Transport, Cleaner Fuels & Vehicles, pp. 1-10, 2009.

[134] DieselNet, "Emission Test Cycles," DieselNet, 2019. [Online]. Available: https://www.dieselnet.com/standards/cycles/index.php. [Accessed 23 March 2019].

[135] B. Degraeuwe and M. Weiss, "Does the New European Driving Cycle (NEDC) really fail to capture the NOX emissions of diesel cars in Europe?," *Environmental Pollution,* vol. 222, pp. 234-241, 2017.

[136] DieselNet, "Worldwide Harmonized Light Vehicles Test Cycle (WLTC)," DieselNet, [Online]. Available: https://www.dieselnet.com/standards/cycles/wltp.php. [Accessed 12 July 2018].

[137] K. P. Divakarla, A. Emadi and S. N. Razavi, "Journey Mapping—A New Approach for Defining Automotive Drive Cycles," *IEEE Transactions on Industry Applications,* vol. 52, no. 6, pp. 5121-5129, 2016.

[138] M. Pfriem and F. Gauterin, "Development of real-world Driving Cycles for Battery Electric Vehicles," *World Electric Vehicle Journal,* vol. 8, pp. 14-24, 2016.

[139] J. L. Ziyou Song, X. Han, L. Xu, L. Lu, M. Ouyang and H. Hofmann, "Multi-objective optimization of a semi-active battery/supercapacitor energy storage system for electric vehicles," *Applied Energy,* vol. 135, pp. 212-224, 2014.

[140] A. Sciarretta, M. Back and L. Guzella, "Optimal Control of Parallel Hybrid Electric Vehicles," *IEEE Transactions on control systems technology,* vol. 12, no. 3, pp. 352-363, 2004.

[141] N. Mohan, T. Undeland and W. Robbins, "DC-DC Switch-Mode Converters," in *Power Electronics*, Minnesota, John Wiley & Sons, Inc, 1995, pp. 161-199.

[142] B. Hauke, "Basic Calculation of a Boost Converter's Power Stage," [Online]. Available: http://www.ti.com/lit/an/slva372c/slva372c.pdf. [Accessed 12 November 2018].

[143] B. Hauke, "Basic Calculation of a Buck Converter's Power Stage," [Online]. Available: http://www.ti.com/lit/an/slva477b/slva477b.pdf. [Accessed 13 November 2018].

[144] T. Azib, K. Hemsas and C. Larouci, "Energy Management and Control Strategy of Hybrid Energy Storage System for Fuel Cell Power Sources," *International Review on Modelling and Simulations,* vol. 7, pp. 935-944, 2014.

[145] J. Hu, X. Jiang, M. Jia and Y. Zheng, "Energy Management Strategy for the Hybrid Energy Storage System of Pure Electric Vehicle Considering Traffic Information," *Applied Sciences,* vol. 8, p. 1266, 2018.

[146] T. Mesbahi, N. Rizoug, P. Bartholomeüs, R. Sadoun, F. Khenfri and P. L. Moigne, "Optimal Energy Management for a Li-Ion Battery/Supercapacitor Hybrid Energy Storage System Based on a Particle Swarm Optimization Incorporating Nelder–Mead Simplex Approach," *IEEE Transactions on Intelligent Vehicles,* vol. 2, no. 2, pp. 99-110, 2017.

[147] A. Mamun, Z. Liu, D. M. Rizzo and S. Onori, "An Integrated Design and Control Optimization Framework for Hybrid Military Vehicle Using Lithium-Ion Battery and Supercapacitor as Energy Storage Devices," *IEEE Transactions on Transportation Electrification,* vol. 5, no. 1, pp. 239-251, 2019.

[148] Q. Zhang, W. Deng and G. Li, "Stochastic Control of Predictive Power Management for Battery/Supercapacitor Hybrid Energy Storage Systems of Electric Vehicles," *IEEE Transactions on Industrial Informatics,* vol. 14, no. 7, pp. 3023-3030, 2018.

# Appendix A - Publications

The research generated from this project was presented at a conference and an article was generated and submitted for peer review. This project was peer reviewed by:

- *IEEE International Multidisciplinary Information Technology and Engineering Conference.* This is an international conference where the design and simulated results of the project were presented. The article, with the title "Intelligent controller for a hybrid energy storage system", will be available in the IEEE Xplore Digital Library with the following identification number, IEEE ISBN: 978-1-7281-0040-1, IEEE Conference Number: #45504.

- *World Electric Vehicle Journal:* The WEVJ is a peer-reviewed international scientific journal that covers studies related to battery, hybrid and fuel cell electric vehicles. This is the official journal of the World Electric Vehicle Association (WEVA) and is published quarterly by MDPI. The article has the title "Active hybrid energy storage system utilising a fuzzy logic rule-based control strategy". The journal has the following identification number, ISSN: 2032-6653.

# Intelligent controller for a hybrid energy storage system

Maarten van Jaarsveld
*School for Electrical, Electronic and*
*Computer Engineering*
*North-West University*
Potchefstroom 2531, South Africa
maartenvanjaarsveld@gmail.com

Rupert Gouws
*School for Electrical, Electronic and*
*Computer Engineering*
*North-West University*
Potchefstroom 2531, South Africa
rupert.gouws@nwu.ac.za

**Abstract— The performance and range of electric vehicles are largely determined by the characteristics of the energy storage system (EES) used. The EES should be sufficiently sized to be able to provide the necessary power and energy requirements of the vehicle. Batteries are typically energy dense, although batteries that are both energy and power dense exist, they are much more expensive. The life and usable capacity of batteries are negatively impacted by power impulses. Battery packs in electric vehicles (EV) are typically oversized to be able to provide enough power during these impulses experienced when the vehicle accelerates. An additional EES with a high power density, such as an ultracapacitor, can be used as a buffer to provide power during power surges to reduce the power impulses experienced by the battery. Isolating the battery from the power impulses would allow the EV to utilize more energy dense batteries, increasing the range of the EV as well as increasing the lifetime of the utilized batteries. A hybrid energy storage system (HESS) allows one to utilize the complimentary characteristics of both the battery and ultracapacitor in one system. The method proposed uses a fuzzy logic controller, multiple dc/dc converters, batteries and ultracapacitors in a HESS to minimize the power impulses experienced by the battery, thereby increasing the usable capacity of the battery, whilst being able to deliver high amounts of power for short durations.**

*Index Terms—Hybrid Energy Storage System, Drive Cycle, Fuzzy Logic, Matlab®/Simulink®, Boost Converter, Buck Converter*

## 1 INTRODUCTION

Fossil fuels are considered as the main causes of global warming. Growing consumer expectations and legislation to reduce fossil fuels impact on the environment has resulted in the automotive industry focusing on electric and hybrid electric vehicles (EVs, HEVs). By the end of 2018 the cumulative sales of plug-in EVs (PEVs) have surpassed 5 million units, with 49.1% of new car sales in Norway consisting out of PEVs [1]. The limiting factor in developing EVs that have adequate performance compared to that of internal combustion vehicle (ICEV) is the energy storage system (ESS) [2] - [3]. Batteries are the most commonly used ESS in EVs due to their high energy density and reliability compared to other ESSs. However, batteries have a low cycle life, are expensive and their energy density pales in comparison to that of gasoline/diesel as used in ICEVs. Batteries also have a low power density and exhibits poor performance at low temperature.

One-third of the total production cost of an EV is dedicated to the ESS, but this is dependent on the type of ESS used [4]. EVs require a high power, high energy dense ESS, but batteries in general possess either of these characteristics, not both [5], [6]. Considering the cost, size and weight of the battery pack, a small energy dense pack would be ideal, but they are usually unable to provide the necessary power to the vehicle during acceleration. This requires the use of additional batteries, increasing the weight and cost of the battery pack, or more power dense batteries need to be used, reducing the total amount of energy stored.

## 2 HYBRID ENERGY STORAGE SYSTEMS

Hybrid energy storage systems (HESS) have been proposed to solve the problems listed above [7] - [8]. A HESS is characterized as a system that beneficially couples two or more ESS with supplementary characteristics (such as power and energy density, cost, cycle life, etc.). The degree of improvement that the HESS provides depends intrinsically on how the sources are integrated and controlled. Two ESSs that complement each other are batteries and ultracapacitors (UCs). UCs have a high power density but a low energy density compared to batteries [9]. The cycle life of UCs is also orders of magnitude larger than that of batteries [10]. Hence UC can be used in as part of a HESS for the following purposes:

1) to improve vehicle acceleration;
2) to improve overall drive efficiency;
3) reduce life cycle costs by extending battery life through power smoothing.

HESS are divided into three types: passive, semi-active and active HESS topologies. The passive HESS topologies simply connect the ESS devices in parallel with the dc bus. When batteries and UCs are combined in this topology, the power sharing ratio between the two devices is dependent on their internal resistances [11] - [13]. UCs usually have a much lower internal resistance compared to batteries and therefore acts as a low pass filter in this topology [11], [13]. When power is supplied to a periodically pulsing load the power sharing ratio is also dependant on the frequency and duty cycle of the pulsed load [13]. Although this topology improves the performance of a battery only system for pulsed loads, the system has limited benefit in other load profiles [14]. An advantage of this topology is the simplicity, but has the disadvantage that the energy flow between the devices cannot be controlled. To be able to control the energy flow between the devices and the load, semi-active and active HESS topologies were developed.

Semi-active topologies utilize one dc/dc converter to be able to control the flow of energy from one of the ESS devices to the other [11]. The drawback of this topology is that the limited control in the flow of energy in this topology. For the semi-active topology shown in figure 1 the battery is directly connected to the dc bus and is susceptible to power spikes from the dc bus [2], [11]. This topology is able to sufficiently utilize the energy stored in the UC, but the dc/dc converter needs to be sufficiently sized. The nominal voltage of the UC does not have to match that of the battery as in the parallel topology. The topology shown in figure 2 directly connects the UC to the dc bus, which results in the battery being isolated from the dc bus, but results in dc bus voltage swings as the UC is depleted or charged [11].
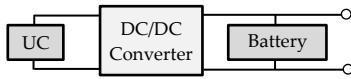


Fig. 1. Semi-active topology UC/battery [14], [21]



Fig. 2. Semi-active topology battery/UC [14]

Active HESS topologies utilize more than one dc/dc converter to be able to control the flow of energy from each ESS device. The cascaded topology as depicted in figures 3 and 4, improves on the semi-active topology by utilizing one more dc/dc converter. This allows the voltage of the SC and battery to vary independently from the dc bus [12], [14]. This allows this topology to effectively use the energy stored within the SC. Although this topology allows the effective use of the EES devices, additional costs and weight results from this topology, seeing that an additional converter is required.
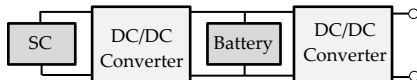


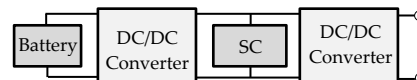Fig. 3. Cascaded UC/battery topology [14]



Fig. 4. Cascaded battery/UC topology [14]

The multiple converter topology as depicted in figure 5, also makes use of two dc/dc converters as in the cascaded topology, but connects each ESS device through the dc/dc converter in to the dc bus in parallel. This topology also allows the voltage of each ESS to vary independently. The flow of energy throughout this system is also easy to control. The topology is also tolerant of failures, even if one converter fails, the other ESS device can still supply power.

One way of improving on the above described topology is by utilizing a multiple input converter topology. The multi input converter topology simply utilizes a multiple input dc/dc converter. This reduces the cost and weight of the overall system due to the fact that only one dc/dc

converter is required, but requires a more complex control strategy.
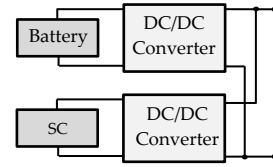


Fig. 5. Multiple converter topology [14]

In this paper the topology depicted in figure 6 was investigated and simulated. This topology utilizes a switch to directly connect the battery to the load, to avoid the losses induced by connecting the battery to the load through a dc/dc converter. Two dc/dc converters are utilized in this topology.
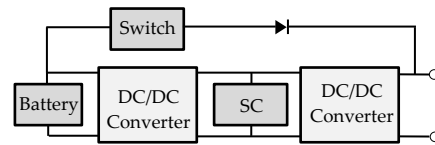


Fig. 6. Topology used in this paper [21]

## METHODOLOGY

### 3 DRIVE CYCLE

In various countries emission tests are required by law for all new light-duty ICE vehicles. Vehicle exhaust emissions are inherently variable, thus standardized drive cycles were developed to be able to conduct an emission test under reproducible conditions [15]. Drive cycles are also used to determine engine or drive train durability [15]. Three drive cycles were used in this paper to evaluate the performance of the deployed HESS, this includes the EPA New York City Cycle (NYCC) and the ECE 15 drive cycle. The NYCC drive cycle as illustrated in figure 7 was developed to simulate low speed urban driving with frequent stops. The ECE-15 drive cycle was designed to represent typical driving conditions in busy European cities.
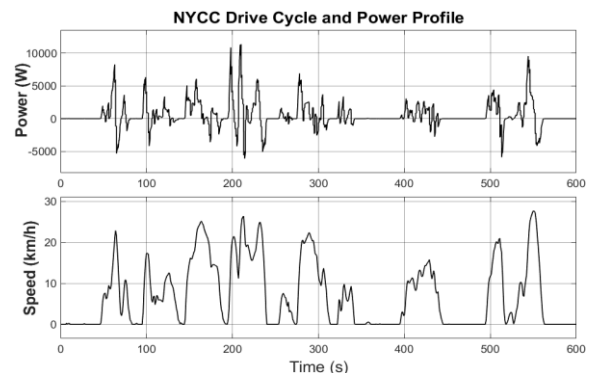


Fig. 7. NYCC drive cycle and calculated power profile [15]

As the reader may note, the profiles only specify the speed at which the vehicle must be travel at a certain point in time, but not the power that needs to be generated by the motor.

To calculate the power required, the resistive forces on the vehicle at a speed $v(t)$ can be calculated using (3):

$$F_d(v(t)) = \frac{1}{2}\rho_a c_D A v(t)^2 + g m_t \sin\varphi(t) + F_r(v(t)) \qquad (1)$$

where $c_R$ is the coefficient of rolling resistance, $m$ is the mass of the vehicle, $g$ is the gravitational constant, $\rho$ is the density of air, $c_D$ is the drag coefficient, $A$ is the frontal surface area of the vehicle and $V$ is the vehicle velocity. $F_d(v(t))$ is the resultant force of the summation of the aerodynamic drag, grading resistance and the rolling resistance $F_r(v(t))$. The rolling resistance is described by a fifth-order polynomial function of the vehicle speed i.e.

$$F_r(v(t)) = g m_t \cos\varphi(t)\{ a_0 + a_1 v(t) + a_2 v(t)^2 + \\ a_3 v(t)^3 + a_4 v(t)^4 + a_5 v(t)^5\} \qquad (2)$$

where $a_0,\ldots,a_5$ are experimentally determined coefficients. In this paper the coefficients determined in the work of Sciarretta $et\ al.$ [16]. The torque at the wheels required to accelerate the vehicle is calculated as

$$\tau_{wh} = \mathrm{r}_{wh} F_d(t) + \frac{\theta_v}{\mathrm{r}_{wh}}\frac{dv(t)}{dt} \qquad (3)$$

where $\theta_v$ is the inertia of the vehicle and $\mathrm{r}_{wh}$ is the radius of the wheels. The rotational speed of the wheels is simply calculated as

$$\omega_{wh}(t) = v(t)/\mathrm{r}_{wh}. \qquad (4)$$

When the vehicle utilizes a gearbox, the rotational torque ($\tau_m$) and speed ($\omega_m$) of the motor inverter is calculated as

$$\tau_m(t) = \tau_{wh}(t)/G_r \qquad (5)$$

$$\omega_m(t) = \omega_{wh}(t)/G_r. \qquad (6)$$

The input power of the motor-inverter is then

$$P_m = \begin{cases} \tau_m(t)\omega_m(t)/\eta_{inv}, & for\ \tau_m(t) > 0 \\ \tau_m(t)\,\omega_m(t)\,\eta_{inv}, & otherwise \end{cases} \qquad (7)$$

where $\eta_{inv}$ is the motor inverter efficiency, which is a function of $\omega_m(t)$ and $\tau_m(t)$.

## 4 CONTROL APPROACH

This section discusses the approach taken to control the system.

### 4.1 Overall control scheme

The control system consists out of two dc/dc converters, which are used to control the flow of energy from the battery/UC throughout the system. The overhead controller measures the SOC of the battery and UC as well as the load power as shown in figure 8 and utilizes the control scheme shown in figure 9 to determine the flow of energy in the system. The maximum nominal battery power is set by the user and the controller then attempts to limit the maximum power draw from the battery. The two dc/dc converter that are used utilize fuzzy logic control to control the flow of power throughout each dc/dc converter. The overhead controller determines how power should flow throughout the system and relays that information to the fuzzy logic controllers.
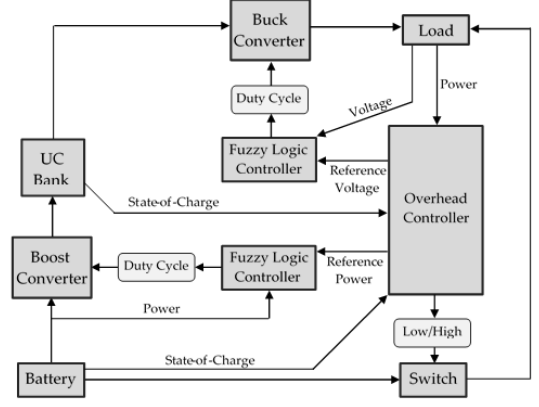


Fig. 8. Overall control topology

### 4.2 Power flow

The operating modes of the HESS is discussed in this section. When the load power is lower than that of the nominal battery power, the battery is directly connected to the load through the switch, bypassing any dc/dc converter losses. If the SOC of the UC is below 95%, the battery charges the UC so that the following holds true

$$P_{load} + P_{UC} \leq Battery\ Power\ Limit. \qquad (8)$$

If the SOC of the UC is above 95%, then the battery only provides the required power to the load through the switch.
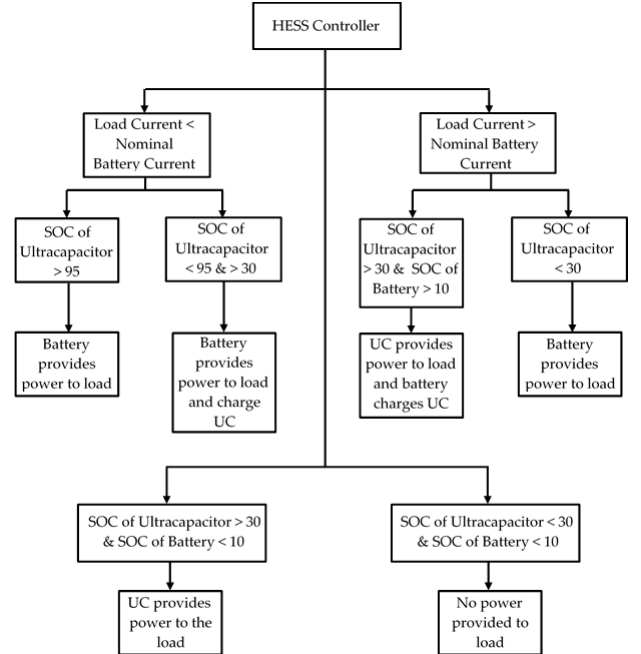


Fig. 9. Control scheme

If the load power is higher than the nominal battery current and the SOC of the UC is higher than 30%, the UC provides power through the buck converter to the load, whilst the battery charges the UC at the maximum nominal battery power limit. If the SOC of the UC is below 30% and the SOC of the battery is above 10%, then the battery provides power to the load. If the SOC of the battery is below 10%, but the UCs SOC is above 30% then the UC provides power to the load, independent of the load size. If the SOC of the UC is below 30% and the SOC of the battery is below 10%, no power is provided to the load.

The system is structured in such a way that output reference voltage of the buck converter connected to the load is equal to that of the battery, to try and reduce any voltage dips/spikes on the load bus as the system switches between the battery and the buck converter. The battery's nominal voltage was chosen at a voltage lower than half of that of the UC bank, to ensure that a large percent of energy stored in UC could be utilized. A boost converter was then necessary to be able to charge the UC from the battery. This configuration allows the SOC of the UC and the battery to vary as required, whilst reducing any power spikes on the dc bus as the system switches between the battery and the buck converter.

## 4.3 Fuzzy Logic Control

Fuzzy logic, which provides a formalized method of reasoning which is approximate rather than exact, was used to control the two dc/dc converters in the HESS. A buck and a boost converter were used, as can be seen from figure 8. A control system was required for these dc/dc converters in order to be able to control the amount of energy being transferred throughout the system, according to the control structure depicted in figure 9. The fuzzy logic controller structure is shown in figure 10.
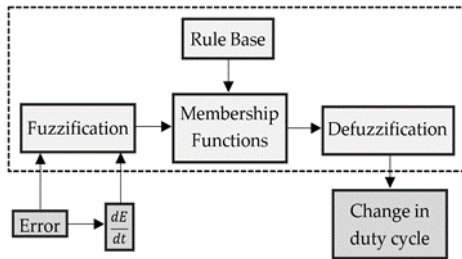


Fig. 10. Fuzzy controller [22]

A fuzzy logic controller was independently implemented for the buck converter and the boost converter. The fuzzy logic controller does not require a detailed model of the dc/dc converter; instead it only uses the error and rate of change of the error, wherein the error is the difference between the set-point value and the actual value of the system. The same fuzzy logic controller was used for both control systems. There was thus still two fuzzy controller units, as depicted in figure 8. The fuzzy logic controller subsystem as implemented in Matlab®/Simulink® is shown in figure 11. A saturation block limits the maximum and minimum output duty cycle of the controller.
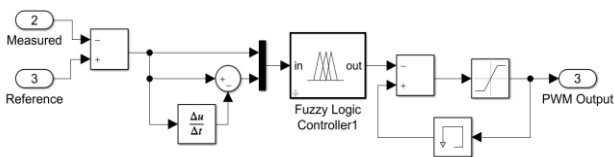


Fig. 11. Fuzzy controller subsystem

The fuzzy logic controller has two inputs, i) error between the controlled value and the reference value and ii) the rate of change of the error. The two input membership functions are shown in figure 12 and figure 13 respectively.

The input range of the membership functions were changed and varied during the simulation process until the controller performed satisfactorily. Adjusting the input range of the membership functions, adjusts the gain and inversely the sensitivity of the input functions.
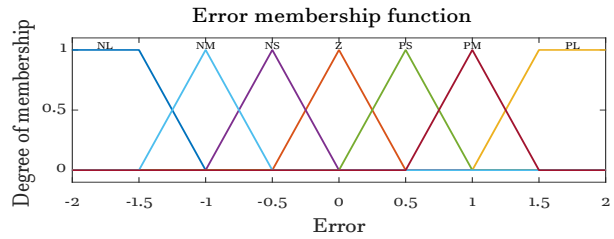


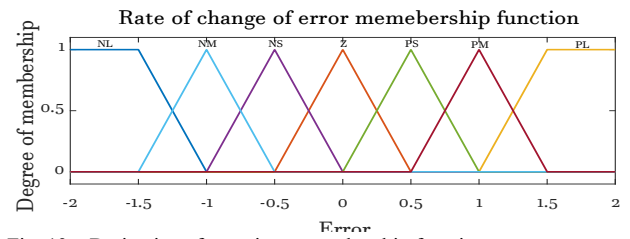Fig. 12. Error input membership function



Fig. 13. Derivative of error input membership function

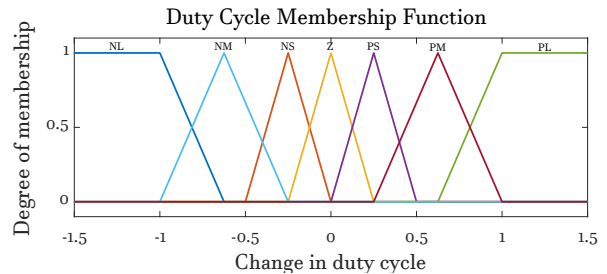The output membership function is shown in figure 14.



Fig. 14. Output membership function

The fuzzy rules employed for the fuzzy logic controller is shown in table I.

Table I. Fuzzy rules

| | | Δ Error | | | | | | |
|---|---|---|---|---|---|---|---|---|
| | | NL | NM | NS | Z | PS | PM | PL |
| Error | NL | NL | NL | NL | NM | NM | NS | Z |
| | NM | NL | NM | NM | NS | NS | Z | PS |
| | NS | NB | NM | NS | NS | Z | PS | PM |
| | Z | NM | NS | NS | Z | PS | PS | PM |
| | PS | NM | NS | Z | PS | PS | PM | PL |
| | PM | NS | Z | PS | PS | PM | PM | PL |
| | PL | Z | PS | PM | PM | PL | PL | PL |

Where:
**N** - Negative     **Z** – Zero     **P** – Positive
**S** - Small       **M** – Medium     **L** - Large

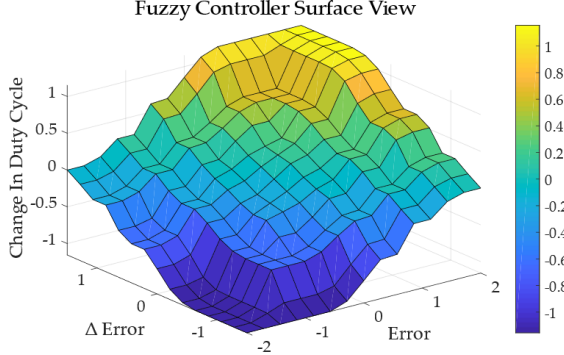The rule surface resulting from these rules is shown in figure 15.



Fig. 15. Fuzzy rules surface view

The rules resulting from the rule table can be summed up as
follows:

- If the error is zero and the change in the error is also zero, keep the duty cycle the same.
- If the error is negative and the change in error is negative, the duty cycle decreases.
- If the error is negative and the change in error is positive, the duty cycle increases.
- If the error is positive and the change in error is negative, the duty cycle decreases.
- If the error is positive and the change in error is positive, the duty cycle increases.

### 4.4 DC/DC converter

The dc/dc converter topologies utilized in the HESS to control the flow of energy throughout the system. The topology for a buck converter is shown in figure 16.
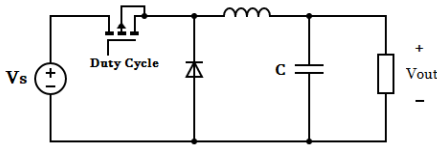


Fig. 16. Buck converter topology

The output voltage of the buck converter is
$$V_{out} = V_s D \qquad (8)$$
and the output current is
$$I_{out} = I_s D. \qquad (9)$$

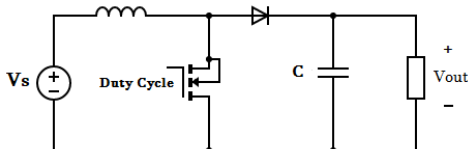The topology for the boost converter is shown in figure 17.



Fig 17. Boost converter topology

The output voltage and current for the boost converter is inversely proportional to the duty cycle, as described by
$$V_{out} = V_s \frac{D}{1 - D}$$
and the output current is
$$I_{out} = I_s \frac{D}{1 - D}.$$

## 5 RESULTS

The HESS was simulated in Matlab®/Simulink®. The performance of the active HESS structure was compared to that of a passive HESS structure. The load profiles that were tested consisted out of a periodically repeating pulsed load, the NYCC, ECE 15 and the LA 92 drive cycles. The performance of the passive structure is shown first for a specific load profile, then the active systems performance is shown.

### 5.1 Pulsed load profile

A periodically repeating load profile with a period of 25s with a duty cycle of 20% was tested. The performance of the passive system is shown in figure 18. The load profile is shown in black, the ultracapacitor power is shown in red, whilst the battery power is shown in blue.
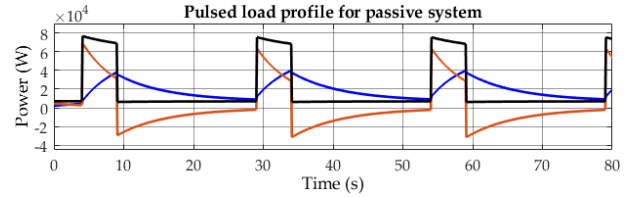


Fig. 18. Passive system performance for a pulsed load

From figure 18 we can see that the initial load sharing is solely determined by the ratio of the internal resistance of the UC and the battery. An UC with a large capacitance would be able to supply the load for longer at the initial power sharing ratio. Figure 16 shows the performance of the active HESS topology. The user sets the maximum allowable power draw from the battery, and the system limits the power draw accordingly.
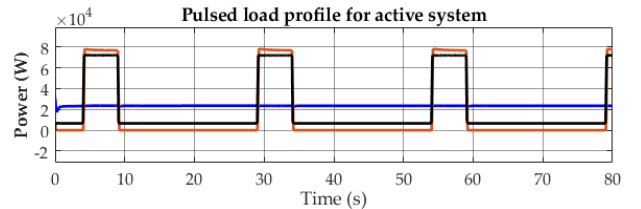


Fig. 19. Active system performance for a pulsed load

It might appear as if the system only provides a constant amount of power through the boost converter to the UC, but the system actively switches into the different modes as outlined in the control strategy shown earlier in figure 9. To show this, figure 17 shows the power flowing from the battery, through the boost converter, to the UC ("Boost

Converter Power") and the power flowing from the battery, through the bypass switch, to the load ("Switch Power").
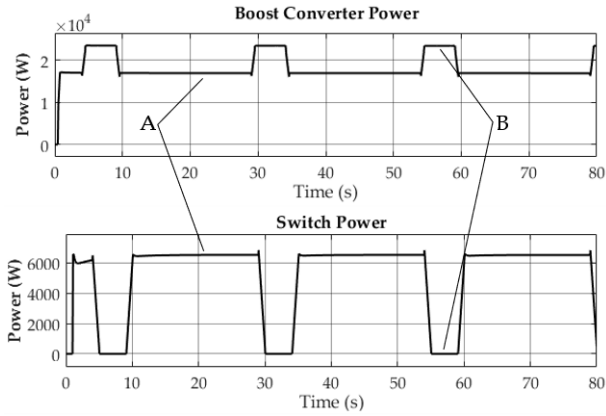

Fig. 20. Boost converter and switch power during mode switches

At point A in time, when the load current is low, the battery provides power through the switch to the load, whilst any reserve power is used to charge the UC. The rate at which the UC is charged at is equal to the battery power limit minus load power. The load power is equal to switch power in the operating mode at point A, thus the switch power plus the load power is equal to the battery power. At point B, the system provides power through the UC to the load, whilst the battery charges the UC through the boost converter at a rate equal to the maximum power limit of the battery.

## 5.2 Drive cycle load profile

The NYCC drive cycle was simulated and the performances of the passive and active system are compared. We can note from figure 21 that the passive system does reduce the maximum power spikes experienced by the battery.
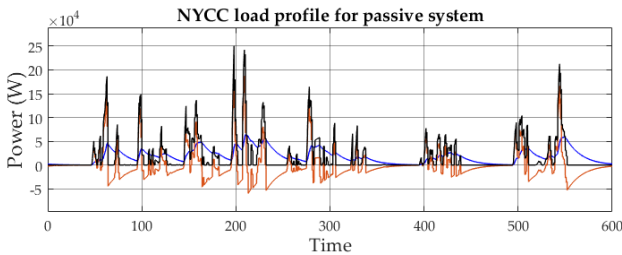

Fig. 21. NYCC load profile for passive system

The performance of the active system is shown in figure 22. We can see that the system satisfactorily limits the maximum power drawn from the battery. Figure 23 shows a section of the NYCC load profile to show the power flowing through the boost converter and the switch as the HESS switches between different operating modes.
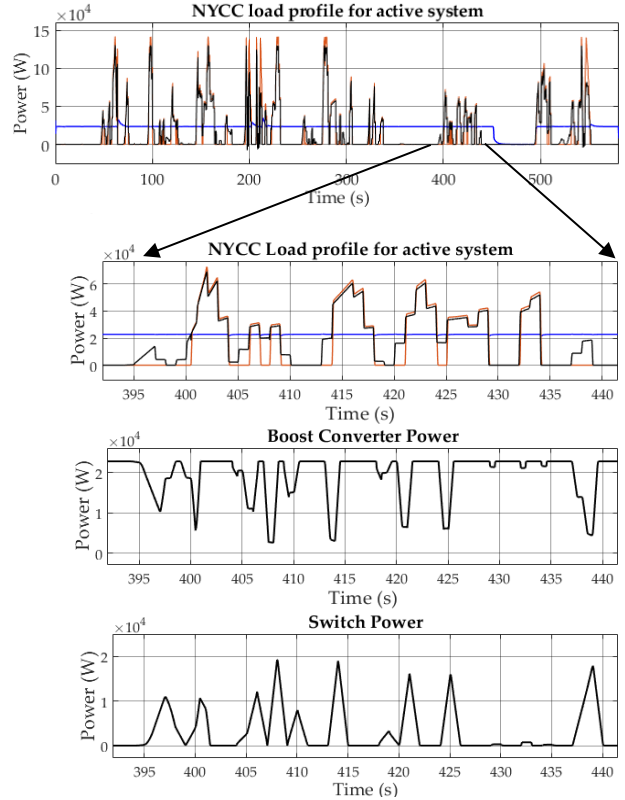

Fig. 22. NYCC load profile for active system. A magnified portion of the drive cycle is also shown, with the power flowing through the boost converter and the switch.

The ECE15 drive cycle was also simulated. The resultant load profile for the passive topology is shown in figure 23.
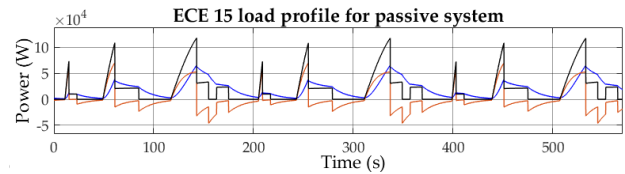

Fig. 23. ECE 15 load profile for passive system

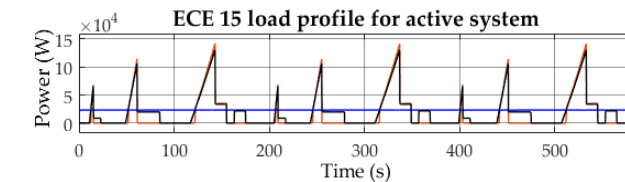The resultant load profile for the active system is shown in figure 24.


Fig. 24. ECE 15 load profile for active system

## 6 LIMITATIONS

The main limitation of this study is that only unidirectional dc/dc converters were used. Ideally bidirectional dc/dc converters would be used, so that the UC bank can be used to absorb the power generated by the vehicle during regenerative breaking. Unidirectional converters were chosen to simplify the physical design complexity of the system, seeing that the work used in the

paper was used to construct a scaled-down physical system of the simulated system. Future work could alter the design to include bidirectional converters. Fuzzy logic controllers can still be used to control these bidirectional dc/dc converters whilst the overall control scheme can be altered to include the control conditions to manage bidirectional power flow.

## 7    CONCLUSION

In this paper a controller and control topology for a HESS was proposed that limits the maximum amount of power that can be drawn from a battery. This was done by using an overhead controller that measures the load power and the SOC of the battery and UC, and then accordingly outputs the required power to a fuzzy logic controller to control the flow of power through the boost converter accordingly.

The controller was simulated using Matlab®/Simulink® and the results show that the topology and control strategy improves over the passive topology in reducing the peak power impulses on the battery. This would allow one to utilize batteries with a high energy density, instead of power dense batteries, which would increase the range of the vehicle.

## REFERENCES

[1]  F. Watson, "December global electric vehicle sales set new record: S&P Global Platts data," 11 Feb 2019. [Online]. Available: https://www.spglobal.com/platts/en/market-insights/latest-news/electric-power/021119-december-global-electric-vehicle-sales-set-new-record-sampp-global-platts-data.

[2]  Z. Song, H. Hofmann, J. Li, X. Han, X. Zhang and M. Ouyang, "A comparison study of different semi-active hybrid energy storage," *Journal of Power Sources,* vol. 274, pp. 400-411, 2015.

[3]  M. Choi, J. Lee and S. Seo, "Real-Time Optimization for Power Management Systems of a Battery/Supercapacitor Hybrid Energy Storage System in Electric Vehicles," *IEEE Transactions on Vehicular Technology,* vol. 63, no. 8, pp. 3600-3611, 2014.

[4]  M. Hannan, M. Hoque, A. Mohamed and A. Ayob, "Review of energy storage systems for electric vehicle applications: Issues and challenges," *Renewable and Sustainable Energy Reviews,* vol. 69, pp. 771-789, 2017.

[5]  T. Amietszajew, E. McTurk, J. Fleming and R. Bhagat, "Understanding the limits of rapid charging using instrumented commercial 18650 high-energy Li-ion cells," *Electrochimica Acta,* pp. 346-352, 2018.

[6]  P. V. Braun, J. Cho, J. H. Pikul, W. P. King and H. Zhang, "High power rechargeable batteries," *Current Opinion in Solid State and Materials Science,* vol. 16, no. 4, pp. 186-198, 2012.

[7]  J. Dixon, I. Nakashima, E. F. Arcos and M. Ortuzar, "Electric Vehicle Using a Combination of Ultracapacitors and ZEBRA Battery," *IEEE Transactions on Industrial Electronics,* vol. 57, no. 3, pp. 943-949, 2010.

[8]  R. Xiong, H. Chen, C. Wang and F. Sun, "Towards a smarter hybrid energy storage system based on battery and ultracapacitor - A critical review on topology and energy management," *Journal of Cleaner Production,* vol. 202, pp. 1228-1240, 2018.

[9]  A. Khaligh and Z. Li, "Battery, Ultracapacitor, Fuel Cell, and Hybrid Energy Storage Systems for Electric, Hybrid Electric, Fuel Cell, and Plug-In Hybrid Electric Vehicles: State of the Art," *IEEE Transactions on Vehicular Technology,* vol. 59, no. 6, pp. 2806-2814, 2010.

[10]  J. M. Miller, "Energy storage system technology challenges facing strong hybrid, plug-in and battery electric vehicles," in *IEEE Vehicle Power and Propulsion Conference*, Dearborn,USA, 2009.

[11]  A. Kuperman, I. Aharon, S. Malki and A. Kara, "Design of a Semiactive Battery-Ultracapacitor Hybrid Energy Source," *IEEE Transactions on Power Electronics,* vol. 28, no. 2, pp. 806-815, 2013.

[12]  L. H. Seim, "Modeling, Control and Experimental Testing of a Supercapacitor/Battery Hybrid System -Passive and Semi-Active Topologies," Norwegian University of Life Sciences, Ås, Norway, 2011.

[13]  Z. Song, J. Li, X. Han, L. Xu, L. Lu, M. Ouyang and H. Hofmann, "Multi-objective optimization of a semi-active battery/supercapacitor energy storage system for electric vehicles," *Applied Energy,* vol. 135, pp. 212-224, 2014.

[14]  J. C. a. A. Emadi, "A New Battery/UltraCapacitor Hybrid Energy Storage System for Electric, Hybrid, and Plug-In Hybrid Electric Vehicles," *IEEE Transactions on Power Electronics,* vol. 27, no. 1, pp. 122-132, 2012.

[15]  T. J. Barlow, S. Latham, I. S. McCrae and P. G. Boulter, "A reference book of driving cycles for use in the measurement of road vehicle emissions," TRL Limited, Department for Transport, Cleaner Fuels & Vehicles , 2009.

[16]  A. Sciarretta, M. Back and L. Guzella, "Optimal Control of Parallel Hybrid Electric Vehicles," *IEEE Transactions on control systems technology,* vol. 12, no. 3, pp. 352-363, 2004.

[17]  S. M. Lukic, J. Cao, R. C. Bansal, F. Rodriguez and A. Emadi, "Energy Storage Systems for Automotive Applications," *IEEE Transactions on Industrial Electronics,* vol. 55, no. 6, pp. 2258-2267, 2008.

[18]  P. J. Kollmeyer, A. Shridar and T. M. Jahns, "Modeling of low-temperature operation of a hybrid energy storage system with a Butler-Volmer equation based battery model," in *IEEE Energy Conversion Congress and Exposition (ECCE)*, Milwaukee, 2016.

[19]  M. O. Badawy, T. Husain, Y. Sozer and J. A. D. Abreu-Garcia, "Integrated Control of an IPM Motor Drive and a Novel Hybrid Energy Storage System for Electric Vehicles," *IEEE Transactions on Industry Applications,* vol. 53, no. 6, pp. 5810-5819, 2017.

[20]  M. Masih-Tehrani, M.-R. Ha'iri-Yazdi, V. Esfahanian and A. Safaei, "Optimum sizing and optimum energy management of a hybrid energy storage system for lithium battery life improvement," *Journal of Power Sources,* vol. 244, pp. 2-10, 2013.

[21]  C. Xiang, Y. Wang, S. Hu and W. Wang, "A New Topology and Control Strategy for a Hybrid Battery-Ultracapacitor Energy Storage System," *Energies,* vol. 7, pp. 2874-2896, 2014.

[22]  A. Ali, "Hybrid Fuzzy Logic Scheme for Efficient Channel Utilization in Cognitive Radio Networks," *IEEE Access,* vol. 7, pp. 24463-24476, 2019.

# Appendix B

Figure B.1 shows a 3D rendering of the PCB that was designed for the integrated system. The 3D rendering allows one to visually check that all the components have enough physical space on the designed PCB.
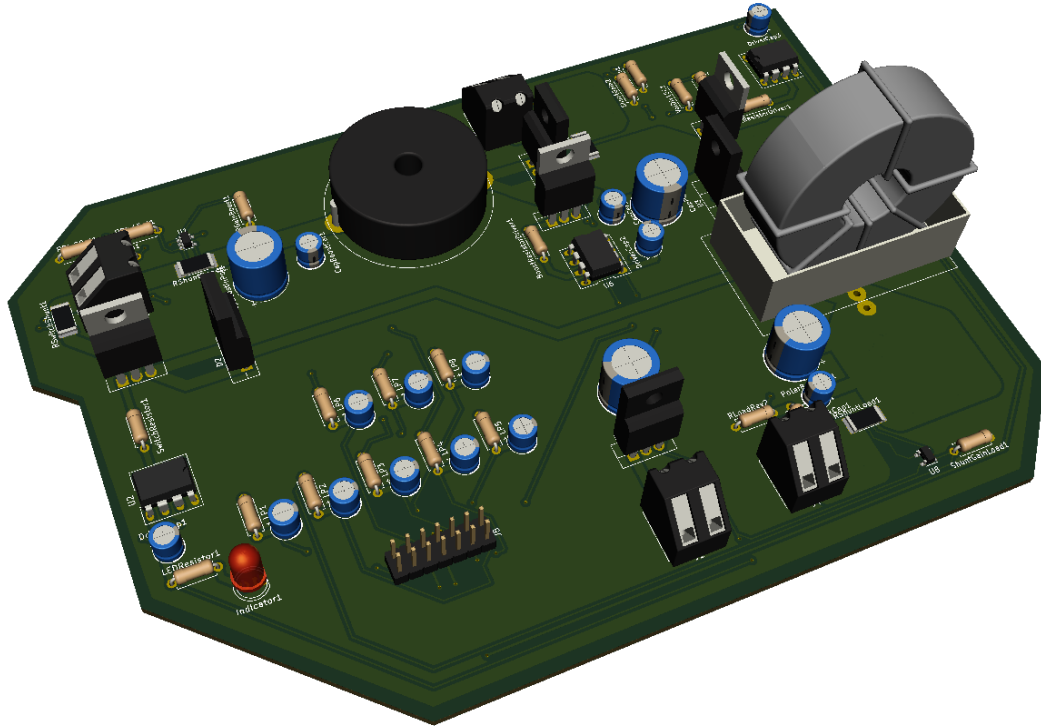


Figure B.1: PCB Rendering

Figure B.2 shows a portion of the schematic that was created to design the PCB. The full schematic is available in the "Schematics and PCB" folder as indicated in appendix C.
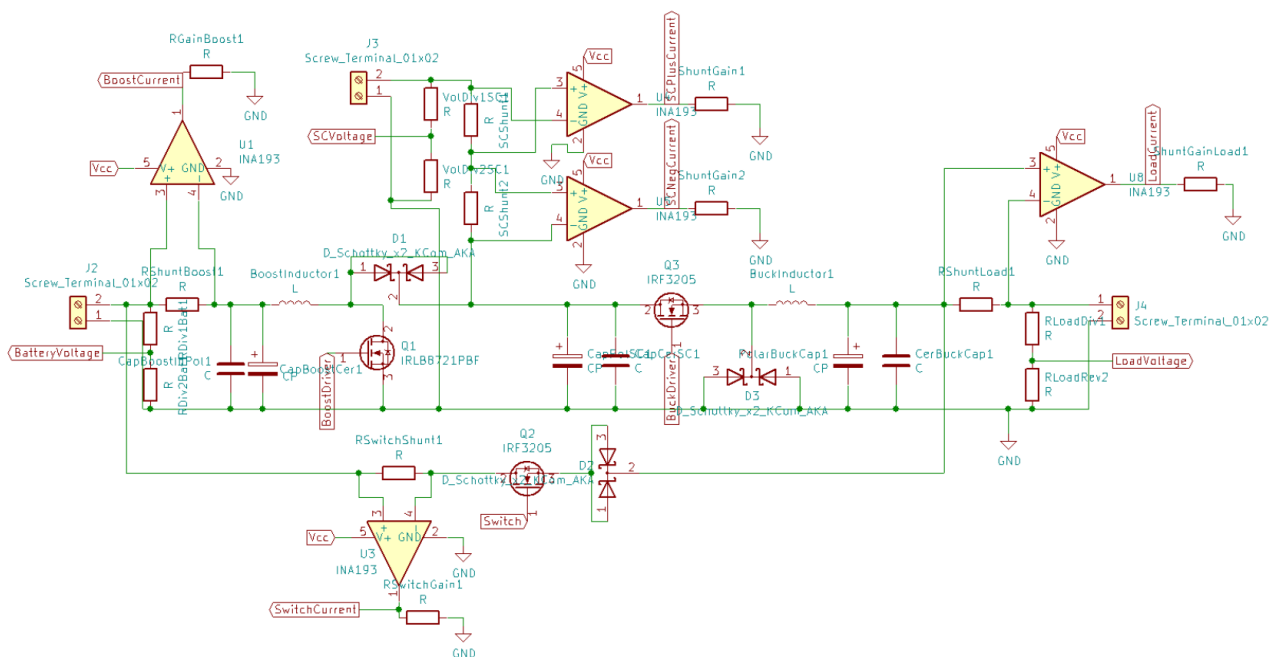


Figure B.2: Portion of the schematic created for the PCB